PUBLICATION OF THE SEMINAR PROCEEDINGS IS DEDICATED TO THE MEMORY OF V. F MASTEROV

INTAS–RFBR Seminar on Rare-Earth Impurities in Semiconductors and Low-Dimensional Semiconductor Structures, St. Petersburg State Technical University, October 26, 1998

OPENING ADDRESS

B. P. Zakharchenya

Fiz. Tekh. Poluprovodn. **33**, 641 (June 1999)

[S1063-7826(99)00106-4]

As is widely known, the creation of emitters based on silicon (in the crystalline or amorphous state) doped with erbium ions has attracted the attention of many research groups throughout the world. The attention is attributable to the possibility of producing efficient emitters that operate at a wavelength of 1.5 μm, where fibers transmitting optical signals exhibit their peak transparency, as well as the fact that such an emitting element can be smoothly integrated into silicon optoelectronic devices.

The creation of such a laser is clearly the ''dream'' of integrated optics. The realization of this dream depends on a deep understanding of the physical processes involved in exciting electronic levels of the erbium ion that are located in the valence band of the semiconductor and on knowledge of the details of the energy level diagram of erbium, which often forms large centers with its local environment in the matrix. Unfortunately, for a number of reasons, the electron paramagnetic resonance signal of Si–Er systems is poorly displayed or not observed at all. Therefore, the most effective experimental method is measurement of the luminescence excited by a current in a $p-n$ junction or photoluminescence.

Representatives of groups from Italy, the Netherlands, and Russia (Moscow and St. Petersburg), who are involved in the technology of fabricating Si–Er devices and are developing physical methods for investigating these objects, have gathered in the A. F. Ioffe Physicotechnical Institute and the St. Petersburg State Technical University to participate in this seminar.

The research teams in the Physicotechnical Institute (which is closer to me) have obtained the following noteworthy results.

— A new mechanism for exciting erbium ions in a reverse-biased $p-n$ junction as a result of the recombination of electrons from the upper conduction subband with valence-band holes has been discovered.

— The mechanism of electroluminescence in amorphous silicon has been thoroughly studied.

— Electroluminescent structures based on crystalline silicon, which exhibit diverse luminescence characteristics, have been obtained on substrates with various crystallographic orientations.

I wish this small seminar success and our guests pleasant impressions of St. Petersburg.

Translated by P. Shelnitz

 © 1999 American Institute of Physics

Erbium-doped silicon epilayers grown by liquid-phase epitaxy

S. Binetti and S. Pizzini

INFM and Department of Materials Science, Via Cozzi 53, I-20126 Milano, Italy

A. Cavallini and B. Fraboni

INFM and Department of Physics, Via Berti Pichat 6/2 I-40137 Bologna, Italy

(Submitted January 12, 1999; accepted for publication January 12, 1999)
Fiz. Tekh. Poluprovodn. **33**, 642–643 (June 1999)

A careful analysis of the features of the spectroscopic properties of Er-doped and undoped epitaxial silicon films grown by liquid-phase epitaxy at 950 °C in silicon-saturated indium melts shows that threading dislocations work as effective gettering sites for erbium and oxygen. The last impurity is incorporated in the epitaxial film by back diffusion from the Czochralski substrate during the growth. The photoluminescence emitted by these films appears to be related to the dislocation and is enforced by the presence of erbium-oxygen complexes. © *1999 American Institute of Physics.* [S1063-7826(99)00206-9]

INTRODUCTION

We have already shown in previous papers[1,2] that Er:Si epilayers grown by liquid-phase epitaxy (LPE) in indium melts present, in the alternative to the intrinsic Er^{3+} photoluminescence (PL) band at 0.8 eV, two intense PL bands at 0.807 and 0.873 eV (at 10 K), of which the first falls within few meV in the same energy range of the Er band but quenches out at higher temperatures.

In addition to the band edge luminescence, the band at 0.8 eV was also observed in the Er-free samples. Since the band at 0.8 eV in Er-doped samples does not exhibit the fine structure associated with the Er^{3+} multiplet and since both bands fall in the energy range of the $D1$ and $D2$ bands of the dislocations, these PL effects are attributed to dislocations generated by strain-release effects at the interface between the epilayer, which incorporates Er and In as dopants at a concentration level on the order of $10^{17}\,cm^{-3}$ for Er and $10^{16}\,cm^{-3}$ for In, and the substrate. Dislocations were, in fact, clearly identified by selective etching, but no clear indication about a possible role of the erbium dopant at the dislocation luminescence was found.

Our aim in this paper is to add further insights into these effects, which might help in the future development of silicon-based optoelectronics.

EXPERIMENTAL DETAILS

The LPE Si:Er epilayers were grown from 99.99% pure indium melts which are saturated in silicon and which contain variable amounts of Er deposited on the Czochralski (CZ) or float-zone (FZ) silicon substrates. The growth temperature was held at 950 °C. Other details about the growth conditions were reported in Ref. 2. The indium concentration in the epilayer was found to be reasonably close to the saturation at the growth temperature, while that of Er ranged between 10^{17} and $10^{18}\,cm^{-3}$. The average thickness of the layers was close to 4 μm, as measured by spreading resistance measurements.

EXAFS measurements, addressed at the study of the local structure of the Er^{+3} ion in the silicon matrix, were carried out at the European Synchrotron Radiation Facility in Grenoble (France) using the Italian GILDA beam line. Details about the measurement conditions were reported in Ref. 3.

Photoluminescence measurements were performed in the 2 to 300-K range using the multiline emission of an Ar ion laser as the exciting sources, as was described in Ref. 1.

Deep level transient spectroscopy (DLTS) and optical DLTS measurements were carried out with a SULA Tech. Inc. system in the 80 to 350-K temperature range.[4]

EXPERIMENTAL RESULTS

Local structure of erbium in LPE-grown epilayers

The results of EXAFS measurements showed that the local structure of Er ions in a dislocation-free LPE-grown Si:Er epilayer is that of the erbium silicide, regardless of the nature of the substrate, which could be either FZ or CZ silicon. In the case of epilayers grown onto CZ silicon substrates, the presence of threading dislocations in the epilayer causes instead a strong change in the local coordination of Er, which gives the typical features of Er in a matrix of erbium oxide. The same Er coordination could be observed in Er-O coimplanted samples. As in the case of LPE samples grown on CZ substrates, oxygen back diffuses from the substrates, which acts as an oxygen source. It can be concluded that only in the presence of dislocations does the formation of Er-O clusters occur during the growth process, where dislocations act as heterogeneous nucleation centers of the erbium oxide.

Photoluminescence of dislocations in Er-free and Er-doped LPE materials

A comparison of the PL spectra of a reference LPE-grown Er-free sample and of a Er-doped sample is shown in

 © 1999 American Institute of Physics

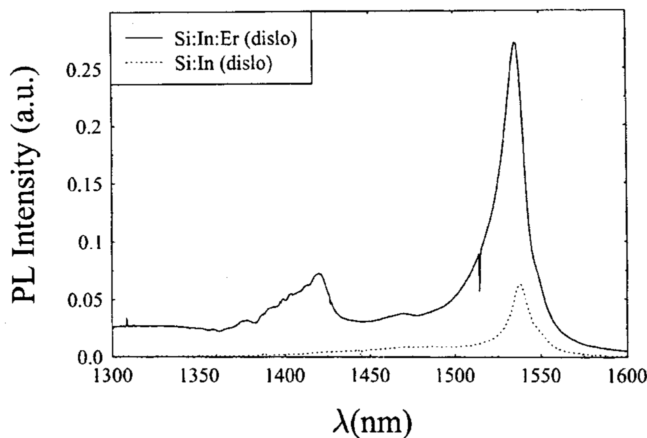

FIG. 1. PL spectra of a reference LPE-grown Er-free sample (dotted line) and of an Er-doped sample at $T=10$ K, $P=1.7$ W/cm^2.

Fig. 1. It is evident that the PL intensity at the same exciting power (1.7 W/cm^2) is larger by a factor of 5 in the case of Er-doped silicon, and that in the case of the reference sample only the $D1$ band is observed. We have then examined the temperature dependence of the intensity of the $D1$ band in Er-doped, dislocated material.

The results showed that the $D1$-PL quenches out at the temperatures close to 250 K, in good agreement with the Kveder results on plastically deformed silicon.[5]

DLTS results

Deep level transient spectroscopy and optical DLTS measurements were performed on the same samples studied in EXAFS and PL experiments. The main results of these experiments are reported in Table I, where we have also presented the results for a reference Er-free sample, also with a dislocation-related PL.

All majority and minority traps were shown to be present at concentrations ranging between 10^{13} and 10^{15} cm^{-3} (Ref. 6).

The traps labeled HX and $H4$ are dislocation related, and thus labeled D. Since no dislocation-related trap was observed in DLTS measurements by Kveder in single-crystal silicon deformed at 1100 °C under clean conditions, these traps are present in our samples at a concentration at least two orders of magnitude larger than those present in Kveder's[5] samples. Of these traps, the $H4$ trap, which is present only in Er-doped dislocated samples, apparently works as a nonradiative recombination center. From the table one can further recognize the presence of the $E2$ level at $E=E_c-0.20$ eV in the luminescent Er-doped sample.

TABLE I. Summary of the results for the majority (H) and minority (E) trap centers.

Level	Energy, eV	Reference sample	Er-doped sample	Remarks
$H0$	$E_v+0.18$		√	
HX	$E_v+0.45$	√	√	D
$H4$	$E_v+0.65$	√	√	D
$E1$	$E_c-0.18$	√		
$E2$	$E_c-0.20$		√	Er

It closely corresponds to a level at $E_c-0.18$ eV, assigned in the literature to an Er-O center[7] since it is present only in Er-O coimplanted samples. Finally, a shallow level at $E_c-0.18$ eV is present only in the reference sample.

DISCUSSION AND CONCLUSIONS

One of the most striking effects of dislocations in LPE-grown epilayers is the drastic change in the local structure of Er, which resembles that of erbium in a cluster of oxygen atoms, while the structure of erbium in erbium silicide in materials without dislocations contains comparable amounts of oxygen.

We could then argue that both oxygen and erbium are gettered at dislocations, which play the role of centers responsible for the $D1$ luminescence band, in agreement with Kveder.

This effect could be unspecific, as for most of the impurities which are called upon to enhance the photoluminescence. We believe, however, that it is peculiar to erbium.

In fact, the permanence of the dislocation-related PL at Er concentrations much larger than those at which transition metals kill the PL is certainly associated with the enhancement of Er solubility associated with the presence of oxygen and/or Er-O centers. Work is in progress to obtain more details on the Er-O centers in dislocated and dislocation-free samples from recent results of EXAFS experiments, which could further support our conclusion.

This paper was presented at the annual INTAS-RFBR Meeting, held in St. Petersburg on 24–29 October 1998, in the frame of the INTAS-RFBR 95-531 Program. INTAS is acknowledged for the financial support of the entire Project.

[1] S. Binetti, M. Donghi, S. Pizzini, A. Castaldini, A. Cavallini, B. Fraboni, and N. A. Sobolev, Solid State Phenom. **57-58**, 197 (1997).
[2] S. Pizzini, M. Donghi, S. Binetti, G. Wagner, and M. Bersani, J. Electrochem. Soc. **145**, 8 (1998).
[3] S. Pizzini, M. Donghi, S. Binetti, I. Gelmi, A. Cavallini, B. Fraboni, and G. Wagner, Solid State Phenom. **54**, 86 (1997).
[4] A. Castaldini, A. Cavallini, B. Graboni, S. Binetti, M. Donghi, S. Pizzini, and G. Wagner, Inst. Phys. Conf. Ser. **160**, 297 (1997).
[5] V. V. Kveder, E. A. Steinman, S. A. Shevchenko, and H. G. Grimmeiss, Phys. Rev. B **51**, 520 (1995).
[6] A. Cavallini, B. Fraboni, S. Pizzini, S. Binetti, S. Sanguinetti, I. Lazzarini, and G. Salviati, J. Appl. Phys. (in press).
[7] S. Libertino, S. Coffa, G. Franzó, and F. Priolo, J. Appl. Phys. **78**, 3867 (1995).

Published in English in the original Russian journal. Reproduced here with stylistic changes by the Translation Editor.

Photoluminescence of erbium-doped silicon: excitation power dependence

C. A. J. Ammerlaan, D. T. X. Thao, and T. Gregorkiewicz

Van der Waals-Zeeman Institute, University of Amsterdam, Valckenierstraat 65, NL-1018 XE Amsterdam, The Netherlands

N. A. Sobolev

A. F. Ioffe Physicotechnical Institute, Russian Academy of Sciences, 194021 St. Petersburg, Russia

(Submitted January 19, 1999; accepted for publication January 20, 1999)
Fiz. Tekh. Poluprovodn. **33**, 644–648 (June 1999)

The intensity of the photoluminescence of erbium in silicon is analyzed by a model which takes into account the formation of free excitons, the binding of excitons to erbium ions, the excitation of inner-shell $4f$ electrons of erbium ions and their subsequent decay by light emission. Predictions of this model for the dependence of luminescence intensity on laser excitation power are compared with experimental observations. The results for float-zone and Czochralski-grown silicon, in which erbium is introduced by implantation with or without oxygen co-implantation, are remarkably similar. To obtain agreement between model analysis and experimental data it is necessary to include in the model terms describing energy dissipation by an Auger process of both the erbium-bound excitons and the erbium ions in excited state with free electrons in the conduction band. A good quantitative agreement is achieved. © *1999 American Institute of Physics.* [S1063-7826(99)00306-3]

1. INTRODUCTION

The luminescence of rare-earth-doped semiconductors is presently under intense study. In the more fundamentally oriented research, the complex physical processes active in energy transfer from excitation in the entrance channel to light emission in the output channel are investigated. Stimulated by the prospects of practical application of this light source, erbium in silicon, which emits at a wavelength of 1.54 μm, is a prominent system. In a currently accepted model energy fed into the system leads to light emission by erbium ions in a multistep process. Radiation incident on the silicon, with photon energy larger than its bandgap, creates free electrons and holes. Free carriers combine into excitons which can be trapped at the erbium ions. The energy of erbium-bound excitons is transferred to erbium ions and results in excitation of $4f$ core electrons from the $^4I_{15/2}$ ground state into the $^4I_{13/2}$ excited state. The characteristic luminescence is produced upon decay of excited erbium ions. In the present report this chain of processes is analyzed in a mathematical model with the aim of giving a quantitative description.

2. PHOTOLUMINESCENCE MODEL

2a. Energy transfer without Auger processes

The physical model mentioned above, which we examine in this paper, is illustrated in Fig. 1. In a recent paper by Bresler and co-workers the model without the Auger processes has been put on a mathematical basis.[1] A set of rate equations was formulated for free electrons with concentration n, free excitons with concentration n_x, erbium-bound excitons with concentration n_{xb}, and erbium ions in the excited state, with concentration n^*_{Er}. The steady state is described by the balance equations (1)–(4), which we will discuss.

The chain of processes leading to photoluminescence has as the first step the generation of free electrons and holes, to equal concentrations, with rate G by the incident light. Free carriers can combine in a second-order process with rate $\gamma_x n^2$ into free excitons. Trapping of the excitons at erbium sites is proportional to the concentrations of the free excitons and the available free erbium sites. The latter concentration is given as the total concentration of erbium n_{Er} multiplied by the fraction of free sites $[(n_{\mathrm{Er}}-n_{xb})/n_{\mathrm{Er}}]$. The energy is transferred to erbium $4f$ core electrons with a transfer time τ^* but again only to the erbium ions still available in their ground state, i.e., to the fraction $[(n_{\mathrm{Er}}-n^*_{\mathrm{Er}})/n_{\mathrm{Er}}]$. At high excitation power level these fractions between square brackets tend to zero and lead to saturation of the luminescence output. This manifestation of saturation is related to exhaustion of available erbium centers. Finally, luminescence is produced by the decay with time constant τ_d of erbium ions n^*_{Er} in the excited state. The photon emission rate equal to n^*_{Er}/τ_d is the quantity measured in the experiment.

Reverse processes, as indicated in Fig. 1 by arrows that point to the left, are thermally activated. They include the dissociation of excitons into free electrons and holes fn_x requiring energy gain of E_x, the release of excitons from erbium trapping sites cfn_{xb}, and a back transfer process in which an erbium-bound exciton is recreated from an excited erbium ion. Although these reverse processes hamper the energy transfer toward light emission, they do not remove energy from the chain. The coefficients of forward and reverse processes are related by considerations of detailed balancing.

 © 1999 American Institute of Physics

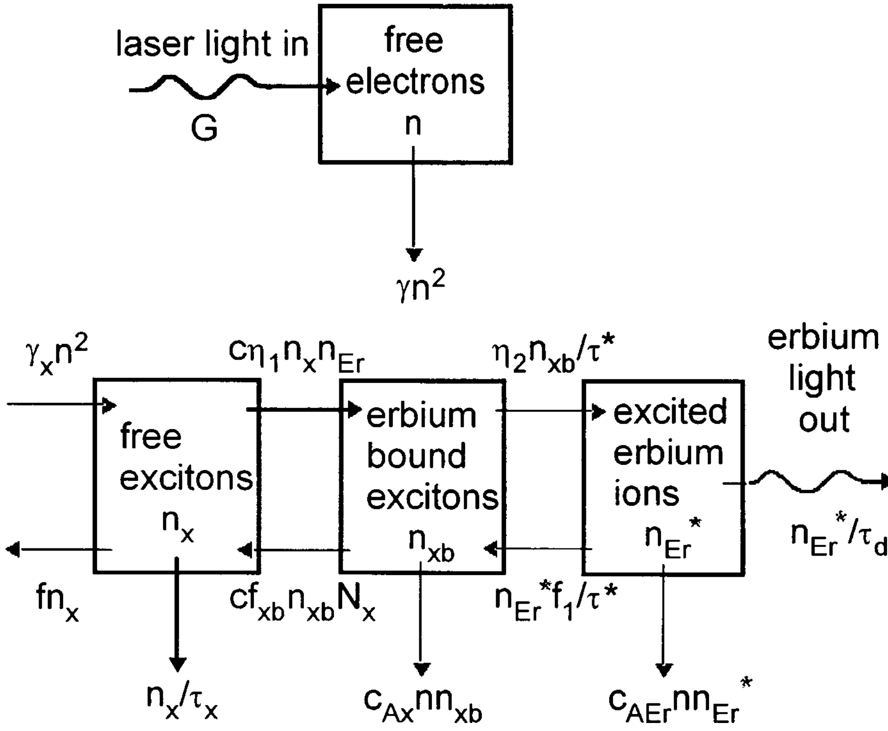

FIG. 1. Two-stream model for the photoexcitation of erbium luminescence showing generation and loss of free electrons n, free excitons n_x, erbium-bound excitons n_{xb}, and erbium ions in the excited state n^*_{Er}. Notation: $\eta_1=(n_{\mathrm{Er}}-n_{xb})/n_{\mathrm{Er}}$, $\eta_2=(n_{\mathrm{Er}}-n^*_{\mathrm{Er}})/n_{\mathrm{Er}}$.

Energy is permanently lost by processes which remove energy irreversibly from the chain. Such processes, as indicated in Fig. 1 by vertical arrows downwards, are recombination of electrons and holes via other centers, with the rate γn^2, and recombination of free excitons directly or via alternative centers, n_x/τ_x. The Auger processes represented in Fig. 1 remove energy irreversibly from the luminescence path.

The balance equations based on these processes are

$$G+fn_x=\gamma n^2+\gamma_x n^2, \tag{1}$$

$$\gamma_x n^2+cf_{xb}n_{xb}N_x=cn_x n_{\mathrm{Er}}[(n_{\mathrm{Er}}-n_{xb})/n_{\mathrm{Er}}]+fn_x+n_x/\tau_x, \tag{2}$$

$$cn_x n_{\mathrm{Er}}[(n_{\mathrm{Er}}-n_{xb})/n_{\mathrm{Er}}]+n^*_{\mathrm{Er}}f_1/\tau^*=n_{xb}[(n_{\mathrm{Er}}-n^*_{\mathrm{Er}})/n_{\mathrm{Er}}]/\tau^*+cf_{xb}n_{xb}N_x, \tag{3}$$

and

$$n_{xb}[(n_{\mathrm{Er}}-n^*_{\mathrm{Er}})/n_{\mathrm{Er}}]/\tau^*=n^*_{\mathrm{Er}}/\tau_d+n^*_{\mathrm{Er}}f_1/\tau^*. \tag{4}$$

The generation terms are given on the left-hand sides of these equations; loss terms appear in each case on the right-hand side. An exact solution for the equations, in the form of a quadratic equation for n^*_{Er}, is given by Bresler *et al.*[1] The result takes a more simplified form by the restriction to low temperatures, e.g., liquid-helium temperature, when all reverse processes, which require thermal activation, are suppressed. Under these conditions, when $f=f_{xb}=f_1=0$, we obtain

$$a_0(n^*_{\mathrm{Er}}/n_{\mathrm{Er}})^2-(b_0+b_2G)(n^*_{\mathrm{Er}}/n_{\mathrm{Er}})+c_2G=0, \tag{5}$$

where

$$a_0=1+cn_{\mathrm{Er}}\tau_x[1+(\tau^*/\tau_d)], \tag{5a}$$

$$b_0=1+cn_{\mathrm{Er}}\tau_x, \tag{5b}$$

$$b_2=\gamma_x\tau_x c\tau_d[1+(\tau^*/\tau_d)]/\gamma, \tag{5c}$$

and

$$c_2=\gamma_x\tau_x c\tau_d/\gamma. \tag{5d}$$

In general form, the equation predicts saturation of n^*_{Er} at the level $n^*_{\mathrm{Er}}/n_{\mathrm{Er}}=c_2/b_2$ for high excitation power level G. For low power a linear relationship $n^*_{\mathrm{Er}}/n_{\mathrm{Er}}=(c_2/b_0)G$ is predicted. In comparing experimental data with these model equations one must be aware that neither generation power nor output luminescence is known very well in absolute numbers. For example, the volume in the sample where excitation takes place is not well defined. For this reason it is useful to eliminate these uncertain factors by resorting to relative units. As regards luminescence intensity, the obvious unit for normalization is the saturation value c_2/b_2. A dimensionless normalized intensity is therefore introduced as $I\equiv(n^*_{\mathrm{Er}}/n_{\mathrm{Er}})/(c_2/b_2)$. For the excitation power the unit is obtained as the value at which the extrapolated linear increase at low power crosses the saturation level. This occurs at $G_1=b_0/b_2$. The normalized power $P\equiv G/G_1$ is again a dimensionless quantity. In terms of normalized units Eq. (5) is modified to

$$I^2-\alpha(1+P)I+\alpha P=0, \tag{6}$$

where

$$\alpha\equiv b_0b_2/a_0c_2. \tag{6a}$$

It turns out that the dependence of intensity I on generation power P is governed by one parameter α, through which the specific aspects of the luminescence process as a whole are represented. However, from Eq. (6) it is easily concluded

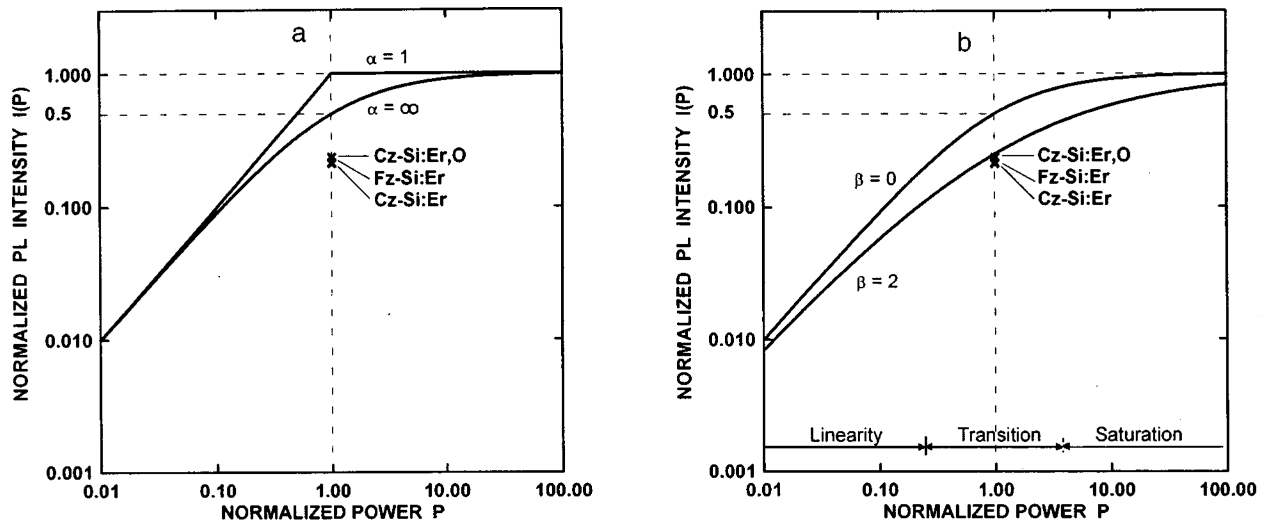

FIG. 2. Normalized luminescence output I plotted as a function of normalized laser power input P; a) for a model without Auger processes, b) for a model including strong Auger decay processes. Experimental data for three samples of type Fz-Si:Er, Cz-Si:Er, and Cz-Si:Er,O are given for unit power $P=1$.

that for low power $I=P$, and for high power $I=1$, irrespective of the value of the parameter α. In normalized form the parameters a_2, b_0, b_2, and c_2 or in basic, more physical form γ, γ_x, c, τ_x, τ^*, and τ_d have no effect on the power dependence in the low and high power regions. Only at intermediate power, i.e., at $P\approx 1$, the results will depend on α. Only in the transition region from linear increase to saturation the observed luminescence provides insight into the luminescence process. The most typical value to study the luminescence mechanism is therefore at power $P=1$. At this level the luminescence intensity is given by

$$I=\alpha-(\alpha^2-\alpha)^{1/2}. \tag{7}$$

From the equality $\alpha=b_0b_2/a_0c_2$ and the parameters as given by Eqs. (5a)–(5d) one concludes that $1\leqslant\alpha\leqslant\infty$. For such values of α solutions from Eq. (7) always exist. For $\alpha=1$ we obtain $I(P=1)=1$ and for $\alpha=\infty$ we have $I(P=1)=0.5$. The range of possible luminescence intensities at unit power $P=1$ is restricted between 0.5 and 1, consistent with Eq. (6). The limiting curves for an extended power range are drawn in Fig. 2a.

Experimental data are also shown in Fig. 2a. They result from measurements at liquid-helium temperature on three samples with different specifications. The sample Fz-Si:Er is float-zoned silicon implanted with erbium. Sample labeled Cz-Si:Er is Czochralski silicon which is similarly implanted. The third sample, labeled Cz-Si:Er,O was codoped with oxygen by implantation. In all cases the luminescence intensity was measured as a function of excitation power. Experimental data are plotted for normalized power $P=1$ at the observed values $I\approx 0.22$. Obviously, this is outside the range of the results as can be described by the model.

2b. Energy transfer with Auger processes

One has to conclude that the presented model cannot give a quantitative description of the luminescence process. In order to improve the model energy losses through Auger processes may be considered, as has been explored before by Palm *et al.*[2] Erbium-bound excitons can dissipate their energy in an Auger process with the involvement of free electrons. Similarly, erbium ions in the excited state can decay in an Auger process also with conduction band electrons. These processes are also shown in Fig. 1. In the balance equations they are implemented by including on the loss side the Auger rates $c_{Ax}nn_{xb}$ and $c_{A\mathrm{Er}}nn^*_{\mathrm{Er}}$. The extended balance equations for bound excitons and excited erbium ions become

$$cn_xn_{\mathrm{Er}}[(n_{\mathrm{Er}}-n_{xb})/n_{\mathrm{Er}}]+n^*_{\mathrm{Er}}f_1/\tau^*$$
$$=n_{xb}[(n_{\mathrm{Er}}-n^*_{\mathrm{Er}})/n_{\mathrm{Er}}]/\tau^*+cf_{xb}n_{xb}N_x+c_{Ax}nn_{xb}, \tag{8}$$

and

$$n_{xb}[(n_{\mathrm{Er}}-n^*_{\mathrm{Er}})/n_{\mathrm{Er}}]/\tau^*=n^*_{\mathrm{Er}}/\tau_d+n^*_{\mathrm{Er}}f_1/\tau^*+c_{A\mathrm{Er}}nn^*_{\mathrm{Er}}. \tag{9}$$

In order to solve the new set of equations (1), (2), (8), and (9) it is helpful to introduce appropriate simplifications. Considering the numerical values, we conclude that the loss of free electrons and holes is dominated by their recombination via traps with the rate γn^2. The loss via exciton formation $\gamma_x n^2$ is comparatively much lower, i.e., $\gamma_x\ll\gamma$. Under such conditions the energy transfer model can be cascaded into two parts. In stream I the balance of electrons is considered separately by Eq. (1). The loss of electrons through exciton formation is ignored in this mainstream. At low temperature this leads to

$$G=\gamma n^2, \tag{10}$$

$$n=(G/\gamma)^{1/2}. \tag{11}$$

The electron concentration obtained from this solution is used to describe the Auger processes. Typical numbers are $G=10^{22}\,\mathrm{cm}^{-3}\,\mathrm{s}^{-1}$, $\gamma=10^{-10}\,\mathrm{cm}^3\,\mathrm{s}^{-1}$, and $n=10^{16}\,\mathrm{cm}^{-3}$.

In energy stream II the balance of free excitons, bound excitons, and excited erbium ions is considered separately. Solution of the equations leads to a cubic equation in $n^*_{\mathrm{Er}}/n_{\mathrm{Er}}$, which, accepting an approximation, can be factorized to yield a quadratic equation

$$(a_0+a_1G^{1/2}+a_2G)(n^*_{\rm Er}/n_{\rm Er})^2-(b_0+b_1G^{1/2}+b_2G+b_3G^{3/2})(n^*_{\rm Er}/n_{\rm Er})+c_2G=0, \quad (12)$$

where

$$a_0=1+cn_{\rm Er}\tau_x[1+(\tau^*/\tau_d)], \quad (12a)$$

$$a_1=[(1+cn_{\rm Er}\tau_x)c_{A\rm Er}\tau_d+2cn_{\rm Er}\tau_x\times(\tau^*/\tau_d)c_{A\rm Er}\tau_d]/\gamma^{1/2}, \quad (12b)$$

$$a_2=cn_{\rm Er}\tau_x(\tau^*/\tau_d)(c_{A\rm Er}\tau_d)^2/\gamma, \quad (12c)$$

$$b_0=1+cn_{\rm Er}\tau_x, \quad (12d)$$

$$b_1=(1+cn_{\rm Er}\tau_x)(c_{A\rm Er}\tau_d+c_{Ax}\tau^*)/\gamma^{1/2}, \quad (12e)$$

$$b_2=\{(1+cn_{\rm Er}\tau_x)c_{A\rm Er}\tau_d c_{Ax}\tau^*+\gamma_x\tau_x c\tau_d\times[1+(\tau^*/\tau_d)]\}/\gamma, \quad (12f)$$

$$b_3=\gamma_x\tau_x c\tau_d C_{A\rm Er}\tau_d(\tau^*/\tau_d)/\gamma^{3/2}, \quad (12g)$$

and

$$c_2=\gamma_x\tau_x c\tau_d/\gamma. \quad (12h)$$

At a low power level the model equations reflect the linear increase $n^*_{\rm Er}/n_{\rm Er}=(c_2/b_0)G$, just as before. At high power, however, the consistent solution $n^*_{\rm Er}/n_{\rm Er}=(c_2/b_3)/G^{1/2}$ predicts decreasing luminescence intensity with increasing excitation source. Such behavior is to be expected since in our case two independent saturation mechanisms are active. The first one drives the concentration of erbium-bound excitons, n_{xb}, toward the concentration of available erbium ions but is limited to stay below or become equal to this concentration. The second saturation mechanism is the combined action of the two Auger processes. At high power, and hence high concentrations of free electrons, the Auger mechanism, which removes excited erbium ions nonradiatively, is very effective. This results in a reduction of $n^*_{\rm Er}$, which becomes proportional to $1/n$ or $1/G^{1/2}$. Such a decrease has not been observed in our experiments; it has also not been reported in the literature. Inspection of the equations shows that one should expect the decrease to set in at excitation values where $c_{A\rm Er}\tau_d(\tau^*/\tau_d)(G/\gamma)^{1/2}>1$. Considering the numerical values ($c_{A\rm Er}\approx10^{-12}\,{\rm cm^3\cdot s^{-1}}$, $\tau^*\approx10^{-6}$ s), this corresponds to high values of G near and above $10^{26}\,{\rm cm^{-3}\cdot s^{-1}}$, which are not reached in actual experiments. This can be attributed to the small value of (τ^*/τ_d) since τ^* is in the range of microseconds and τ_d is on the order of several milliseconds. Introducing the approximation $\tau^*/\tau_d\approx0$, Eqs. (12) reduce in many respects to Eqs. (6). In particular, the term $b_3G^{3/2}$ in Eq. (12) is lost and the equation predicts saturation at c_2/b_2.

For low and for high power levels the solution of Eq. (12) is

$$n^*_{\rm Er}/n_{\rm Er}=c_2G/(b_0+b_1G^{1/2}+b_2G). \quad (13)$$

This result is also valid for intermediate power if the Auger processes are strong. Following solution (13), one has saturation at c_2/b_2, linear increase at low power with $(c_2/b_0)G$, and $G_1=b_0/b_2$. Casting Eq. (13) in terms of normalized units, as before, the result will read

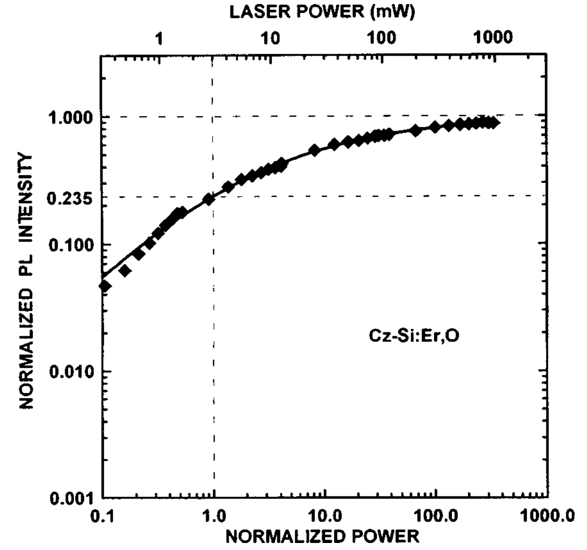

FIG. 3. Photoluminescence intensity, in normalized units I, as a function of applied laser excitation power, both in units G of laser power and in normalized units P for the sample Cz-Si:Er,O. Experimental data points and theoretical curve according to Eq. (14) with the parameter $\beta=2.25$.

$$1=P/(1+\beta P^{1/2}+P), \quad (14)$$

where

$$\beta=b_1/(b_0b_2)^{1/2}, \quad (14a)$$

or

$$\beta=(c_{A\rm Er}\tau_d+c_{Ax}\tau^*)/\times[c_{A\rm Er}\tau_d c_{Ax}\tau^*+\gamma_x\tau_x c\tau_d/(1+cn_{\rm Er}\tau_x)]^{1/2}. \quad (14b)$$

Under the assumed condition of strong Auger effect it reduces to

$$\beta=(c_{A\rm Er}\tau_d+c_{Ax}\tau^*)/(c_{A\rm Er}\tau_d C_{Ax}\tau^*)^{1/2}, \quad (14c)$$

or

$$\beta=(c_{A\rm Er}\tau_d/c_{Ax}\tau^*)^{1/2}+(c_{Ax}\tau^*/c_{A\rm Er}\tau_d)^{1/2}. \quad (14d)$$

As usual, the power dependence of the luminescence has linear increase at low power with $I=P$ and saturates at high power at $I=1$. Features of the luminescence process are revealed at intermediate power, e.g., at $P=1$, where $I=1/(2+\beta)$. In general, the parameter β will be positive following Eq. (14b); for the case of strong Auger effect $\beta\geqslant2$, as follows from Eqs. (14c) and (14d). Figure 2b illustrates the curves obtained from Eq. (14) for $\beta=0$ and $\beta=2$. Compared to the previous case, without the Auger effect, the transition region between linear behavior and saturation is broader, because of the appearance of the $P^{1/2}$ term as a result of the Auger effect.

Considering again the experiment, the measured data for the luminescence power dependence for sample Cz-Si:Er,O are plotted in Fig. 3. The solid curve is the best fit using Eq. (14) with the parameter $\beta=2.25$. Similar fits were also made for the samples Fz-Si:Er and Cz-Si:Er; the parameter values are then $\beta=2.63$ and 2.73, respectively.[3] The data points for the three samples for $P=1$ and $I=1/(2+\beta)$ are also plotted in Fig. 2b. The results for the three samples are similar with

β=2.5±0.25. With Eq. (14d) the result is converted to $(c_{A\mathrm{Er}}\tau_d/c_{Ax}\tau^*)^{\pm 1}\approx(4\pm 1)$. This compares favorably with the data published in the literature, e.g., $c_{A\mathrm{Er}} = 10^{-12}\,\mathrm{cm}^3\cdot\mathrm{s}^{-1}$, $\tau_d = 10^{-3}$ s, $c_{Ax} = 10^{-10}\,\mathrm{cm}^3\cdot\mathrm{s}^{-1}$, and $\tau^* = 4\times 10^{-6}$ s (Ref. 2). From our analysis we conclude that $c_{A\mathrm{Er}}\tau_d/c_{Ax}\tau^*$ is very similar for three kinds of test materials. This can be attributed to an accidental combination of parameters, but one is tempted to believe that all process parameters, i.e., $c_{A\mathrm{Er}}$, τ_d, c_{Ax}, and τ^*, have similar values. In this case the possible difference in structure of the luminescent centers in the three materials has very little influence on the efficiency of the photoluminescence process.

This work was supported in part by the INTAS-RFBR (Grant 95-0531).

[1] M. S. Bresler, O. B. Gusev, B. P. Zakharchenya, and I. N. Yassievich, Phys. Solid State **38**, 813 (1996).
[2] J. Palm, F. Gan, B. Zheng, J. Michel, and L. C. Kimerling, Phys. Rev. B **54**, 17603 (1996).
[3] D. T. X. Thao *et al.* (to be published).

Published in English in the original Russian journal. Reproduced here with stylistic changes by the Translation Editor.

Impurity centers in silicon doped with rare-earth impurities of dysprosium, holmium, erbium, and ytterbium

V. V. Emtsev, V. V. Emtsev, Jr., D. S. Poloskin, N. A. Sobolev, and E. I. Shek

A. F. Ioffe Physicotechnical Institute, Russian Academy of Sciences, 194021 St. Petersburg, Russia

J. Michel and L. C. Kimerling

Materials Processing Center, Massachusetts Institute of Technology, Cambridge, MA 02139, USA
(Submitted December 22, 1998; accepted for publication December 23, 1998)
Fiz. Tekh. Poluprovodn. **33**, 649–651 (June 1999)

The results of an investigation of the donor centers in Czochralski-grown silicon ion-implanted with rare-earth impurities of Dy, Ho, Er, and Yb are presented. The formation of three groups of dominant donors with ionization energies less than 0.2 eV in silicon after annealing at 700 and 900 °C is discussed. The shallow donors at $\approx E_c - 40$ meV are interpreted as thermal donors containing oxygen and intrinsic defects. The two other groups of donor states are identified as centers containing rare-earth ions. © *1999 American Institute of Physics.*
[S1063-7826(99)00406-8]

Impurities of rare-earth metals in silicon are unquestionably of interest from the physical standpoint as suitable objects for studying the behavior of lanthanide ions in group-IV semiconductors with pronounced covalent bonding. The most thoroughly studied among them is the erbium impurity with a characteristic photoluminescence band at a wavelength near 1.54 μm, which allows us to regard such a semiconductor material as promising for use in optoelectronics.

Silicon is most often doped with erbium by ion implantation followed by thermal annealing at temperatures above 700 °C. However, until recently the information on the local centers in Si:Er appearing during such a doping procedure was confined mainly to data from deep-level transient spectroscopy (DLTS) (see, for example, Refs. 1–3). The limited information, in turn, hampered the detailed examination of the excitation and relaxation processes of erbium-related centers, as well as precluded correct estimation of their efficiency. The existing gap in the investigation of shallower donor states in erbium-doped silicon was successfully filled only very recently as a result of systematic Hall measurements, which provided information on the concentration and ionization energy of such donor centers.[4,5] The introduction of other dopants from the lanthanide series (Dy and Ho) made it possible to preliminarily identify impurity centers with ionization energies less than 0.2 eV.[4] In the present work ytterbium was added to this impurity series, permitting more reliable disclosure of the dominant tendencies in the variation of the properties of the respective donor centers along the series Dy→Ho→Er→Yb.

The original samples with a thickness of 1 mm were cut from various ingots of Czochralski-grown *p*-type silicon (CZ Si). The oxygen concentration ranged from 2×10^{17} to 1×10^{18} cm^{-3}. The concentration of shallow acceptors (boron) in the samples varied from 8×10^{13} to 2×10^{15} cm^{-3}; the degree of compensation was less than 0.3. The lanthanides were introduced by implanting ions with energies from 1 to 1.3 MeV. The postimplantation annealing of the samples was carried out successively in two stages (each lasting 30 min) at $T=700$ and 900 °C in a chlorine-containing atmosphere. The radiation damage in the surface layer of the samples after implantation healed mainly in the first stage of annealing. A doped *n*-type layer with a thickness of about 0.5 μm formed in this stage on the *p*-type silicon substrate. Measurements of the electron concentration in this layer were performed by the Hall method in the temperature range from 20 to 300 K using the van der Pauw configuration. The higher annealing temperature ($T=900$ °C) was selected because, according to the literature data for erbium-doped silicon, just this temperature is most suitable for the formation of erbium-related centers with a characteristic photoluminescence band at a wavelength close to 1.54 μm (see, for example, Ref. 6). The n versus T plots were analyzed using the corresponding electroneutrality equations, which permitted determination of the concentration and ionization energy of local centers at a depth of less than 0.2 eV from the conduction-band edge. The experimental data and a detailed analysis of the $n(T)$ curves will be presented in a separate paper. In this communication we present only the main results for silicon doped with rare-earth impurities at a maximum dose of implanted ions $D=1\times10^{13}$ cm^{-2}.

Among the donors with small ionization energies appearing in the doped *n*-layer after annealing at $T=700$ °C, three groups of dominant centers can be identified (see Fig. 1).

The first group consists of shallow centers, whose donor states range from 20 to 40 meV. Their total concentration depends both on oxygen concentration and on irradiation dose. According to their properties, these centers are similar to thermal donors, i.e., small electrically active oxygen precipitates which appear in silicon with an oxygen concentration of about 1×10^{18} cm^{-3} during thermal treatment at

 © 1999 American Institute of Physics

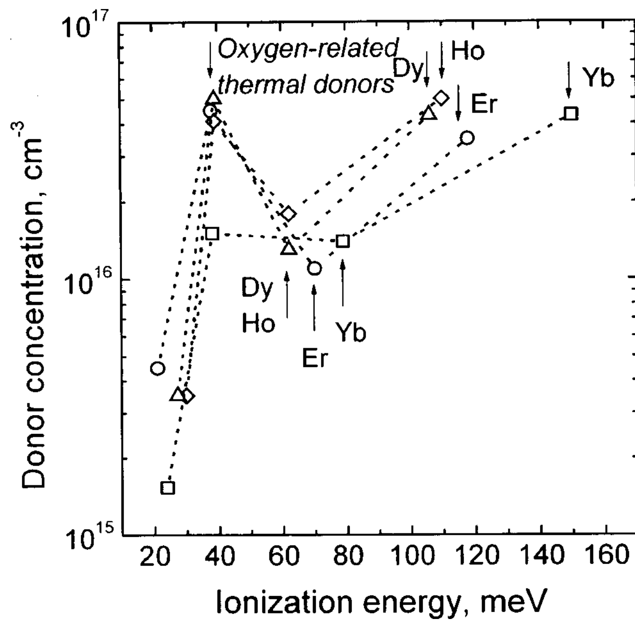

FIG. 1. Distribution of donor centers with respect to their ionization energy for CZ Si ion-implanted with Dy, Ho, Er, and Yb impurities after annealing at $T=700\,^\circ$C. The implantation doses were $D(\mathrm{Dy,Ho,Yb})=1\times10^{13}$ cm^{-2} and $D(\mathrm{Er})=1\times10^{13}$ cm^{-2} with additional implantation of oxygen at a dose $D(\mathrm{O})=1\times10^{14}$ cm^{-2} (the energy of the oxygen ions was 0.17 MeV). The dotted lines join the experimental points for clarity.

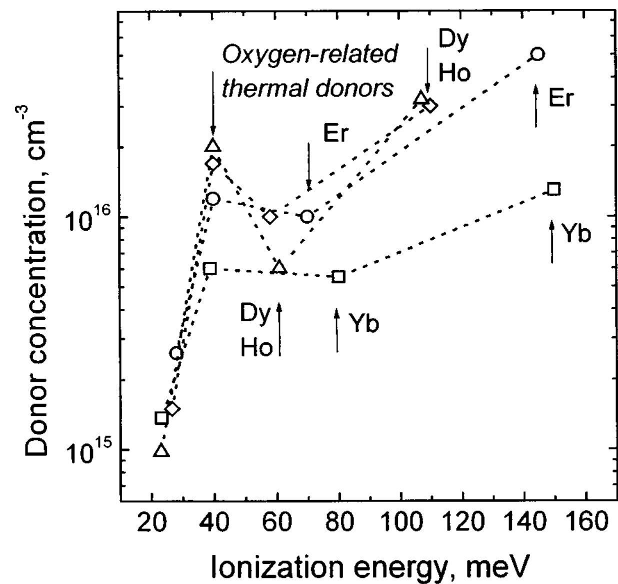

FIG. 2. Distribution of donor centers with respect to their ionization energy for CZ Si ion-implanted with Dy, Ho, Er, and Yb impurities after annealing at $T=900\,^\circ$C. The implantation doses were $D(\mathrm{Dy,Ho,Yb})=1\times10^{13}$ cm^{-2} and $D(\mathrm{Er})=1\times10^{13}$ cm^{-2} with additional implantation of oxygen at a dose $D(\mathrm{O})=1\times10^{14}$ cm^{-2} (the energy of the oxygen ions was 0.17 MeV). The dotted lines join the experimental points for clarity.

$T=600^\circ$–$700\,^\circ$C (see, for example, Ref. 7). However, there is one significant difference between the annealing of implanted layers and the ordinary thermal treatment of silicon, although Czochralski-grown silicon is involved in both cases. The precipitation of oxygen in the former case takes place in the presence of a large concentration of intrinsic defects, which play the role of nucleation centers for the precipitates and appear in their composition. In our opinion, this situation accounts for the significantly higher rate of formation of thermal donors, as well as their higher stability compared to the analogous oxygen-containing thermal donors appearing during the ordinary thermal treatment of silicon (see also Ref. 8 in this regard). No explicit dependence on the type of rare-earth impurity was discovered for the shallow donors. In the case of CZ Si:Yb there is a feature which calls for further study.

The second group of donor centers has ionization energies from 60 to 80 meV, depending on the type of rare-earth impurity. The portions of the $n(T)$ curves corresponding to the ionization of these centers are described well by one ionization energy for a given type of impurity; therefore, we assume that they are centers with a single donor state.

The third group of donor centers have ionization energies greater than 100 meV. Although the ionization energies of the corresponding levels are determined to a lower accuracy in this case than in the case of the shallower levels, they still display the same law of ''level deepening'' that is observed for centers with ionization energies in the range from 60 to 80 meV along the series Dy, Ho$\rightarrow$Er$\rightarrow$Yb. Thus, it can be concluded that the donor centers under consideration also include impurity atoms in their composition.

When the annealing temperature is raised to $T=900\,^\circ$C, the positions of the levels in the first two groups of donor centers do not undergo appreciable changes for any of the rare-earth impurities, and only their concentrations decrease significantly (compare Figs. 1 and 2). However, the situation is different for the deep centers with an ionization energy greater than 0.1 eV. In the case of Dy and Ho impurities, the positions of the corresponding donor levels remain essentially unchanged, although their concentrations decrease somewhat. Conversely, for an erbium impurity in silicon, the disappearance of the donor states at $E_c-(117\pm5)$ meV along with the appearance of other donor states at $E_c-(145\pm5)$ meV in a roughly equal concentration in response to the rise in temperature is notable, i.e., we may be dealing with transformation of the centers. The interpretation of the data for the ytterbium impurity presents definite difficulties because the analysis of the experimental $n(T)$ curves at $T>200$ K is not as reliable for centers with an ionization energy greater than 150 meV as for the rare-earth impurities considered above, and, in principle, a similar transformation of donor centers may also take place when the annealing temperature is raised from $T=700$ to $900\,^\circ$C.

Thus, three groups of dominant donor centers have been discovered in the present work in Czochralski-grown silicon ion-implanted with rare-earth impurities of Dy, Ho, Er, and Yb. The shallow donor states with ionization energies from 20 to 40 meV have been interpreted as thermal donors containing oxygen atoms and intrinsic defects. The two other groups of donor centers with ionization energies from 60 to 80 meV and above 100 meV have been identified as centers containing impurity atoms of rare-earth elements. It has been shown that raising the temperature of the postimplantation anneal from $T=700$ to $900\,^\circ$C leads to significant transformation of the deep centers in erbium-doped silicon with the

resultant formation of donor states at $\approx E_c - 145$ meV. The latter are assumed to play an important role in the excitation and relaxation of erbium-related centers (see, for example, Refs. 9–12). The result of the present work can be useful in discussing concrete mechanisms and in estimating their efficiency. In particular, in several studies[9,11] the quenching of the luminescence of erbium ions in silicon at $T \geqslant 100$ K is assumed to be caused by thermal ionization of the centers mentioned above, which prevents the appearance of bound excitons on them. However, it follows from our experimental data that this quenching mechanism cannot be the actual mechanism, since under real conditions the extent of ionization of the donor states discussed is totally insignificant up to room temperature due to the presence of a large concentration of shallower donors.

This work was performed with financial support from the INTAS–RFBR (Grant 95-0531) and the CRDF (Grant 235).

[1] J. L. Benton, J. Michel, L. C. Kimerling, D. C. Jacobson, Y. H. Xie, D. J. Eaglesham, E. A. Fitzgerald, and J. M. Poate, J. Appl. Phys. **70**, 2667 (1991).
[2] S. Libertino, S. Coffa, G. Franzó, and F. Priolo, J. Appl. Phys. **78**, 3867 (1995).
[3] H. Przybylinska, W. Jantsch, Yu. Suprun-Belevitch, M. Stepikhova, L. Palmetshofer, G. Hendorfer, A. Kozanecki, R. J. Wilson, and B. J. Sealy, Phys. Rev. B **54**, 2532 (1996).
[4] V. V. Emtsev, V. V. Emtsev, Jr., D. S. Poloskin, E. I. Shek, and N. A. Sobolev, J. Lumin. (1999) (in press).
[5] V. V. Emtsev, V. V. Emtsev, Jr., D. S. Poloskin, E. I. Shek, N. A. Sobolev, J. Michel, and L. C. Kimerling, Appl. Phys. Lett. (1999) (in press).
[6] J. Michel, L. J. Benton, R. F. Ferrante, D. C. Jacobson, D. J. Eaglesham, E. A. Fitzgerald, Y.-H. Xie, J. M. Poate, and L. C. Kimerling, J. Appl. Phys. **70**, 2672 (1991).
[7] V. V. Emtsev, G. A. Oganesyan, and K. Schmalz, in *Solid State Phenomena*, H. Richter, M. Kittler, and C. Claeys (Eds.), Scitec Publications, Switzerland (1996), Vol. 47–48, p. 259.
[8] V. V. Emtsev, D. S. Poloskin, N. A. Sobolev, and E. I. Shek, Fiz. Tekh. Poluprovodn. **28**, 1084 (1994) [Semiconductors **28**, 624 (1994)].
[9] F. Priolo, G. Franzó, S. Coffa, A. Polman, S. Libertino, R. Barklie, and D. Carey, J. Appl. Phys. **78**, 3874 (1995).
[10] J. Palm, F. Gan, B. Zheng, J. Michel, and L. C. Kimerling, Phys. Rev. B **54**, 17 603 (1996).
[11] M. S. Bresler, O. B. Gusev, B. P. Zakharchenya, and I. N. Yassievich, Fiz. Tverd. Tela (St. Petersburg) **38**, 1474 (1996) [Phys. Solid State **38**, 813 (1996)].
[12] F. Priolo, G. Franzó, S. Coffa, and A. Carnera, Phys. Rev. B **57**, 4443 (1998).

Translated by P. Shelnitz

Redistribution of erbium during the crystallization of buried amorphous silicon layers

O. V. Aleksandrov, Yu. A. Nikolaev, N. A. Sobolev, V. I. Sakharov, I. T. Serenkov, and Yu. A. Kudryavtsev

A. F. Ioffe Physicotechnical Institute, Russian Academy of Sciences, 194021 St. Petersburg, Russia
(Submitted December 17, 1998; accepted for publication December 17, 1998)
Fiz. Tekh. Poluprovodn. **33**, 652–655 (June 1999)

The redistribution of Er during its implantation in silicon at doses close to the amorphization threshold and its subsequent solid-phase epitaxial (SPE) crystallization is investigated. The formation of a buried amorphous (a) layer is discovered at Er doses equal to 5×10^{13} and 1×10^{14} cm^{-2} using Rutherford backscattering. The segregation of Er in this case takes place inwardly from the two directions corresponding to the upper and lower boundaries of the buried αlayer and leads to the formation of a concentration peak at the meeting place of the two crystallization fronts. A method for calculating the coordinate dependence of the segregation coefficient k from the distribution profiles of the erbium impurity before and after annealing is proposed. The $k(x)$ curve exhibits a drop, whose width increases with decreasing Er implantation dose. Its appearance is attributed to the nonequilibrium nature of the segregation process at the beginning of SPE crystallization. © *1999 American Institute of Physics.* [S1063-7826(99)00506-2]

The concentration profiles of silicon layers implanted with ions of the rare-earth element erbium at doses exceeding the amorphization threshold exhibit considerable variation during annealing at 600–850 °C, at which the diffusion coefficients of Er in both the amorphous and single-crystal phases are negligible.[1–4] These changes are due to segregation of the impurity at the moving boundary between the amorphous (a) layer and the single-crystal (c) substrate during solid-phase epitaxial (SPE) crystallization. The character of the redistribution of Er depends on the implantation conditions: target temperature, implantation energy and dose, and additional implantation of an oxygen impurity.[3,4] The concentration profiles of Er after SPE crystallization of the skin layer of a-silicon are described by the quantitative model in Ref. 5, whose parameters are the width of the transition layer and the segregation coefficient, which depends on the coordinate. Under definite implantation conditions the amorphous layer can be buried and separated from the surface by an intermediate layer of single-crystal silicon. Such conditions are realized, for example, in the technology used to create SIMOX structures for microelectronics[6] during the implantation of oxygen ions at fairly high energies ($E>200$ keV) and doses ($D\approx1\times10^{18}$ cm^{-2}). The formation of a buried a-layer has also been observed following the implantation of Er ions ($E=0.5$ MeV, $D=1\times10^{15}$ cm^{-2}) in (100) Si with a target temperature equal to 200 °C (Ref. 3). The redistribution of Er during subsequent rapid thermal annealing in this case differed significantly from the case of implantation at 20 °C with an a-layer reaching the surface.

The purpose of the present work was to investigate the features of the segregation of Er during the SPE crystallization of buried silicon layers amorphized by ion implantation.

The implantation of Er ions was carried out at room temperature with energies of 1.0, 1.2, and 2 MeV and doses close to the amorphization threshold in the range $1\times10^{13}-1\times10^{14}$ cm^{-2} on the High Voltage Engineering Europe K2MV facility in a substrate of single-crystal Czochralski-grown p-type (100) silicon with a resistivity of 1 $\Omega\cdot$cm. Some samples were also implanted with oxygen ions to a depth corresponding to the range of Er ions at a dose 10 times greater than the Er dose. After implantation, anneals were carried out at 620 °C for 1 h in a chlorine-containing atmosphere. The concentration profiles of Er across the thickness were determined by secondary-ion mass spectrometry on a Cameca IMS 4f system. The appearance of an a-layer, its thickness, and its position were determined by recording the Rutherford backscattering of 230-keV protons.

At low Er implantation doses up to $D=3\times10^{13}$ cm^{-2} the backscattering spectra of the channeled ions do not contain a signal of an amorphous phase. At Er doses in the range $5\times10^{13}-1\times10^{14}$ cm^{-2} the appearance of an amorphous phase with preservation of the surface layer in the single-crystal state is observed (Fig. 1, curves *2* and *3*). At doses above 4×10^{14} cm^{-2} the single-crystal layer near the surface vanishes, and the α-layer becomes continuous.

At low implantation doses in the range $D=(1-3)\times10^{13}$ cm^{-2} the distribution profiles of Er after the anneals scarcely differ from the original profiles. An appreciable difference appears at a dose of 5×10^{13} cm^{-2}, which corresponds to the expected critical dose for the amorphization of silicon by Er ions with a mass of 168 (Ref. 7). At doses equal to 5×10^{13} and 1×10^{14} cm^{-2} the segregation of Er begins from two sides, which are positioned asymmetrically relative to the distribution maximum of the impurity at $x=R_p$, where R_p is the mean projected range ($R_p=0.4$ μm when $E=1.2$ MeV) (Fig. 2, curve *2*). It is directed into the interior of the buried a-layer and leads to the formation of a concentration peak at the meeting place of the two crystallization fronts. In the case of combined implantation with oxygen, the redistribution of Er is appreciably weaker, and the posi-

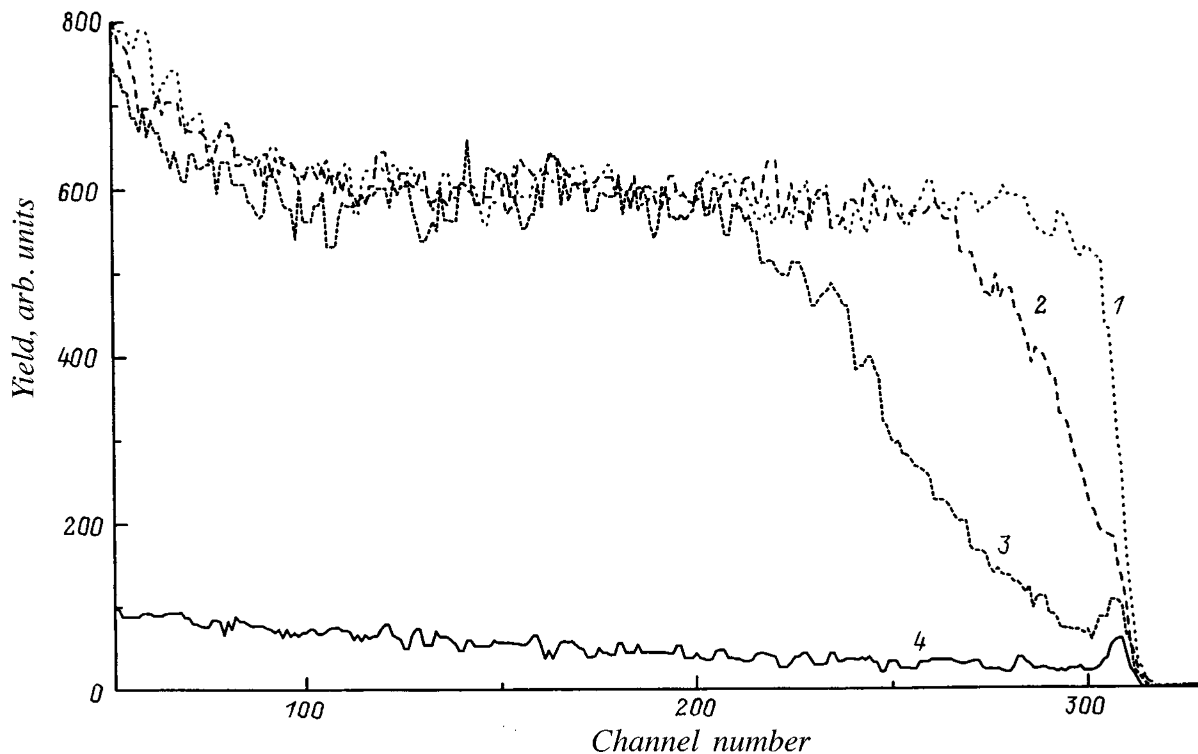

FIG. 1. Rutherford backscattering energy spectra: random (*1*), channeled along the ⟨100⟩ axis after the implantation of Er ions at $D=1\times10^{14}$ cm^{-2} (*2*) and $D=5\times10^{13}$ cm^{-2} (*3*), and channeled along the ⟨100⟩ axis for as-grown single-crystal silicon (*4*).

tion of the segregation concentration peak shifts toward the maximum of the Er and O concentrations (Fig. 2, curve *3*). According to the data in Ref. 4, when the Er dose is increased to 4×10^{14} cm^{-2}, the erbium impurity is displaced only toward the surface, providing evidence that the α-layer reaches the surface.

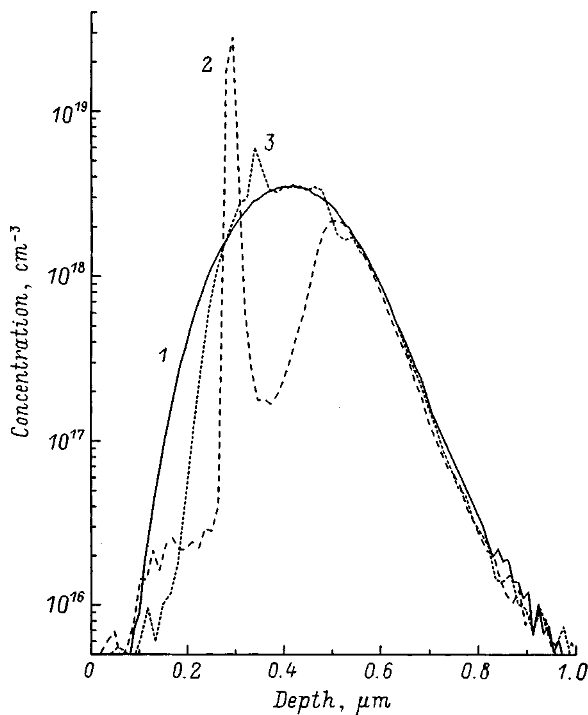

FIG. 2. Concentration profiles of Er in Si(100) after the implantation of Er^+ ions ($E=1.2$ MeV, $D=1\times10^{14}$ cm^{-2}) (*1, 2*) and O^+ ions ($E=0.17$ MeV, $D=1\times10^{15}$ cm^{-2}) (*3*) before (*1*) and after (*2, 3*) annealing.

At implantation doses equal to 5×10^{13} and 1×10^{14} cm^{-2} the segregation peak of Er is located at a distance of $\sim0.7R_p$. This is attributed to the location of the midplane of the buried *a*-layer at a distance of $\sim(0.75-0.8)R_p$ from the surface, in accordance with the distribution of the loss maximum and, accordingly, the radiation defects for heavy ions.[8] The additional implantation of oxygen ions leads to displacement of the segregation peak toward the concentration maximum of Er and O to a distance of $(0.8-0.85)R_p$. This result is attributable to the decrease in the crystallization rate of *a*-Si under the influence of the electrically inactive oxygen impurity.[9,10] We note that in Ref. 2 the position of the segregation peak essentially coincided with the midplane of the buried α-layer and with the maximum of the original distribution of Er ($R_p=0.16$ μm for $E=0.5$ MeV), probably due to the specific features of the distribution of the radiation defects in the heated target.

Thus, when structures with a buried *a*-layer are annealed, SPE crystallization takes place not only on the lower a/c boundary with the single-crystal substrate with advancement toward the surface, but also on the upper α/c boundary with the surface unamorphized single-crystal layer with advancement into the interior of the substrate. For this reason, the quantitative model of the segregation of Er that we developed for a surface amorphous layer[5] must be supplemented by a second crystallization front moving into the interior of the substrate. In this case a change from zone crystallization to a directional process occurs when the upper (1) and lower (2) crystallization fronts approach one another

to within a distance $b=L_1+L_2$, where L_1 and L_2 are the widths of the corresponding transition layers. The inverse problem of finding the segregation coefficient $k(x)$ from the concentration profiles of Er in the implanted layer before and after segregation was solved for constant values of L_1 and L_2.

For zone crystallization, as long as $b \geqslant L_1+L_2$, the segregation coefficient can be found by integrating Eq. (1) of the model in Ref. 5

$$\frac{dC_a}{dy}=\frac{C_0(y)-kC_a(y)}{L}, \tag{1}$$

where y is the current thickness of the zone-crystallized layer measured from the initial a/c boundary, $C_0(y)$ is the initial distribution of the impurity in the amorphous layer before annealing, and $C_a(y)$ is the current concentration of the impurity in the transition a-layer of width L (L_1 or L_2). After integrating (1) with consideration of the equality

$$C(y)=kC_a(y), \tag{2}$$

where $C(y)$ is the concentration of the impurity in the recrystallized layer after annealing, and the condition $k=1$ for $C(y)=C_0(y)$, we obtain

$$k(y)=\frac{LC(y)}{Q_0(y+L)-Q(y)}, \tag{3}$$

where $Q_0(y+L)$ and $Q(y)$ are the quantities of the impurity in layers of thickness $y+L$ and y, respectively, before and after crystallization.

When $b \leqslant L_1+L_2$, the segregation coefficient for directional crystallization can be found from Eq. (3) of the model in Ref. 5:

$$\frac{dC_a(z)}{dz}=(1-k)\frac{C_a(z)}{L-z}, \tag{4}$$

where z is the current thickness of the directionally crystallized layer measured from x_p-L_1 or x_p+L_2, where x_p is the meeting point of fronts 1 and 2. Taking into account the equality $C(z)=kC_a(z)$ and representing the derivative in a finite-difference form, we obtain

$$k(z)=\frac{L-z-\Delta z}{\dfrac{(L-z)}{k(z-\Delta z)}\dfrac{C(z-\Delta z)}{C(z)}-\Delta z}, \tag{5}$$

where Δz is the increment along z.

The segregation coefficients were calculated as a function of depth using formulas (3) and (5) for the Er profiles shown in Fig. 2. The values of the widths of the transition regions were taken from Ref. 4: $L_1=L_2\approx 50$ nm for the implantation of only Er ions ($E=1$ MeV) and $L_1=L_2\approx 16$ nm for the combined implantation of Er and O ions. As can be seen from Fig. 3, at the beginning of the crystallization process there is a drop in the value of the segregation coefficient from 1 to $(2.5-5)\times 10^{-2}$, which subsequently gives way to an increase in k, and the latter is especially fast in the vicinity of the erbium concentration peaks. The higher concentration of oxygen in the lower part of the buried a-layer weakens the decrease in the segregation coefficient in the initial stage of SPE crystallization and its increase in the later stage of SPE crystallization. This finding can be associated with the formation of Er–O complexes and a decrease in the crystallization rate in the presence of a high concentration of the electrically inactive oxygen impurity.

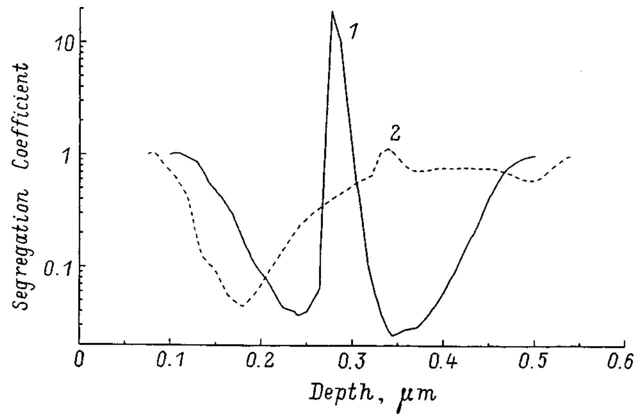

FIG. 3. Dependence of the segregation coefficient of Er on depth for profiles 2 (curve *1*) and 3 (curve *2*) in Fig. 2.

One special feature of the Er concentration profile for bilateral SPE crystallization at a relatively small implantation dose is the relatively large distance between the maximum and the minimum at the break on the concentration profile near the original lower a/c boundary (Fig. 2, curve *2*). This distance increases with decreasing Er dose from 0.05 μm for $D=2\times 10^{15}$ cm^{-2}, according to the data in Ref. 4, to 0.14 μm for $D=5\times 10^{13}-1\times 10^{14}$ cm^{-2}, according to the data from the present study. In this region the segregation coefficient decreases from 1 to the value of k_0 on the coordinate dependence of $k(x)$ found in Ref. 5 and is not described by that dependence. Such behavior of $k(x)$ can be attributed to the nonequilibrium character of segregation at the beginning of the SPE crystallization process, when the formation of a transition layer with an increased diffusion coefficient takes place. This process is slower for the a-layers with low defect densities formed at small Er implantation doses near the amorphization threshold ($D \gtrsim D_a$) than for the a-layers with higher defect densities formed at large doses ($D \gg D_a$).

Thus, we have investigated the redistribution of Er during the SPE crystallization of buried amorphous layers. Segregation with convergent motion of the crystallization fronts leads to displacement of the Er distribution profiles within the buried a-layer with the formation of a segregation concentration peak near the midplane. Combined implantation with oxygen ions lowers the erbium concentration at the segregation peak and displaces it toward the maximum of the distribution of Er and O. A method for calculating the dependence of the segregation coefficient on depth is proposed. The drop on the $k(x)$ curve at the beginning of SPE crystallization is attributed to the nonequilibrium character of segregation in that period.

We thank E. O. Parshin for performing the ion implantation. This work was performed with partial support from the ISTC (Grant 168) and the INTAS–RFBR (Grant 95-0531).

*)E-mail: Nick@Sobolev.ioffe.rssi.ru; Fax: +7-812-2471017

[1] D. Mountonnet, H. L'Haridon, P. N. Favennec, M. Salvi, M. Gauneau, F. A. D'Avitaya, and J. Chroboczek, Mater. Sci. Eng., B **4**, 75 (1989).
[2] W. P. Gillin, Z. Jingping, and B. J. Sealy, Solid State Commun. **77**, 907 (1991).
[3] J. S. Custer, A. Polman, and H. M. van Pinxteren, J. Appl. Phys. **75**, 2809 (1994).
[4] O. V. Aleksandrov, Yu. V. Nikolaev, and N. N. Sobolev, Fiz. Tekh. Poluprovodn. **33**, 114 (1999) [Semiconductors **33**, 101 (1999)].
[5] O. V. Aleksandrov, Yu. V. Nikolaev, and N. N. Sobolev, Fiz. Tekh. Poluprovodn. **32**, 1420 (1998) [Semiconductors **32**, 1266 (1998)].
[6] M. A. Guerra, Semicond. Sci. Technol. **33**, 75 (1990).
[7] V. M. Gusev, M. I. Guseva, and C. V. Starinin, Radiat. Eff. **15**, 251 (1972).
[8] H. Ryssel and I. Ruge, *Ionenimplantation* [Teubner, Stuttgart (1978); Nauka, Moscow (1983)].
[9] A. F. Vyatkin, Poverkhnost', No. 4, 5 (1991).
[10] G. L. Olson and J. A. Roth, in *Handbook of Crystal Growth*, D. T. J. Hurle (Ed.) (1994), Vol. 3, p. 257.

Translated by P. Shelnitz

Influence of intrinsic point defects on the formation of structural defects and optically active centers during the annealing of erbium- and dysprosium-implanted silicon

N. A. Sobolev*) and E. I. Shek

A. F. Ioffe Physicotechnical Institute, Russian Academy of Sciences, 194021 St. Petersburg, Russia

A. M. Emel'yanov

St. Petersburg State Technical University, 195251 St. Petersburg, Russia

V. I. Vdovin and T. G. Yugova

Institute of Chemical Problems in Microelectronics, 109017 Moscow, Russia

(Submitted December 17, 1998; accepted for publication December 17, 1998)
Fiz. Tekh. Poluprovodn. **33**, 656–659 (June 1999)

The photoluminescence spectra and behavior of the structural defects in layers obtained by implanting 1.0–1.8-MeV Er and Dy ions at a dose of 1×10^{13} cm^{-2} are investigated after annealing at 1000–1200 °C for 0.5–1 h in argon or a chlorine-containing atmosphere. The structural defects are studied using transmission electron microscopy and selective chemical etching. The dominant features in the luminescence spectra of the Si:Er and Si:Dy layers following annealing in the chlorine-containing atmosphere are lines associated with the formation of edge dislocations, while the dominant features following the annealing of Si:Er and Si:Dy layers in argon are the erbium-related lines. A comparative analysis of the luminescence spectra of the Si:Er and Si:Dy layers shows that the highest intensity of dislocation-related luminescence is achieved in the erbium-implanted structures. A significant influence of intrinsic point defects on the structural and optical properties of erbium- and dysprosium-implanted silicon is revealed. © *1999 American Institute of Physics.* [S1063-7826(99)00606-7]

1. INTRODUCTION

One promising way to create silicon light-emitting devices is to dope this widely used semiconductor with rare-earth elements, among which erbium is of greatest interest.[1] The electronic transitions between the levels of the $4f$ shell in Er^{3+} are responsible for the appearance of a narrow temperature-independent line in the luminescence spectrum with a wavelength of ~1.54 μm, which corresponds to the dispersion minimum and the loss minimum in systems of fiber-optic communications lines. At the same time, there is definite interest in investigations of the optical properties of structures based on silicon doped with other rare-earth elements, particularly dysprosium, which can also be sources of infrared radiation.

Ion implantation is widely used to fabricate silicon semiconductor devices. Ion implantation results in the formation of radiation defects, whose removal requires a high-temperature anneal. Moreover, the defects which determine the structural, optical, and electrical properties of silicon layers doped with rare-earth (RE) elements form specifically in this step. Some preliminary results regarding the defect-formation processes accompanying the implantation of RE elements in silicon were presented in Refs. 2–5. The purpose of the present work was to investigate the influence of the postimplantation annealing conditions on the structural and optical properties of erbium- and dysprosium-doped silicon layers.

2. EXPERIMENTAL CONDITIONS

The substrates used were boron-doped wafers of Czochralski-grown p-type $\langle 100\rangle$ silicon with a thickness of 300 μm, a diameter of 100 mm, and a resistivity of 20 $\Omega\cdot$cm. Erbium and dysprosium ions were implanted at $1-1.8$ MeV and a dose of 1×10^{13} cm^{-2} on the High Voltage Engineering Europe K2MV facility. The implanted samples were annealed at 1000–1200 °C for 0.5–1 h. In order to reveal the influence of intrinsic point defects on the formation of structural defects, anneals were performed in argon and a chlorine-containing atmosphere.[6] The latter was a stream of oxygen containing 1 mol % carbon tetrachloride.

The photoluminescence (PL) measurements were performed at 77 K. The photoluminescence was excited by the visible radiation from a halogen lamp with a power of ~50 mW, which can be mechanically interrupted at a frequency of 36 Hz. The radiation from the sample was collected by a lens and, after passage through a monochromator, was measured by an InGaAs photodetector operating at room temperature. The photocurrent was amplified by a selective amplifier. The resolution of the monochromator was 7 nm. The structural defects were investigated by transmission electron microscopy and selective chemical etching.

3. RESULTS AND DISCUSSION

Figure 1 shows the PL spectrum of implanted Si:Er layers ($E=1.0$ MeV and $D=1\times10^{13}$ cm^{-2}), which were annealed under various conditions. After annealing in argon at

 © 1999 American Institute of Physics

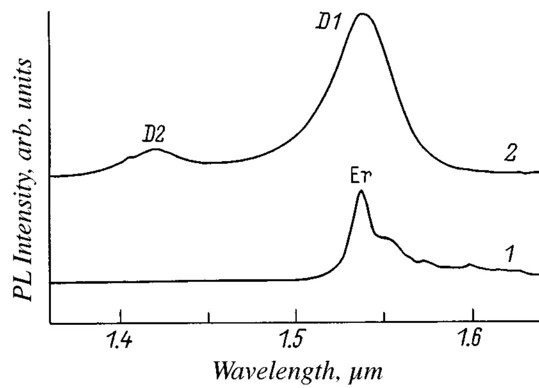

FIG. 1. Photoluminescence spectra (measured at 77 K) of Si:Er layers annealed at $T = 1100$ °C for 0.5 h in argon (*1*) and the chlorine-containing atmosphere (*2*).

1100 °C for 0.5 h, the luminescence spectrum displays a line with a maximum at 1.538 μm (curve *1*). After annealing in the chlorine-containing atmosphere under the same temperature-time conditions, there are two dominant lines in the luminescence spectrum: *D1* (1.525 μm) and *D2* (1.417 μm) (curve *2*). The presence of a fine structure in the line on curve *1* is evidence that the luminescence peak of the Si:Er samples annealed in argon is caused by intracenter transitions of electrons in the $4f$ shell of the Er^{3+} ions.[1] The lack of a fine structure in the *D1* and *D2* lines suggests that the PL peaks in the Si:Er samples annealed in the chlorine-containing atmosphere are attributable to the presence of defects in the implanted Si:Er layers. The hypotheses just advanced were confirmed by measuring the temperature dependence of the position of the maxima of the luminescence lines. It was found that the position of the maximum of the Er line does not depend on measurement temperature, as is typical of intracenter transitions in rare-earth ions. At the same time, the blue shift of the maximum of the *D1* line with increasing temperature closely correlates with the analogous behavior of the lines in the dislocation-related luminescence spectrum observed in Refs. 7 and 8. Such a dependence for the *D* lines can be associated with the recombination of pairs of charge carriers on centers belonging to the dislocations formed.

The relationship between the structural and optical properties was elucidated by studying the structural defects in the same samples on which the PL measurements were performed. After annealing in argon, the Si:Er and Si:Dy layers did not display etching pits in the selective etching experiment or variation of the diffractive contrast upon electron microscopy. Conversely, annealing in the chlorine-containing atmosphere led to the appearance of several types of defects. Tiny etching pits of the dislocation type and narrow strips demarcated by etching pits, which are usually assigned to stacking defects, were revealed as a result of selective chemical etching. Transmission electron microscopy revealed the presence of three types of defects: Frank loops (stacking defects), perfect prismatic dislocation loops, and pure edge dislocations.[2] The Frank loops are dislocation loops of the interstitial type, which lie in $\{111\}$ planes and have a Burgers vector $\mathbf{b} = a/3\langle 111 \rangle$. The perfect prismatic

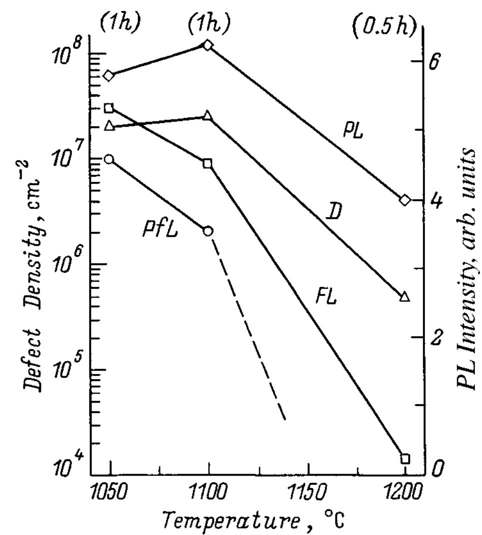

FIG. 2. Dependence of the density of structural defects (*FL* — Frank loops, *PfL* — prismatic dislocation loops, *D* — edge dislocations) and the intensity of the dislocation photoluminescence (*PL*) on the annealing temperature of Si:Er layers in the chlorine-containing atmosphere.

dislocation loops, which are located mainly in $\{110\}$ planes, are also interstitial loops with a Burgers vector $\mathbf{b} = a/2\langle 110 \rangle$. The pure edge dislocations form as a result of the interaction of large, perfect loops during annealing. Investigations of transverse sections of the implanted layers showed that the structural defects are present in layers with a thickness of ~ 1 μm. The Frank loops of small and moderate size are distributed fairly evenly across the entire thickness of the implanted layers. The small prismatic loops are located mainly in the upper half of the implanted layer. Measurements of the contrast from the defects demonstrated the absence of erbium precipitates.

The significant difference between the defect structures of the implanted Si:Er and Si:Dy layers annealed in the inert (argon) and oxidizing (chlorine-containing) media can be explained in the following manner. It is known that high-temperature annealing leads to the supersaturation of silicon with intrinsic point defects and that different defects dominate, depending on the annealing atmosphere.[6] Annealing in an oxidizing atmosphere leads to supersaturation with intrinsic interstitials, and annealing in an inert medium leads to supersaturation with vacancies. The picture in implanted layers is complicated by the fact that the interaction of the radiation defects with the intrinsic point defects must be taken into account. In the case of annealing in the chlorine-containing atmosphere the resultant supersaturation of silicon with interstitials is sufficient for the formation of dislocation loops of the interstitial type. The absence of defects following annealing in argon is attributed to annihilation of the excess interstitials created by implantation and the vacancies appearing during annealing.

The sizes and density of the structural defects vary when the duration and temperature of the anneal in the chlorine-containing atmosphere are varied. Variations of the intensity of the *D* lines in the PL spectrum are also observed. Variation of the annealing conditions allows us to trace the rela-

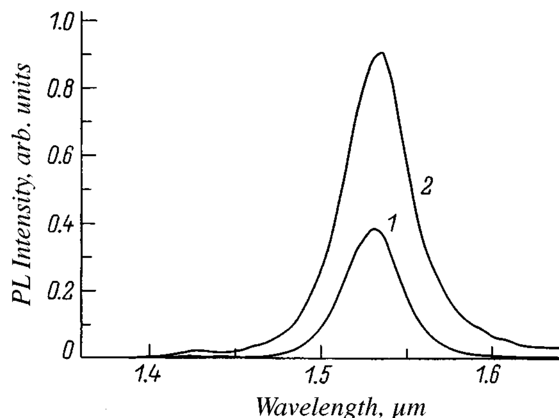

FIG. 3. Photoluminescence spectra (measured at 77 K) of Si:Dy layers annealed at $T=1100$ °C in the chlorine-containing atmosphere for 0.5 h (*1*) and 1 h (*2*).

tionship between the structural and optical properties of Si:Er. We presented plots of the dependence of the density of the various types of defects and the PL intensity on the annealing time at $T=1100$ °C in Ref. 2. In this paper we present results which characterize the variation of the density of the various defects and the PL intensity of the *D* lines in response to variation of the annealing temperature (Fig. 2). Anneals of the Si layers implanted with Er at $E=1.8$ MeV were carried out in the temperature range 1000–1100 °C over the course of 1 h. No dislocations were discovered in the samples annealed at 1000 °C. Since essentially the entire implanted layer passes into the oxide over the course of 1 h during an anneal in the chlorine-containing atmosphere at 1200 °C, the annealing at $T=1200$ °C was carried out for 0.5 h. The data presented in Fig. 2 attest to the existence of a correlation between the intensity of the *D1* PL line and the density of edge dislocations. This confirms the conclusion in Ref. 2 that edge dislocations are responsible for the appearance of dislocation-related luminescence.

The PL spectra of Si layers implanted with Dy at $E=1.0$ MeV are shown in Fig. 3. The anneals were carried out in the chlorine-containing atmosphere at 1100 °C for 0.5–1 h. As is seen from the figure, the dominant feature in the luminescence spectra is the *D1* line. After annealing in argon, no PL lines were observed at 1.4–1.6 μm. The investigation of the structural defects in the Si:Dy layers annealed in the chlorine-containing atmosphere revealed the presence of Frank loops and edge dislocations. Detailed investigations showed that the density of these defects in the Si:Dy layers is 1.2–1.6 times less than the density of the same defects in Si:Er layers formed under identical conditions. The intensity of the defect-related PL was also greater in the Si:Er layers than in the Si:Dy layers. More prolonged annealing of Si:Dy is accompanied by an increase in the density of edge dislocations and a decrease in the density of Frank loops.[5] The correlation discovered between the intensity of the *D1* line in the PL spectrum and the density of edge dislocations provides evidence that dislocations are responsible for the appearance of these PL lines in Si:Dy, just as in Si:Er.

It has been established that the annealing of implanted Si:Er and Si:Dy layers at 1050–1200 °C in a chlorine-containing atmosphere leads to the appearance of identical structural defects. Their formation is associated with the supersaturation of silicon with intrinsic interstitials, and the appearance of the *D* lines in the PL spectra is caused by pure edge dislocations. No structural defects were detected after annealing in argon, and only the Er line is present in the spectra of the Si:Er layers.

We thank E. O. Parshin for performing the implantation.

This work was performed with partial support from the INTAS–RFBR (Grant 95-0531).

*)E-mail: Nick@Sobolev.ioffe.rssi.ru; Fax: +7-812-2471017

[1] N. A. Sobolev, Fiz. Tekh. Poluprovodn. **29**, 1153 (1995) [Semiconductors **29**, 595 (1995)].

[2] N. A. Sobolev, O. B. Gusev, E. I. Shek, V. I. Vdovin, T. G. Yugova, and A. M. Emel'yanov, Appl. Phys. Lett. **72**, 3326 (1998).

[3] O. V. Aleksandrov, A. O. Zakhar'in, N. A. Sobolev, E. I. Shek, M. I. Makoviĭchuk, and E. O. Parshin, Fiz. Tekh. Poluprovodn. **32**, 1029 (1998) [Semiconductors **32**, 921 (1998)].

[4] N. A. Sobolev, O. B. Gusev, E. I. Shek, V. I. Vdovin, T. G. Yugova, and A. M. Emel'yanov, J. Lumin. **80**, 357 (1998).

[5] V. I. Vdovin, T. G. Yugova, N. A. Sobolev, E. I. Shek, M. I. Makovijchuk, and E. O. Parshin, Nucl. Instrum. Methods Phys. Res. B **147**, 116 (1999).

[6] N. A. Sobolev, in *Semiconductor Technology: Processing and Novel Fabrication Techniques*, M. Levinstein and M. Shur (Eds.), Wiley, New York (1997), Chap. 5.

[7] V. V. Kveder, E. A. Steinman, S. A. Shevchenko, and H. G. Grimmeiss, Phys. Rev. B **51**, 10 520 (1995).

[8] S. Fukatsu, Y. Mera, M. Inoue, K. Maeda, H. Akiyama, and H. Sakaki, Appl. Phys. Lett. **68**, 1889 (1996).

Translated by P. Shelnitz

Influence of the orientation of the silicon substrate on the properties of avalanche Si:Er:O light-emitting structures

N. A. Sobolev*) and Yu. A. Nikolaev

A. F. Ioffe Physicotechnical Institute, Russian Academy of Sciences, 194021 St. Petersburg, Russia

A. M. Emel'yanov

St. Petersburg State Technical University, 195251 St. Petersburg, Russia

V. I. Vdovin

Institute of Chemical Problems in Microelectronics, 109017 Moscow, Russia

(Submitted December 28, 1998; accepted for publication December 29, 1998)
Fiz. Tekh. Poluprovodn. **33**, 660–663 (June 1999)

The influence of the orientation of silicon on the structural and luminescence properties of avalanche light-emitting diodes fabricated by the coimplantation of erbium and oxygen followed by solid-phase epitaxial (SPE) crystallization of the amorphized layer is considered. The luminescence properties are a consequence of the formation of various structural defects during the SPE crystallization: V-shaped dislocations and erbium precipitates form in (100) Si:Er:O layers, and larger structural defects, i.e, twins, are observed in (111) Si:Er:O layers along with an increase in the dislocation density by more than four orders of magnitude in comparison with the (100) orientation. The luminescence properties of avalanche and tunnel light-emitting diodes are also compared. In contrast to tunnel diodes, in avalanche diodes erbium ions are excited in the entire space-charge layer, and the effective excitation cross section of the Er^{3+} ions and their lifetime in the excited state are 3–4 times larger. © *1999 American Institute of Physics.* [S1063-7826(99)00706-1]

The functioning of Si:Er:O light-emitting diodes is based on radiative transitions from the first excited state($^4I_{13/2}$) to the ground state ($^4I_{15/2}$) in the inner $4f$ shell of the Er^{3+} ions. These transitions produce a narrow luminescence line at a wavelength of ~ 1.54 μm, whose position in the spectrum is essentially temperature-independent. The technology for fabricating Si:Er:O light-emitting diodes includes the formation of an electrically and optically active silicon layer doped with erbium and oxygen. The electroluminescence (EL) of Er^{3+} ions is observed at room temperature when either a forward-bias[1–5] or reverse-bias[3–12] voltage is applied to Si:Er:O diodes. The maximum EL intensity at room temperature is usually achieved in a breakdown regime for the $p-n$ junction, i.e., when a reverse-bias voltage is supplied.[3–12] In this case the EL of erbium ions is observed in the cases of both tunnel[3–6] and avalanche[7–12] breakdown. Our goal in this study was to investigate the influence of the orientation of the silicon substrate on the properties of avalanche Si:Er:O light-emitting diodes and comparing the properties of avalanche and tunnel light-emitting diodes.

EXPERIMENTAL CONDITIONS

Wafers of n-type Si with a resistivity of 20 $\Omega \cdot$cm and the (100) orientation and with a resistivity of 5 $\Omega \cdot$cm and the (111) orientation were implanted with erbium ions at energies of 2.0 and 1.6 MeV and doses of 1×10^{14} cm^{-2}, as well as oxygen (0.28 and 0.22 MeV, 1×10^{15} cm^{-2}). Annealing at 620 °C/1 h + 900 °C/0.5 h led to recrystallization of the amorphous layer formed as a result of implantation and the creation of erbium-containing, electrically and optically active centers. The implantation of boron (40 keV and 5×10^{15} cm^{-2}) and a postimplantation anneal (900 °C/0.5 h) resulted in the formation of $p-n$ junctions. The light-emitting diodes with a mesa-like outline for the structure had a working area for the $p-n$ junction equal to $S=5.5$ mm^2. The EL spectra, the rise time and decay time of the erbium EL intensity observed when rectangular current pulses are supplied to the diode, and the temperature dependence of the Er^{3+} EL intensity were investigated. The technology and procedure for measuring the luminescence characteristics of the avalanche Si:Er:O light-emitting diodes were previously described in detail in our earlier publications.[7–12] The structural defects were investigated by transmission electron microscopy. An analysis of the studies on Si:Er:O light-emitting structures operating in a tunnel-breakdown regime[3–6] reveals that the fundamental deviation from the technology for avalanche diodes described above is the higher implantation doses for tunnel diodes (no less than 10^{15} cm^{-2} for Er and 10^{16} cm^{-2} for O, respectively). This led to a higher concentration of donor centers in the optically active Si layer. It may also be noted that investigations of tunnel diodes were performed only for Si(100). The characteristics of the tunnel diodes were taken from publications of other researchers.

 © 1999 American Institute of Physics

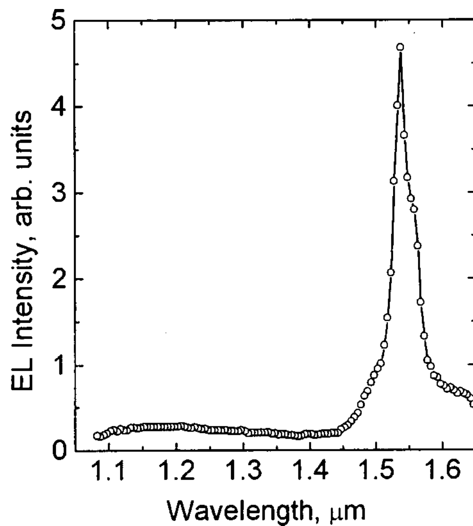

FIG. 1. EL spectrum of an avalanche Si:Er:O diode recorded at room temperature with a reverse-bias current density $j=6.3$ A/cm^2.

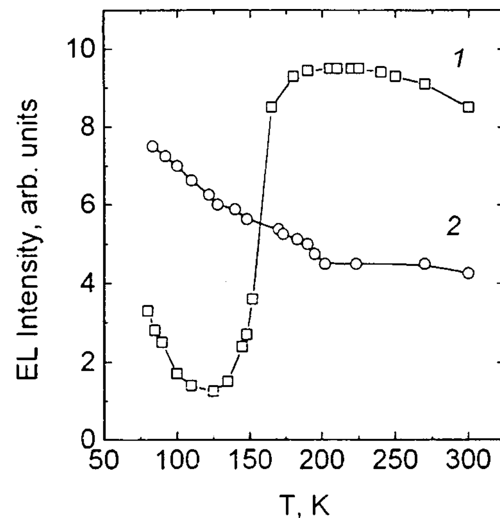

FIG. 2. Temperature dependence of the EL intensity of avalanche Si:Er:O diodes at $\lambda=1.538$ μm for the (111) (*1*) and (100) (*2*) orientations of Si ($j=4.5$ A/cm^2).

EXPERIMENTAL RESULTS AND DISCUSSION

Figure 1 shows the EL spectrum of an avalanche Si:Er:O light-emitting diode with Si(111) measured at room temperature and a reverse-bias current density $j=6.3$ A/cm^2 in the wavelength range $\lambda \sim 1.1-1.65$ μm. Apart from the sharp peak with a maximum at $\lambda=1.538$ μm, which is caused by transitions of electrons from the $^4I_{13/2}$ excited state to the $^4I_{15/2}$ ground state of the erbium ions, the EL spectrum displays emission which is nearly independent of λ in the transparency region of silicon and is usually associated with transitions of hot electrons within the conduction band.[13,14] A series of studies carried out in the last 10 years[15–18] showed that the emission is caused mainly by direct transitions of electrons between the upper and lower subbands of the Si conduction band: $\Delta_2 \rightarrow \Delta_1$. No fundamental differences were observed in the spectra for the avalanche diodes with Si(111) and Si(100), as well as for the tunnel diodes described in the literature.

Figure 2 presents plots of the temperature dependence of the EL intensity of light-emitting diodes at $\lambda=1.538$ μm for two substrate orientations. The (100) samples exhibit the usual dependence, on which an increase in the luminescence measurement temperature is accompanied by a decrease in the EL intensity (so-called thermal luminescence quenching). In the case of the (111) substrate orientation, an increase in the EL intensity (''brightening'') is observed. As a result, the EL intensity is higher at room temperature than at liquid-nitrogen temperature. We first observed this phenomenon in Ref. 8. More detailed investigations of this anomalous temperature dependence of erbium EL showed that this phenomenon is due to the appearance of a high concentration of hole traps in the lower half of the silicon band gap in the space-charge layer of the $p-n$ junction.[9]

Our investigations of the defects in Si:Er:O light-emitting layers for the (111) and (100) orientations of Si gave the following results. In Si:Er:O samples with the (100) orientation we discovered V-shaped (hairpin) dislocations with a density $\approx 10^6$ cm^{-2} and erbium precipitates of plate-like shape (with a diameter of ~ 20 nm and a thickness of ~ 1 nm). In Si:Er:O structures with the (111) orientation we observed dislocations with a density $>10^{10}$ cm^{-2} and twins of irregular shape with effective dimensions equal to 10–350 nm. Thus, in the (111) Si:Er:O diodes there are larger structural defects (twins), and the dislocation density is four orders of magnitude higher than in the diodes with the (100) orientation. These structural defects are probably responsible for the appearance of the anomalous temperature dependence of the erbium EL.

We also note that despite the considerably higher defect density, the avalanche light-emitting diodes with the (111) orientation significantly surpass the diodes with the (100) orientation, primarily with respect to the uniformity of the distribution of the emission over the area of the $p-n$ junction.[12] Consequently, the luminescence parameters of the avalanche (111) Si:Er:O light-emitting diodes are highly reproducible, while a considerable spread of luminescence parameters is observed for the (100) orientation even within a single production batch of diodes.

The important characteristics of light-emitting structures are the effective luminescence excitation cross section (σ) and the lifetime (τ) of the excited states of the light-emitting centers. These parameters can be determined from the dependence of the rise time of the EL intensity on the amplitude of the rectangular pulses of reverse-bias current applied to the $p-n$ junction. A method for calculating σ and τ in Si:Er:O light-emitting diodes under the assumption of an impact mechanism for exciting erbium EL was described in Refs. 5 and 6. The use of this method as applied to tunnel Si:Er:O diodes in a breakdown regime at room temperature gave the values $\sigma=6\times10^{-17}$ cm^2 and $\tau=100$ μm.[5,6] The values of σ and τ determined in a similar manner for our avalanche Si:Er:O diodes with the (111) orientation were 2.3×10^{-16} cm and 280–390 μs, respectively.[10,11] We note that the values of σ and τ are 3–4 times greater in the avalanche diodes than in the tunnel analogs. The values of the product $\sigma\tau$ obtained for the avalanche Si:Er:O diodes are roughly an

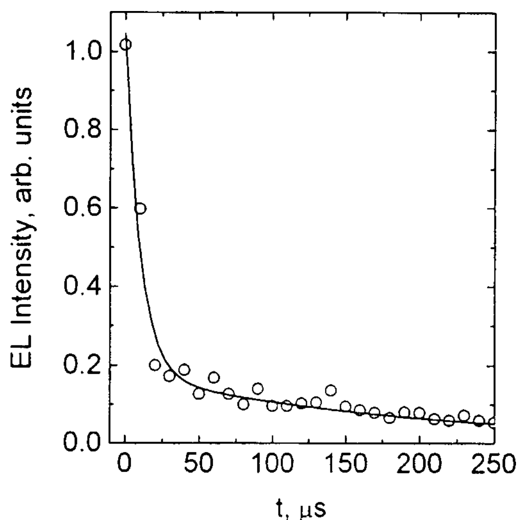

FIG. 3. Dependence of the EL intensity at $\lambda \sim 1.54$ μm on the time (t) elapsed after switching an avalanche Si:Er:O diode from a reverse-bias regime with $j = 6.3$ A/cm^2 to a regime with $j = 0$.

order of magnitude greater than the values of $\sigma\tau$ in the tunnel diodes. As a result, saturation of the erbium EL intensity is achieved at current densities an order of magnitude smaller in the avalanche diodes than in the tunnel analogs.[9–12]

The investigation of the decay kinetics of erbium EL following removal of the reverse-bias current in both tunnel[5,19] and avalanche[12] Si:Er:O light-emitting diodes has demonstrated the existence of a decay time constant smaller than 10 μs, which is determined by the speed of the recording instrumentation. Such short EL decay times have been explained using the following model.[5,20] After removal of the reverse current, the Er^{3+} ions excited in the space-charge layer of the $p-n$ junction are in a quasineutral region with a high concentration of free charge carriers and are rapidly de-excited as a result of Auger recombination involving these carriers. Estimates show that the EL decay time constant can equal 10–100 ns in this case.[21]

Investigations of the EL decay kinetics in various regimes led Coffa *et al.*[19] to the conclusion that only erbium ions located on the edge of the space-charge layer are excited in tunnel Si:Er:O light-emitting diodes. The EL decay kinetics in the avalanche Si:Er:O diodes that we investigated include not only a fast component with $\tau < 10$ μs (Fig. 3), but also a slow component with $\tau \cong 300$ μs (the time constant of the response of the recording instrument was ~ 5 μs). This shows that in the avalanche diodes erbium ions are excited throughout the space-charge layer, including the region directly adjacent to the plane of the $p-n$ junction.

CONCLUSIONS

Thus, the results presented here demonstrate that not only the concentration of the electrically and optically active centers that were introduced, but also the orientation of the silicon have a considerable influence on the EL characteristics of avalanche Si:Er:O light-emitting diodes.

This work was performed with partial support from the INTAS–RFBR (Grant 95-0531).

*)E-mail: Nick@Sobolev.ioffe.rssi.ru; Fax: +7-812-2471017

[1] F. Y. G. Ren, J. Michel, Q. Sun-Paduano, B. Zheng, H. Kitagawa, D. S. Jacobson, J. M. Poate, and L. C. Kimerling, Mater. Res. Soc. Symp. Proc. **301**, 87 (1993).

[2] B. Zheng, J. Michel, F. Y. G. Ren, L. C. Kimerling, D. S. Jacobson, and J. M. Poate, Appl. Phys. Lett. **64**, 2842 (1994).

[3] G. Franzo, F. Priolo, S. Coffa, A. Polman, and A. Carnera, Appl. Phys. Lett. **64**, 2235 (1994).

[4] S. Coffa, F. Priolo, G. Franzo, A. Polman, S. Libertino, M. Saggio, and A. Carnera, Nucl. Instrum. Methods Phys. Res. B **106**, 386 (1995).

[5] G. Franzo, S. Coffa, F. Priolo, and C. Spinella, J. Appl. Phys. **81**, 2784 (1997).

[6] S. Coffa, G. Franzo, and F. Priolo Appl. Phys. Lett. **69**, 2077 (1996).

[7] N. A. Sobolev, A. M. Emel'yanov, and K. F. Shtel'makh, Appl. Phys. Lett. **71**, 1930 (1997).

[8] N. A. Sobolev, A. M. Emel'yanov, Yu. A. Nikolaev, K. F. Shtel'makh, Yu. A. Kudryavtsev, V. I. Sakharov, I. T. Serenkov, M. I. Makovijchuk, and E. O. Parshin, Mater. Sci. Forum **258–263**, 1527 (1997) (19th International Conference on Defects in Semiconductors, Aveiro, Portugal, July 21–25, 1997).

[9] A. M. Emel'yanov, N. A. Sobolev, and A. N. Yakimenko, Appl. Phys. Lett. **72**, 1223 (1998).

[10] N. A. Sobolev, Yu. A. Nikolaev, A. M. Emel'yanov, K. F. Shtel'makh, A. N. Yakimenko, M. I. Makovĭchuk, and E. O. Parshin, in *Proceedings of the All-Russian Conference "Silicon- and Germanium-Based Nanostructures* [in Russian], Nizhniĭ Novgorod, March 10–13, 1998, p. 89.

[11] N. A. Sobolev, Yu. A. Nikolaev, A. M. Emel'yanov, K. F. Shtel'makh, P. E. Khakuashev, and M. A. Trishenkov, J. Lumin. **80**, 315 (1998).

[12] N. A. Sobolev, A. M. Emel'yanov, S. V. Gastev, P. E. Khakuashev, Yu. A. Nikolaev, and M. A. Trishenkov, Mater. Res. Soc. Symp. Proc. **486**, 139 (1998).

[13] A. G. Chynoweth and K. G. McKay, Phys. Rev. **102**, 369 (1956).

[14] L. A. Kosyachenko, E. F. Kukhto, and V. M. Sklyarchuk, Fiz. Tekh. Poluprovodn. **18**, 426 (1984) [Sov. Phys. Semicond. **18**, 226 (1984)].

[15] J. Bude, N. Sano, and A. Yoshii, Phys. Rev. B **45**, 5848 (1992).

[16] L. Carbone, R. Brunetti, A. Lacaita, and M. Fischetti, Semicond. Sci. Technol. **9**, 674 (1994).

[17] T. Puritis and J. Kaupzs, in *Proceedings of the 21st International Conference on Microelectronics*, NIS, Yugoslavia, Sept. 14–17, 1997, Vol. 1, p. 161.

[18] E. Cartier, J. C. Tsang, M. V. Fischetti, and D. A. Buchanan, Microelectron. Eng. **39**, 103 (1997).

[19] S. Coffa, G. Franzo, F. Priolo, A. Pacelli, and A. Lacaita, Appl. Phys. Lett. **73**, 93 (1998).

[20] J. Palm, F. Gan, B. Zheng, J. Michel, and L. C. Kimerling, Phys. Rev. B **54**, 17 603 (1996).

[21] F. Priolo, G. Franzo, S. Coffa, and A. Carnera, Phys. Rev. B **57**, 4443 (1998).

Translated by P. Shelnitz

Mechanisms of excitation of the $f-f$ emission in silicon codoped with erbium and oxygen

V. F. Masterov and L. G. Gerchikov*)

St. Petersburg State Technical University, 195251 St. Petersburg, Russia
(Submitted December 24, 1998; accepted for publication December 28, 1998)
Fiz. Tekh. Poluprovodn. **33**, 664–670 (June 1999)

The Er_2O_3 cluster in silicon is discussed as a possible source of the Er-related emission in Si:Er, O. We propose a mechanism that gives a simple explanation of the high efficiency of Er atom excitation in Er-O clusters. The cases of photoluminescence and electroluminescence are considered. In the case of photoluminescence the high efficiency of Er excitation is attributed to the electron state localized at the Er-O cluster. The excitation of *f*-shell electrons in Er atoms occurs via the Auger recombination of the exciton bound at the Er-O cluster. We calculate the rate of this Auger process and discuss the dependence of the photoluminescence intensity on the carrier concentration. In the case of electroluminescence under reverse bias the impact excitation cross section is enhanced due to resonant scattering of the hot electrons at the quasi-discrete levels formed by the Er-O cluster quantum-well potential. The calculated impact excitation cross section is close to the experimental value. © *1999 American Institute of Physics.* [S1063-7826(99)00806-6]

The problem of energy transfer from photo- and electrogenerated carriers to *f*-electrons of a rare-earth center is a primary consideration in physics of rare-earth-doped semiconductors. It is a complicated problem, especially in the case of complex centers involving rare-earth ions and other impurity atoms. In spite of numerous papers on this subject,[1,2] the nature of the excitation mechanisms of rare-earth centers in semiconductors has not yet been clarified. In this paper we propose a simple model which describes the excitation of the Er-related emission in Er_2O_3 clusters in silicon in terms of the photo- and electrogeneration of carriers. The high efficiency of excitation is connected with the presence of the discrete and quasi-discrete electron states localized at Er_2O_3 clusters in silicon. In the case of photoluminescence and electroluminescence under forward bias the excitation of Er ions occurs via the Auger recombination of excitons localized at Er-O complexes. In the case of electroluminescence under reverse bias the electron capture of hot carriers in the conduction band of silicon into the quasi-bound states of the Er_2O_3 clusters leads to a large value of the impact excitation cross section.

COMPLEXES Er–O IN Si

Silicon codoped with erbium and oxygen is the most studied material due to the high intensity of the Er-related emission. Many studies[1,2] have shown that the optically active center in erbium-doped silicon is a complex formed as a result of interaction between erbium and oxygen atoms. Adler *et al.*[3] used the EXAFS method to identify the optically active complex in CZ-silicon. The EXAFS analysis indicates that more than 80% of the Er atoms are coordinated with the oxygen atoms. The first shell around the Er atom resembles the six-oxygen coordination in Er_2O_3 (Ref. 4). The value 2.25 Å of the Er-O bond length is, however, slightly smaller than the mean value 2.27 Å of the bond length in the oxide.

Terrasi *et al.*[5] have obtained by EXAFS data analyses almost the same result for silicon coimplanted by Er and O after annealing of the sample at 900 °C. In this case the coordination number of oxygen atoms is equal to 5, and the value in the range 2.26–2.27 Å of the Er-O bond length is close to the mean value 2.27 Å in Er_2O_3.

Masterov *et al.*,[6,7] using $^{169}Er(^{169}Tm)$ emission Mössbauer spectroscopy (EMS), established a correlation between the Er–O clusters and the $f-f$ photoluminescence intensity in amorphous (a-Si:H) and crystalline (c-Si) silicon. The Mössbauer spectra of the silicon samples, codoped with erbium and oxygen, have been compared with the spectrum of Er_2O_3.

The Mössbauer spectrum is a superimposition of the quadrupole doublet (spectrum I) and singlet (spectrum II). Spectrum I belongs to the erbium centers with low symmetry, whereas spectrum II belongs to the centers with cubic or almost cubic surrounding. As regards the correlation between the relative intensity of spectrum I and the intensity of Er-related emission, the corresponding erbium centers should be responsible for the Er-doped Si photoluminescence at the wavelength of 1.54 μm. It is believed that spectrum I corresponds to the complex consisting of the Er^{3+} ion with the six-oxygen environment. Spectrum II might be attributed to the erbium ion surrounded by silicon atoms only in $ErSi_2$ configuration.

Electron spin resonance (ESR) has been used by Carey *et al.*[8] to examine the structure of the Er-O complexes formed in silicon codoped with Er and O. In order to observe ESR sharp lines for Er concentration of 10^{19} Er/cm^3, it is necessary to have O concentration in excess of

 © 1999 American Institute of Physics

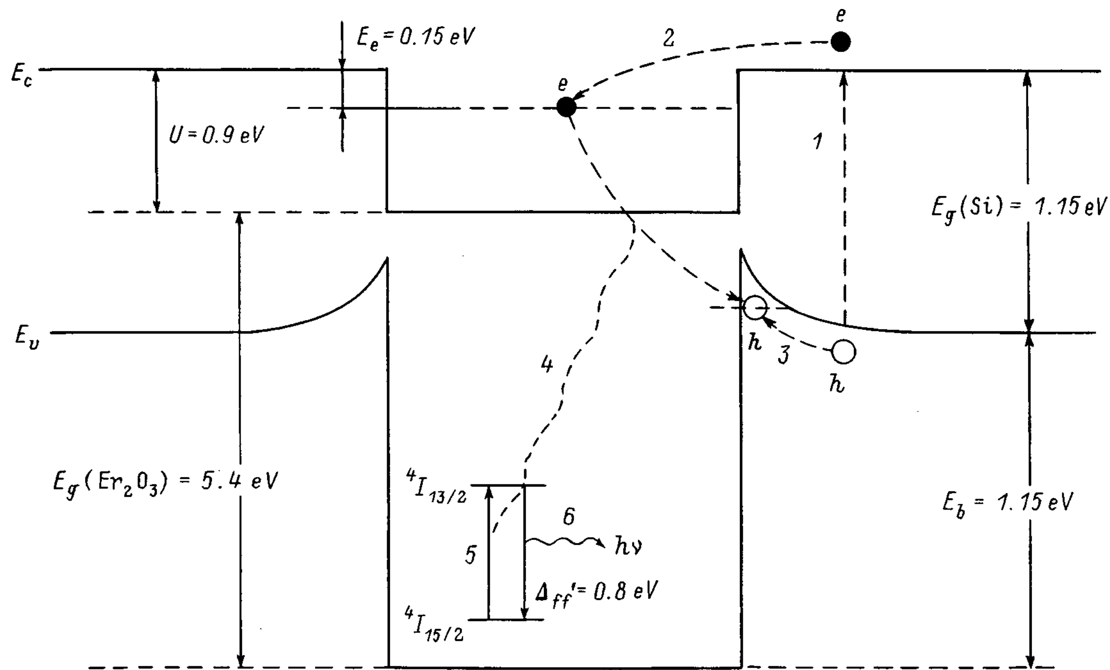

FIG. 1. Schematic diagram of the quantum well Er_2O_3 in silicon: *1*—Photogeneration of the electron-hole pair; *2*—capture of the electron at the level within the quantum well; *3*—capture of the hole, forming of the exciton; *4*—Auger process; *5*—Er^{3+} ion excitation; *6*—$f-f$ emission.

3×10^{19} O/cm^3. At oxygen concentrations below or equal to this value, only broad resonance lines are observed. According to Ref. 8, in samples of silicon containing Er and O in the ratio 1:10 sharp ESR lines were observed. The principal g-values and the paramagnetic center concentration are shown to be extremely sensitive to post-regrowth processes. The angular dependence of the several lines measured on the sample codoped with 10^{20} O/cm^3 and annealed at 900 °C for 30 s, allowed the authors of Ref. 8 to attribute the spectra observed to Er^{3+} at the sites of monoclinic (C_{1h}) and trigonal symmetries. The principal g-values for the monoclinic center are $g_1=0.80$, $g_2=5.45$, and $g_3=12.60$ and for the trigonal center $g_\perp=0.69$ and $g_\parallel=3.24$. The authors suggest that the monoclinic center consists of an Er^{3+} ion surrounded by six oxygen ions in a configuration characteristic of the monoclinic center in Er_2O_3. In fact, cubic erbium oxide occurs in two forms, each with one Er atom surrounded by six O atoms: the monoclinic C_2 center and the trigonal C_{3i} center.[3] However, the ESR studies of Er^{3+} in Y_2O_3, whose crystal structure is similar to Er_2O_3, have shown that the monoclinic and trigonal centers have g-values $g_x=1.645$, $g_y=4.892$, $g_z=12.314$, and $g_\parallel=12.176$, $g_\perp=3.318$, respectively.[9] It should be noted that erbium oxide is an antiferromagnetic material with the Neél temperature equal to 3.4 K (Ref. 3). In Er_2O_3 clusters in silicon the Er–O–Er exchange bonded pairs of Er^{3+} ions must therefore exist. These pairs are responsible for considerable distinctions between g-values of Er^{3+} ions in silicon and those in Y_2O_3, where erbium atoms are distributed in the crystal lattice randomly. It should be noted that in the unit cell of erbium oxide twenty-four rare-earth ions are at the sites with twofold rotational symmetry (C_2) and eight ions are at the sites with threefold rotary inversion symmetry (C_{3i}).[4]

QUANTUM DOT MODEL FOR Er_2O_3 CLUSTER IN SILICON

In our model we consider the Er_2O_3 cluster in silicon as a quantum dot (nanoplatelet in Ref. 10) with size close to the lattice parameter in silicon, $a(\text{Er}_2\text{O}_3)\approx1.05$ nm.[11] It is necessary to add to this size the correction length d, which represents an adaptation or transition length needed to change the cation coordination number from $N_c=6$ in Er_2O_3 to $N_c=4$ in silicon. According to Ref. 10, this length is about 0.12 nm. Hence, the characteristic diameter of the Er_2O_3 quantum dot is about 1.2 nm. As a first approximation, we assume that this quantum dot represents a spherical quantum well with the radius $R\approx0.6$ nm in the energy scheme of Si:Er, O. The depth of the well may be obtained from the band gaps of erbium oxide and silicon $E_g(\text{Er}_2\text{O}_3)=5.4$ eV, $E_g(\text{Si})=1.17$ eV (at $T=0$ K), and the energy parameters of oxygen and silicon atoms. The top of the valence band is formed by $2p$ states of oxygen in Er_2O_3 and by $3p$ states in silicon. That is why we should estimate the energies of p states (E_p) in free O and Si atoms. Using the method of determination of atomic parameters which was proposed previously,[12] we obtained $E_p(\text{O})=-13.6$ eV and $E_p(\text{Si})=-8.15$ eV. Thus the valence band edge in the Er-O complex $E_v(\text{Er}_2\text{O}_3)$ lies about 5 eV below that in the bulk silicon $E_v(\text{Si})$. The complex constitutes a weakly transparent 5-eV-high-barrier for holes, while for electrons it acts as a quantum well $U=0.9$ eV in depth with a discrete electron level with binding energy 0.15 eV observed experimentally in DLTS measurements.[13] The f-levels lie close to the bottom of the quantum well according to the band structure of rare-earth metal oxides. Figure 1 shows the energy scheme described above.

The electron level localized in the quantum well (QW)

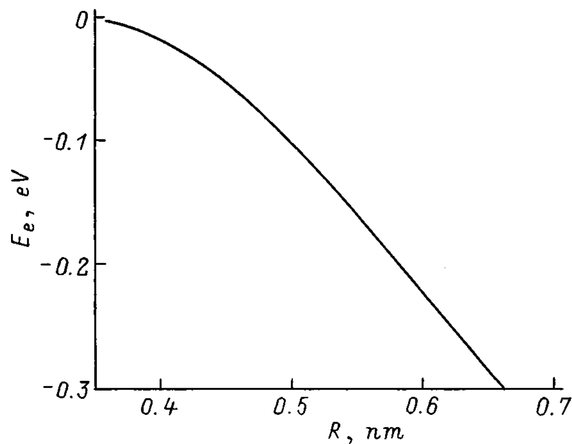

FIG. 2. The energy of the Er–O cluster localized electron level plotted as a function of the Er–O complex radius R.

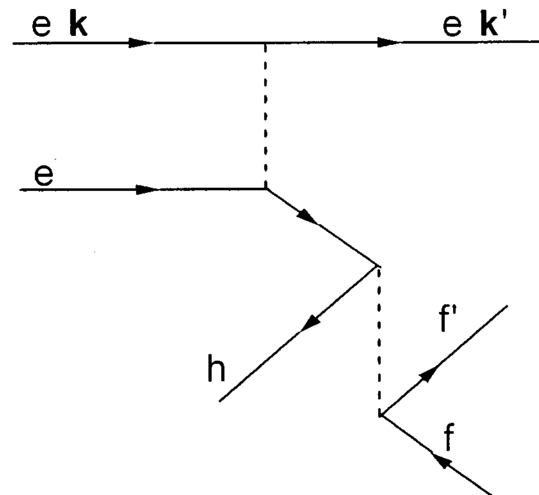

FIG. 3. The Feynman diagrams of the Auger recombination processes when ΔE is transferred to the free carrier. The letters f and f' represent the f-shell states of Er, e and h denote the electron and hole states bound to the Er–O complex, and **k** and **k**′ are the initial and final states of the free carrier in silicon.

plays the role of an electron trap. The trapped electron attracts, through the Coulomb interaction, the hole in the valence band of silicon, forming an ''indirect'' (in space) exciton. The Auger recombination of the electron and the hole will then take place, leading to the excitation of the f-shell electrons of the Er^{3+} ion in the Er_2O_3 cluster.

Let us now estimate the energy E_e of an electron bound to the Er–O complex using the proposed model. The electron effective mass should be different inside and outside the QW. Inside the QW we set the effective mass equal to the free electron mass m_0 and in the bulk semiconductor we use the average mass m_c in the conduction band of silicon. There is a single, spherically symmetric electronic state with the energy determined by the transcendental equation

$$\tan(kR) = -\frac{km_c}{\varkappa}, \tag{1}$$

where $k = \sqrt{2m_0(U-E_e)}/\hbar$ is the electron wave vector in the QW region, and $\varkappa = \sqrt{2m_c(-E_e)}/\hbar$ is the wave function decay in the bulk; the electron energy E_e is measured from the conduction band edge in silicon E_c. The result of the solution of Eq. (1), the energy of the electron level as a function of the quantum dot radius, is shown in Fig. 2. Clearly, the proposed model is very crude. The aim of this simulation is to demonstrate that the electron localized in the Er-O complex with the characteristic radius $R \approx 0.6$ nm has energy which corresponds to the position of the real electron level, $E_e = -0.15$ eV.

The localized electron attracts via Coulomb field the hole in the valence band of silicon. We use the system of differential equations[14] to describe the hole motion in the bulk semiconductor with the degenerate valence band in the presence of the electric field of the localized electron. We assume that these equations describe also the hole in the Er–O complex. Since the Er–O complex represents a weakly permeable barrier for holes, the parameters of the valence band in the quantum well region are not essential for the hole binding energy. We therefore use the same heavy hole mass value m_{hh} in the quantum well and in the bulk. For light holes we take into account the nonparabolicity in the Kane model[15] of the energy spectrum, caused by mixing of the valence states and the states of the bottom of the quantum well, which lies close to the hole energies. The details of these calculations were published elsewhere[12] and we do not present them here. The boundary conditions were obtained by integration of the differential equations for the hole radial wave functions through the quantum-well border. The numerical calculations give the following results for the hole binding energies of the upper hole states localized by the Er–O cluster: $E_h - E_v(\mathrm{Si}) = 0.021$ eV for the even state with angular momentum $J = 3/2$ and $E_h - E_v(\mathrm{Si}) = 0.011$ eV for the odd state with angular momentum $J = 1/2$. Because of the selection rules, the last state plays the main role in the Auger excitation of the Er ion in the Er–O cluster. This state has the light hole nature, and the characteristic size of the hole orbit is a few times larger than the Er–O complex radius.

AUGER EXCITATION

In the case of photoluminescence and electroluminescence under forward bias, when there are not enough hot carriers in silicon, the excitation of Er f-shell electrons proceeds via the Auger recombination of the exciton localized at the Er–O cluster. As indicated above, the energy that binds the exciton to the Er–O complex, $E_{\mathrm{Ex}} = E_e - E_h = 0.96$ eV, is larger than the transition energy, $\Delta_{ff'} = 0.8$ eV, between the first excited state $^4I_{13/2}$ and the ground state $^4I_{15/2}$ of Er^{3+} ion. Thus the energy excess $\Delta E = E_{\mathrm{Ex}} - \Delta_{ff'} \approx 0.2$ eV should be transferred to a ''third body.'' Usually (see, for example, Ref. 16) this difference is attributed to electron-phonon interaction, but the rate of this process is too small to describe the actual energy transfer from the carriers in silicon to the Er ions. We shall therefore consider another Auger excitation process, in which the energy excess ΔE is transferred to the free carriers (electrons or holes) in the host semiconductor.

Figure 3 shows the Feynman diagram of this process. Note that the electron energy in the intermediate state is close to the discrete level energy E_e. It differs from E_e by

the energy ΔE only. Since the value $\Delta E \approx 0.16\,\mathrm{eV}$ is much smaller than the electron quantum-well energy $\hbar^2/m_0R^2 \approx 1\,\mathrm{eV}$, the main contribution to the Auger recombination amplitude is given by the term in which the intermediate state is the electron level bound to the Er–O complex. The given Auger recombination therefore has a resonance character. It proceeds mostly via the discrete electron level E_e. In the resonance approximation we can write the Auger recombination amplitude as

$$M=\frac{M_A M_{\mathrm{Ex}}}{\Delta E}, \tag{2}$$

where

$$M_A=\int \Psi_e^*(\mathbf{r})\Psi_e(\mathbf{r})\frac{e^2}{|\mathbf{r}-\mathbf{r}'|}\Psi_{\mathbf{k}'}^*(\mathbf{r}')\Psi_{\mathbf{k}}(\mathbf{r}')d\mathbf{r}d\mathbf{r}' \tag{3}$$

is the Auger amplitude which corresponds to the upper part of the Feynman diagram (Fig. 3), Ψ_e is the wave function of the discrete electron level, and $\Psi_{\mathbf{k}}$ and $\Psi_{\mathbf{k}'}$ are the free carrier wave functions of the initial and final states with wave vectors $\mathbf{k}$ and $\mathbf{k}'$, respectively. This part of the Auger amplitude describes the energy transfer of the excess energy to the free carriers. The amplitude M_{Ex}, which corresponds to the lower part of the Feynman diagram (Fig. 3)

$$M_{\mathrm{Ex}}=\int V(\mathbf{r})\Psi_h^*(\mathbf{r})\Psi_e(\mathbf{r})d\mathbf{r},$$

$$V(\mathbf{r})=\int \frac{e^2}{|\mathbf{r}-\mathbf{r}'|}\Psi_{f'}^*(\mathbf{r}')\Psi_f(\mathbf{r}')d\mathbf{r}', \tag{4}$$

describes the Auger recombination of the electron and hole bound to the Er-O complex and excitation of the Er *f*-electron from the ground level *f* to the exited level f' (Ref. 16); Ψ_h and Ψ_e are the wave functions of the hole and electron bound to the Er-O complex; $\Psi_{f'}$ and Ψ_f are the wave functions of the Er *f*-electrons. Since the characteristic value of the *f*-shell radius, $r' \approx r_f \approx 0.08\,\mathrm{nm}$, is much smaller than the radius of the electron and hole motion, we can use the multipolar expansion for $V(\mathbf{r})$:

$$V(\mathbf{r})=\frac{ed_{ff'}}{r^2}P_1(\cos\theta)+\frac{eQ_{ff'}}{r^3}P_2(\cos\theta), \tag{5}$$

where P_1 are the Legendre polynomials, and $d_{ff'}$ and $Q_{ff'}$ are the dipole and quadrupole Er matrix elements. The zero term of the expansion $\propto 1/r$ does not contribute to Eq. (5) because of the orthogonality of the Er wave functions $\Psi_{f'}$ and Ψ_f. Since the $f-f'$ optical transition is forbidden, the dipole matrix element is small $d_{ff'}/er_f \approx 10^{-3}$, while $Q_{ff'}/er_f^2 \approx 1$ (Ref. 16). Thus the quadrupole transitions turn out to be more effective in the Auger excitation processes,[12,16] and we will consider below only the second term in Eq. (5).

We use the effective-mass approximation to calculate the Auger amplitudes (3) and (4). We thus write the wave functions of the electron and hole states as a composition of distinct components which correspond to the different energy bands $\Psi_{e,h}=\Sigma_i\Psi_i^{(e,h)}u_i$, where u_i are the Bloch functions of the *i*-band, and $\Psi_i^{(e,h)}$ are the envelope wave functions which were obtained by solving the corresponding eigenvalue problem for the electron and hole states localized the Er–O complex, and which were described in the previous section. The silicon conduction band is closest to the electron level and might have the largest wave function component for the electron state. As was shown in Ref. 3, however, the overlapping integral of the valence and conduction band Bloch functions gives zero contribution to M_{Ex}. Thus the main contribution to the amplitude M_{Ex} provides the overlapping of the valence components of the electron ($\Psi_\nu^{(e)}$) and hole ($\Psi_\nu^{(h)}$) functions, namely, the light hole component. These components can be easily written if we again use the assumption concerning the mixing of the conduction and valence band states in the Er–O complex according to the Kane model. The details of such calculations have been described in our previous study.[12] Here we present the final result:

$$M_{\mathrm{Ex}}=6\times10^{-2}Q_{ff'}/er_f^2\ \ \mathrm{meV}. \tag{6}$$

Note that in our estimations we set $Q_{ff'}/er_f^2 \approx 1$. The main contribution to the Auger matrix element M_{Ex} (6) is given by the area of the bulk semiconductor close to the Er–O complex.

The estimation for the amplitude M_A can be obtained by taking into account that the characteristic value of the bound electron coordinates is $r \approx R$, while the radius vector for free carriers in silicon is $r' \approx \lambda\!\!\!^{-} = 1/k' > R$, and also that $\Psi_e \approx R^{-3/2}$ and $\Psi_{\mathbf{k}} \approx 1$. We have the following estimation:

$$M_A=\frac{e^2}{\lambda\!\!\!^{-}}\lambda\!\!\!^{-3}. \tag{7}$$

According to the Fermi golden rule, the probability of the Auger processes for *n*-type Si is given by

$$W=\frac{2\pi}{\hbar}\int |M|^2 f_e(k)\,\delta\!\left(\frac{\hbar^2\mathbf{k}'^2}{2m_c}-\frac{\hbar^2\mathbf{k}^2}{2m_c}-\Delta E\right)\frac{d\mathbf{k}}{(2\pi)^3}\,\frac{d\mathbf{k}'}{(2\pi)^3}, \tag{8}$$

where $f_e(k)$ is the free electron distribution function. After integration over $\mathbf{k}'$ and $\mathbf{k}$ and substituting Eq. (2), (6), and (7) for the Auger amplitude, we obtain

$$W \approx \frac{|M_{\mathrm{Ex}}|^2 e^4 m_c}{\pi\hbar^3\Delta E^2}(n_e\lambda\!\!\!^{-3}). \tag{9}$$

Here $\lambda\!\!\!^{-} = \hbar/\sqrt{2m_c\Delta E}$ is the wavelength of the outgoing electron, and n_c is the electron concentration. Thus the rate of this Auger process is concentration dependent. Expression (9) is proportional to the number of electrons in the reaction area ($n_e\lambda\!\!\!^{-3}$). According to Eq. (9), the Auger pumping time is $\tau_{\mathrm{Ex}} = 1/W \approx 10^{12} n_e^{-1}$.

In the *p*-type semiconductor the energy excess is transferred to the free hole. In this case we obtained the results described by Eq. (9) with the replacement of n_e by n_h and m_c by m_{hh}. The factor ($n\lambda\!\!\!^{-3}$) is the same for heavy and light holes. The energy excess is therefore transferred mostly to the heavy holes. Thus, in both cases the efficiency of Auger pumping is determined by the concentration *n* of the major carriers. If $n \geqslant 10^{18}$, the time of the Auger recombination turns out to be small enough ($\tau_A \leqslant 10^{-6}$ s) to excite the major part of the Er ions in the Er–O complex.

The photoluminescence intensity is determined by the two pairs of forward and reverse processes: Auger excitation of the Er ion in the Er–O cluster and Er deexcitation; formation and dissociation of the exciton localized at the Er–O complex.[19] The time scale of the first two processes is much larger than that of the last two. This circumstance allows us to separate their influence on the photoluminescence intensity I_{PL}. The photoluminescence intensity I_{PL} in the steady state far from saturation can be written as follows:[13]

$$I_{PL}=\frac{1}{\tau_{rad}}N_{Er}^{*}=\frac{\tau}{\tau_{rad}\tau_{Ex}}N_{Ex}, \tag{10}$$

where N_{Er}^{*} is the concentration of excited Er ions, τ_{rad} is the radiative lifetime of the excitation, $\tau_{Ex}=1/W$ is the time of Auger excitation of Er ion described by Eq. (9), τ is the deexcitation time, and N_{Ex} is the concentration of excitons localized at the Er–O clusters. The N_{Ex} is determined by the processes of formation and dissociation of bound excitons:[13]

$$N_{Ex}=\frac{N_{Er\text{-}O}}{1+\sigma_e v_e n_c e^{E_e/kT}/\sigma_p v_p G \tau_c}, \tag{11}$$

where N_{Er-O} is the concentration of Er–O clusters, $\sigma_{e,h}$ are the cross sections of the electron and hole capture by the Er–O cluster, $v_{e,h}$ are the electron and hole thermal velocities, n_c is the effective density of states in the bottom of the conduction band, G is the optical generation rate of electron-hole pairs, and τ_c is the carrier lifetime. The dissociation of the bound exciton is connected with the thermal activation of the captured electron back to the conduction band of silicon. Thus the number of bound excitons N_{Ex} has a strong temperature dependence (11), which leads to the trivial temperature quenching of photoluminescence.

The deexcitation of the Er ions was comprehensively studied recently by Priolo *et al.*[18] It was shown that the main contribution to the deexcitation of the Er ions at temperatures above 15 K is given by the Auger processes with the participation of free carriers. Thus the deexcitation time has the same strong carrier concentration dependence, $\tau=4.4\times10^{-13}/n$ (Ref. 18), as the excitation time τ_{Ex} [see Eq. (9)]. Therefore, the resulting photoluminescence intensity I_{PL} (10) should have much weaker dependence on the concentration of the free carriers than the times of Auger processes. Note that Eq. (10) is obviously valid in the case of electroluminescence under forward bias when the excitation of Er ion also occurs via the recombination of the bound exciton described here.

IMPACT EXCITATION

In the case of electroluminescence under reverse bias, the impact excitation of the Er ions takes place when there are enough hot electrons in silicon with energies above 0.8 eV. The impact excitation occurs through the quadrupole interaction between the silicon hot electrons and *f*-shell electrons of Er (Refs. 12 and 16). The matrix element of this interaction is

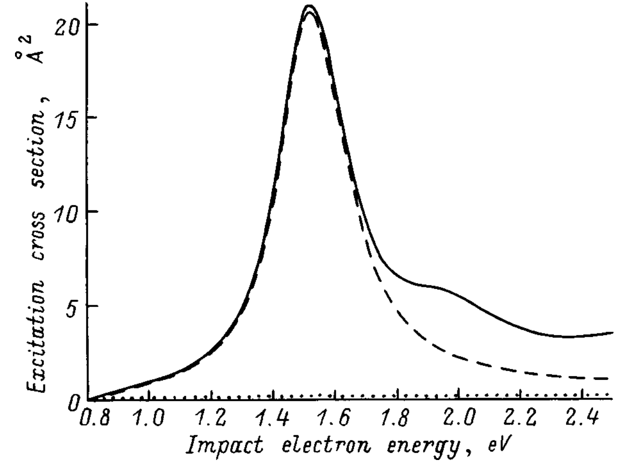

FIG. 4. The impact excitation cross section $\sigma(E)$ of Er as a function of the incident electron energy (solid line), the partial cross section for angular momenta of the incident and outgoing electron of unity $\sigma_{1\to1}$ (dashed line), and the excitation cross section σ_0 of an isolated Er atom (dotted line).

$$M_{fLm,fL'm'}(E)=\sqrt{\frac{4\pi}{5}}Q_{ff'}^{2m'-m}\times\int\frac{e}{r^3}\Psi_{L'm'}^{*}(\mathbf{r})\Psi_{Lm}(\mathbf{r})Y_{2m''1-m}(\mathbf{n})d\mathbf{r}. \tag{12}$$

Here e is the electron charge, $Q_{ff'}^{2m'-m}$ are the quadrupole matrix elements between the ground state $^4I_{13/2}$ and the first excited state $^4I_{15/2}$ of the Er *f*-shell, $\Psi_{Lm}(\mathbf{r})$ and $\Psi_{L'm'}(\mathbf{r})$ are the wave functions of the incident and outgoing silicon electrons, E,L,m and E',L',m' are the energy, angular momentum, and its projection of the incident and outgoing electrons, respectively. The energy of the outgoing electron E' after excitation of Er is smaller than E by the excitation energy $\Delta_{ff'}=0.8$ eV: $E'=E-\Delta_{ff'}$. The wave functions of the silicon electrons were obtained as the solution of the Schrödinger equation with the electron effective mass and the cluster potential described above.

The impact excitation cross section for the given energy of the incident electron can be calculated by using the matrix elements (12) summed over all possible angular momenta of the initial and final electron states:

$$\sigma(E)=\frac{\pi}{4\sqrt{E^3E'}}\sum_{LmL'm'ff'}|M_{fLm,f'L'm'}(E)|^2. \tag{13}$$

Here m is the average effective mass in the silicon conduction band. Figure 4 shows the energy dependence of the impact excitation cross section. The strong maximum on the $\sigma(E)$ dependence at $E=E_1+\Delta_{ff'}\approx1.6$ eV is due to the resonant excitation of Er by the silicon electrons with angular momentum $L=1$ accompanied by the electron capture into the Er–O cluster resonant state with energy $E_1=0.8$ eV and angular momentum $L=1$ (Ref. 19). The partial cross section $\sigma_{1\to1}$ of this process is represented by a dashed line. It is clearly seen that this process dominates in the Er excitation below the energy 1.7 eV. The maxima in $\sigma(E)$ dependence at higher energies are connected with the resonant states with higher angular momenta $L>1$. For comparison we plot the excitation cross section σ_0 for isolated Er

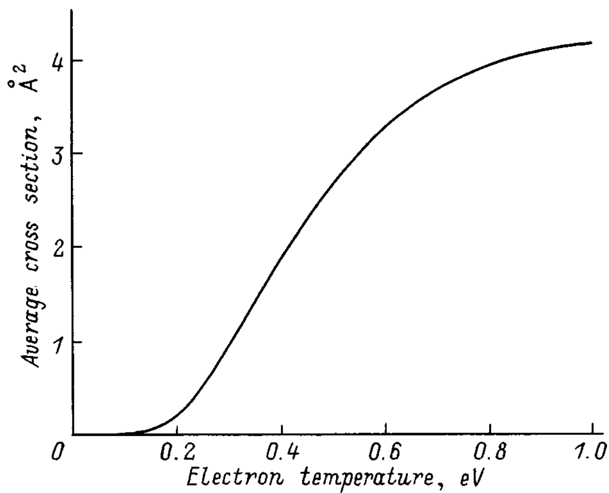

FIG. 5. The average impact excitation cross section σ plotted as a function of the electron temperature T_e.

atoms (dotted line). In the resonant region the impact cross section $\sigma(E)$ of Er in the cluster exceeds the cross section σ_0 of an isolated Er atom by two orders of magnitude.

Note that in the electroluminescence experiments on Er-doped Si diodes only a small fraction of the hot electrons falls into the resonance region. One should therefore average $\sigma(E)$ over the energy distribution of the hot electrons in order to obtain the experimentally observed cross section σ. Assuming the energy distribution function to be Maxwellian with the electron temperature T_e, we obtain the following expression for the excitation cross section:

$$\sigma = \frac{1}{T_e^2} \int_{\Delta_{ff'}}^{\infty} \sigma(E) e^{-E/T_e} E dE. \quad (14)$$

In Fig. 5 we plot the average impact excitation cross section σ as a function of the electron temperature T_e. The actual value of the electron temperature in the experiments[20,21] is estimated to be 0.65 eV. The corresponding value of the excitation cross section (14) is $\sigma = 3.5$ Å^2, which is close to the experimental value $\sigma \approx 4$ Å^2 (Refs. 20 and 21).

CONCLUSIONS

A model for excitation of the Er-related emission in silicon codoped with erbium and oxygen is proposed. This model provides a deeper insight into the energy transfer processes in photoluminescence and electroluminescence that proceed from the carriers of the semiconductor host toward the Er^{3+} ions in Er–O clusters. In both cases the discrete and quasi-discrete electron levels localized at the Er–O cluster play the main role.

In the case of photoluminescence and electroluminescence under forward bias, when there are not enough hot carriers in silicon, the excitation of Er *f*-shell electrons occurs via the Auger recombination of the exciton bound at the Er–O cluster. In this paper we proposed a concrete scheme of this process in which the excess energy is transferred to the free carriers. The excitation rate and the rate of the reverse process of energy backtransfer are proportional to the concentration of the free carriers in silicon. This results in a rather weak dependence of the luminescence intensity on the carrier concentration.

In the case of electroluminescence under reverse bias the suggested mechanism for the Er impact excitation in Si:Er, O explains the role of O in the enhancement of the Er-doped silicon diode electroluminescence. The proposed mechanism is based on the presence of the resonance levels with nonzero angular momentum formed by the quantum-well potential of the Er–O cluster. The resonance scattering of the hot electrons on these quasi-discrete levels enhance the impact excitation cross section.

Of course, the model used by us is rather crude and simple but it reproduces the main features of the excitation processes quite well and explains the high efficiency of Er luminescence in Si:Er, O.

This work was supported by INTAS-RFBR (Grant N 95031).

*)E-mail: leonid@priv.hop.stu.neva.ru

[1] *Rare Earth Doped Semiconductors*, edited by G. S. Pomrenke, P. B. Klein, and D. W. Langer, MRS Symp. Proc. **301**, (1993).
[2] *Rare Earth Doped Semiconductors II*, edited by A. Polman, S. Coffa, and R. N. Schwartz, MRS Symp. Proc. **422**, (1996).
[3] D. L. Adler, D. C. Jacobson, M. A. Marcus, J. L. Benton, J. M. Poate, and P. H. Citrin, Appl. Phys. Lett. **61**, 2181 (1992).
[4] R. M. Moon, W. C. Koehler, H. R. Child, and I. J. Raubenheimer, Phys. Rev. **176**, 722 (1968).
[5] A. Terrasi, G. Frazo, S. Coffa, F. Priolo, F. D'Acapito, and S. Mobilio, J. Appl. Phys. **78**, 3874 (1995).
[6] V. F. Masterov, F. S. Nasredinov, P. P. Seregin, V. Kh. Kudoyarova, A. N. Kuznetsov, and E. I. Terukov, Appl. Phys. Lett. **72**, 728 (1997).
[7] V. F. Masterov, F. S. Nasredinov, P. P. Seregin, M. Yu. Mezdrogina, and E. I. Terukov, Semiconductors **32**, 636 (1998).
[8] J. D. Carey, R. C. Barklie, J. F. Doregan, F. Priolo, G. Frazo, and S. Coffa, Private communications, 1998 (in press).
[9] G. Schafer and S. Scheller, J. Phys.: Condens. Matter **5**, 48 (1966).
[10] J. C. Phillips, J. Appl. Phys. **76**, 5896 (1994).
[11] N. P. Il'in and V. F. Masterov, Semiconductors **31**, 886 (1997).
[12] V. F. Masterov and L. G. Gerchikov, MRS Symp. Proc. **422**, 227 (1996).
[13] F. Priolo, G. Frazo, S. Coffa, S. Librtino, R. Barclie, and D. Caery, J. Appl. Phys. **78**, 3874 (1995).
[14] B. L. Gel'mont and M. I. D'yakonov, Zh. Éksp. Teor. Fiz. **62**, 713 (1972).
[15] E. O. Kane, *Semiconductors and Semimetals* (Academic Press Inc., 1966), V. 1, p. 75.
[16] I. N. Yassievich and L. C. Kimerling, Semicond. Sci. Technol. **8**, 718 (1993).
[17] P. G. Kik, M. J. A. de Good, K. Kikoin, and A. Polman, Appl. Phys. Lett. **70**, 1721 (1997).
[18] F. Priolo, G. Frazo, S. Coffa, and A. Carnera, Phys. Rev. B **57**, 4443 (1998).
[19] L. G. Gerchikov and V. F. Masterov, Appl. Phys. Lett. **73**, 532 (1998).
[20] S. Coffa, F. Priolo, A. Polman, S. Librtino, M. Saggio, and A. Carnera, Nucl. Instrum. Methods Phys. Res. B **106**, 386 (1995).
[21] S. Lombarto, S. U. Comprisano, G. N. van den Hoven, and A. Polman, J. Appl. Phys. **77**, 6504 (1995).

Published in English in the original Russian journal. Reproduced here with stylistic changes by the Translation Editor.

Mechanism of erbium electroluminescence in hydrogenated amorphous silicon

M. S. Bresler, O. B. Gusev, P. E. Pak, E. I. Terukov, K. D. Tséndin, and I. N. Yassievich

A. F. Ioffe Physicotechnical Institute, Russian Academy of Sciences, 194021 St. Petersburg, Russia
(Submitted November 17, 1998; accepted for publication December 15, 1998)
Fiz. Tekh. Poluprovodn. **33**, 671–673 (June 1999)

The mechanism of the electroluminescence of erbium under a reverse bias in structures based on hydrogenated amorphous silicon is studied. Erbium ions are excited through an Auger process, in which conduction electrons are trapped by neutral dangling bonds (D^0 centers) located near the erbium ions. A stationary current through the structure is sustained by a reverse process involving the thermally stimulated tunneling emission of electrons by negatively charged dangling-bond defects (D^- centers) into the conduction band of the amorphous matrix.
© *1999 American Institute of Physics.* [S1063-7826(99)00906-0]

1. INTRODUCTION

Efficient photo- and electroluminescence from erbium ions in erbium-doped hydrogenated amorphous silicon (a-Si:H⟨Er⟩) have recently been observed.[1–4] The interest in this semiconductor matrix was sparked both by the very simple and inexpensive method for doping it with erbium [magnetron sputtering of metallic erbium in an atmosphere of silane (SiH_4) or magnetically assisted silane decomposition (MASD)] and the comparably weak thermal quenching of erbium luminescence in it, which render this material promising for the fabrication of 1.54-μm light-emitting diodes operating at room temperature.

It was theorized in Refs. 4 and 5 that the excitation of erbium ions in a-Si:H⟨Er⟩ takes place through an Auger process, in which an electron from the conduction band is trapped by a neutral dangling-bond defect (a D^0 center), converting it into a negatively charged defect (a D^- center). The transition energy is transferred by a Coulomb interaction to a $4f$ electron of the erbium ion and excites it from the ground state ($^4I_{15/2}$) to the first excited state ($^4I_{13/2}$).

In a stationary regime there must be a reverse process, which returns the defects from the D^- state to the D^0 state. The present study revealed that the multiphonon tunneling ionization of D^- centers by an applied electric field serves as such a process in the case of electroluminescence. This ionization specifies an increase in the electron concentration in the conduction band and a dependence of the erbium electroluminescence on electric field.

2. EXPERIMENTAL RESULTS

Electroluminescent structures based on erbium-doped hydrogenated amorphous silicon were fabricated by the magnetron sputtering of erbium in a silane atmosphere (MASD), in which the sputtering takes place in a discharge in a mixture of argon and silane (SiH_4). Films with a thickness of 1 μm were deposited on an n-type silicon substrate with a donor concentration equal to 5×10^{17} cm^{-3}. The erbium concentration in the structures investigated reached about 10^{20} cm^{-3}. The electroluminescence was measured in the temperature range 77–300 K. The emission of erbium was observed with transillumination through the crystalline silicon substrate. The measurements were performed in a dc regime.

Erbium luminescence in the form of a narrow line at 1.54 μm was observed only when a reverse bias was applied to the structure. The dependence of the erbium luminescence intensity I_{EL} and the electric current through the structure on the electric field intensity E at high fields $E>1.5\times10^5$ V/cm tends asymptotically to an $\ln I_{EL}\propto E^2$ law . The temperature dependence of the erbium luminescence intensity for various values of the current passing through the structure is shown in Fig. 1.

3. DISCUSSION OF THE RESULTS

The implantation of erbium ions in the amorphous matrix is accompanied by the formation of a large number of defects in the form of dangling bonds with a concentration of the order of 10^{18} cm^{-3}. Therefore, we can presume that dangling-bond defects (D centers) are found near erbium ions. It can also be expected that the implantation of erbium in amorphous silicon with a large concentration of oxygen causes the formation of donorlike erbium-oxygen complexes, like those formed in crystalline silicon. In this case there is an approximately equal number of D centers in the neutral (D^0) and negatively charged (D^-) states.

Under a reverse bias, excess electrons appear in the conduction band as a result of the thermally stimulated tunneling ionization of D^- centers in the electric field. Their concentration rises exponentially with applied electric field according to the relation $n=n_0\exp(E^2/E_c^2)$, where E_c is the characteristic electric field. As they move in the amorphous layer, these electrons are trapped by D^0 centers and can excite erbium or defect-related luminescence. The corresponding diagram of the transitions is shown in Fig. 2.

The $e+D^0\rightarrow D^-$ transition can be radiative or nonradiative. If D centers are located near erbium ions, another recombination channel is opened: an Auger process, which is accompanied by excitation of an erbium ion due to a Coulomb interaction between an electron trapped by a D^0 center and a $4f$ electron of the erbium ion, is possible. Such a

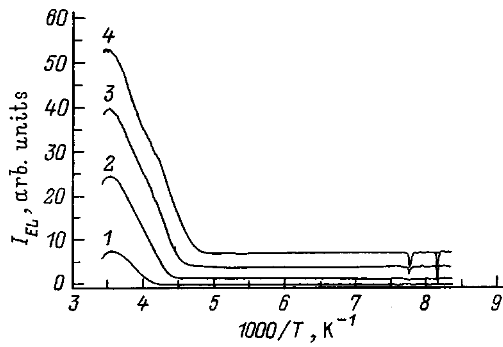

FIG. 1. Temperature dependence of the erbium electroluminescence intensity for various values of the current *I*, mA: *1* — 5, *2* — 10, *3* — 15, *4* — 20.

defect-related Auger excitation (DRAE) process is especially efficient due to its almost resonant character. The excess energy of the transition is imparted to local phonons. A detailed theoretical treatment of the DRAE process was presented in Ref. 6. The erbium luminescence intensity is described by the relation

$$I_L = c_A n N_{D^0}(\tau/\tau_R) = c_A n_0 \exp(E^2/E_c^2) N_{D^0}(\tau/\tau_R),$$

where c_A is the contribution of the DRAE process to the capture coefficient, τ and τ_R are the total and radiative lifetimes of erbium ions in the excited state, and n and N_{D^0} are the concentrations of electrons in the conduction band and on D^0 centers, respectively. The magnitude of the characteristic field determined from an experimental plot of $\ln I_{\mathrm{EL}} \propto E^2$, $E_c = 1.6 \times 10^5$ V/cm, is consistent with the results of an investigation of the multiphonon tunneling ionization of deep centers in crystalline silicon.[7]

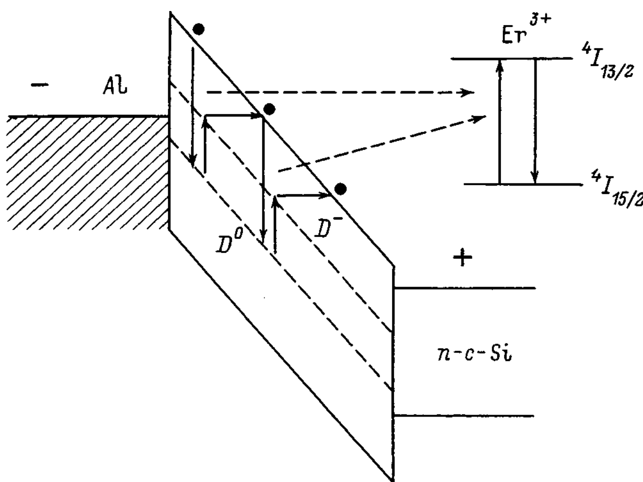

FIG. 2. Energy band diagram and electron transitions under a reverse bias.

The temperature dependence of the electroluminescence (EL) intensity was measured with a constant current passing through the structure. It can easily be shown that the observed temperature-induced increase in the EL intensity is caused by the exponential growth of the concentration of D centers in the neutral state (N_{D^0}) with increasing temperature.

4. CONCLUSIONS

In summary, we have observed strong electroluminescence of erbium ions at room temperature in a semiconductor structure based on amorphous silicon. The characteristics of the structure seem promising for the further development of light-emitting diodes which emit at a wavelength of 1.54 μm and can be integrated into silicon electronics. The mechanism for passage of an electric current through the structure has been revealed: it is controlled by the multiphonon tunneling ionization of D^- centers in the applied electric field and a reverse process involving the trapping of free electrons by D^0 centers. Defect-related Auger excitation (DRAE) provides a strong channel for trapping electrons from the conduction band and is responsible for the excitation of erbium ions which are found close to dangling-bond defects. The entire body of our experimental data is consistent with the proposed mechanisms.

This work was supported by the Russian Fund for Fundamental Research (Grants No. 96-02-16931a and No. 98-02-18246), the Ministry of Science of the Russian Federation (Grant 97-1036), the INCO-COPERNICUS program (Grant 977048-SIER), and a NATO Grant (HTECH.LG 972032).

[1] M. S. Bresler, O. B. Gusev, V. Kh. Kudoyarova, A. N. Kuznetsov, P. E. Pak, E. I. Terukov, I. N. Yassievich, B. P. Zakharchenya, W. Fuhs, and A. Sturm, Appl. Phys. Lett. **67**, 3599 (1995).
[2] J. H. Shin, R. Serna, G. N. van den Hoven, A. Polman, W. G. J. M. van Stark, and A. M. Vredenburg, Appl. Phys. Lett. **68**, 997 (1996).
[3] A. R. Zanatta, Z. A. Nunes, and Z. R. Tessler, Appl. Phys. Lett. **70**, 511 (1997).
[4] O. B. Gusev, A. N. Kuznetsov, E. I. Terukov, M. S. Bresler, V. Kh. Kudoyarova, I. N. Yassievich, B. P. Zakharchenya, and W. Fuhs, Appl. Phys. Lett. **70**, 240 (1997).
[5] W. Fuhs, I. Ulber, G. Weiser, M. S. Bresler, O. B. Gusev, A. N. Kuznetsov, V. Kh. Kudoyarova, E. I. Terukov, and I. N. Yassievich, Phys. Rev. B **56**, 9545 (1997).
[6] I. N. Yassievich, M. S. Bresler, and O. B. Gusev, J. Phys. C **9**, 9415 (1997).
[7] V. N. Abakumov, V. I. Perel, and I. N. Yassievich, *Nonradiative Recombination in Semiconductors*, North Holland, Amsterdam (1991).

Translated by P. Shelnitz

Effect of annealing on the optical and structural properties of GaN:Er

N. A. Sobolev,*) V. V. Lundin, V. I. Sakharov, I. T. Serenkov, and A. S. Usikov

A. F. Ioffe Physicotechnical Institute, Russian Academy of Sciences, 194021 St. Petersburg, Russia

A. M. Emel'yanov

St. Petersburg State Technical University, 195251 St. Petersburg, Russia

(Submitted January 12, 1999; accepted for publication January 13, 1999)
Fiz. Tekh. Poluprovodn. **33**, 674–676 (June 1999)

The effect of annealing on the optical and structural properties of gallium nitride layers grown by metalorganic chemical vapor deposition and implanted with 0.8 to 2.0-MeV erbium ions at doses of $(1-4)\times 10^{14}$ cm^{-2} is investigated. Additional implantation of 0.11 to 0.28-MeV oxygen ions at doses of $(1-4)\times 10^{15}$ cm^{-2} is performed on some samples. Measurements of the Rutherford backscattering of protons show that amorphization of the gallium nitride layers does not occur at the erbium implantation doses investigated. The formation of erbium-related luminescence centers which emit at 1.54 μm ends before the defect structure of the implanted layers is restored during a postimplantation anneal in the temperature range $700-1300$ °C. © *1999 American Institute of Physics.* [S1063-7826(99)01006-6]

The interest in the study of the luminescence of erbium ions in semiconductors is due to the prospects of employing them in optoelectronics. To obtain a better understanding of the defect-formation processes and the luminescence of Er^{3+} ions, various semiconductors, from silicon to gallium nitride, have been investigated. According to the results, the thermal quenching of the photoluminescence (PL) intensity of erbium ions decreases significantly as the gap width of the semiconductor increases. For example, in Si:Er the PL intensity of the erbium ions decreases by several orders of magnitude as the measurement temperature is raised from liquid-nitrogen temperature to room temperature,[1] whereas in GaN:Er a severalfold decrease in the intensity is observed.[2] The behavior of structural defects in GaN:Er has been studied to a clearly insufficient extent. The purpose of the present work was to investigate the influence of the postimplantation annealing conditions on the optical and structural properties of erbium-doped gallium nitride layers.

EXPERIMENTAL CONDITIONS

Undoped n-type GaN films with a charge-carrier density $n\sim 10^{18}$ cm^{-3} and a thickness of 1.2 μm were grown on (0001) sapphire substrates by metalorganic chemical vapor deposition (MOCVD). The growth procedure was described in detail in Ref. 2. Erbium ions with $E=0.8-2.0$ MeV and doses $D=(1-4)\times 10^{14}$ cm^{-2} and oxygen ions with $E=0.11-0.28$ MeV and $D=(1-4)\times 10^{15}$ cm^{-2} were implanted at room temperature. The energies of the oxygen ions were selected so that their projected ranges would coincide with the corresponding values for erbium ions. The implanted samples were annealed in a furnace for rapid thermal annealing at $T_0=700-1300$ °C during a time $t=15-1800$ s in a stream of nitrogen. The time needed to heat the samples to the assigned temperature was much shorter than the duration of the anneal.

The PL was excited by the emission of a halogen lamp. The radiated power focused by a lens system onto the sample was $\sim$50 mW. The PL signal was measured by an InGaAs photodetector operating at room temperature. The radiant flux from the halogen lamp was modulated by an interrupter at a frequency of 18 Hz. The detector photocurrent pulses were converted into a variable voltage, which was recorded using a selective voltmeter. The resolution of the system was $\sim$3 nm. The crystal structure of the implanted layers was investigated by measuring the Rutherford backscattering (RBS) of 230-keV protons scattered at a 120° angle.

RESULTS AND DISCUSSION

Figure 1 shows the PL spectra, measured at 300 and 80 K, of a GaN sample implanted with erbium ions having several energies $E=2$, 1.6, 1.2, and 0.8 MeV at partial doses of 1×10^{14} cm^{-2} and annealed at 1300 °C for 360 s. The calculated values of the projected range of the ions are 0.5, 0.4, 0.3, and 0.2 μm, respectively. The most intense emission peak with a maximum at $\lambda=1.538$ μm is caused by transitions of electrons from the first excited state ($^4I_{13/2}$) to the ground state ($^4I_{15/2}$) of the Er^{3+} ions. The broad emission band at $\lambda\sim 1-1.4$ μm with a maximum at $\lambda=1.17$ μm is associated with the PL of defects in GaN, since it is observed both after the implantation of erbium ion and after the implantation of neodymium[3] or chromium.[4] The series of small peaks near $\lambda\sim 1$ μm is probably caused by transitions of electrons from the second excited state ($^4I_{11/2}$) of the Er^{3+} ion to the ground state ($^4I_{15/2}$).[2] We note that we did not detect significant differences between the PL spectra of GaN:Er and GaN:Er:O. For the samples whose spectra are shown in Fig. 1 the PL intensity at $\lambda=1.538$ μm increased by a factor of 2.2 when the measurement temperature was

 © 1999 American Institute of Physics

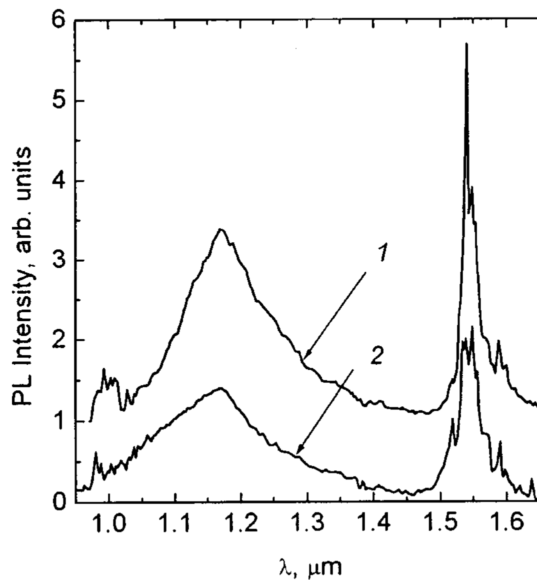

FIG. 1. Photoluminescence spectra of a GaN:Er sample after annealing at 1300 °C for 360 s. The spectra were measured at 80 (*1*) and 300 K (*2*). For convenience, curve *1* has been displaced upward by 1 arb. unit.

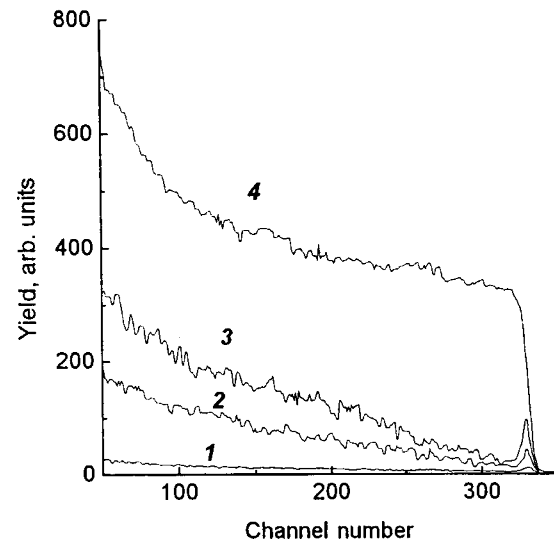

FIG. 2. RBS spectrum of protons for the same sample as in Fig. 1: before implantation (*1*, *4*), after implantation (*3*) and after annealing at 900 °C for 1800 s (*2*). The spectra were measured with the sample in channeling (*1–3*) and unoriented (*4*) positions.

lowered from 300 to 80 K. The intensity of the PL signal at the maximum of the defect band increased more than twofold upon cooling from 300 to 80 K.

The PL intensity of Er^{3+} at $\lambda=1.538$ μm rises monotonically as the temperature of the isochronal anneal (with a duration of 15 s) is increased in the range 700−1300 °C, reaching a tenfold increase for the 1300 °C anneal in comparison to the 700 °C anneal. The strongest increase is observed at $T_0>900$ °C. The emission from defects rises sharply at $T_0>1100$ °C and increases with increasing annealing time. The intensity of the erbium-related PL of GaN:Er at $T_0=1300$ °C scarcely increases when the annealing time is increased from 15 to 400 s. However, the intensity of the defect-related band rises.

Figure 2 presents the RBS spectra of protons for GaN:Er:O. Spectra *1*, *2*, and *3* were measured with channeling along the ⟨0001⟩ axis of the single crystals investigated, and spectrum *4* was measured in the unoriented (''random'') regime. Curve *1* is the channel spectrum for the as-grown layer before implantation and essentially corresponds to the signal for an ideal GaN single crystal. For this sample the relative proton scattering yield χ_{min} (the ratio between the counts in the channeling and random regimes for channels beyond the surface peak: channels 286–315) equals ~0.015, which is close to the theoretical values for a perfect single crystal. The RBS spectrum obtained in the channeling regime after the implantation of erbium and oxygen ions is represented by curve *3*. It can be seen that the implantation of oxygen has essentially no influence on the RBS spectrum. Curve *2* is the spectrum for the same sample after annealing at 900 °C for 30 min.

The distributions of intrinsic point defects (gallium and nitrogen atoms displaced into interstitial positions) across the thickness of the sample were calculated from curves *2* and *3* in Fig. 2 within the model described in Refs. 5 and 6. The relative defect concentrations at the maxima of the distributions are equal to 0.17 after implantation and to 0.08 after annealing. It is noteworthy that in the case of the implantation of erbium ions with the same energies in silicon, complete amorphization of the surface layer occurs already at an Er implantation dose of 1×10^{14} cm^{-2} (Ref. 7). In other words, at the same dose and energy of the erbium ions the extent of damage in the crystal lattice is considerably smaller in gallium nitride layers than in silicon.

The ratio between the value of χ_{min} for a sample of GaN:Er:O after annealing and the value for the as-grown single crystal is ~3.5. At the same time, in silicon subjected to the same implantation and annealing conditions the value of χ_{min} essentially coincides with the value for the as-grown sample before implantation, i.e., the defect structure of silicon is completely restored during the postimplantation anneal.

Thus, it has been established that the formation of optically active erbium-related centers during postimplantation annealing is considerably faster than the restoration of the defect structure of erbium-implanted gallium nitride samples. The accumulation of radiation defects during implantation and their removal during annealing is significantly slower in GaN:Er layers than in Si:Er.

We wish to thank E. O. Parshin for the implantation.

This work was carried out with financial support from the INTAS-RFBR (Grant 95-0531).

*)E-mail: nick@sobolev.ioffe.rssi.ru; Fax: +7-812-2471017

[1] J. Michel, J. L. Benton, R. F. Ferrante, D. C. Jacobson, D. J. Eaglesham, E. A. Fitzgerald, Y.-H. Xie, J. M. Poate, and L. C. Kimerling, J. Appl. Phys. **70**, 2672 (1991).

[2] V. Yu. Davydov, V. V. Lundin, A. N. Smirnov, N. A. Sobolev, A. S. Usikov, A. M. Emel'yanov, M. I. Makoviĭchuk, and E. O. Parshin, Fiz. Tekh. Poluprovodn. **33**, 3 (1999) [Semiconductors **33**, 1 (1999)].

[3] E. Silkowski, Y. K. Yeo, R. L. Hengehold, B. Goldenberg, and G. S. Pomrenke, Mater. Res. Soc. Symp. Proc. **422**, 69 (1996).

[4] S. Kim, S. J. Rhee, D. A. Turnbull, E. E. Reuter, X. Li, J. J. Coleman, and S. G. Bishop, Appl. Phys. Lett. **71**, 231 (1997).
[5] E. Bogh, Can. J. Phys. **46**, 653 (1968).
[6] F. F. Komarov, M. A. Kumakhov, and I. S. Tashlykov, *Non-destructive Ion Beam Analysis of Surfaces*, Gordon and Breach, New York (1990) [Russ. original, Izd. BGU, Minsk (1987), p. 108].
[7] R. N. Kyutt and N. A. Sobolev, Fiz. Tverd. Tela (St. Petersburg) **39**, 853 (1997) [Phys. Solid State **39**, 759 (1997)].

Translated by P. Shelnitz

Optical activity of Yb in GaAs and low-dimensional GaAs/GaAlAs structures

A. A. Gippius, V. M. Konnov, V. A. Dravin, N. N. Loĭko, I. P. Kazakov, and V. V. Ushakov

P. N. Lebedev Physics Institute, Russian Academy of Sciences, 117924 Moscow, Russia
(Submitted December 15, 1998; accepted for publication December 15, 1998)
Fiz. Tekh. Poluprovodn. **33**, 677–679 (June 1999)

It is shown that the optical activation of Yb in GaAs and low-dimensional GaAs/GaAlAs structures can be achieved by forming three-component (Yb+S/Se/Te+O) luminescence centers based on the Yb^{3+} ion. A correlation between the characteristics of these centers and the parameters of the chalcogen coactivators is discovered. Oxygen is shown to play a decisive role in transferring the energy of electron-hole pairs to the luminescence centers. © *1999 American Institute of Physics.* [S1063-7826(99)01106-0]

The investigations of rare-earth (RE) elements as impurities in semiconductors are motivated by the prospects of creating optoelectronic devices which combine the emission characteristics of intracenter optical transitions within the $4f$ shell (narrow, thermally stable lines) with the compactness of semiconductor devices. The intensity of the $f-f$ luminescence in semiconductors doped with RE elements is determined, in particular, by the probability of optical transitions within the $4f$ shell of the RE centers and the efficiency of the transfer of energy from electron-hole pairs to the luminescence centers. Both of these factors depend on the structure of the luminescence centers, i.e., on the position of the RE impurity in the crystal lattice and its possible association with other impurities and/or defects.

This paper summarizes the results of the investigations of luminescence centers based on the Yb^{3+} ion in GaAs and low-dimensional GaAs/GaAlAs structures carried out in the P. N. Lebedev Physics Institute of the Russian Academy of Sciences during the last three years. The results of the preceding studies of other investigators can be reduced to the fact that Yb can be optically active in binary and ternary III–V compounds only if it is located at lattice points.[1] On the basis of such ideas the very low luminescence intensity associated with Yb^{3+} ions in GaAs was attributed to the small fraction (as follows from Rutherford scattering data) of substitutional Yb ions. We have been able to show that Yb can be optically active in GaAs when it is associated with other impurities.

A Yb impurity was introduced into GaAs and GaAs/GaAlAs structures either by ion implantation or during the molecular-beam epitaxial (MBE) process. The implantation was carried out at ion energies and doses which ensure a ''flat'' distribution profile of the Yb impurity and the coactivators (O, S, Se, and Te) to a depth of 150 nm with a concentration in the range $10^{17}-10^{19}$ cm^{-3}. To eliminate the radiation damage created by the implantation process, the samples were annelated at temperatures up to 800 °C. A compromise growth regime for doping during the MBE process, which permits the introduction of Yb in concentrations up to 10^{18} cm^{-3} without adversely affecting the quality of the crystalline matrix, was determined.

In the initial stage of this study we performed systematic investigations of the conditions for the formation of luminescence centers based on Yb^{3+} ions in GaAs single crystals with various concentrations of background impurities, which were monitored by secondary-ion mass spectrometry (SIMS). When Yb was implanted in a material with a comparatively low ($<10^{17}$ cm^{-3}) content of background impurities, it was found that ytterbium-related luminescence centers do not appear, in agreement with the literature data available. The additional implantation of oxygen led to the appearance of luminescence lines in the spectral range corresponding to $^2F_{5/2}-^2F_{7/2}$ transitions of the Yb^{3+} ion. In the case of a material with a high ($\sim 10^{18}$ cm^{-3}) concentration of background impurities (Se, O, Si, C, etc.) luminescence associated with $f-f$ transitions of Yb^{3+} was observed after the implantation of Yb ions alone, and its intensity differed by more than an order of magnitude for different (identically implanted) samples in this group. The additional implantation of oxygen sharply increased the luminescence intensity and diminished its spread for different samples. It follows from these data that oxygen plays a decisive role in the ''optical activation'' of Yb in GaAs.

The data for different samples and different implantation and annealing conditions enabled us to identify several striking groups of lines (X_1/X_2, Y_1/Y_2) assigned to different centers in the spectral range 980−1020 nm, i.e., 1.264−1.215 eV (where up to 100 lines were observed in the spectra of some samples) (Fig. 1a). The considerably less intense lines at 1030−1100 nm, which are shifted toward lower energies by 70 meV and are assigned to optical transitions involving phonons, were correlated with lines of the X_1/X_2 and Y_1/Y_2 systems.

The appearance of different combinations of lines in the luminescence spectra of different, but identically (Yb+O) implanted and annealed samples points to the possible formation of Yb^{3+}-based luminescence centers containing background impurities (Se, O, Si, C, etc.), which can be detected by SIMS in some of the samples investigated. The combined implantation of Yb, oxygen, and one of the chalcogens (S, Se, or Te) in samples with a small content of background impurities led to the appearance of luminescence

 © 1999 American Institute of Physics

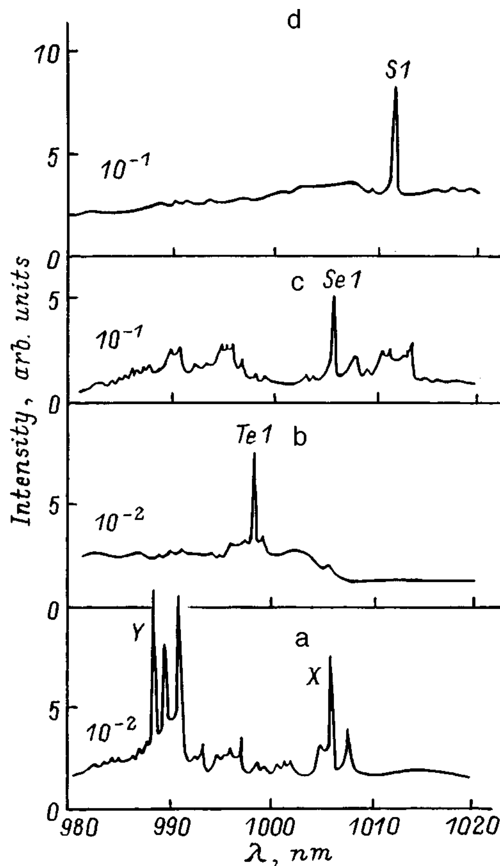

FIG. 1. Luminescence spectra associated with the $^2F_{5/2}-^2F_{7/2}$ transitions of Yb^{3+} ions in GaAs for various combinations of implanted impurities (the concentration of each was 10^{19} cm^{-3}): a — Yb+O, b — Yb+Te+O, c — Yb+Se+O, d — Yb+S+O. Annealing temperature, °C: a, b — 700; c, d — 660.

lines which are specific for each of the chalcogens (Figs. 1b–1d). Thus, the optical activation of Yb in GaAs can be achieved by forming Yb^{3+}-based three-component (Yb+S/Se/Te+O) luminescent complexes, which probably form as a result of fairly complicated reactions between their components during the annealing.[2,3]

The characteristics of three-component complexes of a single type correlate with the properties of the chalcogen atoms appearing in them. For example, the annealing temperature at which the Yb+S/Se/Te+O complexes form increases (580/620/650 °C) with the mass of the chalcogen. As can be seen from Table I, the energy of the optical transition increases with the size of the chalcogen atom appearing in the composition of the center, and the phonon energy decreases as its mass increases.

The role of the chalcogens in the optical activation of Yb is probably confined to the formation of a definite charge state of the RE ion (Yb^{3+}) and the creation of low-symmetry crystal fields, which depend on the parameters of the coactivator and remove the parity prohibition on $f-f$ transitions. As for oxygen (which appears in the composition of all the luminescence centers investigated without exception), it is not clear whether it influences their energy spectrum at all. It has not been ruled out that it participates somehow in transferring excitation energy of the system of electron-hole pairs to the luminescence centers.

TABLE I. Energy characteristics of Yb^{3+} luminescence centers.

Center	E_0, eV	$\delta=E_f-E_0$, meV	E_{ph}, eV	$\hbar\omega_{ph}$, meV
X_1	1.2321	38.4	1.1615	70.6
X_2	1.2329	37.6	1.1634	69.5
Y_1/Y_2	1.2518	18.7	1.1849	66.7
S_1	1.2254	45.1	1.1347	90.7
Se_1	1.2321	38.4	1.1615	70.6
Te_1	1.2415	29.0	1.1848	56.7

Note: Here $E_f=1.2705$ eV is the energy of the $^2F_{5/2}-^2F_{7/2}$ transition of a free Yb^{3+} ion, E_0 is the energy of the zero-phonon transition, E_{ph} is the energy of the transition with the participation of a phonon, and $\hbar\omega_{ph}=E_0-E_{ph}$ is the phonon energy.

The intensity of the luminescence associated with three-component centers in GaAs is comparable to the intensity in GaP:Yb and even in InP:Yb (where the high luminescence intensity is associated with the substitutional position of the isolated Yb atoms). This provides some basis to postulate that the position of the rare-earth atoms in the lattice is not

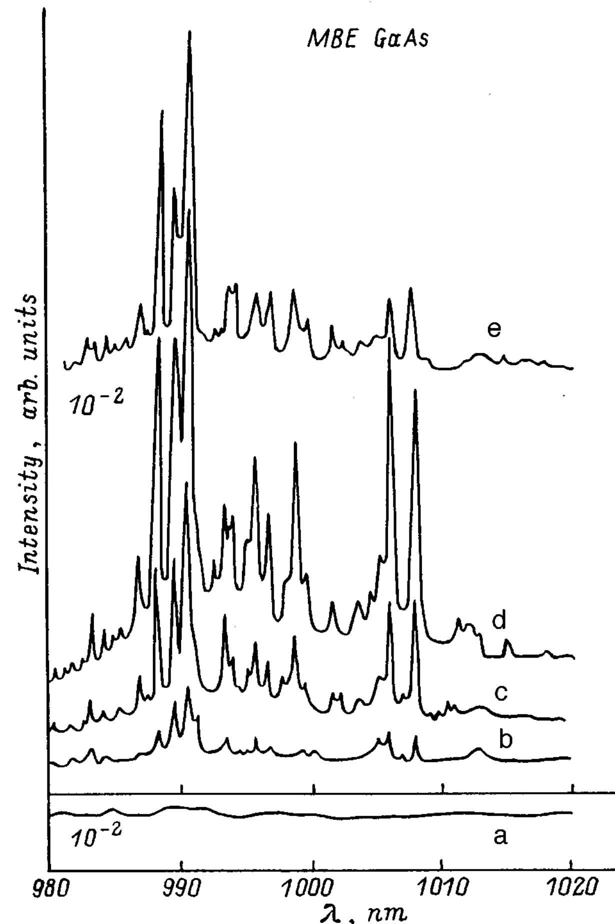

FIG. 2. Luminescence spectra of GaAs doped with Yb during the MBE process (a) and additionally doped with oxygen by implantation (b–e). The Yb concentration was 10^{18} cm^{-3}. Oxygen concentration: b — 10^{18}, c — 3×10^{18}, d — 6×10^{18}, e — 10^{19} cm^{-3}. The annealing temperature was 700 °C.

the only (and, possibly, not even the main) factor determining their optical activity in cases where they appear in the composition of luminescent complexes.

The formation of luminescence centers in Yb-doped GaAs layers during molecular-beam epitaxy takes place, as a whole, just as it does in the bulk material: luminescence associated with $f-f$ transitions of Yb^{3+} is observed only after the implantation of oxygen and annealing.[4] The spectrum exhibits numerous lines, which are associated with centers containing Yb, O, and background impurities, particularly Se (Fig. 2).

Luminescence centers associated with Yb^{3+} were created in quantum-well structures based on GaAs/GaAlAs either by doping during the MBE process or by ion implantation (with the additional implantation of oxygen and annealing in both cases). In the structures consisting of a sequence of quantum wells of various thicknesses, specific lines of intrinsic luminescence from different wells served as probes for monitoring the spatial distribution of the radiation defects, and implantation and annealing regimes, which ensure that the structures have an acceptable quality after implantation, were determined.[5] According to the preliminary data, the luminescence intensity (per unit of concentration) of the Yb^{3+}-based centers in the quantum wells is more than an order of magnitude greater than that in the bulk material, apparently because of the spatial confinement of the electron-hole pairs.[6]

This work was carried out with financial support from the RFBR (No. 96-02-18206), the Physics of Solid-State Nanostructures Program (No. 97-1046), the INTAS-RFBR (No. 95-053), and the CRDF (No. RE1-235).

[1] A. Kozanecki and R. Gratzschel, J. Appl. Phys. **68**, 517 (1990).
[2] V. M. Konnov, T. V. Larikova, N. N. Loyko, V. A. Dravin, V. V. Ushakov, and A. A. Gippius, Solid State Commun. **96**, 839 (1995).
[3] V. M. Konnov, T. V. Larikova, N. N. Loyko, V. A. Dravin, V. V. Ushakov, and A. A. Gippius, Mater. Res. Soc. Symp. Proc. **422**, 187 (1996).
[4] A. A. Gippius, V. M. Konnov, N. N. Loyko, V. V. Ushakov, I. P. Kazakov, V. A. Dravin, and N. N. Sobolev, Mater. Sci. Forum **258–263**, 917 (1997).
[5] N. N. Loĭko, V. M. Konnov, and T. V. Larikova, Kratk. Soobshch. Fiz. No. **9–10**, 48 (1996).
[6] V. M. Konnov, V. A. Dravin, N. N. Loĭko, I. P. Kazakov, and A. A. Gippius, Kratk. Soobshch. Fiz. (in press).

Translated by P. Shelnitz

ATOMIC STRUCTURE AND NON-ELECTRONIC PROPERTIES OF SEMICONDUCTORS

Photothermoacoustic and photoelectric microscopy of silicon

R. M. Burbelo, A. G. Kuz'mich,*) and I. Ya. Kucherov

Taras Shevchenko Kiev University, 252017 Kiev, Ukraine
(Submitted August 11, 1998; accepted for publication October 1, 1998)
Fiz. Tekh. Poluprovodn. **33**, 680–686 (June 1999)

Combined photothermoacoustic and photoelectric microscopy is used to investigate silicon-based structures: an epitaxially grown *n*-type region in a *p*-type substrate, a $p-p^{+}$ interface obtained by implanting boron ions, and a region near a crack tip. It is concluded that the visualization of epitaxial regions by thermal waves most probably stems from the elastic stresses appearing during fabrication of the structures. It is shown that the spatial distribution of the elastic stresses appearing upon ion implantation is visualized by thermal waves. In the region near the crack tip inhomogeneities in the thermoelastic and energy properties extending over hundreds of microns can be diagnosed by thermal waves and electron-hole plasma waves. Spatial periodicity with a period ~85 μm is discovered in the variation of the thermoelastic properties near the crack tip. © *1999 American Institute of Physics.* [S1063-7826(99)01206-5]

Photothermoacoustic microscopy is being developed for the diagnostics of materials and devices.[1–3] Information is conveyed in it by thermal waves. They are generally excited by modulated optical radiation. The light absorbed by a sample periodically heats it, exciting thermal waves. The amplitude and phase of the thermal waves are functions of the optical and thermal parameters of the sample. Information on the properties of a sample can be obtained by recording the variable component of the temperature (θ) by any effective method. Several different methods for recording θ have been proposed. The dependence of the information obtained on the method used to record θ is significant in photothermoacoustic microscopy. Piezoelectric detection, which is one of the most sensitive methods,[2] is used in the present work.

When semiconductors are irradiated by modulated light, electron-hole plasma waves of the nonequilibrium carriers are excited in them along with the thermal waves. This leads to variation of the distribution of the bulk heat sources and, consequently, to a dependence of θ on the generation-recombination parameters of the semiconductors (the lifetimes of the nonequilibrium carriers, the carrier diffusion coefficient, the recombination rates, etc.).[4] The electron-hole plasma waves of nonequilibrium carriers can serve as an independent information carrier for semiconductor diagnostics. The latter are described by a dispersion relation similar to that for thermal waves.[5] One special feature of electron-hole plasma waves is the finite lifetime of the nonequilibrium electron-hole pairs. This leads to a dependence of their diffusion length which differs somewhat from the dependence of the diffusion length for thermal waves. This creates favorable conditions for combining two diagnostic methods for semiconductors and semiconductor devices, which employ thermal waves and electron-hole plasma waves as the information carrier, in a single instrument. Since the parameters of thermal waves and electron-hole plasma waves are determined by different constants of semiconductor materials and since their properties are similar, these two methods can complement one another in a single instrument.[6]

This paper is devoted to an investigation of several silicon-based structures using combined photothermoacoustic (PA) and photoelectric (PA) microscopy. These experiments seem interesting to us, because, although the PA effect is widely used to study semiconductors (see, for example, Ref. 7), the PA microscopy of semiconductors with piezoelectric detection has scarcely been studied and there are only a few reports concerning it.[8–10] Moreover, there have been no comparative studies of semiconductors by PA and PE microscopy at all.

A block diagram of a combined PA-PE microscope, in which the amplitude and phase of the PA and PE signals serve as the information parameters, is shown in Fig. 1. Laser radiation modulated with a frequency $f=80$ kHz (*1*) ($\lambda=488$ μm) is focused by a lens (*2*) onto the surface of the sample (*3*) in a spot having a diameter no greater than 10 μm. The laser radiation absorbed by the sample heats it and generates nonequilibrium electrons and holes. As a result, thermal waves and electron-hole plasma waves are excited in the sample. Because of the thermoelastic effect, the thermal waves produce ultrasonic oscillations, which are detected by a piezoelectric transducer (*4*). The electrical signal from the piezoelectric transducer is fed through a commutator (*7*) into two identical synchronous amplifiers (*5* and *6*), which output PA signals with a $\pi/2$ phase shift. These signals are processed by a computer (*9*), and the amplitude (in relative units) and the phase shift of the PA signal are calculated. The information obtained can be represented in the form of gray-scale amplitude and phase topograms or single-line plots. Information on the variable component of the concentration of nonequilibrium carriers on the sample surface was ob-

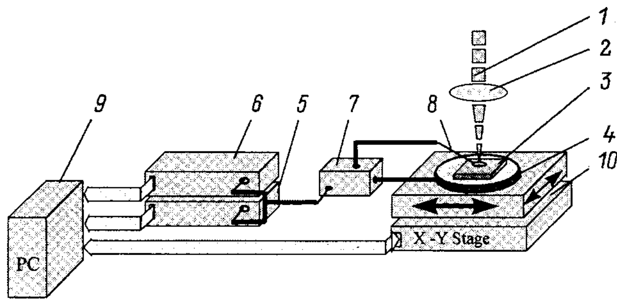

FIG. 1. Block diagram of a combined photothermoacoustic and photoelectric microscope.

tained by measuring the capacitive photovoltage.[11] For this purpose, a thin metallic electrode (*8*) in the form of a disk having a diameter of 1 mm with a hole at its center for passage of the laser beam was placed on the sample surface. The electrical photovoltage signal was processed precisely as the PA signal. The sample was scanned with the laser beam by moving the sample together with the piezoelectric sensor on a computer-controlled $X-Y$ stage (*10*) with a 0.01-mm step.

Samples of the following types were used:

–*p*-Si wafers with an *n*-type region of epitaxial growth (a ''pocket'');

–*p*-Si wafers with an interface between undoped and doped regions (implantation of B^+ ions at a dose of 0.05 μC/cm^{-2});

–*p*-Si wafers with a crack appearing in the primary processing stage (KMD silicon, $\rho = 6\times10^3\ \Omega\cdot$cm, dislocation density $\sigma = 5\times10^{-4}\ \mathrm{cm}^{-2}$).

The surfaces of all the samples were polished to a perfectly reflecting state.

Figures 2–4 present the PA and PE amplitude (ampl.) and phase topograms of these samples and plots of the variation of the amplitude and phase within a single scanning line with the coordinate indicated, which is marked on the topograms by the LS–LS′ line. Lighter areas on the topograms correspond to higher values of the respective signal parameter. The dimensions of the image region are 2.4×2.4 mm.

It can be seen from the examples presented that the PA and PE topograms convey the inhomogeneities in the test structures differently, but fairly clearly. The oblique light and dark bands and spots on the PA and PE topograms of the pocket (Fig. 2) are not observed optically and are probably images of polished defects (scratches, microcracks, pits, etc.) that appear during the finishing (cutting) of the pockets. A comparison of the PA and PE images of the different structures with one another reveals the following:

– inhomogeneities of different nature in silicon are conveyed differently to the PA and PE topograms;

– the PE images reflect a $p-n$ junction more clearly than do the PA images;

– conversely, the PA images convey polished scratches, pits, and fluctuations of properties near a crack more completely.

This can be attributed to the fact that the PA signal is determined primarily by the thermoelastic parameters of the material (the thermal conductivity, specific heat, thermal expansion coefficient, and elastic constants), which vary little in response to variation of the electrical parameters of the semiconductor, such as the carrier concentration. Therefore, the variations of the PA signal (amplitude and phase) are determined mainly by the variation of the thermoelastic properties. This means that the visualization of a $p-n$ junction by thermal waves is probably not related to variation of the carrier concentration, but to something else (see below). The PE signal, on the other hand, is determined predominantly by the electrical parameters (the concentration of nonequilibrium electrons and holes, the surface band bending, etc.), on which defects of different kinds can also have an appreciable influence.[12] The conditions for their visualization by electron-hole plasma waves are thereby created.

Comparing the images obtained from samples with $p-n$ and $p-p^+$ junctions (Figs. 2 and 3), we see that in the case of the $p-n$ junction the amplitudes of the PA and PE signals increase upon passage from the *p*-type region to the *n*-type region (from a region with a high concentration of holes to a region where their concentration is lower). The phase shift of the PA signal in the *n*-type region is low (of the order of $2°-5°$) and increases somewhat (by roughly $7°-10°$) upon passage to the *p*-type region. The oscillation phase of the PE signal essentially decreases by π upon passage from the *p*-region to the *n*-region, i.e., the oscillations of the PE signal in the *p*- and *n*-regions are out of phase. For the $p-p^+$ junction, which was created by implanting B^+ ions, the amplitude of the PE signal is smaller in the implanted region (which is enriched with holes) than in the unimplanted region. The phase shift of the PE signal is roughly 80° greater in the ion-implanted region than in the unimplanted part of the crystal. This is qualitatively consistent with the variations of the PE signal upon passage through the *p*-Si–*n*-Si interface in the $p-n$ junction. Conversely, the amplitude of the PA signal is greater in the boron-implanted region than in the unimplanted region. For the $p-n$ junction, as was noted above, the amplitude of the PA signal decreases upon passage from the *n*-type region to the *p*-type region. The phase shift of the PA signal in the unimplanted region amounts to $\sim$12°, while in the implanted region it decreases to $\sim$2°. We thus see that the variations of the amplitude and phase of the PA signal upon passage from the *p*-region to the p^+-region are similar to those in the $p-n$ structure upon passage through the *p*-Si–*n*-Si interface. This means that the visualization of the $p-p^+$ structure, like the $p-n$ junction, by thermal waves is not related to the variation of the electrical properties. Such behavior of the PA signal in ion-implanted silicon can be explained in the following manner. During the implantation of boron ions, elastic stresses appear in the surface layer of Si.[13] It was shown by direct experiments in Ref. 14 that the PA response is sensitive to the presence of elastic stresses in the solid. Moreover, its relative amplitude depends on the sign of the elastic stresses (compressive or tensile stresses) with respect to the direction of the thermoelastic strains that shape the PA signal. In our case ion implantation should lead to the appearance of tensile elastic stresses at depths where B^+ ions are implanted. The presence of these stresses can lead to an increase in the linear

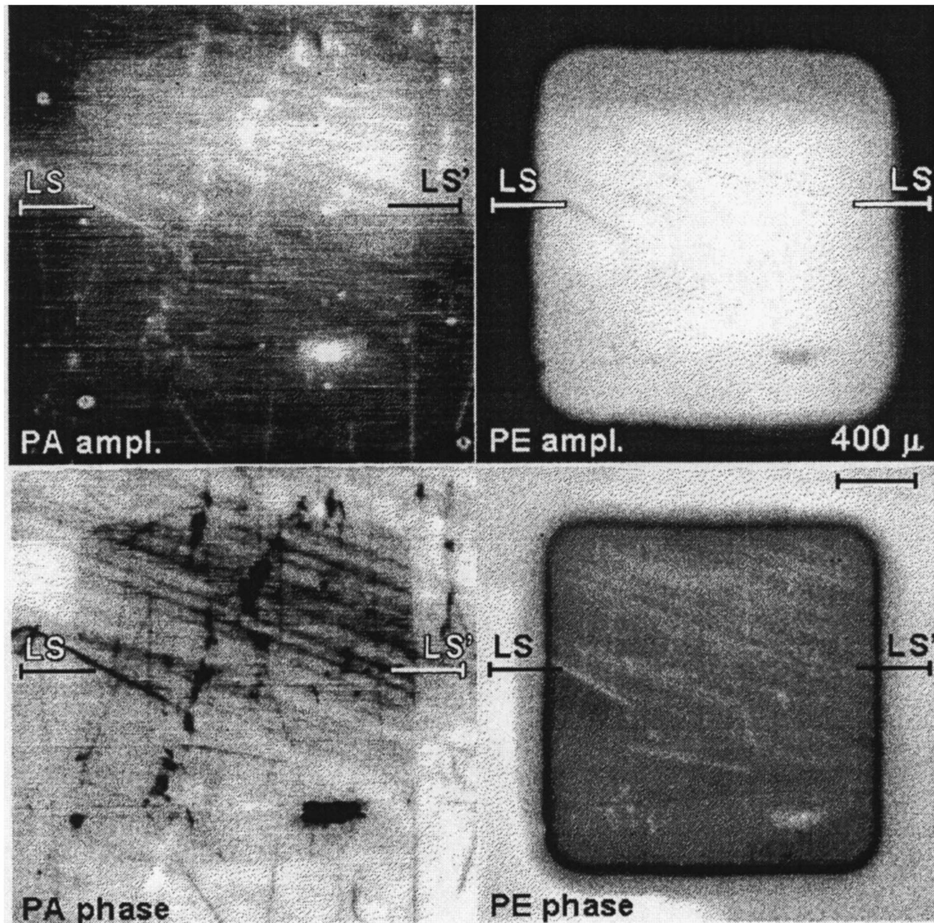

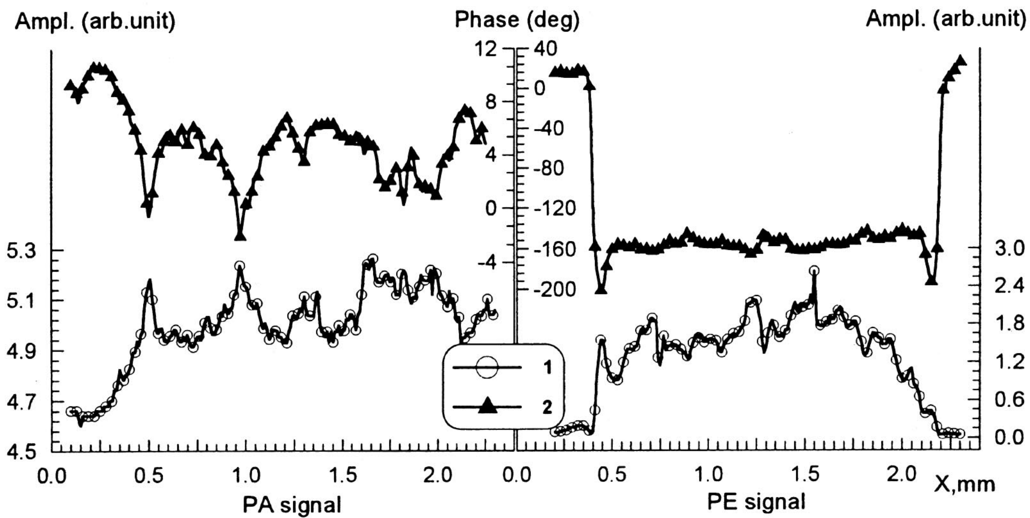

FIG. 2. Photothermoacoustic (PA ampl., PA phase) and photoelectric (PE ampl., PE phase) images of a p-type Si sample with an n-type region of epitaxial growth (a pocket) and plots of the variation of the amplitude and phase of the signals along a single scanning line, which is indicated on the images by LS–LS′ (*1* — amplitude, *2* — phase).

thermal expansion coefficient α_T. Also, since the amplitude of the PA signal recorded with piezoelectric detection is directly proportional to α_T (Ref. 15), the amplitude of the PA response should increase in the implanted region. All this provides some basis to assume that, in all likelihood, the increase in the amplitude of the PA signal in the implanted region is caused by the appearance of elastic stresses in the crystal during implantation of the impurity.

Since the electrical parameters do not have an appreciable effect on the PA signal in the $p-p^+$ structure, it can be concluded that visualization of an n-type pocket in a p-type substrate by thermal waves (Fig. 2) is likewise not

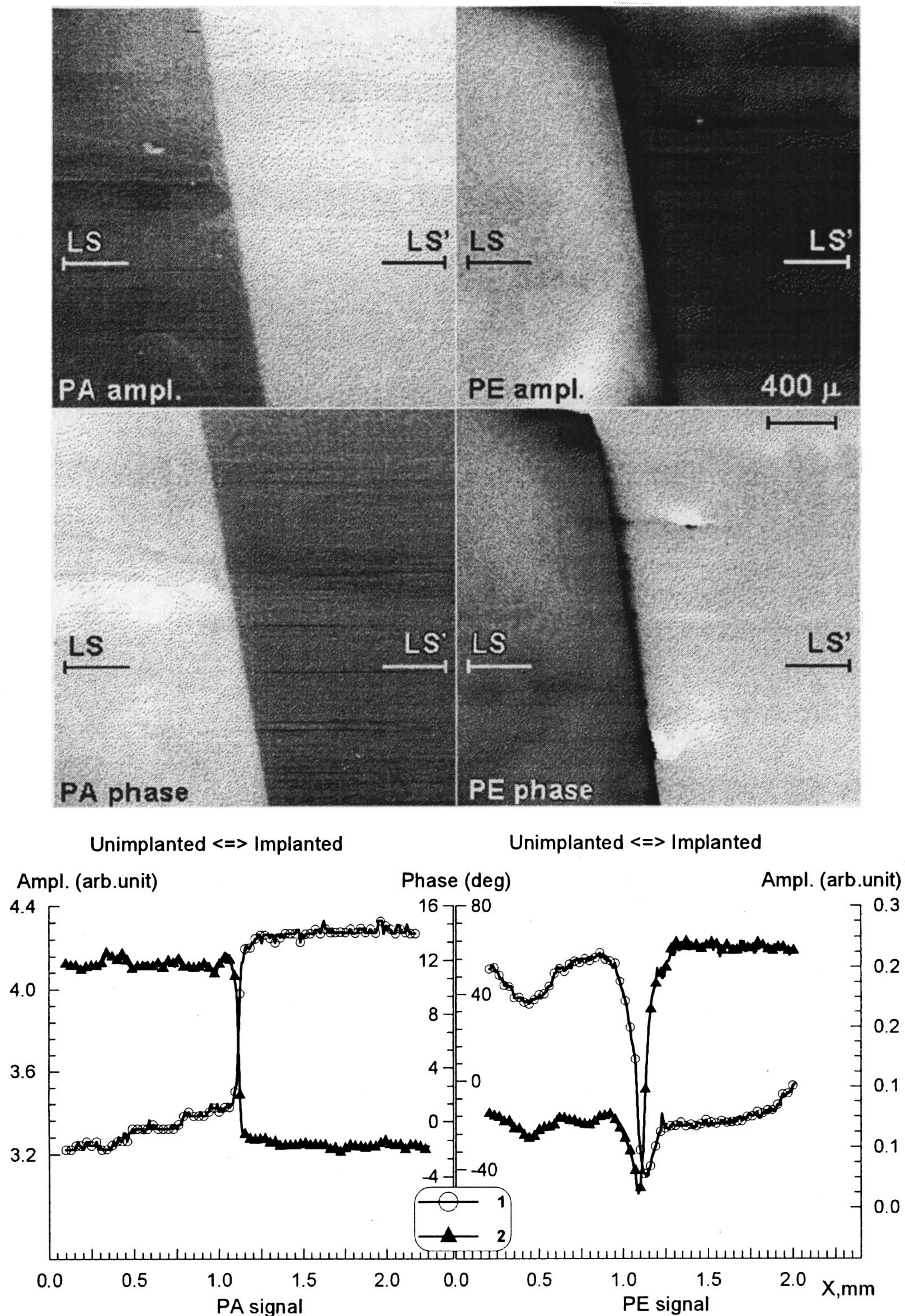

FIG. 3. Photothermoacoustic (PA ampl., PA phase) and photoelectric (PE ampl., PE phase) images of the interface between the unimplanted and implanted regions in a $p-p^+$-Si sample and plots of the variation of the amplitude and phase of the signals along a single scanning line, which is indicated on the images by LS–LS′ (*1* — amplitude, *2* — phase).

related to the differences between the electrical properties of the *p*- and *n*-type silicon regions. The most likely factor permitting PA visualization of the pocket is the presence of elastic stresses in the pocket region, which appear during the epitaxial growth of *n*-silicon on the *p*-substrate. Thus, the PA visualization of the pocket attests to the presence of residual elastic stresses in it.

Let us analyze the PA and PE topograms of a sample with a crack (Fig. 4). It is seen that the boundaries of the crack are diffuse and that the length of the defect is signifi-

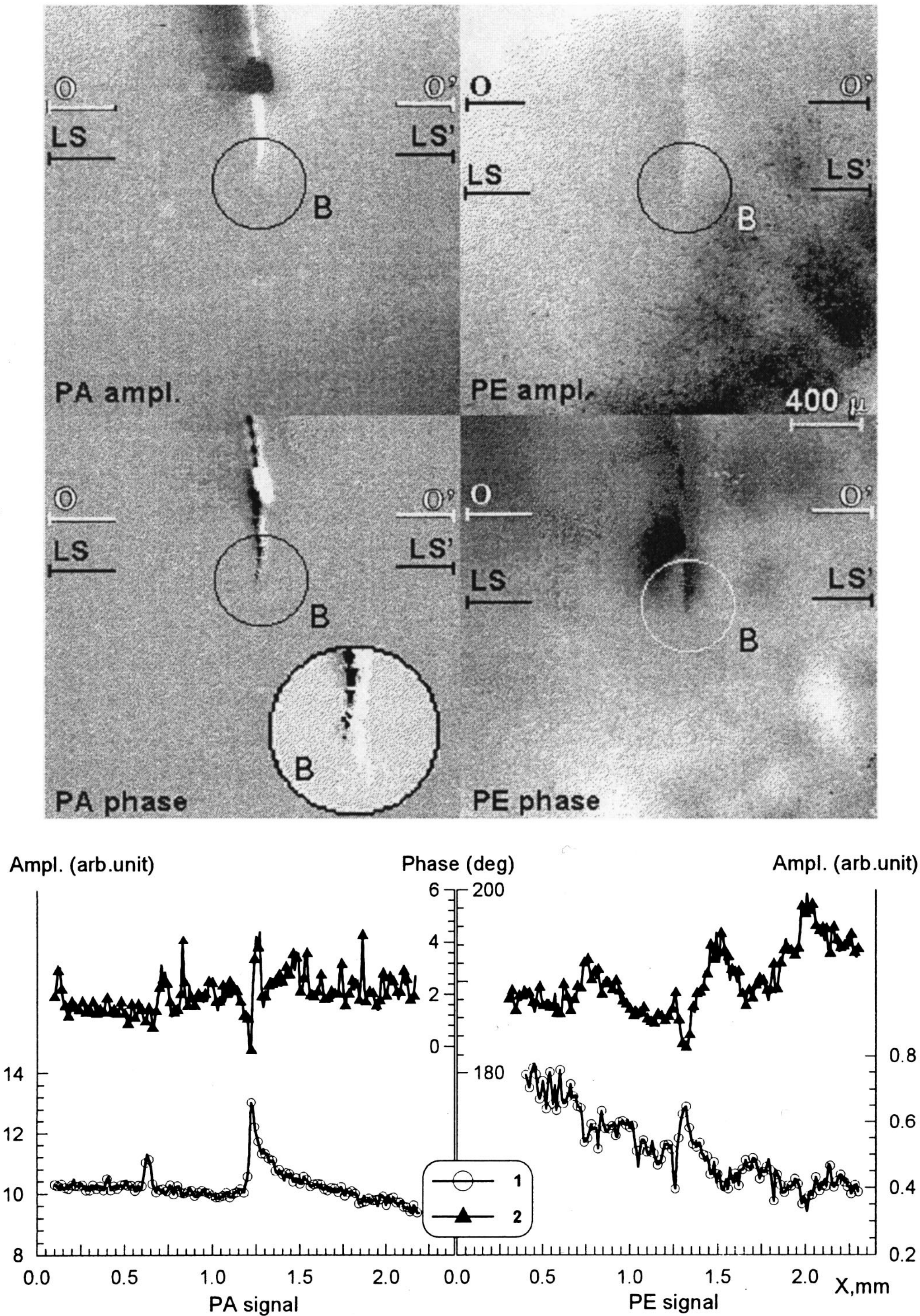

FIG. 4. Photothermoacoustic (PA ampl., PA phase) and photoelectric (PE ampl., PE phase) images of a *p*-Si sample with a crack and plots of the variation of the amplitude and phase of the signals along a single scanning line, which is indicated on the images by LS–LS′ (*1* — amplitude, *2* — phase).

cantly greater than in the case of optical observation (the optical visualization boundary of the crack was determined using a microscope with a visual magnification of 300 and is indicated on the images by the O–O′ line). On the PA topogram the crack image is ~0.4 mm longer than the optical image, and on the PE topogram it is ~0.56 mm longer than the optical image. This can be explained in the following manner. The formation of a crack in a crystal is preceded by an increase in the dislocation density. The branched dislocation structure and the fields of elastic stresses near the crack tip (*B*) influence the thermoelastic and electrical parameters of the semiconductor. As a result, the PA and PE images of the crack are significantly larger than the optical image. The PA and PE topograms of the crack in silicon exhibit periodicity in the crack inhomogeneity. The length of the period of this inhomogeneity is ~85 μm. The same periodicity in the inhomogeneity of the properties occurs in the part of the sample near the crack tip, where the crack is not visualized

optically. It is most clearly seen on the phase PA topogram, attesting to its thermoelastic nature. This is probably because the crack development process, which begins with the generation of irregularities in the physical properties of the crystal, primarily the elastic properties, has a spatially periodic character. This can apparently explain the abrupt character of crack development observed experimentally.[16] The results presented above lead to the conclusion that the regions in a stressed state appearing in a crystal before its fracture can be visualized with the aid of thermal waves and electron-hole plasma waves.

The PE topograms and plots of the variation of the amplitude and phase of the PE signal within a single scanning line in the region with elastic stresses near the crack tip (Fig. 4) exhibit a change in the contrast of the image, which is associated with a fairly significant drop in the measured PE signal.

The amplitude and phase shift of the PE signal undergo similar variations upon passage through a region with a smaller concentration of hole-type carriers (compare Fig. 4 with Figs. 2 and 3). This provides some basis to assume that the hole concentration is lowered in the region of defect formation at the crack tip in *p*-type Si.

Thus, these experiments show that a combination of two methods (the photothermoacoustic and photoelectric methods) provides complementary information on the properties of semiconductor wafers and permits the diagnostics of structures and various types of defects. In particular, it has been shown that:

– the observed PA contrast of regions of epitaxial growth is most probably a consequence of the presence of elastic stresses in them, which appear during their fabrication, and can serve as a diagnostic of the quality of semiconductor structures;

– the elastic stresses appearing during the ion implantation of semiconductor wafers can be diagnosed by the PA method;

– the elastically stressed region near the tip of a crack in silicon has a spatially periodic strength, which is probably responsible for the abrupt development of the crack;

– a region with a reduced hole concentration appears in the elastically stressed region near a crack tip in *p*-type silicon.

This work was carried out with financial support from the Ukrainian Scientific-Technical Center and with basic financing by the Taras Shevchenko Kiev University of the Ministry of Education of Ukraine.

*⁾E-mail: akuzmich@genphys.ups.kiev.ua

[1] A. Rosencwaig, *Photoacoustics and Photoacoustic Spectroscopy*, Wiley, New York (1980).

[2] A. Rosencwaig and G. Busse, Appl. Phys. Lett. **36**, 725 (1980).

[3] B. C. Forget, I. Barberean, D. Furnnier, S. Tuli, and A. B. Battacharyya, Appl. Phys. Lett. **69**, 1107 (1996).

[4] A. N. Vasil'ev, V. A. Sablikov, and V. V. Sandomirskiĭ, Izv. Vyssh. Uchebn. Zaved. Fiz. **30**(6), 119 (1987).

[5] J. Opsal and A. Rosencwaig, Appl. Phys. Lett. **47**, 498 (1985).

[6] R. M. Burbelo, A. L. Gulyaev, A. G. Kuz'mich, and I. Ya. Kucherov, Zh. Tekh. Fiz. **66**(4), 121 (1996) [Tech. Phys. **41**, 361 (1996)].

[7] ''Photoacoustic and Photothermal Phenomena,'' J. Prog. Nat. Sci., Suppl. (Beijing) **6**, (1996).

[8] W. Kipert, H.-J. Obramski, R. Meckenstack, J. Pelzl, D. Fournier, and V. Zammit, J. Prog. Nat. Sci., Suppl. (Beijing) **6**, 524 (1996).

[9] J. He, S. Y. Zhang, Z. L. Qian, Y. Y. Guo, and H. B. Wang, J. Prog. Nat. Sci., Suppl. (Beijing) **6**, 531 (1996).

[10] G. I. Bulakh, R. M. Burbelo, A. L. Gulyaev, and I. Ya. Kucherov, Fiz. Tekh. Poluprovodn. **24**, 926 (1990) [Sov. Phys. Semicond. **24**, 582 (1990)].

[11] V. G. Litovchenko and A. P. Gorban', *Principles of the Physics of Metal-Insulator-Semiconductor Microelectronic Systems* [in Russian], Naukova Dumka, Kiev (1978), p. 316.

[12] H. F. Matare, *Defect Electronics in Semiconductors* [Wiley–Interscience, New York (1971); Mir, Moscow (1974), p. 463].

[13] P. Zavmsil, V. Winter, F. Cembal, M. Servidori, and Z. Sovrek, Phys. Status Solidi A **100**, 95 (1987).

[14] R. M. Burbelo, M. K. Zhabitenko, J. Prog. Nat. Sci., Suppl. (Beijing) **6**, 720 (1996).

[15] W. Jackson and N. M. Amer, J. Appl. Phys. **51**, 3343 (1980).

[16] V. A. Kalitenko, I. Ya. Kucherov, V. M. Perga, and V. A. Tkhorik, Fiz. Tverd. Tela (Leningrad) **30**, 3677 (1988) [Sov. Phys. Solid State **30**, 2112 (1988)].

Translated by P. Shelnitz

Radiation-thermal activation of silicon implanted in gallium arsenide

V. M. Ardyshev and A. P. Surzhikov

Tomsk Polytechnical University, 634004 Tomsk, Russia

(Submitted October 19, 1998; accepted for publication November 10, 1998)
Fiz. Tekh. Poluprovodn. **33**, 687–690 (June 1999)

The layer density, density profile, and mobility of electrons in ^{28}Si-ion-doped layers of semiinsulating GaAs after radiation annealing with electron energy above and below the defect formation threshold and after thermal annealing in the temperature range $T_a = 590-830\,^\circ$C are investigated. It is shown that for radiation annealing energy above the defect formation threshold ion-doped layers are formed with much lower annealing temperatures, and the degree of electrical activation of silicon in these layers is high and the density of electron mobility limiting defects is low. © *1999 American Institute of Physics.* [S1063-7826(99)01306-X]

1. INTRODUCTION

It is well known that isothermal radiation annealing (RA) is performed at temperatures comparable to the temperature of thermal annealing (TA).[1] At the same time the generation of point defects during isochronous TA makes it possible to lower substantially the annealing temperature of radiation defects in amorphized silicon and gallium arsenide layers.[2] In this connection, the objective of the present work is to investigate the electrical activation and depth distribution of silicon implanted in gallium arsenide and the electron mobility in layers under conditions of generation of point defects and heating of the material.

These conditions were produced by irradiating a semiconductor with intense electron beams with particle energy above the point defect production threshold.

2. EXPERIMENTAL PROCEDURE

The investigations were performed on 400 μm thick semiinsulating GaAs$\langle Cr_2O_3, In\rangle$ wafers, oriented in the (100) plane, with resistivity $\rho \geq 10^7\ \Omega\cdot$cm, electron mobility 3900–4200 cm^2/V·s at 300 K, and dislocation density $N_D \leq 8\times10^4$ cm^{-2}. After the wafers were treated in the etchant H_2SO_4:H_2O_2:H_2O=1:1:10, 30-keV^{28}Si ions with dose 8.75×10^{12} cm^{-2} and then 100-keV^{28}Si ions with dose 5×10^{12} cm^{-2} at 300 K were implanted. Measures were taken to eliminate axial and planar channeling during implantation.[3] After implantation a 100 nm thick SiO_2 film was deposited by a plasma chemical method on both sides of the wafer in order to conduct RA and a 300 nm thick SiO_2 film was deposited to conduct TA. Next, ''high-energy electron annealing'' (HEA) with electron energy 1–2 MeV and current density $0.3-0.6$ mA/cm^2 for 13–21 s in air was conducted by the method of Ref. 4. The temperature during annealing was monitored with a chromel–alumel thermocouple and varied in the range $T_a = 590-800\,^\circ$C. Thermal annealing at temperatures $T_a = 660-830\,^\circ$C for 30 min in a hydrogen flow as well as ''low-energy electron annealing'' (LEA) in the Modul' setup[5] with electron energy 10 keV and power density 6.8 W/cm^2 for 16 s in vacuum with residual pressure not exceeding 10^{-5} Pa were performed on the control wafers.

After the insulator was removed, measurements of the layer electron density N_s and mobility μ were performed in the ion-doped layers by the van der Pauw method. Next, $100\times100\ \mu$m^2 Schottky barriers, surrounded by ohmic contacts, were prepared on the wafers by photolithography to measure the electron density profile $n(x)$ by the capacitance–voltage method. The alloy 86%AuGe+ 14%Ni, deposited by thermal evaporation, was used for metallization during the fabrication of the Schottky barriers and ohmic contacts. The ohmic contacts were formed at 420 °C in 2–5 min in a hydrogen atmosphere. The capacitance measurements were performed at 1 MHz, and the reverse bias was modulated with frequency 50 Hz.

The density N_I of scattering centers was determined from the mobility measurements as[6]

$$N_I[\mathrm{cm}^{-3}] = 10^{17}(10^4/\mu[\mathrm{cm}^2/\mathrm{V\cdot s}] - 1)^2 \qquad (1)$$

and the parameter $K = 1-(N_{idl}+N_0)/N_l$ was estimated, where N_{idl} and N_0 are the ionized impurity densities in ion-doped layers and in the initial material, respectively. The density N_0 was determined from measurements of the electron mobility in the initial GaAs. The density $N_{idl} = N_s/Nd$, where $d = R_p + 2(2/\pi)^{1/2}\Delta R_p$,[7] and R_p and ΔR_p are the ^{28}Si ion ranges in GaAs. In our case $d = 168$ nm. We interpreted values $K>0$ as evidence that the ion-doped layers contain additional electron scattering centers as compared with n-GaAs doped by other methods to comparable electron densities. These additional centers could be due to, for example, incomplete annealing of radiation defects.

3. EXPERIMENTAL RESULTS AND DISCUSSION

A. Layer density and the parameter K

Figure 1 shows the results of measurements of N_s and the values of the paraemeter K as a function of the HEA temperature (curves *1, 1'*) and the TA temperature (curves *2, 2'*). It is evident that electrical activation of silicon (n-type layers) at the level $N_s \simeq 1\times10^{12}$ cm^{-2} is observed after HEA

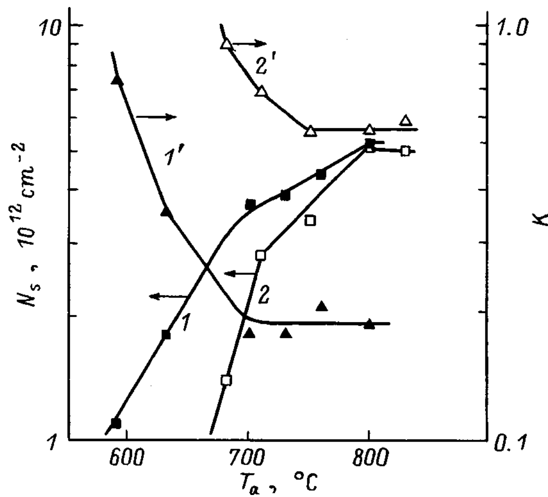

FIG. 1. Layer density N_s (*1,2*) and the parameter K (*1′,2′*) versus the annealing temperature T_a. *1, 1′* — HEA, *2, 2′* — TA.

at a lower temperature (by $\sim 90\,°C$) compared with TA (curves *1* and *2*). We note that after TA at $T_a < 680\,°C$, N_s could not be measured by the van der Pauw method in ion-doped layers. This attests to a low degree of activation of silicon (transition into an electrically active state) and possibly a high density of compensating defects, which is due to the comparatively large value of K ($K \simeq 0.91$ at $T_a = 680\,°C$ Fig. 1, curve *2′*). As the annealing temperature increases, the differences in the values of N_s after HEA and TA decrease, and at $T_a = 800\,°C$ these values are essentially identical. After HEA the parameter K decreases from 0.74 (590 °C) to 0.18 (700 °C) and then remains unchanged with increasing temperature (curve *1′*). The values of K were three to four times higher (curve *2′*) after TA in the temperature range investigated. The differences noted in the values of K agree on the whole with the much lower densities of deep levels in ion-doped layers after HEA as compared with TA (the data on the densities were obtained by DLTS[8]).

Figure 2 shows $\ln N_s$ versus the reciprocal of the HEA

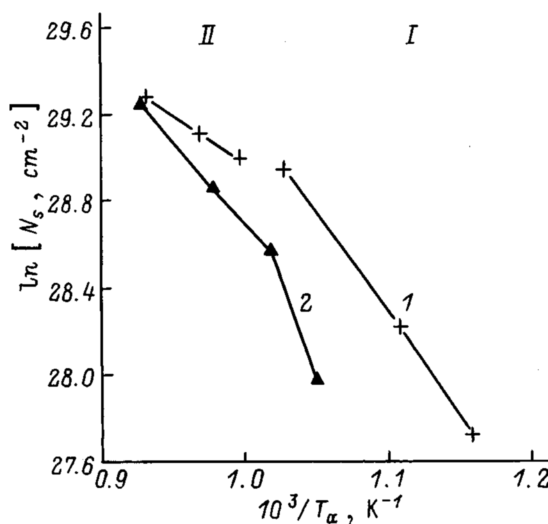

FIG. 2. Logarithm of the layer density N_s versus the reciprocal of the annealing temperature T_a. *1* — HEA, *2* — TA.

TABLE I. Activation energies for the formation of ion-doped layers during HEA and TA.

Form of annealing	E_A, eV	
	Stage I	Stage II
HEA	0.83	0.38
TA	1.87	0.57

temperature (curve *1*) and TA temperature (curve *2*). It is evident that these curves are straight lines and for both forms of annealing they shw two stages of formation of ion-doped layers: less than (I stage) and greater than (II stage) $T_a \simeq 710\,°C$. The activation energies E_A estimated from the slope of the straight lines are presented in Table I.

According to Table I E_A after TA is greater than the analogous values after HEA by 1 eV at stage I and by 0.2 eV at stage II. The energy $E_A = 1.87$ eV obtained for the stage I of TA is somewhat greater than the value[9] $E_A = 1.0 - 1.4$ eV characteristic for annealing of point defects in GaAs. This difference is probably due to the fact that two processes occur simultaneously during the formation of an ion-doped layer: annealing of compensating defects with activation energy ~ 1.3 eV and embedding of silicon at the sites of the gallium sublattice with activation energy near 0.57 eV. It is also possible that annealing of defect–impurity complexes followed by electrical activation of silicon occur at stage I. The value 0.57 eV is close to $E_A = 0.5$ eV,[10] the characteristic value of the electrical activation energy of Si in GaAs with TA. On the other hand, the value $E_A = 0.38$ eV in the temperature range 730–800 °C is essentially identical to the activation energy E_A of Si for LEA with a protective dielectric coating,[3] though the values of N_s in the ion-doped layers, scaled to the implantation dose, are on average 1.6 times greater than after LEA.

B. Electron density profiles

Figure 3 shows the electron density profiles $n(x)$ of electrically activated silicon in ion-doped layers after HEA (curves *1–4*), after LEA (curve *5*), and after TA (curve *6*). Curve *7* shows the density distribution of the implanted silicon, calculated in the approximation of two semi-Gaussians[11] using the central moments of the distribution from Ref. 12. We note that the first two moments in Ref. 12 agree satisfactorily with the values of R_p and ΔR_p determined by secondary-ion mass spectrometry.[13]

It is evident from Fig. 3 that after HEA at $T_a = 590\,°C$ (curve *1*) the electron density n is 2.0×10^{17} cm^{-3} at depth $x = 110$ nm. In addition, for $x > 140$ nm the experimental profile agrees well with the computed profile (compare the points 1 and the solid curve). As the HEA temperature increases, n increases as a result of the electrical activation of silicon in the layer next to the SiO_2–GaAs boundary and at 800 °C reaches the value 8.8×10^{17} cm^{-2} at depth 40 nm (curve *3*). Moreover, the electron density at $x \geqslant 220$ nm increases with increasing HEA temperature (curves *1–3*).

For comparable annealing temperatures (Fig. 3, curves *4–6*) the electron density in the layer $x \geqslant 60$ nm after HEA is

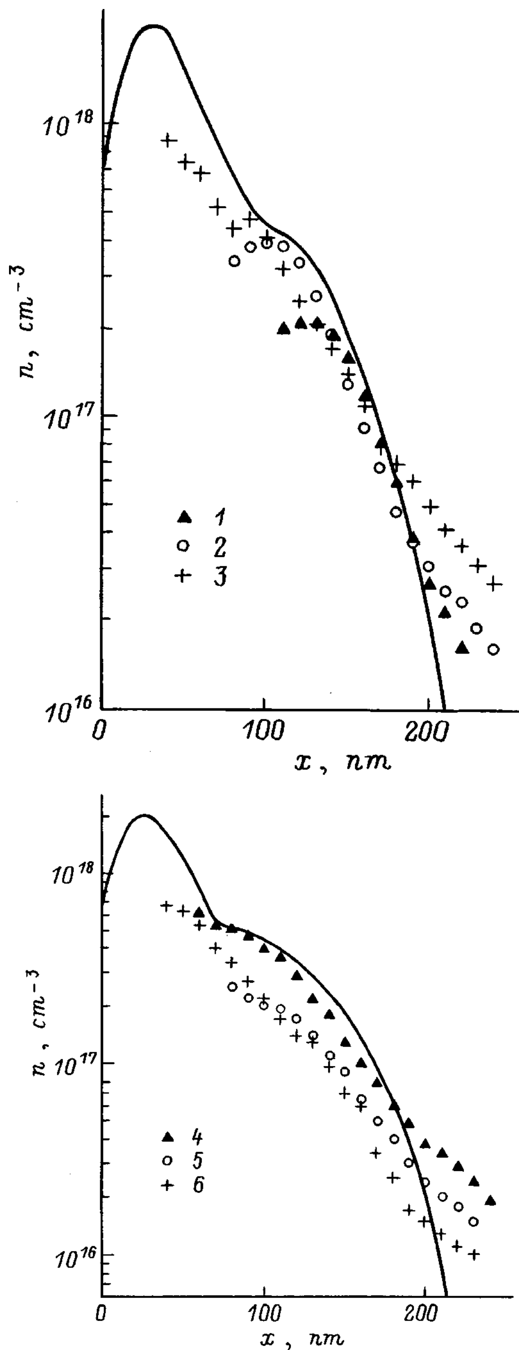

FIG. 3. Electron density profile in ion-doped layers after HEA (*1–4*), LEA (*5*), and TA (*6*). HEA regime, T_a, °C/t_a, s: *1* — 590/21; *2* — 630/15; *3* — 800/21; *4* — 730/13. LEA regime: *5* — T_a=730 °C, t_a=16 s. TA regime: *6* — T_a=750 °C, t_a=30 min. t_a — annealing time. Solid line — computed density profile of implanted silicon.

higher than after LEA and after TA, attesting to more efficient activation of silicon. At the same time the density profile after TA is measured with a lesser depth (40 nm, curve *6*) than with HEA and LEA. In addition, the distribution $n(x)$ after TA lies higher for $x<110$ nm and lower for $x>110$ nm than after LEA. This result could be due to the diffusion redistribution of silicon into the interier volume of GaAs during LEA,[3] since the electron density is higher in the ''tail'' of the distribution (curves *5* and *6*). These features of the electron density profiles attest to a different degree of silicon activation for radiation forms of annealing and TA in layers lying directly next to the SiO_2–GaAs boundary and in deeper layers.

TABLE II. Parameters of ion-doped layers after different types of annealing.

Form of annealing	T_a, °C	t_a, s	N_s, 10^{12} cm^{-3}	μ, cm^2/V·s	K	η, %
TA	750	1800	3.4	2380	0.56±0.18	56.8
LEA	730	16	1.8	3100	0.35±0.12	52.8
HEA	730	13	3.9	2930	0.18±0.06	95.0

Table II gives the values of N_s and μ and the computed average values of K and degree η of electrical activation of silicon. The latter quantity was determined as the ratio of the area under experimental curve $n(x)$ (Fig. 3b) to the corresponding area under the computed density distribution of implanted silicon.

It follows from Table II that HEA forms an ion-doped layer with the highest degree of electrical activation of silicon and the lowest density of residual defects (the parameter K) which limit the electron mobility. The layer electron density N_s is lower after LEA than after TA. According to the data in Fig. 3 (curves *5* and *6*), this is due to the higher activation of silicon in the layer $x<110$ nm after TA. With respect to the value of K LEA falls between TA and HEA.

In our view the differences in the characteristics of ion-doped layers obtained by radiation annealings and TA are due to ionization during LEA and both ionization and generation of point defects during HEA. These processes stimulate the activation of silicon and annealing of radiation defects produced as a result of the ^{28}Si ion implantation.

4. CONCLUSIONS

1. Ion-doped layers are formed during HEA at much lower annealing temperatures than for TA, and even at $T_a=590$ °C the electron density profile at depths $x\geqslant 140$ nm is identical to the computed profile of implanted silicon.

2. The increase in the layer density N_s with increasing HEA temperature in the range $T_a=630-800$ °C is due to activation of the impurity in a layer located next to the SiO_2–GaAs boundary, and even at $T_a=730$ °C the degree of activation of silicon reaches 95% according to measurements of the density profiles.

3. The process leading to the formation of ion-doped layers with HEA occurs in two stages with different activation energies E_A, where the value of E_A at both stages is less than the corresponding values for TA.

4. The parameter K for HEA is lower than for LEA and TA. With respect to the values of K LEA falls between HEA and TA.

We thank V. V. Peshev for performing the HEA.

[1] A. V. Chernyaev, *Ion Implantation Method in Gallium Arsenide Device and Integrated Circuit Technology* (Radio i svyaz', Moscow, 1980).
[2] A. V. Dvurechenskiĭ, B. P. Kashnikov, and L. S. Smirnov, Fiz. Tekh. Poluprovodn. **14**, 1837 (1980) [Sov. Phys. Semicond. **14**, 1095 (1980)].
[3] V. M. Ardyshev and M. V. Ardyshev, Fiz. Tekh. Poluprovodn. **32**, 1153 (1998) [Semiconductors **32**, 1029 (1998)].

[4] V. M. Ardyshev, V. V. Peshev, and A. P. Surzhikov, Inventor's Certificate No. 1554670.
[5] Yu. E. Kreĭndel', N. I. Lebedev, V. Ya. Martens, G. A. Mesyats, and D. I. Proskurovskaya, Pis'ma Zh. Tekh. Fiz. **8**(23), 1465 (1982) [Sov. Tech. Phys. Lett. **8**, 630 (1982)].
[6] S. Hilsum, Electron. Lett. **10**, 259 (1974).
[7] *Gallium Arsenide Field-Effect Transistors* (Radio i svyaz', Moscow, 1988).
[8] V. M. Ardyshev, V. V. Peshev, and A. P. Surzhikov, Fiz. Khim. Organ. Mater., No. 4 (1998) (in press).
[9] D. Lang, in *Point Defects in Solids* (Mir, Moscow, 1979), p. 187.
[10] B. M. Goryunov, E. I. Zorin, P. V. Pavlov *et al.*, in *Gallium Arsenide* (Tomsk State University, Tomsk, 1974), No. 4, p. 102.
[11] *MOS–VLIC. Simulation of Components and Technological Processes*, edited by P. Antonetti *et al.* [Radio i svyaz', Moscow, 1988].
[12] A. V. Burenkov, F. F. Komarov, M. A. Kumakhov, and M. M. Temkin, *Tables of the Parameters of the Spatial Distribution of Ion-Implanted Impurities* [Minsk University Press, Minsk, 1980].
[13] D. H. Lee and R. M. Malbon, Appl. Phys. Lett. **30**, 327 (1977).

Translated by M. E. Alferieff

ELECTRONIC AND OPTICAL PROPERTIES OF SEMICONDUCTORS

Photoionization of short-range acceptor states in uniaxially deformed semiconductors

A. A. Abramov and V. N. Tulupenko*)

Donbass State Machine Building Academy, 343916 Kramatorsk, Ukraine

V. T. Vas'ko

Institute of Semiconductor Physics, 252650 Kiev, Ukraine

D. A. Firsov

St. Petersburg State Technical University, 195251 St. Petersburg, Russia

(Submitted July 1, 1998; accepted for publication October 1, 1998)
Fiz. Tekh. Poluprovodn. **33**, 691–696 (June 1999)

The photoionization cross section (the absorption coefficient) of holes which are localized on deep centers with a short-range potential and make transitions into the valence band of a uniaxially deformed Ge-type semiconductor is calculated. As a result of the fact that the acceptor level and the extremum of the hole subbands split the photoionization threshold also splits, and four types of transitions of this kind arise. The population of the split impurity states and the contributions of transitions of each type to the absorption coefficient change with increasing temperature. Since deformation destroys the spherical symmetry of the problem, an appreciable polarization dependence of the absorption coefficient appears. The calculation is based on a general quantum-mechanical formula with a transition matrix element employing the wave function of an impurity center accompanying deformation. © *1999 American Institute of Physics.* [S1063-7826(99)01406-4]

1. INTRODUCTION

The current interest in effects resulting from uniaxial deformation (UD) in bulk semiconductors is due primarily to the observation of a laser effect in the infrared (IR) range[1] and to the fact that the results obtained can serve as a starting point for similar investigations in strained structures based on Ge–Si quantum wells, which have aroused great interest among investigators in the last few years.[2] In addition, the question considered in the present paper stems from the need to supplement what little information is available about optical effects in semiconductors in the presence of UD. The photoionization cross section of a deep impurity center for a simple conduction band (c band) was first calculated in Ref. 3. Optical transitions from a deep h center into a complex semiconductor valence band consisting of heavy- and light-hole subbands were examined in Ref. 4. The optical matrix elements of transitions (and the photoionization cross section) from an impurity center into the conduction band for narrow-gap semiconductors in the presence of UD were calculated in Ref. 5. In the present paper light absorption due to transitions from impurity levels into a complex valence band of a p-Ge type semiconductor in the presence of UD is studied.

Uniaxial deformation qualitatively changes the character of the hole states in the continuous spectrum and of the local states close to the Γ_8 extremum. It is well known that the UD of a semiconductor lowers the symmetry of this extremum.[6] This produces qualitative changes in the spectral and polarization dependences of light absorption in interband[7] and intersubband[8] transitions of electrons (see also references in Ref. 5) and in the photoionization cross sections of acceptors (see the transition scheme in Fig. 1).

In the present paper the spectral and polarization dependences of the absorption coefficient (AC) with IR excitation of holes from split levels on short-range centers into the continuous spectrum are calculated. The low-temperature case, where holes are localized on levels of short-range defects (for example, structural imperfections or substitution impurities; see the discussion of this model in the review in Ref. 9), is studied.

The specific spectral dependences of the AC with various values of the deformation X and temperature T are obtained for Ge:Zn and GaAs:Mn.

2. CALCULATION OF THE ABSORPTION COEFFICIENT

The general formula for the AC is

$$\alpha_\omega=\frac{4\pi^2e^2n_{im}}{c\sqrt{\chi\omega}}\sum_{i\lambda}f_i|\langle i|\hat{\mathbf{v}}\cdot\mathbf{e}|\lambda\rangle|^2\delta(E_i-\varepsilon_\lambda+\hbar\omega), \quad (1)$$

where $\hat{\mathbf{v}}$ is a 4×4 velocity matrix, ω and $\mathbf{e}$ are the frequency and unit polarization vector of the radiation, χ is the permittivity, $i=\pm$ enumerates the deformation-split states E of the center, and ε_λ are states of free holes with momentum $\mathbf{p}$ and spin σ in the upper ($\lambda=(+\sigma\mathbf{p})$) and lower ($\lambda=(-\sigma\mathbf{p})$)

 © 1999 American Institute of Physics

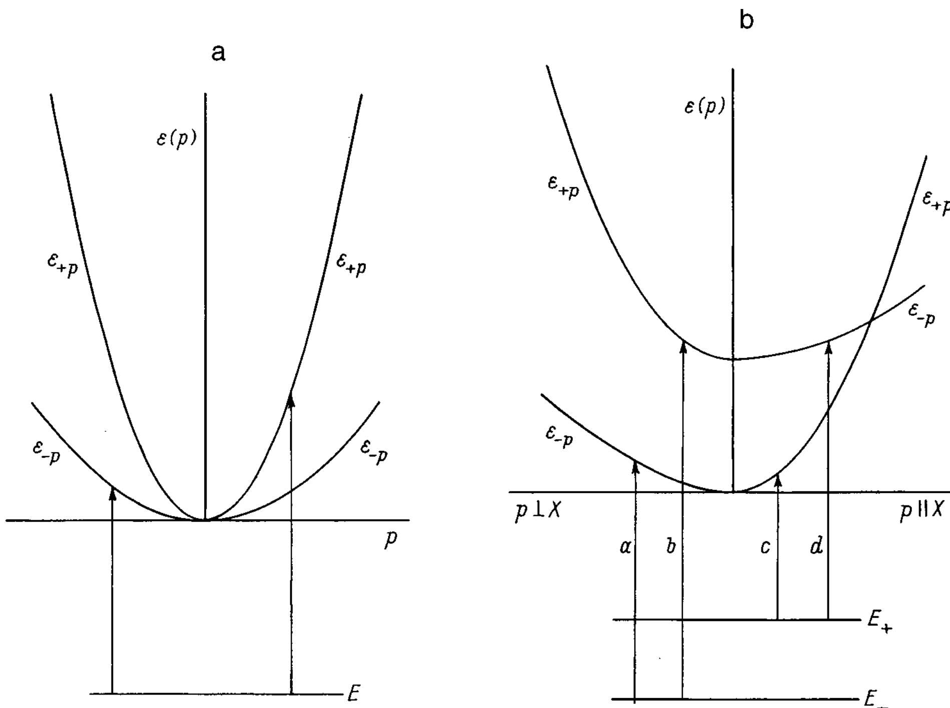

FIG. 1. Scheme of transitions from an impurity center into hole subbands in the absence (a) and presence (b) of a deformation X.

energy subbands split by the uniaxial deformation (Fig. 1). The impurity occupation number f_i describes hole redistribution over the $\pm$ levels with increasing temperature T:

$$f_i = Z^{-1}\exp\left[-\frac{E_i}{T}\right], \quad Z = \sum_i \exp\left[-\frac{E_i}{T}\right]. \tag{2}$$

We note that the spin quantum number of holes on impurity centers is neglected above (even though the levels are spin-degenerate), i.e. because of the strong Coulomb repulsion of the holes only single-hole filling of the centers is studied.

The transition matrix element in Eq. (1) can be transformed into the p representation

$$\langle i|\hat{\mathbf{v}}\cdot\mathbf{e}|\lambda\rangle = \sum_{j'j} \varphi^{i+}_{pj'}(\hat{\mathbf{v}}_p\cdot\mathbf{e})_{j'j}\psi^{\pm\sigma}_{pj}, \tag{3}$$

where the four-row column vectors $\varphi^i_{\mathbf{p}j}$ and $\psi^{\pm\sigma}_{\mathbf{p}j}$ describe local impurity and band states, respectively.

The dispersion laws of the split hole subbands are anisotropic in momentum space and spin-degenerate, as a result of which the spin index σ in ε_λ can be dropped in what follows. In the presence of deformation along the z axis we have (we neglect the crystal anisotropy in the absence of deformation)[6]

$$\varepsilon_{\pm\mathbf{p}} = \frac{\gamma_1 p^2}{2m} \pm \sqrt{\left(\frac{\gamma p^2}{m}\right)^2 + \frac{\gamma p^2}{m}\Delta P_2\left(\frac{p_z}{p}\right) + \left(\frac{\Delta}{2}\right)^2}. \tag{4}$$

Here γ_1, $\gamma \simeq \gamma_{2,3}$ are the Luttinger parameters, m is the mass of a free electron, and $P_2(p_z/p) \equiv P_2(x) = (3x^2-1)/2$. The energy Δ determines the splitting of the hole subbands, which is proportional to the compression, $\Delta = \alpha X$, and for $X \parallel [100]$ $\alpha = 6$ meV/kbar.[6] The free-hole wave functions corresponding to the energies (4) are presented in Ref. 6.

Hole states on a point-like center are described by a Schrödinger matrix integral equation

$$\hat{H}_\mathbf{p}\varphi^i_\mathbf{p} + \frac{u_0}{V}\sum_\mathbf{p} \varphi^i_\mathbf{p} = E_i\varphi^i_\mathbf{p}, \tag{5}$$

where $\hat{H}_\mathbf{p}$ is the Luttinger Hamiltonian, V is the normalization volume, and the potential energy of a short-range center located at the point $r=0$ is $u_0\delta(r)$. From Eq. (5) we have the identity

$$(\hat{H}_\mathbf{p} - E_i)\varphi^i_\mathbf{p} = -\frac{u_0}{V}\sum_\mathbf{p} \varphi^i_\mathbf{p} \equiv N_i|i\rangle, \tag{6}$$

where $|i\rangle$ is a four-row column vector and N_i is a constant. Using the Green's function for free holes we write the wave function, determined by the Koster–Slater type matrix equation (6), as

$$\varphi^i_\mathbf{p} = N_i\hat{G}_{E_i}(\mathbf{p})|i\rangle, \tag{7}$$

whence one can see that N_i is the normalization coefficient, and the column vector $|i\rangle$ is found from the homogeneous equation

$$(\hat{\lambda}(E)+1)|i\rangle = 0, \quad \hat{\lambda}(E) = \frac{u_0}{V}\sum_\mathbf{p} \hat{G}_E(\mathbf{p}). \tag{8}$$

The free-hole Green's function in Eqs. (7) and (8)

$$\hat{G}_E(\mathbf{p}) = \sum_\pm \frac{\hat{P}_{\pm\mathbf{p}}}{\varepsilon_{\pm\mathbf{p}} - E}, \quad (\hat{P}_{\pm\mathbf{p}})_{jj'} = \sum_\sigma \psi^{\pm\sigma *}_{\mathbf{p}j'}\psi^{\pm\sigma}_{\mathbf{p}j} \tag{9}$$

is expressed here in terms of the energy (4) and the projection operators on $\pm$ states, which are given by the matrix

$$\hat{P}_{\pm\mathbf{p}}=\frac{1}{\varepsilon_{\mp\mathbf{p}}-\varepsilon_{\pm\mathbf{p}}}\begin{vmatrix} -a^{\mp} & -f & -g & 0 \\ -f^* & a^{\pm} & 0 & -g \\ -g^* & 0 & a^{\pm} & f \\ 0 & -g^* & f^* & -a^{\mp} \end{vmatrix}, \tag{10}$$

where $a=\gamma_1 p^2/2m-\gamma p^2/m\,P_2(p_z/p)-\Delta/2$, $a^{\pm}=a-\varepsilon_{\pm\mathbf{p}}$, $f=-\sqrt{3}\ \gamma/m\,(p_y+ip_x)$, and $g=\sqrt{3}/2\ \gamma/m\,(p_x-ip_y)^2$. The matrix $\hat{\lambda}(E)$ determined in Eq. (8) is diagonal, and the spin-degenerate levels are determined by the equation $[1+\hat{\lambda}_{\pm}(E)]=0$. This equation is analyzed in Ref. 10, where linear shifts of the levels under an applied pressure are obtained for small deformations. The normalization factor N_i is determined from the standard normalization condition whereby the wave function of the center (7) is normalized to 1:

$$N_i=\left[u_0\Bigg/\frac{d\lambda_i}{d\varepsilon}\Bigg|_{\varepsilon=E_i}\right]^{\frac{1}{2}}. \tag{11}$$

Since $\hat{\lambda}(E)$ is diagonal, the four linearly independent solutions $|i\rangle$ are given by the column vectors

$$|+\uparrow\rangle=\begin{vmatrix}1\\0\\0\\0\end{vmatrix},\quad |+\downarrow\rangle=\begin{vmatrix}0\\0\\0\\1\end{vmatrix},$$

$$|-\uparrow\rangle=\begin{vmatrix}0\\1\\0\\0\end{vmatrix},\quad |-\downarrow\rangle=\begin{vmatrix}0\\0\\1\\0\end{vmatrix}. \tag{12}$$

The formulas (7)–(11) determine the wave function of a hole on an impurity center.

The spin-summed transition matrix element (3) between the i-th level and the $\pm$ hole states has the form

$$\sum_{\sigma}|\langle i|\hat{\mathbf{v}}\cdot\mathbf{e}|k\sigma\mathbf{p}\rangle|^2=\sum_{\sigma}|\langle i|\hat{G}_{E_i}(\mathbf{p})(\hat{\mathbf{v}}_{\mathbf{p}}\cdot\mathbf{e})|k\sigma\mathbf{p}\rangle|^2. \tag{13}$$

where $k=\pm$ enumerates the hole subbands. Substituting into Eq. (12) the expression for the Green's function (9) and using the fact that Eq. (1) contains the matrix element averaged over the xoy plane perpendicular to the deformation axis, we obtain

$$M_{ik}(\mathbf{p})=\int_0^{2\pi}\frac{d\varphi}{2\pi}\sum_{\sigma}\left|\sum_{k'\sigma'}\frac{\langle i|k'\sigma'\mathbf{p}\rangle}{\varepsilon_{k'\mathbf{p}}-E_i}\langle k'\sigma'\mathbf{p}|\hat{\mathbf{v}}_{\mathbf{p}}\cdot\mathbf{e}|k\sigma\mathbf{p}\rangle\right|^2, \tag{14}$$

where φ determines the orientation of the momentum in the xoy plane, and $i,k=\pm$ enumerate states on the center and in the band, respectively. Expressing the velocity matrix $\hat{\mathbf{v}}$ as a 4×4 matrix of the angular momentum $\hat{\mathbf{J}}$ (Ref. 6) and introducing $\gamma=\gamma_1+5\gamma/2$, we obtain

$$\langle k'\sigma'\mathbf{p}|\hat{\mathbf{v}}_{\mathbf{p}}\cdot\mathbf{e}|k\sigma\mathbf{p}\rangle=\frac{\tilde{\gamma}}{m}(\mathbf{p}\cdot\mathbf{e})\,\delta_{k'k}\delta_{\sigma'\sigma}-\frac{\gamma}{m}\langle k'\sigma'\mathbf{p}|\times(\mathbf{e}\cdot\hat{\mathbf{J}}(\mathbf{p}\cdot\hat{\mathbf{J}})+(\mathbf{p}\cdot\hat{\mathbf{J}})(\mathbf{e}\cdot\hat{\mathbf{J}})|k\sigma\mathbf{p}. \tag{15}$$

After calculating the matrix elements in Eq. (14) and performing the quite complicated summations and averaging over the angle we obtain explicit expressions for the transition amplitudes $M_{ik}(p)$.

As one can see from Eq. (13), the absorption coefficient is determined by four types of transitions: from each of the split impurity levels into both valence subbands (the indices i and k assume the values $\pm$).

The energies $E_{\pm}(X)$ of the deformation-split impurity levels have been calculated in Refs. 10 and 11. For the ionization energy (in the absence of pressure) $E_0\sim100$ meV of the centers and pressures (up to 12 kbar) considered in this paper we used the initial sections of the curves obtained in Ref. 10 that can be approximated by the simple linear laws $E_-(X)=E_0-1.9X$ and $E_+(X)=E_0+2.2X$. Here the position of the extremum of the valence subbands at $X=0$ is taken as the zero point of energy, and the positive direction is into the valence band. The functions $E_{\pm}(X)$ for a specific material are determined by the ratio γ_1/λ of the Luttinger parameters, which is the same for Ge and GaAs.

3. ABSORPTION SPECTRA

The spectral dependences of the AC were calculated for centers corresponding to Zn impurity in Ge ($|E_0|=90$ meV) and Mn impurity in GaAs ($|E_0|=100$ meV). The calculation is performed in a geometry where the z axis is in the direction of deformation, the y axis is in the direction of incidence of light polarized along the x axis (x polarization: $e_x=1$, $e_y=e_z=0$) or the z axis (z polarization: $e_x=e_y=0$, $e_z=1$). The expressions for $M_{ik}(p)$ are written out in the *Appendix*.

Figure 2 shows the computed spectral dependences of the AC $\alpha(\hbar\omega)$ at $T=4.2$ K and impurity density 7×10^{14} cm^{-3} for x polarization (Fig. 2a) and z polarization (Fig. 2b). The range of values of $\hbar\omega$ is limited by 350 meV. This is due to the fact that in Ge:Zn transitions into a spin-orbit splitoff subband are possible even for $\hbar\omega\geqslant380$ meV (in GaAs:Mn for $\hbar\omega\geqslant430$ meV); these transitions make only an additive contribution to the AC and do not affect the manner in which the complex valence band of the deformed material is reflected in the spectral dependences. The fact that the AC for Ge:Zn is larger than for GaAs:Mn in Figs. 2 and 3 is explained by the ratio of the Luttinger parameters: $(\gamma)_{\mathrm{Ge}}/(\gamma)_{\mathrm{GaAs}}=2$ and $(\gamma_1)_{\mathrm{Ge}}/(\gamma_1)_{\mathrm{GaAs}}=2$.

At $T=4.2$ K the impurity filling number f_+ for the upper level is essentially zero, and the AC is determined by transitions of the type (a) and (b) in Fig. 1b and 1c from the level E_- into the valence subbands. The threshold value of $\hbar\omega$ is $(\hbar\omega)_a=\varepsilon_{-\mathbf{p}}|_{P=0}-E_-=|E_0|-1.1X$ for transitions of the type (a) and $(\hbar\omega)_b=\varepsilon_{+\mathbf{p}}|_{P=0}-E_-=|E_0|+4.9X$ for transitions of the type (b). Thus the contributions of the transitions (a) and (b) in the spectral curve spread along the $\hbar\omega$ axis with increasing pressure. For $X=1$ kbar $(\hbar\omega)_a$

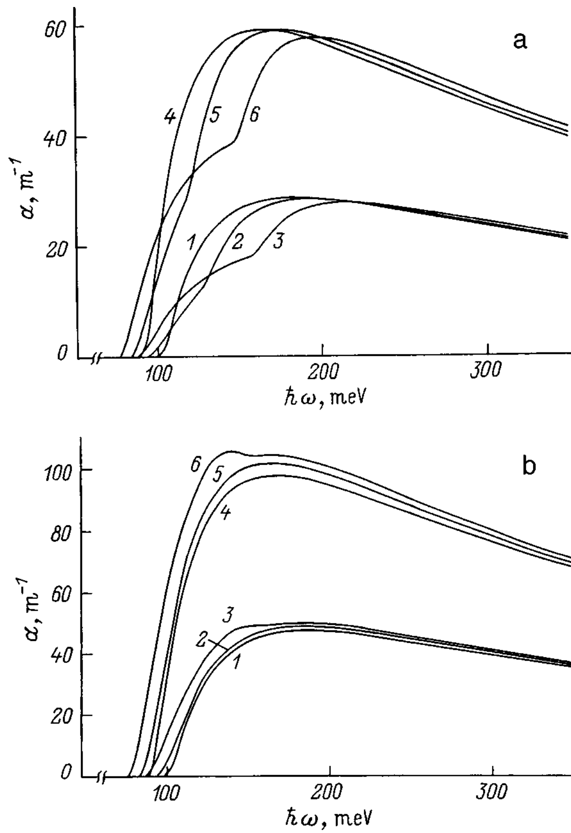

FIG. 2. Spectral curves of the absorption coefficient for various pressures and $T=4.2$ K: a — $e_x=1$, $e_y=e_z=0$; b — $e_x=e_y=0$, $e_z=1$; *1–3* — GaAs:Mn, *4–6* — Ge:Zn; X, kbar: *1, 4* — 1; *2, 5* — 6; *3, 6* — 12.

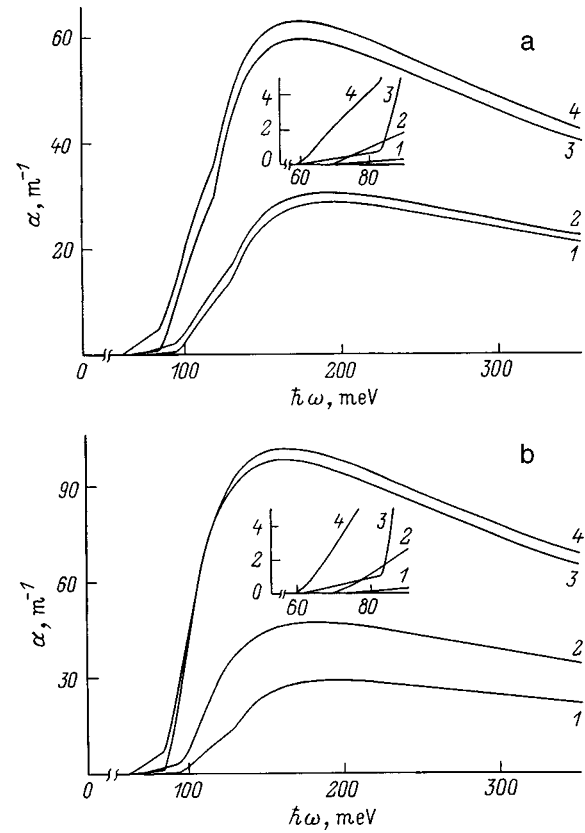

FIG. 3. Spectral curves of the absorption coefficient for various temperatures and $X=6$ kbar: a — $e_x=1$, $e_y=e_z=0$; b — $e_x=e_y=0$, $e_z=1$; *1, 2* — GaAs:Mn, *3, 4* — Ge:Zn; T, K: *1, 3* — 77; *2, 4* — 180.

$\sim(\hbar\omega)_b$ and the spectral curves are quite smooth. For $X=6$ kbar the difference $(\hbar\omega)_b-(\hbar\omega)_a=36$ meV is already substantial, and an inflection corresponding to the onset of transitions of the type (b) is noticeable for $\hbar\omega\geqslant(\hbar\omega)_b$ in the curves *2*, *5* (Fig. 2), which correspond to x polarization. At $X=12$ kbar $((\hbar\omega)_a/(\hbar\omega)_b\approx1.9$, curves *3* and *6* in Fig. 2) the complex structure of the valence band is seen more clearly: The initial growth (corresponding in Fig. 2b to the first maximum) is due to transitions of type (a) only and the maximum (in Fig. 2b the second maximum) is due to transitions of type (b). The transition probabilities for z polarization are less sensitive to the structure of the valence band.

The fact that the maximum values on the spectral curves in Fig. 2 are almost identical for different pressures is explained by the pressure dependences of the transition matrix element M_{ik} and the interband density of states determined by the δ function: $M_{ik}\sim X$ and the density of states $\sim 1/X$.

Intracenter redistribution of the holes and a simultaneous increase in the contributions of transitions of the type (c) and (d) to the AC occur with increasing temperature. In Fig. 3 this fact is manifested as growth of the left shoulder on the spectral curves for temperatures 77 and 180 K at $X=6$ kbar. The inflections on the curves for x polarization demonstrate the type of transitions arising under deformation: (c), (a), and (d) (the inflection corresponding to the transition (b) is not noticeable against the background produced by transitions of the type (d)).

To explain the order of the curves *1–2* (GaAs:Mn) and *3–4* (Ge:Zn) at different temperatures in Fig. 3, we write the AC for fixed deformations X and photon energy $\hbar\omega$ in the form

$$\alpha(T)=f_-(T)B+f_+(T)C, \tag{16}$$

where B and C are factors which to within a constant are the transition matrix elements into the valence subbands from the levels E_- and E_+, respectively. Since $f_+(T_2)-f_+(T_1)=f_-(T_1)-f_-(T_2)$, which follows from Eq. (2), we obtain from Eq. (16)

$$\alpha_{21}=\alpha(T_2)-\alpha(T_1)=[f_+(T_2)-f_+(T_1)](C-B). \tag{17}$$

The fact that the curves *1–2* and *3–4* in Fig. 3 lie one above another in order of increasing temperatures means that, according to Eq. (17), $C>B$ (for $T_2>T_1$ from Fig. 3 follows $\alpha_{21}>0$ and therefore $C>B$), i.e. the probability of transitions from the level E_+ into the valence band is higher than the probability of transitions from the level E_-.

4. CONCLUSIONS

The theoretical spectral dependences obtained for the absorption coefficient in this work

a) reflect the complex structure of the valence band under deformation;

b) contain information about the pressure-induced shift of the impurity levels;

c) make it possible to estimate the contribution of transitions from the deformation-split levels E_- and E_+ to the AC; and,

d) attest to high sensitivity of the transition matrix elements to the valence band structure for x polarization.

The wave function constructed in this paper for an impurity center can be used to investigate various processes in which impurity states participate. We call attention to the anisotropy of the wave function, manifested in the fact that the spectral curves for x and z polarizations are different.

Comparing the theoretical and experimental dependences would make it possible to confirm the theoretical models on which the present calculation is based.

This work was supported in part by the Ukrainian Ministry of Education, by the Ukrainian Fund for Fundamental Research (Grant 2.4/970), and the Russian Fund for Fundamental Research (Grant 96-02-17404a), and by the grant NATO HTECH.LG 960931.

5. APPENDIX

The matrix element in Eq. (14) is given by the expression

$$M_{ik}=A_i[e_x^2(M_{ik}^1+M_{ik}^2)+e_z^2(M_{ik}^3+M_{ik}^4)],$$

where

$$A_i=((\varepsilon_{-\mathbf{p}}-E_i)^2(\varepsilon_{+\mathbf{p}}-E_i)^2a^i(\varepsilon_{-\mathbf{p}}-\varepsilon_{+\mathbf{p}}))^{-1}N_i^2,$$

and the coefficients M_{ik}^l $(l=1-4)$ determine the relative contribution from the x and z polarizations. For transitions from the impurity E_+ we have

$$M_{+k}^1=3\left(\frac{\gamma p_z}{2m}\right)^2\left[\left(\left(\frac{\gamma_1+\gamma}{\gamma}c-\frac{\gamma_1-\gamma}{\gamma}a^k\right)\right.\right.$$
$$\left.-3\frac{\gamma}{m}(p^2+p_z^2)\right)^2\frac{\gamma^2}{m^2}(p^2-p_z^2)^2$$
$$+\left(\left(\frac{\gamma_1+\gamma}{\gamma}c-\frac{\gamma_1-\gamma}{\gamma}a^k\right)\frac{\gamma}{m}(p^2-p_z^2)\right.$$
$$\left.\left.-ca^k-\frac{3\gamma^2}{4m^2}(p^2-p_z^2)^2\right)^2\right],$$

$$M_{+k}^2=3\left(\frac{\gamma}{m}\right)^2(p^2-p_z^2)\left[\frac{1}{4}\left(\frac{1}{2}\left(\frac{\gamma_1+\gamma}{\gamma}c+\frac{\gamma_1-\gamma}{\gamma}a^k\right)\right.\right.$$
$$\left.-\frac{3}{2}\frac{\gamma}{m}(p^2+p_z^2)\right)^2\frac{\gamma^2}{m^2}(p^2-p_z^2)^2$$
$$+\left(\frac{1}{4}\left(\frac{\gamma_1+\gamma}{\gamma}c+\frac{\gamma_1-\gamma}{\gamma}a^k\right)\frac{\gamma}{m}(p^2-p_z^2)\right.$$
$$\left.\left.-ca^++\frac{3\gamma^2}{2m^2}(p^2-p_z^2)^2\right)^2\right],$$

$$M_{+k}^3=3\left(\frac{\gamma}{m}\right)^2(p^2-p_z^2)\left[\left(\frac{\gamma_1-2\gamma}{\gamma}c+\frac{\gamma_1+2\gamma}{\gamma}a^k\right)\right.$$
$$\left.\times\frac{\gamma p_z^2}{m}-a^k(a^{-k}-c)\right]^2,$$

$$M_{+k}^4=\left(\frac{\gamma p_z}{m}\right)^2\frac{3\gamma^2}{4m^2}(p^2-p_z^2)^2$$
$$\times\left(\frac{\gamma_1-2\gamma}{\gamma}c+\frac{\gamma_1+2\gamma}{\gamma}a^k+\frac{6\gamma}{m}(p^2-p_z^2)\right)^2,$$

where $c=\varepsilon_{-\mathbf{p}}+\varepsilon_{+\mathbf{p}}-E_+$.

For transitions from the impurity level E_- we have

$$M_{-k}^3=\left(\frac{\gamma}{m}\right)^2(p^2-p_z^2)\left[\left(\left(\frac{\gamma_1+\gamma}{\gamma}d-\frac{\gamma_1-\gamma}{\gamma}a^{-k}\right)a^k\right.\right.$$
$$\left.-\frac{3\gamma}{2m}(p^2+p_z^2)(d+a^k)\right)^2$$
$$\left.+\left(\frac{3\gamma}{2m}(p^2-3p_z^2)(d-a^k)\right)^2\right],$$

$$M_{-k}^2=\frac{45}{4}\left(\frac{\gamma p_z}{m}\right)^3(d-a^k)^2\frac{\gamma^2}{m^2}(p^2-p_z^2)^2,$$

$$M_{-k}^3=\left(\frac{\gamma p_z}{m}\right)^2\left(\left(\frac{\gamma_1+2\gamma}{\gamma}d+\frac{\gamma_1-2\gamma}{\gamma}a^{-k}\right)a^k\right.$$
$$\left.-\frac{3\gamma}{m}(p^2-p_z^2)(d+a^k)\right)^2,$$

$$M_{-k}^4=\frac{9\gamma}{4m}\left(\frac{\gamma(p^2-p_z^2)}{m}\right)^3(d-a^k)^2,$$

where $d=a-E_-$.

*)E-mail: tvn@laser.donetsk.ua

[1] I. V. Altukhov, M. S. Kagan, and V. P. Sinis, JETP Lett. **47**, 164 (1988).
[2] *Proceedings of the All-Russia Conference on Silicon- and Germanium-Based Nanostructures* (Institute of Miscrostructrue Physics, Russian Academy of Sciences, Nizhniĭ Novgorod, 1998).
[3] G. Lucovsky, Solid State Commun. **3**, 299 (1965).
[4] N. M. Kolchanov, I. D. Loginov, and I. N. Yassievich, Fiz. Tverd. Tela (Leningrad) **25**(6), 1650 (1983) [Sov. Phys. Solid State **6**, 952 (1983)].
[5] M. V. Strikha and F. T. Vasko, Phys. Status Solidi B **181**, 447 (1994).
[6] G. L. Bir and G. E. Pikus, *Symmetry and Strain-Induced Effects in Semiconductors* [Wiley, New York, 1975; Nauka, Moscow, 1972].
[7] F. H. Pollak, Semicond. Semimet. **32**, 17 (1990).
[8] E. V. Bakhanova and F. T. Vasko, Phys. Status Solidi B **182**, 97 (1994).
[9] V. F. Masterov, Fiz. Tekh. Poluprovodn. **18**, 3 (1984) [Sov. Phys. Semicond. **18**, 1 (1984)].
[10] E. V. Bakhanova and F. T. Vas'ko, Fiz. Tverd. Tela (Leningrad) **32**, 86 (1990) [Sov. Phys. Solid State **32**, 47 (1990)].
[11] M. A. Odnoblyudov, A. A. Pakhomov, V. M. Chistyakov, and I. N. Yasievich, Fiz. Tekh. Poluprovodn. **31**, 1180 (1997) [Semiconductors **31**, 1014 (1997)].

Translated by M. E. Alferieff

Electric and luminescence properties of GaAs–$A^{II}B^{IV}C_2^V$ single crystals

I. K. Polushina and Yu. V. Rud'

A. F. Ioffe Physicotechnical Institute, Russian Academy of Sciences, 194021 St. Petersburg, Russia

V. Yu. Rud'

St. Petersburg State Technical University, 195251 St. Petersburg, Russia

(Submitted October 27, 1998; accepted for publication November 2, 1998)
Fiz. Tekh. Poluprovodn. **33**, 697–700 (June 1999)

GaAs–$A^{II}B^{IV}C_2^V$ single crystals are grown by crystallization from dilute gallium fluxed solutions. The electric and luminescence properties of the crystals obtained are investigated. It is shown that the technological process is accompanied by the standard doping of gallium arsenide and makes it possible to grow gallium arsenide single crystals whose optoelectronic properties are controlled by the $A^{II}B^{IV}As_2$ compound introduced into the fluxed solution.
© *1999 American Institute of Physics.* [S1063-7826(99)01506-9]

Professor N. A. Goryunova predicted and discovered more than 40 years ago the semiconductor properties of intermetallic III–V compounds.[1,2] Subsequently, it was determined that a continous series of solid solutions with a sphalerite lattice can be obtained on the basis of these compounds.[3,4] Both discoveries played a very important role in the advancement of semiconductor physics and technology, thereby determining one of the main directions of semiconductor materials science, making it possible to obtain semiconductors with the required properties by continuous control of the atomic composition of multicomponent solid solutions. In this respect the question of the character of the interaction of III–V compounds and their closest electronic analogs — $A^{II}B^{IV}C_2^V$ semiconductors — is of interest. Solubility has been established and the possibility of controlling the fundamental and structure-sensitive properties of these materials have been demonstrated for a variety of systems of this type.[5] The present work, which follows this avenue, is the first attempt to investigate thoroughly structural and optoelectronic phenomena in materials obtained by crystallization from gallium-rich fluxed solutions of gallium arsenide and ternary $A^{II}B^{IV}C_2^V$ semiconductors. This ultimately opened up new possibilities for controlling the electronic properties of III–V semiconductors interacting with the ternary compounds $A^{II}B^{IV}C_2^V$ in dilute gallium-based fluxed solutions.

1. The GaAs crystals were obtained by crystallization from gallium-rich fluxed solutions. Additions of presynthesized single-phase ternary compounds $A^{II}B^{IV}As_2$ were introduced in a definite ratio with GaAs into the initial charge. Table I gives the concentrations (in mole %) of GaAs and $A^{II}B^{IV}As_2$, introduced into evacuated quartz crucibles together with 97% Ga. Crystallization proceeded at 650–700 °C and was controlled by lowering crucibles containing the charge with the indicated composition in a temperature gradient $\Delta T \simeq 30$ °C /cm. Single crystals of the shape as the ampul were formed in the conical part of the crucibles as a result of directed crystallization. The solvent was decanted, and after the crystals were extracted from the ampuls the residues of the solvent were etched off at room temperature in concentrated hydrochloric acid.

X-Ray crystallographic investigations were performed on the single crystals obtained from fluxed solutions with different atomic composition, and the transport coefficients in the temperature range 77–300 K and the spectral dependences of the photoluminescence (PL) at 77 K were also measured. Stationary photoluminescence was excited by argon laser radiation ($\lambda_{exc} = 4579$ Å , $P \simeq 100$ mW/cm^2) and observed from the irradiated side of the crystals. The PL spectra were recorded with an MDR-3 monochromator with a 600 line/mm diffraction grating and an FÉU-62 photomultiplier. The spectral resolution was no worse than 0.5 meV, and the PL spectra were corrected by an instrumental function which takes account of the spectral dependences of the transmission of radiation by the optical channel of the setup and the sensitivity of the photodetector.

2. The x-ray investigations established (see Table I) that the single crystals obtained have the characteristic sphalerite structure for III–V compounds and unit cell parameter a which is the same as for GaAs to within the measurement error.[6] Therefore, for the charge compositions and growth conditions employed appreciable dissolution of the $A^{II}B^{IV}As_2$ compounds in GaAs and changes in the type and parameter of the crystal lattice characteristic for gallium arsenide do not occur.

3. The investigations of the transport coefficients in the samples obtained showed that the changes in the atomic composition of the ternary arsenides added into the crystallization medium make it possible to obtain GaAs crystals with only hole-type conductivity. Taking account of the effect of group-II and -IV impurities on the electrical properties of GaAs,[7,8] there are grounds for believing that the p-type conductivity is due to predominant dissolution of the group-II elements (Zn, Cd), while the presence of the group-IV atoms is responsible only for compensation of the acceptors. It follows from Table I that the maximum level of

 © 1999 American Institute of Physics

TABLE I. Properties of GaAs–$A^{II}B^{IV}As_2$ crystals.

Sample No.	Dopant compound	Ratio of components $A^{II}B^{IV}C_2^V$: GaAs:Ga, mole%	a, Å	Type of conductivity	p, cm^{-3} (T=300 K)	T=77 K: U_p, cm^2/(V·s)	T=77 K: $\hbar\omega_m$, eV	T=77 K: $\delta_{1/2}$, meV*	T=77 K: $\Delta\hbar\omega_m$, eV**
1	$CdSnAs_2$	2.5:0.5:97	5.6530	*p*	5×10^{18}	35	1.400	74(41+33)	0.11
2	$ZnSnAs_2$	2.5:0.5:97	5.6532	*p*	2×10^{18}	20	1.388	90(50+40)	0.12
3	$CdGeAs_2$	2.5:0.5:97	5.6530	*p*	2×10^{17}	10	1.378	74(41+33)	0.13
4	$CdGeAs_2$	1.5:1.5:97	5.6532	*p*	3×10^{19}		1.425	90(61+29)	0.08
5	$CdGeAs_2$	0.5:2.5:97	5.6531	*p*	1.2×10^{18}	75	1.471	40(25+15)	0.14
6	$CdGeAs_2$	0.1:2.9:97	5.65295	*p*	2.5×10^{18}	33	1.425	62(32+30)	0.08
7	$CdSiAs_2$	2.5:0.5:97	5.6530	*p*	8×10^{18}	30	1.380	58(20+33)	0.13
8	$ZnSiAs_2$	2.5:0.5:97	5.6528	*p*	7×10^{18}	20	1.462	34(20+14)	0.05
9		3.0:97	5.6530	*p*			1.509	40(20+19)	0

*The values of the long- and short-wavelength half-widths of the PL bands at half-height are given in parentheses.
**$\Delta\hbar\omega$m is the difference between $\hbar\omega_m$ for undoped GaAs and $\hbar\omega_m$ for GaAs–$A^{II}B^{IV}As_2$ crystals.

doping of GaAs by acceptors is obtained by introducing $CdGeAs_2$ into the charge. Changes in the $CdGeAs_2$ content give rise to changes in the hole density. On the whole it can be assumed that the density and Hall mobility of holes in the samples obtained are the usual values for gallium arsenide obtained by doping with group-II elements, while the dissolution of group–IV elements was found to be insufficient for conductivity inversion $p\rightarrow n$.

The temperature dependences of the Hall coefficient R and conductivity σ (Fig. 1) in crystals grown in the presence of $A^{II}B^{IV}As_2$ compounds are also close to those characteristic for gallium arsenide doped only with zinc or cadmium.[7,8] The temperature dependences of the hole Hall mobility for the crystals obtained (Fig. 2) show that the dominant scattering mechanism in such samples is hole scattering by static lattice defects.

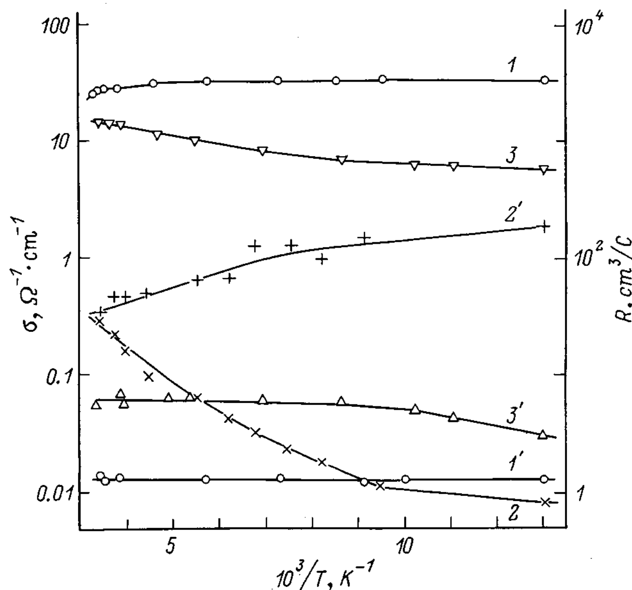

FIG. 1. Temperature dependences of the conductivity σ (1–3) and Hall coefficient R (*1'–3'*) of p-GaAs–$A^{II}B^{IV}As_2$ single crystals. Sample numbers: *1, 1'* — 1; *2, 2'* — 3; *3, 3'* — 5. The numbers correspond to Table I.

4. For p-GaAs crystals grown in the presence of the arsenides $A^{II}B^{IV}As_2$ (see Table I), as a rule, one band prevails in the spectral dependence of the photoluminescence intensity. Figure 3 shows the typical PL spectrum of one such crystal (curves *2* and *3*) compared with a GaAs crystal which was not deliberately doped (curve *1*). One can see that the maximum $\hbar\omega_m$ of this band is red-shifted relative to the

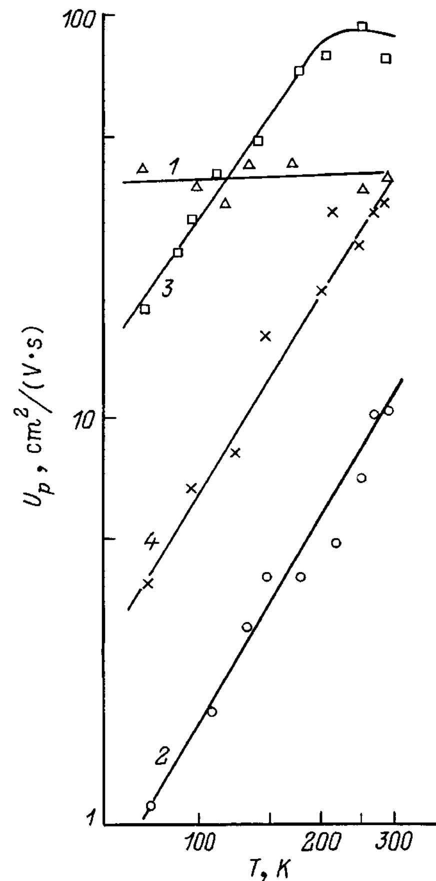

FIG. 2. Temperature dependences of the hole Hall mobility in p-GaAs–$A^{II}B^{IV}As_2$ single crystals. Sample numbers: *1* — 2; *2* — 3; *3* — 5; *4* — 6.

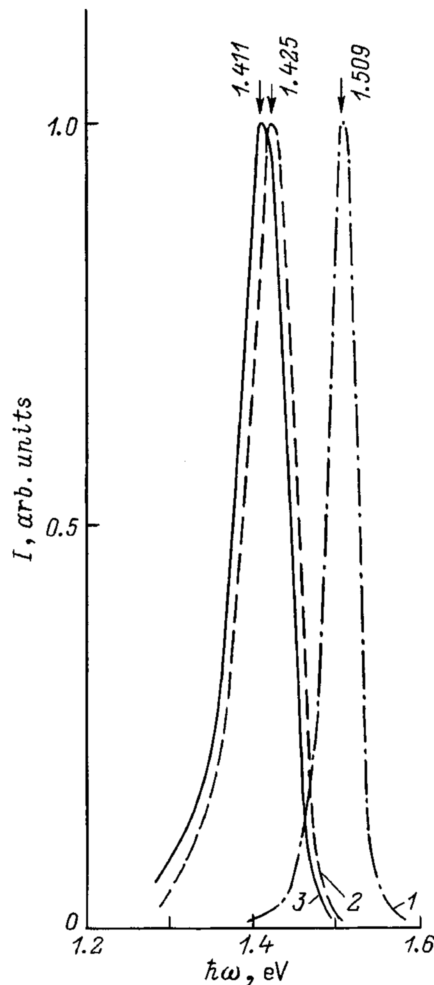

FIG. 3. Spectral dependences of the photoluminescence of *p*-GaAs (1) and *p*-GaAs–$CdGeAs_2$ (*2, 3*) at $T=77$ K . Sample numbers: *1* — 9; *2, 3* — 6. Excitation level *L*, arbitrary units: *1, 2* — 1.0; *3* — 0.15.

maximum of the PL in the crystal which was not specially doped.

Probing of the surface of the crystals by the PL-exciting probe (diameter $\simeq 0.1$ mm) showed that the parameters of the observed bands are quite reproducible from point to point along the surface of the same crystal as well as in different crystals from the same batch. This shows that the technological process based on interaction of GaAs with $A^{II}B^{IV}As_2$ compounds in a gallium solvent makes it possible to obtain quite homogeneous *p*-GaAs crystals. It is also evident from Table I that the energy position of the photoluminescence maximum $\hbar\omega_m$ clearly depends on the atomic composition of the ternary arsenides $A^{II}B^{IV}As_2$ introduced into the crystallization zone. The value of $\Delta\hbar\omega_m$, which is the difference between the energies of the PL maxima in GaAs crystals which have not been deliberately doped and which contain impurities (see Table I), can be used to judge the relative depth of the corresponding centers formed as a result of the interaction between GaAs and ternary arsenides in the fluxed solution.

Investigations of the effect of the excitation density *L* on the photoluminescence of our crystals showed a parallel shift of the band wings and of the band maxima $\hbar\omega_m$ with decreasing *L* into the long-wavelength region of the spectrum. The rate of this shift with an order-of-magnitude decrease of the excitation density is $\partial(\hbar\omega_m)/\partial L \simeq 14-16$ meV at 77 K in all crystals obtained in the presence of added $A^{II}B^{IV}As_2$. This shows that the observed bands are due to donor-acceptor radiative transitions. The group–II atoms (Cd and Zn) apparently are acceptors, while the group–IV elements (Sn, Ge, and Si) are donors. In this case the dependence of $\hbar\omega_m$ on the nature of the ternary compounds $A^{II}B^{IV}As_2$ introduced into the solvent and their concentration (for example, $CdGeAs_2$) can be attributed to changes in the chemical nature of the atoms in the acceptor vapors and the distances between their constituent components. The total width $\delta_{1/2}$ of the PL bands at half-height (see Table I) also depends on the real structure of the ensemble of lattice defects in such single crystals.

5. To determine the possible anisotropy of the physical properties of GaAs crystals, which in principle can arise as a result of positional ordering of group–II and -IV atoms in the gallium sublattice in GaAs, we also attempted to observe the anisotropy of photoluminescence. Our experiments did not show any anisotropy of radiative recombination in the *p*-GaAs–$A^{II}B^{IV}As_2$ crystals obtained. From this it can be inferred that as a result of the technological processes conducted the concentration of group–II and –IV impurities dissolved in GaAs does not exceed the usual doping limits. It is obvious that to attain ordering of group–II and –IV atoms in the GaAs lattice with a lowering of its symmetry, the concentration of the dissolved impurities must be increased. Apparently this is still a substantial technological problem, whose solution could make it possible to achieve high nonlinear susceptibilities of III–V semiconductors and therefore provide real possibilities for using such crystals in nonlinearly-optical laser frequency converters.[9]

We thank A. A. Vaĭpolin for performing the x-ray crystallographic investigations and for a helpful discussion.

[1] G. A. Goryunova, *Author's Abstract of Candidate's Dissertation* (Physicotechnical Institute of the USSR Academy of Sciences, Leningrad, 1950).

[2] Zh. I. Alferov and B. V. Tsarenkov, Fiz. Tekh. Poluprovodn. **19**, 2113 (1985) [Sov. Phys. Semicond. **19**, 1303 (1985)].

[3] N. A. Goryunova, *Complex Diamond-Like Semiconducting Compounds of Group-III and -V Elements* (Mir, Moscow, 1967).

[4] N. A. Goryunova and N. M. Fedorova, Zh. Tekh. Fiz. **25**, 1339 (1955).

[5] $A^{II}B^{IV}C_2^V$ *Semiconductors*, edited by N. A. Goryunova and Yu. A. Valov (Sov. radio, Moscow, 1974).

[6] *Handbook of the Physicochemical Properties of Semiconducting Materials* (Nauka, Moscow, 1978).

[7] C. Hilsum and A. C. Rose-Innes, *Semiconducting III-V Compounds* [Pergamon Press, New York, 1961; Inostr. Lit., Moscow, 1963].

[8] O. Madelung, *Physics of III-V Compounds* [Wiley, New York, 1964; Mir, Moscow, 1967].

[9] M. C. Ohmer and R. Pandey, MRS Bulletin **23**, 16 (1998).

Translated by M. E. Alferieff

Reciprocal drag of electrons and phonons in strongly doped HgFeSe semiconductors

I. I. Lyapilin and Kh. M. Bikkin

Institute of Metal Physics, Ural Branch of the Russian Academy of Sciences, 620219 Ekaterinburg, Russia
(Submitted October 27, 1998; accepted for publication November 3, 1998)
Fiz. Tekh. Poluprovodn. **33**, 701–707 (June 1999)

The previously observed unusual dependences of the thermoelectric and thermomagnetic coefficients of strongly doped HgFeSe crystals on temperature and magnetic field intensity are studied theoretically. It is shown that the observed dependences are due to the combined effect of electron scattering by spatially correlated charged donors Fe(3+) at low temperatures and the reciprocal drag of electrons and phonons, which plays a large role in semiconductors with a high density of itinerant charge carriers. © *1999 American Institute of Physics.* [S1063-7826(99)01606-3]

1. INTRODUCTION

Iron-doped gapless HgSe semiconductors possess a number of unique electronic properties which are responsible for the "anomalous" behavior of the transport coefficients in these materials.[1] Some of the observed features have been explained by electron scattering by a spatially correlated system of iron impurities.[2] However, the unusual field dependence observed for the thermomagnetic coefficients in these materials in Ref. 3 has still not been discussed in the literature.

It is known that the thermoelectric power $\alpha(H)$ of a degenerate electron gas in a classically strong magnetic field H saturates and does not depend on the mechanism of scattering of itinerant charge carriers. However, as follows from the experimental data of Ref. 3, which are presented in Fig. 1, saturation of $|\alpha(H)|$ in HgFeSe crystals occurs only in the most highly iron-doped HgSeFe sample $N_{\mathrm{Fe}} \simeq 4\times 10^{20}\ \mathrm{cm}^{-3}$. For samples with a lower iron density, a maximum of the dimensionless longitudinal Nernst–Ettingshausen (NE) effect $\varepsilon_x = e\Delta\alpha/k_0$, where k_0 is Boltzmann's constant, e is the absolute value of the electron charge, and $\Delta\alpha = |\alpha(H)| - |\alpha(0)|$, is observed at a certain value of the magnetic field $H = H_m$. Such a nonmonotonic dependence is very unexpected and requires additional explanation. Moreover, a minimum, whose magnitude and position depend strongly on the iron content in the sample, is observed in the curve $\alpha(T)$, where T is temperature.

The nonmonotonic behavior of the thermoelectric power observed in the experiment of Ref. 4 as a function of the iron content in a sample at fixed temperature in the low temperature range ($T = 10-20$ K) is also a complete mystery. As the iron impurity content increases, the quantity $\alpha(N_{\mathrm{Fe}})$ at first decreases, starting at $N_{\mathrm{Fe}} = 5\times 10^{18}\ \mathrm{cm}^{-3}$, and then increases, reaching a maximum at $N_{\mathrm{Fe}} = 2\times 10^{19}\ \mathrm{cm}^{-3}$, and once again decreases at higher iron impurity content.

Since these results cannot be explained on the basis of the standard theory of thermomagnetic phenomena,[5] the authors of Ref. 4 proposed a model in which the above-noted anomaly in the thermoelectric power was attributed to suppression of phonon scattering, if the system of charged donors in HgFeSe crystals becomes spatially correlated. Unfortunately, this model cannot explain other anomalies in the thermal magnetic coefficients in HgFeSe.

In our view the anomalous behavior of the thermoelectric and thermomagnetic coefficients in these compounds has a quite simple explanation. Indeed, in the temperature range 10–30 K it is impossible to construct a correct theory of thermomagnetic and thermoelectric phenomena in gapless crystals without taking account of phonon drag, which is due to the appearance of anisotropy of the phonon distribution function in the presence of a temperature gradient. Phonon drag effects greatly increase the thermoelectric power and have been studied in detail for the case where phonon relaxation is determined primarily by nonelectronic scattering mechanisms ($\tau_{pp} \ll \tau_{pe}$), where τ_{pp} is the phonon relaxation time due to nonelectronic scattering mechanisms and τ_{pe} is the phonon relaxation time due to the interaction with electrons.[5]

In the more complicated case where the relaxation times are comparable $\tau_{pp} \approx \tau_{pe}$ and $\tau_{ep} \approx \tau_{ei}$, where τ_{ep} is the relaxation time of electrons on phonons and τ_{ei} is the relaxation time of electrons on impurities, the transport equations for the phonon and electron distribution functions must be solved simultaneously (the situation of reciprocal drag of electrons and phonons). Numerical estimates show that this case of reciprocal drag occurs for HgFeSe and HgSe samples at low temperatures.

Several papers have been devoted to the solution of the system of transport equations for the phonon and electron distribution functions taking account of reciprocal drag. Appel[6] and Parrot[7] have calculated the thermoelectric and thermomagnetic coefficients for nondegenerate semiconductors, and Gurevich and Korenblit[8] have found an expression for the electron and phonon distribution functions for a strongly degenerate electron gas. However, Gurevich and Korenblit[8] considered only the thermoelectric coefficients, leaving aside thermomagnetic effects.

In summary, the field dependence of thermomagnetic effects in degenerate semiconductors under the conditions of reciprocal drag of electrons and phonons has still not been studied at all.

 © 1999 American Institute of Physics

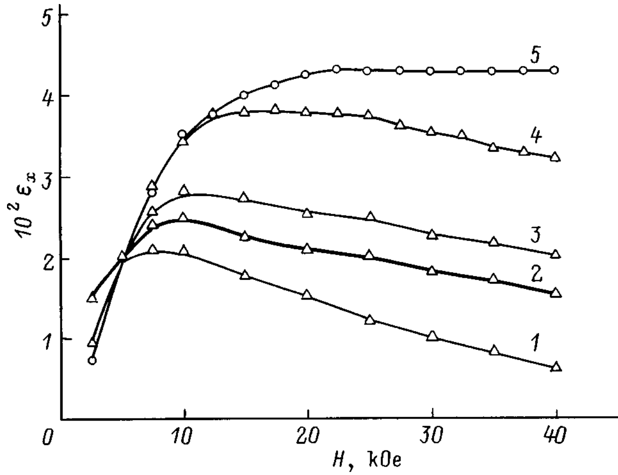

FIG. 1. Dimensionless field of the longitudinal Nernst–Ettingshausen effect versus the magnetic field (according to data of Ref. 3) for two HgFeSe samples with density N_{Fe}, 10^{20} cm^{-3}: *1–4* — 0.1, *5* — 4. Temperature *T*, K: *1* — 18, *2* — 25, *3* — 42, *4* — 64, *5* — 58.

In the present paper we shall show that the conventional theory of thermomagnetic phenomena cannot explain virtually any of the experimental results obtained in Refs. 3 and 4, which can be explained if the reciprocal drag of electrons and phonons is taken into account.

2. SYSTEM OF TRANSPORT EQUATIONS

In studying the transport equation for conduction electrons we shall take account of the interaction of electrons with acoustic phonons and impurities, scattering by which predominates at low temperatures. The collision integral in this case can be written as

$$\left.\frac{\partial f}{\partial t}\right|_s=-\frac{f'}{\tau(k)}-\frac{1}{4\tau_A(k)\hbar k^4}\int_0^{2k}q^3(\hbar\mathbf{k}\cdot\mathbf{b}(q))\left(\frac{\partial f^0}{\partial\varepsilon}\right)dq, \tag{1}$$

where

$$\frac{1}{\tau_A(k)}=\frac{E_0^2k_0Tmk}{\pi\rho s^2\hbar^3},\quad f=f^0+f',$$

$$f'=\left(-\frac{\partial f^0}{\partial\varepsilon}\right)\left(\frac{\hbar\mathbf{k}}{m}\cdot\boldsymbol{\chi}\right), \tag{2}$$

E_0 is the deformation potential constant, s is the sound velocity constant, m is the electron effective mass, and ρ is the density of the crystal, $\tau(k)$ is the effective electron momentum relaxation time due to electron collisions with equilibrium phonons and other scatterers, $f'(k)$ is the nonequilibrium correction to the equilibrium distribution function $f^0(k)$, and $\mathbf{k}$ is the electron wave vector.

We shall write the collision integral in the transport equation for the phonon distribution function, taking into consideration the scattering of acoustic phonons by electrons and other (nonelectronic) phonon relaxation mechanisms, in the form

$$\left.\frac{\partial N_q}{\partial t}\right|_s=-\frac{k_0T\mathbf{b}(q)}{(\hbar\omega_q)^2\tau_{pp}(q)}+\frac{1}{2\tau_A(k)kq_q}\times\int_{q/2}^{2k}k\left(\mathbf{b}(q)-\frac{\hbar}{m}\boldsymbol{\chi}\right)\left(\frac{\partial f^0}{\partial\varepsilon}\right)dk, \tag{3}$$

$$N_q=N_q^0+N_q',\quad N_q'=\left(-\frac{\partial N_q^0}{\partial\hbar\omega_q}\right)(\mathbf{q}\cdot\mathbf{b}),\quad \omega_q=\hbar sq.$$

Here τ_{pp} is the relaxation time due to nonelectronic mechanisms (phonons on phonons, defects, and so on). The unknown functions $\boldsymbol{\chi}$ and $\mathbf{b}(q)$, characterizing the deviations of the systems under study from equilibrium depend only on the modulus of the corresponding wave vectors and must be determined by solving the system of transprot equations.

We shall write the transport equations for our subsystems, taking into consideration the collision integrals (1) and (3). The transport equation for conduction electrons in uniform electric $\mathbf{E}$ and magnetic $\mathbf{H}$ fields in the presence of a temperature gradient ∇T can be written as

$$\mathbf{B}(k)=\boldsymbol{\chi}(\varepsilon_k)-[\mathbf{a}\times\boldsymbol{\chi}(\varepsilon_k)]-\frac{\tau(k)m}{4\hbar\tau_A(k)k^4}\int_0^{2k}q^3\mathbf{b}(q)dq,$$

$$\mathbf{B}(k)=-\tau(k)\left[e\boldsymbol{\varepsilon}+\frac{\varepsilon_k-\varepsilon_F}{T}\nabla T\right],$$

$$\mathbf{a}=\omega_0\tau_A(k)\mathbf{h},\quad \omega_0=\frac{eH}{mc}, \tag{4}$$

$$\boldsymbol{\varepsilon}=\mathbf{E}-\boldsymbol{\nabla}\varepsilon_F/e,$$

where ω_q is the phonon frequency, $\boldsymbol{\varepsilon}$ is the gradient of the electrochemical potential, ε_F is the chemical potential of the electrons, and $\mathbf{h}$ is a unit vector oriented in the direction of the magnetic field. We write similarly the transport equation for the phonon distribution function:

$$\frac{sk_0}{q\hbar\omega_q}\boldsymbol{\nabla}T=-\frac{k_0T\mathbf{b}(q)}{(\hbar\omega_q)^2\tau_{pp}(q)}+\frac{1}{2\tau_A(k)kq}\times\int_{q/2}^{\infty}k\left(\mathbf{b}(q)-\frac{\hbar}{m}\ \boldsymbol{\chi}\right)\left(\frac{\partial f^0}{\partial\varepsilon}\right)dk. \tag{5}$$

The equations (4) and (5) are the starting equations for determining the transport coefficients in the presence of reciprocal drag of electrons and phonons.

As follows from the results of Ref. 8, the system of equations (4) and (5) can be easily solved if the step character of the distribution function $f^0[(\varepsilon-\varepsilon_F)/k_0T]$ is used in the collision integral (3) in the transport equation for the phonon distribution function, taking account of the strong degeneracy of the electron gas. The simplified system of equations so obtained can be solved exactly.

A method for solving the system of equations (4) and (5) has been discussed in detail in Ref. 8, and there is no need to revisit this question here. We can only propose a somewhat different solution procedure, leading to the same results, but demonstrating more clearly the crux of the approximations made.

It is obvious that the system of equations (4) and (5) can be written for electrons with energy $\varepsilon_k=\varepsilon_F$. This system can be easily solved, using the approximation $\partial f^0/\partial\varepsilon_k=\delta(\varepsilon_k-\varepsilon_F)$ in the expression (5); this makes it possible to find the correction to the electron distribution function $\boldsymbol{\chi}(\varepsilon_F)$ at the Fermi surface. Then we can return to the solution of the system of equations (4) and (5) for arbitrary values of ε_k. Retaining on the right-hand side of Eq. (5) the contribution to the integral only at the Fermi surface, we once again have an algebraic system of equations for $\boldsymbol{\chi}(\varepsilon_k)$.

For specific calculations it is necessary to introduce the explicit form of the nonelectronic phonon relaxation mechanism. For the latter we shall consider the mechanism of Simons[5]

$$\tau_{pp}^{-1}=\lambda_s q, \quad \lambda_s=\frac{\hbar}{\rho}\left(\frac{k_0T}{\hbar s}\right)^4. \tag{6}$$

Using the algorithm described above it is easy to find an equation for the correction to the electron distribution function $\boldsymbol{\chi}(\varepsilon_k)$:

$$\mathbf{B}=\boldsymbol{\chi}-[\mathbf{a}\times\boldsymbol{\chi}]-G\{\mathbf{B}(\varepsilon_F)-\nu^2(k_F)\mathbf{h}(\mathbf{h}\cdot\mathbf{B}(\varepsilon_F))-\nu(k_F)[\mathbf{h}\times\mathbf{B}(\varepsilon_F)]\}+\frac{4}{3}\Pi k_0T\tau(k)\frac{\boldsymbol{\nabla}T}{T},$$

$$\mathbf{B}(\varepsilon_F)=-\tau(k)\left(e\boldsymbol{\varepsilon}+\frac{4}{3}\Pi k_0T\frac{\boldsymbol{\nabla}T}{T}\right), \tag{7}$$

$$G=\frac{\Pi}{(1-\Pi^*)}\frac{\tau(k)}{\tau_A(k)R(k_F)}, \quad R(k_F)=1+\nu^3(k_F),$$

$$\Pi=\frac{1}{1+\Pi_1}, \quad \Pi_1=\frac{2k_0T\hbar^2kq}{m(\hbar\omega_q)^2}\frac{\tau_A(k)}{\tau_{pp}(q)}=\frac{2\pi(k_0T)^4}{E_0^2(ms)^2}, \tag{8}$$

$$\Pi^*=\frac{\tau(k_F)}{\tau_A(k_F)}\Pi, \quad \nu(\varepsilon_F)=\tau(k_F)\omega_0(1-\Pi^*)^{-1}. \tag{9}$$

It is evident that the structure of Eqs. (7) is the same as in the classical theory of thermomagnetic phenomena, and all changes are due to the renormalization of the thermodynamic forces and the electron mean-free path lengths. Therefore it can be rewritten in the form

$$-\tau(k)\left(e\varepsilon_i^*+\frac{(\varepsilon_k-\varepsilon_F)\delta_{ij}+A_{\mathrm{p}\,ij}}{T}\nabla_jT\right)=\chi_i-[\mathbf{a}\times\boldsymbol{\chi}]_i,$$

$$\mathbf{a}=\mathbf{h}\tau(k)\omega_0,$$

$$\varepsilon_i^*=\varepsilon_j(S_{\mathrm{p}}\delta_{ij}+S_{\mathrm{p}\,ij}); \quad A_{\mathrm{p}\,ij}=A_{\mathrm{p}}^*\delta_{ij}+A_{\mathrm{p}\,ij}^*. \tag{10}$$

Introducing together with the vector $\boldsymbol{\varepsilon}$ the effective thermodynamic force $\boldsymbol{\nabla}T^*$, we write the solution of Eq. (10) in the form

$$\begin{aligned}\boldsymbol{\chi}(\varepsilon_k)=&-e\tau(k)\\ &\times\left\{(\mathbf{h}\cdot\boldsymbol{\varepsilon}^*)\mathbf{h}+\frac{\omega_0\tau(k)[\mathbf{h}\times\boldsymbol{\varepsilon}^*]-[\mathbf{h}\times[\mathbf{h}\times\boldsymbol{\varepsilon}^*]]}{R}\right\}\\ &-\tau(k)\frac{\varepsilon_k-\varepsilon_F}{T}\left\{(\mathbf{h}\cdot\boldsymbol{\nabla}T)\mathbf{h}\right.\\ &\left.+\frac{\omega_0\tau(k)[\mathbf{h}\times\boldsymbol{\nabla}T]-[\mathbf{h}\times[\mathbf{h}\times\boldsymbol{\nabla}T]]}{R}\right\}\\ &-\tau(k)\frac{k_0T}{T}\left\{(\mathbf{h}\cdot\boldsymbol{\nabla}T^*)\mathbf{h}\right.\\ &\left.+\frac{\omega_0\tau(k)[\mathbf{h}\times\boldsymbol{\nabla}T^*]-[\mathbf{h}\times[\mathbf{h}\times\boldsymbol{\nabla}T^*]]}{R}\right\},\end{aligned} \tag{11}$$

$$R=1+[\omega_0\tau(k)]^2.$$

Here

$$\nabla T_i^*=\nabla T_j(A_{\mathrm{p}}^*\delta_{ij}+A_{\mathrm{p}\,ij}^*), \quad A_{\mathrm{p}}^*=\frac{4}{3}\Pi(1+S_{\mathrm{p}}),$$

$$S_{\mathrm{p}}=\frac{\Pi^*}{(1-\Pi^*)}\frac{\tau_A(k_F)}{\tau_A(k)}\frac{1}{1+\nu^2(k_F)}. \tag{12}$$

The components of the tensors which we have introduced have the form

$$S_{\mathrm{p}\,ij}^*=S_{\mathrm{p}}\nu(k_F)\begin{pmatrix}0 & -1 & 0\\ 1 & 0 & 0\\ 0 & 0 & \nu(k_F)\end{pmatrix}, \tag{13}$$

$$A_{\mathrm{p}\,ij}^*=\frac{4}{3}\Pi S_{ij}^*.$$

Using the expression (11) for the correction to the electron distribution function $\chi(\varepsilon_k)$, we can write an expression for the components of the charge flux density in the sample $J_i=\sigma_{ij}\varepsilon_j-\beta_{ij}\nabla_jT$ and find the components of the electrical conductivity tensor

$$\sigma_{xx}=e^2\left[K_0^{\perp}(1+S_{\mathrm{p}})-K_0^H\frac{\Pi^*}{1-\Pi^*}\frac{\nu(\varepsilon_F)}{1+\nu^2(\varepsilon_F)}\right],$$

$$\sigma_{xy}=e^2\left[-K_0^H(1+S_{\mathrm{p}})-K_0^{\perp}\frac{\Pi^*}{1-\Pi^*}\frac{\nu(\varepsilon_F)}{1+\nu^2(\varepsilon_F)}\right] \tag{14}$$

and the components of the tensor β_{ij} in terms of which the transport coefficients of interest to us can be expressed:

$$\beta_{xx}=\frac{e}{T}\left\{K_1^{\perp}+\frac{4}{3}k_0T\Pi\left[K_0^{\perp}(1+S_{\mathrm{p}})-K_0^H\frac{\Pi^*}{1-\Pi^*}\frac{\nu(\varepsilon_F)}{1+\nu^2(\varepsilon_F)}\right]\right\},$$

$$\beta_{xy}=\frac{e}{T}\left\{-K_1^H(1+S_p)-\frac{4}{3}k_0T\Pi\left[K_0^H(1+S_p)+K_0^\perp\frac{\Pi^*}{1-\Pi^*}\frac{\nu(\varepsilon_F)}{1+\nu^2(\varepsilon_F)}\right]\right\}. \quad (15)$$

The quantity S_p appearing in Eqs. (14) and (15) can be calculated at the Fermi surface for $k=k_F$, and

$$\left|\begin{matrix}K_r^\perp\\ K_r^H\end{matrix}\right|=\frac{(2m)^{3/2}}{3\pi^2\hbar^3m_0}\int_0^\infty d\varepsilon\left(\frac{\partial f_0}{\partial\varepsilon}\right)\varepsilon^{3/2}\tau(\varepsilon)(\varepsilon-\varepsilon_F)^r\times\left|\begin{matrix}\dfrac{1}{1+[\omega_0\tau(\varepsilon)]^2}\\ \dfrac{\omega_0\tau(\varepsilon)}{1+[\omega_0\tau(\varepsilon)]^2}\end{matrix}\right|,\quad r=0,1. \quad (16)$$

3. CALCULATION OF THE THERMOELECTRIC POWER

We shall use the above-obtained expressions to analyze the temperature and magnetic-field dependences of the thermoelectric power in the compounds HgSe and HgFeSe. Assuming the heat flux to be directed along the x axis, we write the expression for the differential thermoelectric power in a magnetic field

$$\alpha_{xx}=\frac{\sigma_{xx}\beta_{xx}+\sigma_{xy}\beta_{xy}}{\sigma_{xx}^2+\sigma_{yy}^2}. \quad (17)$$

Since under the experimental conditions of Refs. 3 and 4 the electron gas is strongly degenerate ($\varepsilon_F\gg k_0T$), we represent the thermoelectric power, after calculating the integrals $K_0^{H,\perp}$ and $K_1^{H,\perp}$, as $\alpha_{xx}=\alpha_{xx}^d+\alpha_{xx}^u$, where α_{xx}^d is the diffusion part of the thermoelectric power

$$\alpha_{xx}^d=-\frac{k_0}{e}\frac{\pi^2}{3}\frac{k_0T}{\varepsilon_F}\times\frac{\left[\frac{3}{2}(1+\nu_0^2)+D\right](1+S_p)+DS_p\nu_0^2(1-\Pi^*)^{-1}}{(1+\nu_0^2)[(1+S_p)^2+\nu^2S_p^2]}, \quad (18)$$

$$\nu_0=\omega_0\tau(\varepsilon_F),\quad D=\varepsilon_F\frac{\tau'(\varepsilon_F)}{\tau(\varepsilon_F)}. \quad (19)$$

The term α_{xx}^u determines the drag thermoelectric power and is different from zero in zeroth order in the parameter k_0T/ε_F:

$$\alpha_{xx}^u=-\frac{k_0}{e}\frac{4}{3}\Pi,\quad \Pi=\frac{1}{1+\Pi_1},\quad \Pi_1=\frac{2\pi(k_0T)^4}{E_0^2(ms^2)^2}. \quad (20)$$

Its value depends on the magnetic field and the nonphonon mechanismcs of electron momentum relaxation. As $T\to0$, the drag thermoelectric power becomes ''anomalously'' large

$$\alpha_{xx}^u=\frac{k_0}{e}\frac{4}{3},\quad T\to0. \quad (21)$$

This result is not unexpected and is due to the fact that at ultarlow temperatures the relaxation of phonons by the sample boundaries must be taken into account.

The expressions (18) and (20) completely determine the temperature and field dependences of the thermoelectric power in a classically strong magnetic field. As follows from the results (18)–(20), the quantity describing the longitudinal Nernst–Ettingshausen effect, in contrast to the case where the reciprocal drag of phonons and electrons is neglected, contains only one additional parameter Π^*, determined by Eqs. (8) and (9). For $S_p=0$ Eq. (18) agrees with the known result obtained in the absence of drag.[5] In the differential measurement method used in Ref. 3, the quantity α_{xx}^u is eliminated from the final result, so that in analyzing the field dependence in what follows we shall analyze only the contribution of the diffusion thermoelectric power α_{xx}^d (18).

4. NUMERICAL RESULTS

The expressions (18) and (20) make it possible to analyze the thermoelectric power as a function of the various parameters for HgSe and HgFeSe crystals. We start with the temperature dependence of the thermoelectric power in a zero magnetic field. For numerical analysis we employed the the effective mass $m=0.065m_0$ and crystal density $\rho=8$ g/cm^3. We assumed the deformation potential constant to be $E_0=10$ eV. This value follows from analysis of the temperature dependence of the conduction–electron mobility. According to Ref. 2, the mobility of itinerant carriers in HgSe and HgFeSe compounds is constant temperature to $T\simeq30-40$ K, which shows that the electron scattering by a system of charged centers predominates. The mobility decrease observed at higher temperatures is due to electron scattering by acoustic phonons. For this reason, to estimate E_0 we assumed $\tau_A=\tau_{ep}$ at $T=40$ K.

The computational results for the thermoelectric power of an HgSe crystal versus temperature are displayed in Fig. 2. Curve *1* corresponds to electron density 2×10^{18} cm^{-3}, and curve *2* was calculated for $n=4\times10^{18}$ cm^{-3}. It follows from the calculations that increasing the content of charged centers in HgFeSe crystals shifts the minimum of the thermoelectric power to lower temperatures, as happens in the experiment of Ref. 9. For comparison, the dependence $\alpha(T)$ from Ref. 10 is presented in the inset in Fig. 2. We note that the shift of the minimum of the thermoelectric power will be stronger if phonon scattering by defects is also taken into account.[9]

We shall now discuss the magnetic-field dependence of the dimensionless Nernst coefficient ε_x. Figure 3a shows the result of a numerical calculation of the dimensionless Nernst coefficient as a function of the magnetic field at low temperatures for an HgSe crystal. It was assumed that the itinerant charge carriers are scattered mainly by a system of randomly distributed impurity centers ($D=3/2$) (Ref. 5; curves *1–3*). The curves *4* and *5* correspond to higher temperatures, where electron scattering by acoustic phonons

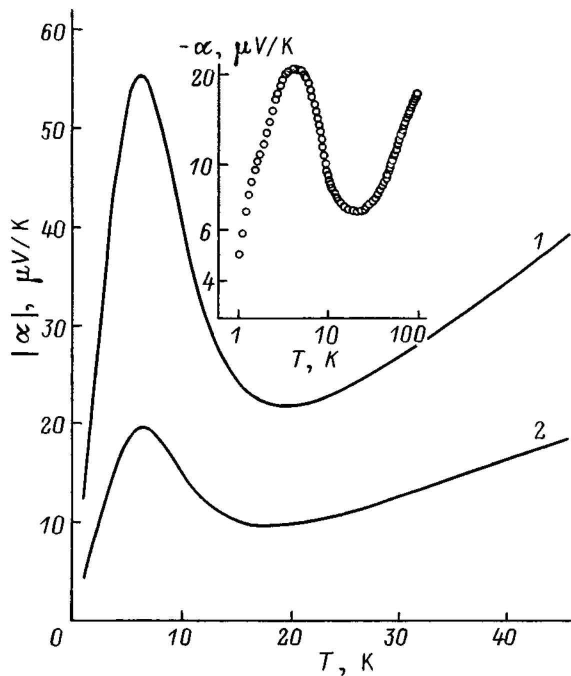

FIG. 2. Absolute thermoelectric power versus the temperature in HgFeSe with iron content N_{Fe}, 10^{18} cm^{-3}: *1* — 2, *2* — 4. Inset: Data of Ref. 10.

makes the main contribution to electron relaxation (for $T > 40$ K, $D = -1/2$) and the drag contribution is substantially suppressed. As one can see from the computational results presented, the magnetic-field dependence of $\varepsilon_x(H,T)$ is more complicated at low temperatures, where electron scattering by impurities dominates and the contribution of drag effects is also substantial. For intermediate magnetic fields ε_x shows a change in the sign of the effect and is a nonmonotonic function of the magnetic field. It is obvious that such an unusual dependence $\varepsilon_x(H,T)$ is due to the reciprocal drag of electrons and phonons. At high temperatures $T > 40$ K scattering by acoustic phonons dominates, and $\varepsilon_x(H) > 0$ and approaches saturation with increasing magnetic field.

We now turn to the analysis of $\varepsilon_x(H,T)$ in HgFeSe crystals (Fig. 1) for a sample with iron content $N_{Fe} = 1 \times 10^{19}$ cm^{-3}.[3] First, in the entire range of magnetic fields investigated $H = 0 - 40$ kOe and in the temperature range $T = 18 - 60$ K the effect has a positive sign. It is obvious that this behavior of the coefficient $\varepsilon_x(H,T)$ is due to the presence of strong Coulomb correlations in the system of donors Fe(2+).[2,9] Comparing the temperature dependence of the mobility in compounds HgFeSe with various iron atom contents shows[2] that for a high iron content the energy dependence of the relaxation time at low temperatures becomes closer to that occurring for electron scattering by acoustic phonons. This is why the sign of the longitudinal Nernst–Ettingshausen effect becomes positive even at $T > 15$ K, while in HgSe crystals the change in the sign (from negative to positive) occurs at $T \simeq 30$ K.[9] On account of these circumstances the sign of the effect $\varepsilon_x(H,T)$ is positive in the experiment, and its behavior as a function of the temperature reflects the character of the evolution of the impurity system as a result of a decrease in the degree of correlation in the

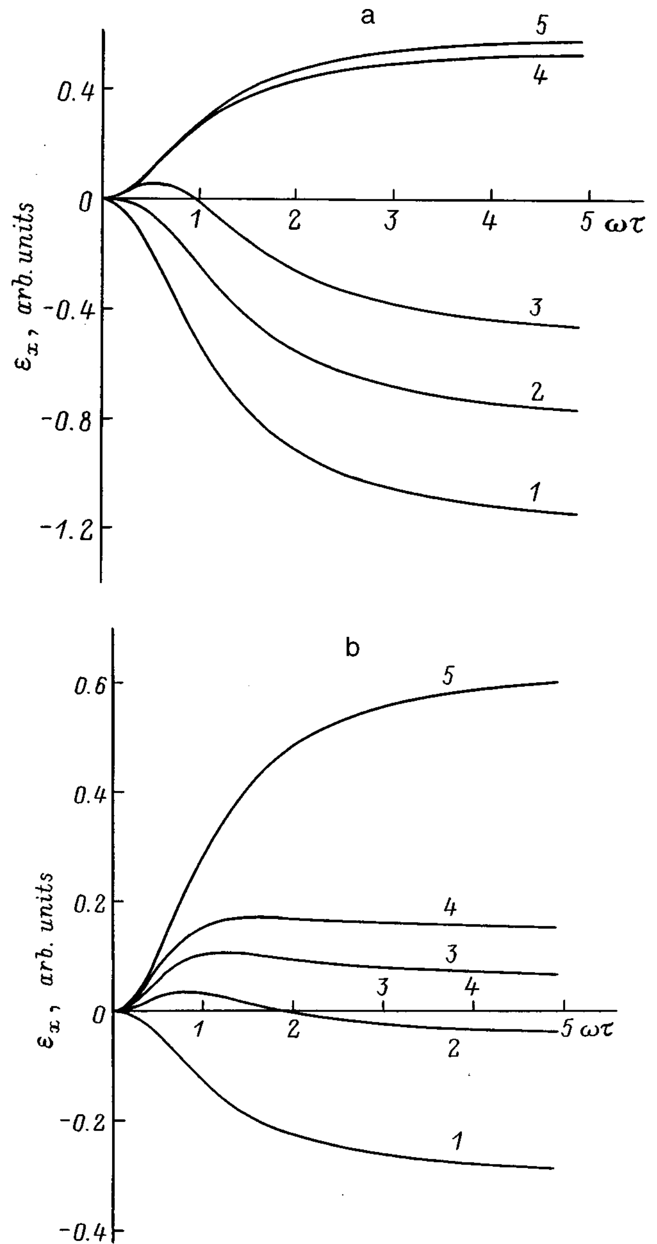

FIG. 3. Computed dimensionless field of the longitudinal Nernst–Ettingshausen effect versus the magnetic field for samples: a — HgSe (the curves *1–3* were calculated for $D = 3/2$, and the curves *4*, *5* were calculated for $D = -1/2$), temperature T, K: *1* — 5, *2* — 35, *3* — 20, *4* – 65, *5* — 50. b — HgFeSe ($D = 1/2$), temperature T, K: *1* — 5, *2* — 35, *3* — 15, *4* — 25, *5* — 45.

impurity system and a decrease in the role of the drag effect with increasing temperature. The coefficient $\varepsilon_x(H,T)$ can be found in explicit form using the computational results for the relaxation time for a strongly correlated impurity system.[2] However, the unusual behavior of $\varepsilon_x(H,T)$ can be illustrated more simply. The computational results for the dimensionless Nernst coefficient for $D = 1/2$ are displayed in Fig. 3b. This value of D reflects an average energy dependence of the relaxation time, falling between the impurity and phonon dependences. As one can see from the curves presented, the coefficient $\varepsilon_x(H,T)$ determined in this manner is very close to that observed experimentally. This is definitely a confirmation of the fact that the reciprocal drag of electrons and

phonons together with electron scattering by a system of charged donors are responsible for the ''anomalous'' behavior of the thermoelectric coefficients in the compounds investigated.

We now consider the anomalous dependence $\alpha(N_{\mathrm{Fe}})$ at low temperatures ($T \simeq 10-20$ K) in a zero magnetic field.[4] The contribution of the drag effect to the thermoelectric power $\alpha(T)$ is predominant in this temperature range.

We anticipate the calculation with two remarks. In the first place, the density of itinerant carriers in HgSeFe crystals is determined by the iron atom content in the sample. It increases linearly with the content of iron atoms in HgFeSe, right up to density $N_{\mathrm{Fe}} \simeq 4.5 \times 10^{18}$ cm^{-3}. As the iron content in the sample increases further, the density of itinerant charge carriers and therefore the density of charged centers Fe(3+) remains constant in a quite wide range.[1] This is due to stabilization of the Fermi level at the iron donor level, located in the conduction band at energy $E_d = 210$ meV. Only the density of neutral iron atoms Fe(2+) increases in this case. In the second place, according to the correlation model[2] electron scattering by charged ions Fe(3+) is suppressed when $N_{\mathrm{Fe}(3+)} \gg N_{\mathrm{Fe}(2+)}$. A mobility increase is observed experimentally with increasing iron content in the density range $N_{\mathrm{Fe}} \ll 2 \times 10^{19}$ cm^{-3}, and the mobility decreases as the iron density increases further.

On this basis we shall now consider the dependence $\alpha(N_{\mathrm{Fe}})$.[4] The decrease of the thermoelectric power ($\alpha_{xx} \sim 1/\varepsilon_F$) with increasing content of iron substitution impurity simply reflects the fact that the Fermi energy $\varepsilon_F \sim (n = N_{\mathrm{Fe}(3+)})^{2/3}$. It is obvious that such a dependence of the thermoelectric power will remain until the Fermi level is pinned at the donor level of iron. As the iron content in HgFeSe crystals increases further, in the standard theory and neglecting other phonon scattering mechanisms (for example, phonon scattering by defects) a plateau should be observed in the curve of the thermoelectric power versus the impurity content. However, the reciprocal drag of electrons and phonons renormalizes the diffusion contribution to the thermoelectric power (an additional dependence on the electron scattering mechanism $S_F(0)$ appears). Since the main source of electron scattering at low temperature is scattering by impurity centers, and it is appreciably suppressed by Coulomb correlations, which are present in the impurity system at high iron atom density,[2] this is the circumstance that leads to a nonmonotonic variation of the thermoelectric power in this concentration range. It is obvious that the nonmonotonicity appearing in $\alpha(N_{\mathrm{Fe}})$ is similar in nature to the nonmonotonicity arising in the investigation of mobility in HgFeSe crystals. As the iron atom density increases further, the decrease of the thermoelectric power, just as the mobility, is due to the predominant contribution to scattering of electrons by the alloy potential[2] and phonons by defects.[9]

In summary, the anomaly in the concentration dependence of the thermoelectric power $\alpha_{xx}(N_{\mathrm{Fe}})$, just as the nonmonotonic dependence of the mobility on substitution impurity content in HgFeSe crystals, simply reflects the character of electron scattering in these compounds, which is due to the appearance of strong Coulomb correlations in the impurity system. The introduction of additional suppression of scattering by phonons, which was studied in Ref. 4, to describe this effect is superfluous.

5. CONCLUSIONS

The unusual experimentally observed dependences of the thermoelectric and thermomagnetic coefficients for HgSe and HgFeSe crystals with different iron content in the classical range of magnetic field intensity at low temperatures have been explained qualitatively and quantitatively. It was shown that these dependences are due to scattering of electrons by spatially correlated charged donors Fe(3+) at low temperatures and the reciprocal drag of electrons and phonons, which plays a large role in semiconductors with a high density of itinerant charge carriers. It would be interesting to investigate on the basis of the model considered above the effect of the reciprocal drag in these compounds on other transport coefficients.

This work was supported by INTAS (Grant 93-3657).

[1] I. G. Kuleev, I. I. Lyapilin, A. T. Lonchakov, and I. M. Tsidil'kovskiĭ, Zh. Éksp. Teor. Fiz. **103**, 1447 (1994) [JETP **76**, 707 (1994)].

[2] I. G. Kuleev, I. I. Lyapilin, and I. M. Tsidil'kovskiĭ, Zh. Éksp. Teor. Fiz. **102**, 1652 (1992) [Sov. Phys. JETP **75**, 8983 (1992)].

[3] I. G. Kuleev, I. I. Lyapilin, A. T. Lonchakov, and I. M. Tsidil'kovskiĭ, Zh. Éksp. Teor. Fiz. **106**, 1205 (1994) [JETP **79**, 653 (1994)].

[4] I. G. Kuleev, A. T. Lonchakov, I. Yu. Arapova, and G. I. Kuleev, Zh. Éksp. Teor. Fiz. **114**, 191 (1998) [JETP **87**, 106 (1998)].

[5] B. M. Askerov, *Electronic Phenomena in Semiconductors* (Nauka, Moscow, 1985).

[6] J. Appel, Z. Naturforsch. A **13**, 386 (1957).

[7] J. E. Parrot, Proc. Phys. Soc. London, Sect. B **70**, 590 (1957).

[8] L. É. Gurevich and I. Ya. Korenblit, Fiz. Tverd. Tela (Leningrad) **6**, 856 (1964) [Sov. Phys. Solid State **6**, 661 (1964)].

[9] I. G. Kuleev, I. I. Lyapilin, A. T. Lonchakov, and I. N. Tsidil'kovskiĭ, Fiz. Tekh. Poluprovod. **28**, 937 (1994) [Semiconductors **28**, 544 (1994)].

[10] B. Tieke, R. Fletcher, J. C. Maan, W. Dobrowolski, A. Mycielski, and A. Wittlin, Phys. Rev. B **54**, 10 565 (1996).

Translated by M. E. Alferieff

SEMICONDUCTOR STRUCTURES, INTERFACES AND SURFACES

Scanning tunneling microscopy investigation of the microtopography of SiO_2 and Si surfaces at the Si/SiO_2 interface in SIMOX structures

D. V. Vyalykh and S. I. Fedoseenko

Scientific-Research Institute of Physics, 198904 Petrodvorets, Russia
(Submitted November 20, 1998; accepted for publication December 23, 1998)
Fiz. Tekh. Poluprovodn. **33**, 708–711 (June 1999)

The microtopography of silicon and silicon oxide surfaces in SIMOX structures is investigated by scanning tunneling microscopy. A method of using scanning tunneling microscopy to study Si/SiO_2 interfacial roughness is developed for this purpose. It is shown that the relief of the silicon surface in SIMOX structures is smoother than that of the oxide surface. The observed Si/SiO_2 interfacial roughness is due to oxygen ion implantation in the silicon single crystal. The roughness of the SiO_2 and Si surfaces at the Si/SiO_2 interface is compared for the standard and high-temperature oxidation of the silicon single crystal. © *1999 American Institute of Physics.* [S1063-7826(99)01706-8]

One way to increase the speed of semiconductor devices is to decrease the thickness of the insulator in metal–oxide–semiconductor (MOS) structures. In so doing it is especially important to monitor the structural perfection of the semiconductor/insulator interface and to know the nature and properties of various defects (electron and hole trapping centers, and so on). In recent years a great deal of attention has been devoted to silicon-on-insulator (SOI) structures,[1] which are promising for radiation-resistant semiconductor devices, and possess high operating speeds. The large class of SOI structures includes SIMOX (Separation by IMplantation of OXygen) layered systems, obtained in a complicated technological process, a result of which is that a buried-oxide layer, the so-called BOX layer, is formed in the silicon substrate. It should be noted that the structure and electrophysical properties of the buried SiO_2 layer[2,3] are substantially different from those of silicon oxide obtained by thermal oxidation of a silicon substrate.

As photoinjection investigations of SIMOX structures show,[4] deep and shallow electron traps are present in the buried oxide layer. Such traps are not observed in thermal oxide. They are due to silicon clusters in the buried-oxide layer in the immediate vicinity of the Si/SiO_2 interface. One model describing Si/SiO_2 interfacial roughness supposes[4,5] that the silicon clusters are several nanometers in size. The density and sizes of these clusters largely depend on the oxygen ion implantation and high-temperature annealing processes. The clusters strongly influence the structural perfection of the interface and can be detected by structure-sensitive methods. In the present work we have developed a method for using scanning tunneling microscopy (STM) to investigate the sizes of the irregularities of the buried silicon oxide and silicon surfaces at the Si/SiO_2 interface in SIMOX structures.

1. EXPERIMENT

Figure 1 shows diagrams of the SIMOX, WITNESS, and THERMAL OX samples investigated in the present work. The arrows show the surfaces studied. The SIMOX structure shown in Fig. 1a was obtained by implanting oxygen ions in a silicon substrate, resulting in the formation of a buried silicon oxide layer with a thin layer of amorphous silicon on top.

Our problem is to investigate the roughness of single-crystal Si/buried-SiO_2 and buried-SiO_2/amorphous-Si interfaces. Since the STM method is a method of direct probing of a surface, the amorphized-Si layer on top must be removed in order to investigate the roughness of the buried SiO_2 surface. To obtain information about the structure of the single-crystal Si/buried-SiO_2 interface, the amorphized Si layer and the buried SiO_2 layer both must be removed. Dry etching (DRY series of samples) and wet etching (WET series of samples) methods were used to remove the top layer of amorphized silicon. Either method can be expected to change the structure of the buried SiO_2 surface and even influence the morphology of the single-crystal Si/buried-SiO_2 interface. In the present work we endeavored to com-

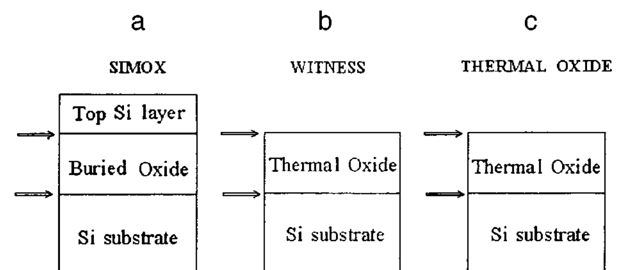

FIG. 1. Diagram of SIMOX (a), WITNESS (the SiO_2 layer was grown at $T = 1325$ °C) (b), and THERMAL OXIDE (the SiO_2 layer was grown at $T = 1100$ °C) (c) structures.

pare the etch results obtained with these two methods. We used the standard method of etching an oxide in a 10% solution of hydrofluoric acid to gain access to the silicon surface.

The STM method requires a uniform conducting surface. For this reason, a 15 nm thick gold layer was deposited thermally on the surface of the experimental samples. Special experiments showed that the deposition of gold on the silicon and silicon oxide surfaces does not change the structure of the surface roughness by more than 1 nm.

In the present work an STM (built in the Laboratory of Physical Electronics, Department of Electrical Engineering, Scientific and Research Institute, St. Petersburg State University, on the basis of PKR-6 piezoelectric ceramic) which permits investigating a conducting surface in air was used to study the microtopography of the silicon and silicon oxide surfaces. The instrument was calibrated using a diffraction grating (2400 lines/mm), highly oriented pyrolytic graphite, and a 22 nm high silicon step. The resolution of the scanning tunneling microscope for these investigations was 0.1 nm along the normal to the surface and 1 nm in a lateral direction.

A program for mathematical analysis of the results and for calculating the average surface roughness was developed to obtain the quantitative characteristics of the surfaces.

In the experiment we used commercially available SIMOX samples. The technical process for preparing the SIMOX samples consisted in single implantation of ~200 keV oxygen ions (series C samples) with dose $\sim 1.8\times 10^{18}$ cm^{-2} in a silicon single crystal at $T=600\,^{\circ}$C, followed by high-temperature annealing at $T=1325\,^{\circ}$C in an Ar + 1%O_2 atmosphere for 5 h. A uniform ~400 nm thick buried silicon oxide layer is formed in the silicon single crystal. A ~200 nm thick amorphized silicon layer remains on top of the buried oxide layer.[2,5] To determine how high-temperature annealing in an oxygen atmosphere at $T=1325\,^{\circ}$C influences the structure of the Si/SiO_2 interface, we investigated the roughness of the silicon and ''thermal'' silicon oxide surfaces in the WITNESS structure (Fig. 1b). This structure was obained by oxidizing a pure silicon surface under the same conditions as the high-temperature anneal used to prepare the SIMOX structure, i.e. at $T=1325\,^{\circ}$C in Ar + 1%O_2 for 5 h. Investigations of the WITNESS structure yielded information about the effect of high-temperature annealing on the Si/SiO_2 interface. We also wanted to compare the roughness of the Si/SiO_2 interface in the SIMOX and THERMAL OX structures (Fig. 1c) obtained by the standard technology for thermal oxidation of single-crystal silicon at $T=1100\,^{\circ}$C. The oxide layer was ~90 nm thick in the WITNESS structure and ~400 nm thick in the THERMAL OX structure.

2. RESULTS

The typical surface microtopographies of some experimental samples are presented in Figs. 2–5. The figures show a three-dimensional image of a surface on a black-and-white scale (a lighter color corresponds to higher locations) with a distinguished direction as well as the surface profile along the direction distinguished by the line. The final estimates of the vertical and lateral sizes of the irregularities for silicon and silicon oxide in the SIMOX, WITNESS, and THERMAL OX structures are summarized in Table I.

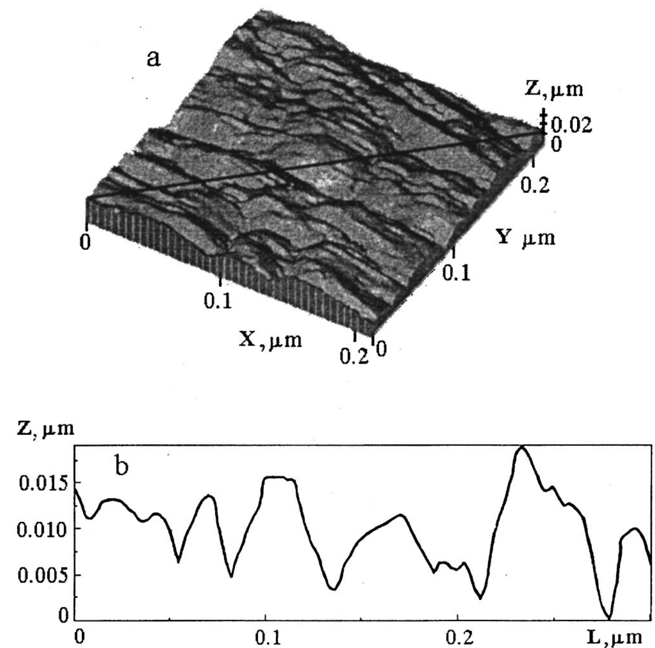

FIG. 2. a — Three-dimensional image of the silicon surface in a SIMOX structure from the ''C DRY'' series. The line marks the distinguished direction *L*. b — Surface profile along the distinguished direction *L*.

Figure 2 shows the microtopography of a silicon surface in the SIMOX structure in the ''C DRY'' series. The surface contains ~6 nm high roughness of ''irregular'' size. Figure 3 shows the surface microtopography of buried silicon oxide

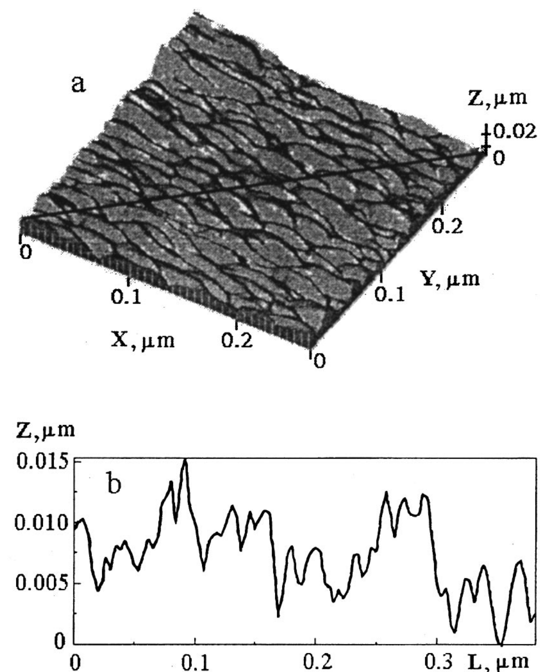

FIG. 3. a — Three-dimensional image of the silicon oxide surface in the SIMOX structure from the ''C DRY''series. The line marks the distinguished direction *L*. b — Surface profile along the distinguished direction *L*.

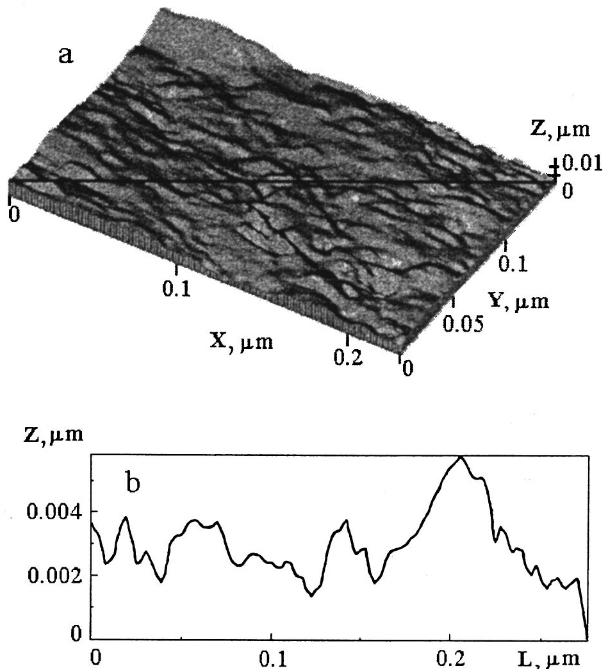

FIG. 4. a — Three-dimensional image of the silicon surface in the WITNESS structure. The line marks the distinguished direction *L*. b — Surface profile along the distinguished direction *L*.

in a ''C DRY'' series SIMOX structure. It is evident that the surface contains a large number of ''regular'' prolate irregularities with ~10 nm height differentials. The oxide surface is rougher than in preceding image of the silicon surface. Figure 4 shows an image of the microtopography of the silicon surface in the WITNESS sample. A small ~6 nm high

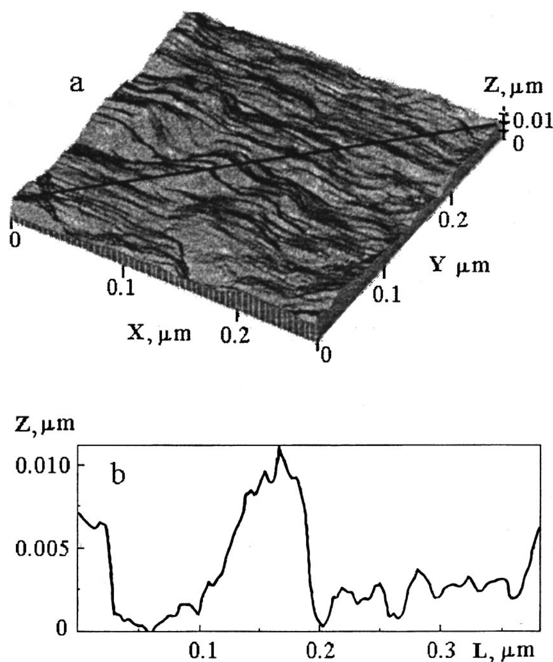

FIG. 5. a — Three-dimensional image of the silicon oxide surface in the WITNESS structure. The line marks the distinguished direction *L*. b — Surface profile along the distinguished direction *L*.

TABLE I. Average sizes of irregularities on the silicon and silicon oxide surfaces, nm.

Sample type	Si surface		SiO_2 surface	
	height	lateral size	height	lateral size
SIMOX ''C WET''	6.3	~40	16.2	~25
SIMOX ''C DRY''	5.1	~35	11.2	~25
WITNESS	3.7	~50	5.9	~35
THERMAL OX	5.2	~45	10.9	~30

and ~90 nm long protuberance can be seen in the upper right-hand corner. Small ~3 nm high irregularities with ~10 nm half-width can be seen. The height differentials are comparatively small, so that the surface is smoother than the surfaces mentioned earlier. Figure 5 shows an image of the silicon oxide surface in the WITNESS sample. The surface contains ~4 nm high irregularities with ~15 nm half-width. Several ~10 nm high ''humps'' with ~35 nm half-width can be seen against the general background.

On the basis of all obtained microtopographies of silicon and silicon oxide surfaces it can be stated that the silicon surface at the Si/buried-SiO_2 interface in the SIMOX structures is smoother than the buried silicon oxide surface, and the average roughness height on the silicon surface is approximately two times smaller for all experimental samples than that of the buried silicon oxide surface. We infer that the smoother relief of the silicon surface can indeed be due to the detachment of silicon clusters, which decreases the mechanical stress at the Si/buried-SiO_2 interface.

High-temperature annealing in an oxygen atmosphere is used in the production of SIMOX structures. It is obvious that annealing can have a very strong effect on the structure of the oxide surface and the Si/buried-SiO_2 interface: A large number of various irregularities can form. For this reason, modern technologies for fabricating semiconductor structures strive to use the lowest possible temperatures, since then the surface will be smoother. It is obvious that the smaller the heights and the larger the lateral sizes of the irregularities, the less subdivided the surface of the silicon layer will be. In our investigations we used a WITNESS sample to see whether or not high-temperature annealing at $T=1325\,^{\circ}\mathrm{C}$ in an oxygen atmosphere introduces additional defects in the structure of the silicon and silicon oxide surfaces. It is evident from Figs. 4 and 5 that the silicon and silicon oxide surfaces in WITNESS are smoother than in the SIMOX structures. Therefore the much larger irregularities that we observe in SIMOX cannot be attributed to high-temperature annealing. This is more likely due to the process of implanation of high-energy oxygen ions into the silicon single crystal.

It would be entirely logical to compare the interfacial roughness in SIMOX structures with the roughness of the sample obtained with standard oxidation of a silicon single crystal at $T=1100\,^{\circ}\mathrm{C}$. To this end the microtopography of a

THERMAL OX sample with a $\sim$400 nm thick oxide layer was investigated. It was shown (see Table I) that the roughness of the SIMOX structures is comparable in height to that of the THERMAL OX sample.

In summary, in the present work the microtopographies of silicon and silicon oxide surfaces in SIMOX structures and in structures obtained by thermal oxidation of a silicon single crystal at $T = 1325$ and $1100\,^{\circ}\mathrm{C}$ were investigated by scanning tunneling microscopy with 0.1 nm resolution in a direction normal to the surface and 1 nm resolution in the lateral direction. Summarizing the experiments performed, we can draw the following conclusions.

1. In SIMOX structures the geometric relief of the silicon surface at the Si/buried-SiO_2 interface is smoother than the surface relief of the buried silicon oxide. For all experimental samples the average roughnes height on the silicon surface is approximately half that on the buried-oxide surface. We infer that the smoother surface relief at the Si/SiO_2 interface is due to the detachment of silicon clusters, which decreases the mechanical stress on the Si/SiO_2 interface.

2. The roughness that we observe on the interface in SIMOX structures is due to the implantation of oxygen ions in the silicon single crystal.

3. In the standard technology of thermal oxidation of silicon at $T = 1100\,^{\circ}\mathrm{C}$, roughness with height comparable to that of the interfacial roughness in SIMOX structures is present on the Si/SiO_2 interface.

We thank Professor V. K. Adamchuk for a discussion of the results obtained in this work.

This work was performed as part of the State Science and Technology Program ''Promising Technologies and Devices for Micro- and Nanoelectronics'' (Project No. 039.04.223/57/2-3/1-95) and Grant No. 95-0-7.1-160 from the Competitive Center for Fundamental Natural Sciences at St. Petersburg State University.

[1] J. P. Colinge, *Silicon-on-Insulator Technology: Materials to VLSI* (Kluwer Academic Publisers, Notwell, MA, 1991).

[2] A. G. Revesz, G. A. Brown, and H. L. Hughes, J. Electrochem. Soc. **140**, 3222 (1993).

[3] V. V. Afanas'ev, A. G. Revesz, G. A. Brown, and H. L. Hughes, J. Electrochem. Soc. **141**, 2801 (1994).

[4] S. I. Fedoseenko, V. K. Adamchuk, and V. V. Afanas'ev, J. Microelectronic Engin. **22**, 367 (1993).

[5] S. W. Crowder, P. B. Griffin, and J. D. Plummer, Appl. Phys. Lett. **65**, 1698 (1994).

Translated by M. E. Alferieff

Reconstruction and electron states of a Ga_2Se_3–GaAs heterointerface

B. L. Agapov, N. N. Bezryadin, G. I. Kotov, and M. P. Sumets

Voronezh State Technological Academy, 394000 Voronezh, Russia

I. N. Arsent'ev

A. F. Ioffe Physicotechnical Institute, Russian Academy of Sciences, 194021 St. Petersburg, Russia
(Submitted September 14, 1998; accepted for publication October 1, 1998)
Fiz. Tekh. Poluprovodn. **33**, 712–715 (June 1999)

It is established by electron microscopy and electron diffraction analysis that the formation of $Ga_2Se_3(110)$ layers on GaAs(100) and (111) surfaces during heat treatment of the latter in selenium vapor is accompanied by the formation of transition regions with crystallographic orientations [310] and $[\bar{2}\bar{1}\bar{1}]$, respectively. It follows from an investigation of the spectrum of surface electron states in the resulting heterostructures that a reduction in the density of surface electron states is achieved only after selenium vapor treatment in a narrow interval of treatment durations (from 5 min to 30 min under the conditions established in the present study). All the results are discussed on the basis of concepts involving reconstruction of the gallium arsenide surface during chalcogen treatment. © *1999 American Institute of Physics.* [S1063-7826(99)01806-2]

INTRODUCTION

The high density of surface electron states (SES) on GaAs places a number of limitations on the feasibility of many potential devices utilizing gallium arsenide, especially devices having a metal-insulator-semiconductor (MIS) configuration and Schottky diodes.[1,2] Various techniques for treating the surface of GaAs, including the application of selenium vapor,[3,4] are currently used to lower the density of SES. The mechanism underlying the reduction of the density of SES through the interaction of selenium with the surface of GaAs has yet to be explained. In this paper we report the first-time application of an N-200 transmission electron microscope (microdiffraction and microimaging) to investigate the surface region of GaAs(111) before and after short-term treatment with selenium vapor and to investigate a GaAs–Ga_2Se_3 heterointerface formed by the substitution of selenium for arsenic in the GaAs lattice, after long-term (~ 30 min) treatment of the GaAs(100) and GaAs(111) substrates in selenium vapor. The density of SES was monitored by deep-level transient spectroscopy (DLTS).[4]

EXPERIMENTAL

A. Electron Microscope Analysis of a Ga_2Se_3–GaAs Interface

The *n*-type GaAs(100) and GaAs(111) substrates with doping levels $\sim 2.6\times 10^{16}\,cm^{-3}$ were subjected to chemodynamic polishing in a solution of $H_2SO_4:H_2O_2:[1]\ H_2O=[1]5:1:1$, and then the residual oxide was removed in a solution of $HCl:H_2O=[1]1:10$. After washing in deionized water and drying, the substrates were treated in selenium vapor in a quasiclosed volume with "hot walls." The temperature of the substrates was chosen in the interval 410–720 K, and the partial pressure of the selenium vapor was in the interval 0.133–1.33 Pa. In addition to short-term selenium vapor treatments similar to those used in Refs. 3 and 4, which lead to Fermi level detachment, in our study we used long-term treatments at elevated substrate temperatures. Under these conditions, based on the results of Ref. 5, chalcogenide Ga_2Se_3 layers of thickness $\sim 20-100$ nm should form on the surface. We note that under the conditions of processes similar to those used in Refs. 3 and 4 the layers formed on the surface are tunnel-transparent. The thickness was monitored by means of an LÉF-3 ellipsometer and from rf capacitance measurements. To thin the samples for diffraction investigations in the transmission electron microscope, the back side of the sample was subjected to two-stage processing. First, a spherical depression with a radius of curvature equal to 7.5 mm was formed by abrasive grinding, and then a hole of controlled diameter was formed all the way through the sample in the center of the depression by sputtering with 5-keV argon ions.

As in Ref. 4, three systems of reflections associated with different planes of the reciprocal fcc lattice were present on the electron diffraction patterns in short-term treatment of the GaAs(100) substrate. One system was associated with the (100) plane, consistent with the crystallographic orientation of the GaAs substrate; the second system was associated with the (110) plane, and the third system with the (310) plane (Fig. 1a). A similar situation is observed for GaAs(111) substrates: the microdiffraction patterns exhibit systems of reflections which correspond to the (111) (substrate), $(\bar{2}\bar{1}\bar{1})$, and (110) planes (Fig. 1b). For recording of the electron diffraction patterns the instrument constant was adjusted to achieve the best match of the interplanar distances calculated from the electron diffraction pattern for the reflections corresponding to gallium arsenide (100) or (111) with tabulated values.[6] The identification of the reflection

 © 1999 American Institute of Physics

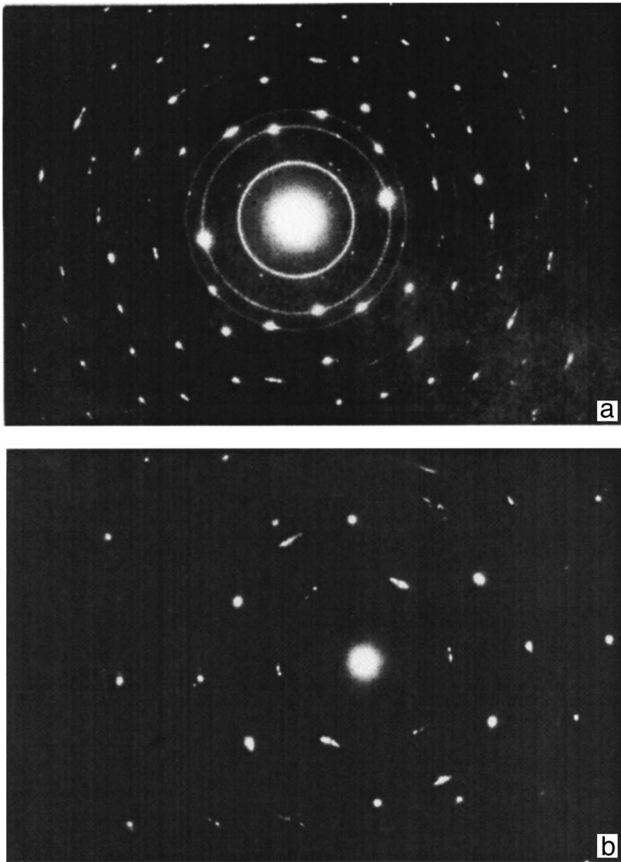

FIG. 1. Typical electron diffraction patterns of the surface region of GaAs(100) (a) and GaAs(111) (b) after short-term (5 min) treatment in selenium vapor.

systems corresponding to the (310) and (110) planes on a GaAs(100) substrate or to the (211) and (110) planes on a GaAs(111) substrate and to another phase (Ga_2Se_3 or a solid solution in the system Ga_2Se_3–GaAs) was established, as in Ref. 4, from a series of reflection intensities (which was compared with the well-known[6] series for Ga_2Se_3 and GaAs) and from a dark-field image of the surface region of the sample.

On diffraction patterns obtained for the surface region of GaAs(100) after short-term selenium vapor treatment of the gallium arsenide the [001] direction is common to the systems of reflections corresponding to the (100) plane of GaAs and the (310) and (110) planes of the phase with Ga_2Se_3. A more complicated situation is observed for GaAs(111): The $[1\bar{1}\bar{0}]$ directions coincide for the (111) plane of GaAs and the (110) plane of Ga_2Se_3. The $[0\bar{1}\bar{1}]$ directions coincide for the (111) plane of GaAs and the $(\bar{2}\bar{1}\bar{1})$ plane of Ga_2Se_3, and the $[\bar{1}\bar{1}\bar{1}]$ directions coincide for the $(\bar{2}\bar{1}\bar{1})$ and (110) planes of Ga_2Se_3.

The same systems of reflections associated with three crystallographic orientations as for structures subjected to short-term treatment emerge in heterostructures with thick Ga_2Se_3 layers ($d > 100$ nm) (Fig. 2). In contrast with structures having thin layers on GaAs(100) substrates, where all three planes are rigidly tied to the [001] direction, disorder is encountered in structures with thick Ga_2Se_3 layers. The

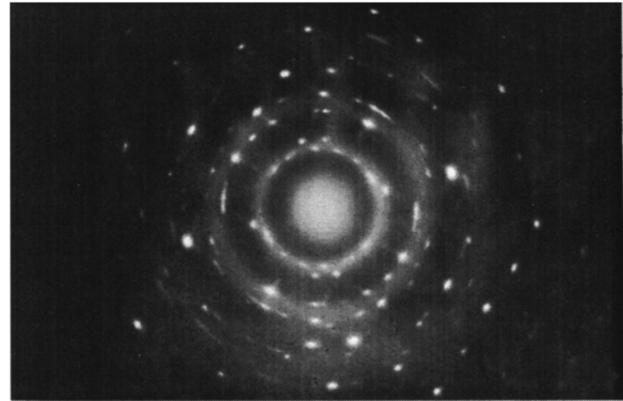

FIG. 2. Typical electron diffraction pattern of a Ga_2Se_3–GaAs(100) heterointerface formed during the long-term (30 min) treatment of a GaAs(100) substrate in selenium vapor.

[001] directions of the (110) plane of Ga_2Se_3 and the (100) plane of GaAs are disoriented by an angle $\sim 8-20°$, depending on the point of observation of microdiffraction. This also gives rise to the appearance of an additional system of reflections which corresponds to the (111) plane and which has the crystallographic [110] direction in common with the (110) plane of Ga_2Se_3. The GaAs (100) and Ga_2Se_3 (310) planes still have the [001] direction in common in this case.

B. Parameters of the Surface Electron States of a Ga_2Se_3–GaAs Interface

Using the method of current-voltage (*I-V*) curves and DLTS, Sysoev et al.[3,4] have shown that the short-term treatment of a GaAs(100) surface in vapors of various chalcogens (selenium, sulfur, or tellurium) lowers the density of SES. The energy positions of the SES approach the bottom of the conduction band as the treatment time is increased.[4] In light of this effect, the authors[4] have been able to attribute the decrease in the density of surface electron states to the gradual transition of these states into the conduction band as the reconstruction of the GaAs(100) surface is completed.

In the present study we have investigated the SES parameters by means of the *I-V* curves and DLTS for GaAs(111) substrates after short-term treatments and for GaAs(100) substrates with thick Ga_2Se_3 layers (with thicknesses exceeding 5 nm after long-term treatment in selenium vapor without raising the substrate temperature). Samples of the Schottky diode type were prepared for measurement of the *I-V* curves and DLTS spectra by spraying aluminum through a mask. The height of the Schottky barrier (φ_b) in Al–GaAs(111) structures formed without pretreatment of the substrates in selenium vapor was determined from the *I-V* curves and had values ~ 0.75 eV in the first case and ~ 0.5 eV in the second case. Consequently, as in the case of GaAs(100) substrates,[3,4] short-term selenium vapor treatments (~ 5 min) of GaAs(111) substrates also lead to Fermi level detachment at the surface, which corresponds to a shift of its position by ~ 0.25 eV during treatment. We note that the theoretical value of φ_b calculated for an Al–GaAs con-

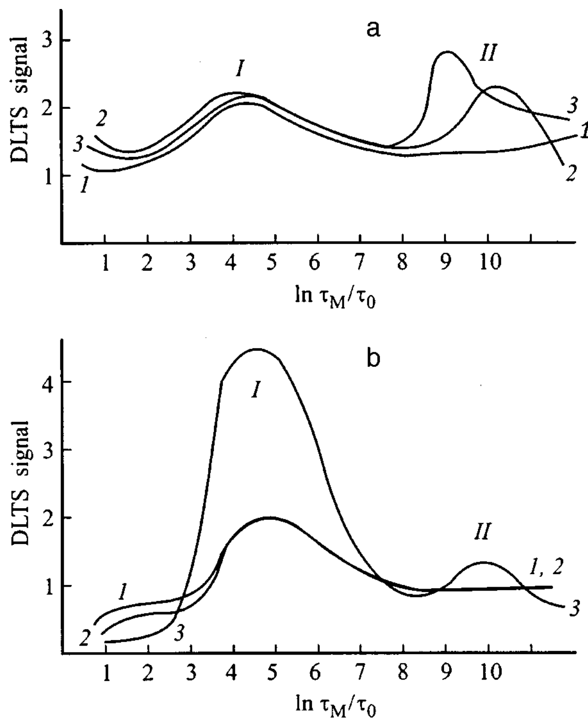

FIG. 3. Typical DLTS spectra of heterostructures with an Al–GaAs Schottky barrier. (a) Without pretreatment in selenium vapor: (*1*) $U_i=0$; (*2*) $U_i=+1$ V; (*3*) $U_i=+2$ V. (b) After selenium vapor treatment: (*1*) 5 min at $U_i=+1$ V; (*2*) 5 min at $U_i=0$; (*3*) 30 min at $U_i=+1$ V.

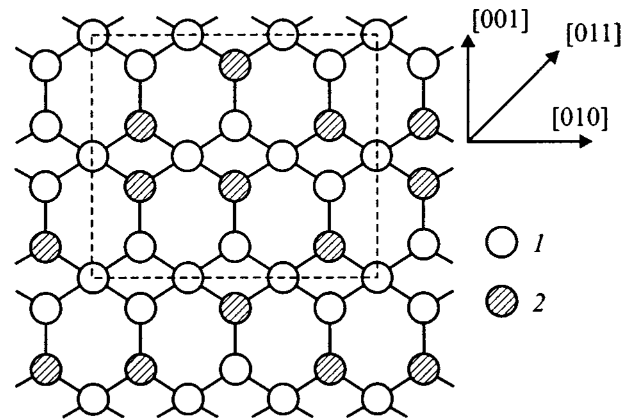

FIG. 4. Type 3×2 reconstructed $Ga_2Se_3(110)$ surface: (*1*) selenium atoms; (*2*) gallium atoms.

tact ($n\sim10^{16}\,cm^{-3}$, according to the Schottky-Mott law, is ~0.52 eV.

The behavior of the SES in structures obtained by the short-term treatment of GaAs(111) is similar to that observed in structures based on GaAs(100) (Fig. 3). The dependence of the amplitude of peak II in Fig. 3a on the amplitude of the injecting pulse indicates its identification with SES.[4] The first maximum corresponds to a deep level in GaAs with energy ~0.6 eV and is usually associated with a complex that involves gallium at an arsenic site.[7] Figure 3 shows the DLTS spectrum at room temperature. The energy positions of the centers are estimated from measurements of the spectra in the temperature interval $90-350$ K (Ref. 4).

As the treatment time is increased, beginning with durations ~30 min, which result in layer thickness >5 nm, the DLTS spectra again acquire a maximum corresponding to SES (Fig. 3b, curve *3*). The energy positions of these SES are fully consistent with those determined in Ref. 4 for the as-prepared (without short-term chalcogen vapor treatment) gallium arsenide surface (Fig. 3a). The deep-level concentration in the gallium arsenide also increases in this case (Fig. 3b), curves *1* and *3*). A further increase in the treatment time or in the substrate temperature causes the thickness of the Ga_2Se_3 layer to increase and is accompanied by an increase in the SES and the deep-level maxima.

DISCUSSION OF THE RESULTS

Treatment of the surface of gallium arsenide in selenium vapor lowers the density of surface electron states in comparison with a natural oxide-coated surface, but only in a narrow range of treatment periods (from 5 min to 30 min under the conditions reported in Refs. 3 and 4). Electron diffraction patterns of the gallium arsenide surface after such treatments indicate mutual ordering of the GaAs (100) plane and the Ga_2Se_3 (310) and (110) planes with respect to the crystallographic [001] direction. Similar ordering also exists after short-term treatments of a GaAs(111) surface. The explanation submitted in Ref. 4 for the reduction of the density of SES after such treatments is based on geometrical matching of the Ga_2Se_3 (110) and GaAs (100) planes: Only after reconstruction of the GaAs(100) surface of the type $C(4\times4)$ is it possible for the severed bonds of the contacting surfaces to close (Fig. 4). As a result, the resultant $Ga_2Se_3(110)$ surface has a 3×2 unit cell (indicated by the dashed line). Characteristically, two-dimensional chains consisting of Se–Se dimers extend in the [011] direction. This result is consistent with the results of earlier investigations[8] of a GaAs(100) surface in a scanning tunneling microscope after selenium treatment. Two-dimensional chains running along the [001] direction are visible on the patterns. In the same paper the authors have observed a 2×3 GaAs(100) structure after selenium treatment of a GaAs(100) surface. The reflections occurring on the electron diffraction patterns from the (310) plane of GaAs(100) and the $(\bar{2}\bar{1}\bar{1})$ plane of GaAs(111) probably refer to surface zones formed during reconstruction of the as-prepared GaAs surface in the initial stages of its treatment in selenium vapor. This conjecture is supported, in particular, by the fact that the (310) plane is always rigidly tied to the [001] direction of the substrate, regardless of the duration of treatment. In the initial stages of treatment there is also a decrease in the activation energy of the surface electron states without any change in their density; this effect has been observed in Ref. 4. In our opinion, insufficient treatment time (less than 5 min) prevents surface reconstruction from going to completion, and the attendant passivating action is not observed. The restoration of the SES spectrum after long-term treatments (greater than 30 min) can also be explained on the basis of the same concepts: The emerging disorientation of the $Ga_2Se_3(110)$ layer

relative to the GaAs(100) substrate disrupts the reconstruction of the gallium arsenide surface after being brought into existence by the passivating action.

CONCLUSIONS

In summary, by means of electron microscopy and electron diffraction analysis we have established that during the heat treatment of GaAs(100) and (111) surfaces in selenium vapors a (110)-oriented Ga_2Se_3 layer is formed on them. The transition region between GaAs(100) and $Ga_2Se_3(110)$ is crystallographically oriented along (310), and the one between GaAs(111) and $Ga_2Se_3(110)$ is oriented along $(\bar{2}\bar{1}\bar{1})$. The attendant reconstruction of the surface creates a passivating action only in a narrow interval of treatment periods. A pseudomorphic $Ga_2Se_3(110)$ layer is formed in this interval of treatment periods, stabilizing the reconstructed state of the gallium arsenide surface.[4] For long durations (>30 min) the resulting disorientation, most likely associated with mismatch of the GaAs and Ga_2Se_3 lattice parameters, disrupts this reconstruction, and the spectrum of surface electronic states is restored.

[1] W. E. Spicer, I. Lindau, P. E. Gregory, C. M. Garner, and P. Pianetta, J. Vac. Sci. Technol. **13**, 780 (1976).
[2] P. Victorovitch, Rev. Phys. Appl. **25**, 895 (1990).
[3] B. I. Sysoev, N. N. Bezryadin, G. I. Kotov, and V. D. Strygin, Fiz. Tekh. Poluprovodn. **27**, 131 (1993) [Semiconductors **27**, 69 (1993)].
[4] B. I. Sysoev, N. N. Bezryadin, G. I. Kotov, B. L. Agapov, and V. D. Strygin, Fiz. Tekh. Poluprovodn. **29**, 24 (1995) [Semiconductors **29**, 12 (1995)].
[5] B. I. Sysoev, V. D. Strygin, E. I. Chursina, and G. I. Kotov, Izv. Akad. Nauk SSSR, Neorg. Mater. **27**, 1583 (1991).
[6] *ASTM Diffraction Data Card File 1957*, Card No. 14–450, 20–437.
[7] W. E. Spicer, I. Lindau, P. R. Sheath, and C. Y. Su, J. Vac. Sci. Technol. **17**, 1019 (1980).
[8] H. Shigekawa, H. Oigawa, and K. Miyake, Appl. Phys. Lett. **65**, 607 (1994).

Translated by James S. Wood

Sulfide passivation of GaAs power diodes

V. M. Botnaryuk, Yu. V. Zhilyaev, and E. V. Konenkova

A. F. Ioffe Physicotechnical Institute, Russian Academy of Sciences, 194021 St. Petersburg, Russia
(Submitted September 29, 1998; accepted for publication October 2, 1998)
Fiz. Tekh. Poluprovodn. **33**, 716–718 (June 1999)

The feasibility of reducing the leakage currents of GaAs power diodes by chemically treating their surfaces in solutions of $(NH_4)_2S$ in isopropanol is investigated. It is established that after chemical surface treatment the leakage current decreases more as the immersion time in the solution is increased (eightfold reduction) and also with an increase in the time of application of a reverse voltage $U_z = 400$ V (2.5-fold reduction). © *1999 American Institute of Physics.* [S1063-7826(99)01906-7]

1. The high density of surface states of GaAs induces rigid attachment of the surface Fermi level and a high surface recombination rate, resulting in the degradation of a number of device parameters.

In power diodes utilizing GaAs *p-n* structures the following expression for the total current through the biased diode is well known:[1]

$$I = j_{01}A[e^{qV/kT} - 1] + (j_{02B}A + j_{02P}P)[e^{qV/2kT} - 1], \quad (1)$$

where j_{01} and j_{02B} are the saturation current densities associated with recombination in the quasineutral region and in the space-charge region, respectively, A is the area of the *p-n* junction, j_{02P} is the current density associated with recombination on the surface of the *p-n* junction, and P is the perimeter of the *p-n* junction.

When a reverse bias is applied, the current in GaAs power diodes at room temperature is estimated from the surface leakages, which are largely related to the high density of surface states around the perimeter of the *p-n* junction.

One of the more promising methods for reducing the density of surface states of GaAs is passivation of the surface in sulfide-containing solutions. For example, the feasibility of decreasing the reverse currents has been reported for GaAs *p-n* diodes[1] and InGaAs/AlGaAs laser diodes[2] after passivation in aqueous sodium sulfide solutions. A new method for reducing the density of surface states more effectively than sulfide passivation in aqueous solutions has been developed in recent years — sulfide passivation in alcohol solutions,[3] which has been used successfully in reducing the level of catastrophic optical degradation of InGaAs/GaAlAs laser diodes by 50% (Ref. 4).

We have investigated the feasibility of reducing the leakage current of GaAs power diodes by the chemical treatment of their surfaces in solutions of $(NH_4)_2S$ in isopropyl alcohol (i-C_3H_7OH).

2. Gallium arsenide power diode structures were grown in an open Ga–H_2-$AsCl_3$ gas transport system in a single technological cycle at a source temperature of 820 °C and a substrate temperature of 730–750 °C. The substrates were GaAs wafers of thickness 400 μm with a density of $2 \times 10^{18}\,cm^{-3}$ disoriented 3–5° from the (100) plane toward (110) and with a density of dislocations $(0.5-1) \times 10^5\,cm^{-2}$. The base i-region of the pin structure (n^-), having a thickness up to $l = 60\,\mu$m, was grown without special doping with a carrier density of $(1-8)\times 10^{14}\,cm^{-3}$. A p^+ layer of thickness $l = 5-15\,\mu$m was grown with a carrier density of $(1-3)\times 10^{18}\,cm^{-3}$ by doping with zinc, which was injected through an auxiliary channel into the growth zone. Ohmic contacts were prepared by the chemical evaporation of nickel onto the n^- and p^+ sides of the structure (Fig. 1). The area of the *p-n* junction of the power diode was $S \approx 0.1\,cm^2$, and its perimeter was $p = 1.3$ cm.

The structures were immersed in a solution of $(NH_4)_2S$ in i-C_3H_7OH for 1–120 s at room temperature with illumination by a 200-W incandescent lamp, and then they were air-dried. Different ratios of the volume concentrations of $(NH_4)_2S$ + (i-C_3H_7OH) were used: 1:0 [pure $(NH_4)_2S$ solution], 1:10, 1:50, and 1:100.

3. The current-voltage (*I-V*) curves of the GaAs power diodes were measured before and after treatment in the sulfide-containing solutions (Fig. 2).

It follows from a comparison of the reverse branches of the *I-V* curves that:

● treatment both in pure $(NH_4)_2S$ and in a solution of $(NH_4)_2S$ in isopropyl alcohol reduces the leakage currents, the greatest reduction in the leakage currents (100-fold at $U = 400$ V) being attained in a $(NH_4)_2S$ + i-C_3H_7OH solution with a ratio of volume concentrations 1:10 (Fig. 2);

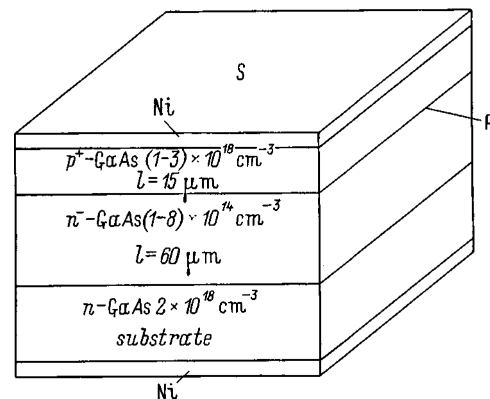

FIG. 1. Schematic view of the GaAs *p-n* structure.

 © 1999 American Institute of Physics

● the optimal treatment time for the GaAs power diodes is approximately 1 min, where in fact the leakage current decreases by one half after a 30-s treatment in a $(NH_4)_2S$ + i-C_3H_7OH solution and decreases eightfold after 1 min, but after longer keeping in the solution, approx 2 min, the decrease in the leakage current is insignificant (Fig. 3);

● the reduction of the leakage current depends on how long a reverse voltage of 400 V is subsequently applied to the GaAs diode: When the application time is increased at least to 15 min, the leakage currents of the diode (Fig. 4) decrease by more than one half.

We note that the *I-V* curves rerecorded after being kept for several days in air without an applied voltage scarcely differ from those recorded 15 min after the application of a reverse voltage.

4. The reduction of the leakage current of GaAs *p-n* structures is probably attributable to a change in the density of surface states through the formation of a sulfide passivating coating on the GaAs surface.

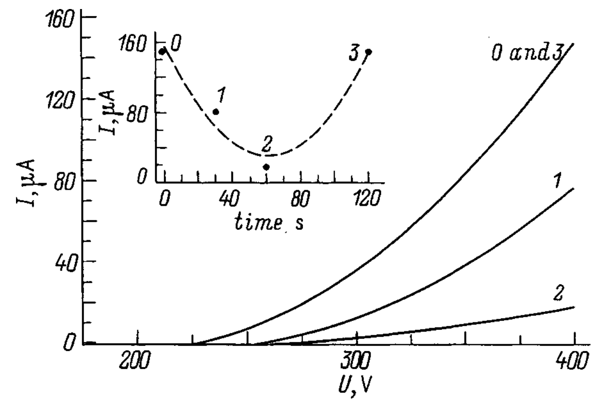

FIG. 3. Reverse branches of the *I-V* curves of GaAs power diodes untreated (*0*) and treated (*1, 2, 3*) in a $(NH_4)_2S$ + i-C_3H_7OH (1:50) solution for various treatment times: (*1*) 30 s; (*2*) 60 s; (*3*) 120 s. Inset: Dependence of the maximum diode leakage current with a 400-V reverse bias on the treatment time.

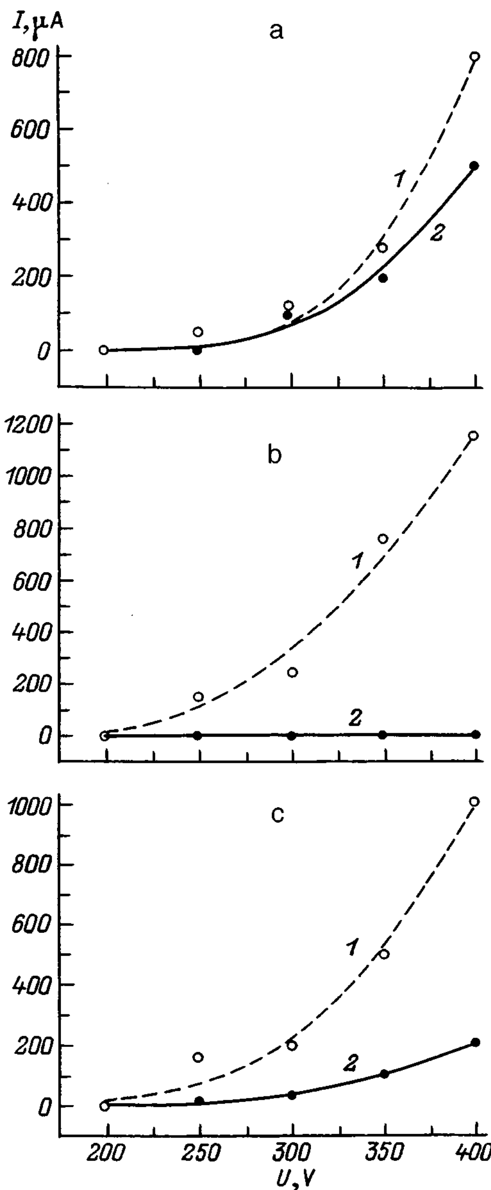

FIG. 2. Reverse branches of the *I-V* curves of GaAs power diodes untreated (*1*) and treated (*2*) in three solutions of $(NH_4)_2S$ in isopropyl alcohol at various concentrations: (a) pure ammonium sulfide solution; (b) 1:10; (c) 1:1000.

The preexponential factor for the recombination current in Eq. (1),

$$I_{02}=A_{j02B}+P_{j02P}, \tag{2}$$

contains a current component associated with the surface. The reduction of the leakage current can be assumed to a consequence of a major restructuring of the spectrum of surface states.

The results of the influence of chemical treatment in solutions of $(NH_4)_2S$ in isopropyl alcohol on the leakage current of GaAs power diodes are consistent with the model of sulfide passivation of the GaAs surface in alcohol solutions[5] and with the results of the kinetics of formation of a sulfide coating in aqueous solutions of sodium sulfide.[6]

According to this model, the rate of formation of the sulfide coating is determined by the rate of escape of elec-

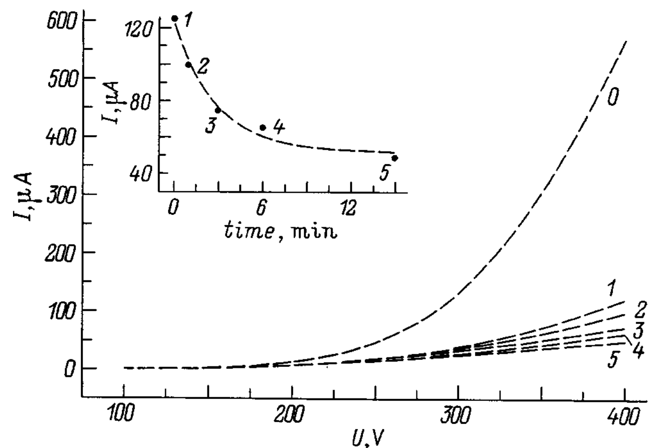

FIG. 4. Reverse branches of the *I-V* curves of GaAs power diodes untreated (*0*) and treated (*1–5*) in a $(NH_4)_2S$ + i-C_3H_7OH (1:50) solution for various durations of application of a 400-V reverse bias to the diode: (*1*) 0.1 min; (*2*) 1 min; (*3*) 3 min; (*4*) 6 min; (*5*) 15 min. Inset: dependence of the maximum diode leakage current on the duration of application of a 400-V reverse bias to the diode.

trons from the semiconductor into the solution during oxidation of the semiconductor, by the rate of breaking of surface chemical bonds of the semiconductor, and by the rate of formation of bonds with surface atoms of the semiconductor. Enhancement of the effectiveness of passivation and, hence, a more pronounced reduction of the diode leakage current will be attained with an increase in the chemical reaction rate,[5] which, first of all, is higher in alcohol solutions of $(NH_4)_2S$ than in pure $(NH_4)_2S$ (Ref. 5) and, second, decreases as the concentration of sulfide ions in the alcohol solution increases (Fig. 2).

The optimal chemical treatment time of approximately 1 min correlates with the result of photoluminescence investigations of GaAs passivated in solutions of $(NH_4)_2S$ in alcohols.[5] The reduction of the leakage currents is not as pronounced after the treatment time is further extended to 2 min, probably because the chemical reaction products create marked shunting channels on the surface of the *p-n* structure.

The further reduction of the leakage currents under the influence of an applied reverse voltage (Fig. 4) is probably attributable to the additional modification of the GaAs surface under the influence of the increase in the diode temperature in this case when the reverse voltage is applied, with the formation of a more energy-favorable surface structure, similar to what happens after passivation in aqueous sulfide solutions with exposure to light.[7]

Consequently, current leakages through the surface can be significantly reduced by chemical treatment of the surface of GaAs *p-n* power diodes in solutions of $(NH_4)_2S$ in isopropyl alcohol.

When the treatment time in the solution is increased to 1 min and when the duration of application of a reverse bias at $U = 400$ V is increased, the reduction of the leakage currents becomes more effective.

The authors gratefully acknowledge V. N. Bessolov for encouraging the present study.

[1] M. S. Carpenter, M. R. Melloch, M. S. Lundstrom, and S. P. Tobin, Appl. Phys. Lett. **52** (25), 2157 (1988).
[2] G. Beister, J. Maege, D. Gutsche, G. Erbert, J. Sebastian, K. Vogel, M. Weyers, J. Würfl, and O. P. Daga, Appl. Phys. Lett. **68** (18), 2467 (1996).
[3] V. N. Bessolov, E. V. Konenkova, and M. V. Lebedev, Mater. Sci. Eng., B **44**, 376 (1997).
[4] V. N. Bessolov, M. V. Lebedev, B. V. Tsarenkov, and Yu. M. Shernyakov, Mater. Sci. Eng., B **44**, 380 (1997).
[5] V. N. Bessolov, E. V. Konenkova, and M. V. Lebedev, Fiz. Tverd. Tela (St. Petersburg) **39**, 63 (1997) [Phys. Solid State **39**, 54 (1997)].
[6] V. N. Bessolov, A. F. Ivankov, E. V. Konenkova, M. V. Lebedev, and V. S. Strykanov, Fiz. Tekh. Poluprovodn. **30**, 364 (1996) [Semiconductors **30**, 201 (1996)].
[7] V. L. Berkovits, A. O. Gusev, V. M. Lantratov, T. V. L'vova, D. Paget, A. B. Pushnyi, and V. P. Ulin, Phys. Low Dim. Structur. **12**, 293 (1995).

Translated by James S. Wood

Electron states in the surface region of gallium arsenide treated in selenium and arsenic vapor

N. N. Bezryadin, É. P. Domashevskaya, G. I. Kotov, R. V. Kuz'menko, and M. P. Sumets

Voronezh State Technological Academy, 394000 Voronezh, Russia

I. N. Arsent'ev

A. F. Ioffe Physicotechnical Institute, Russian Academy of Sciences, 194021 St. Petersburg, Russia

(Submitted October 29, 1998; accepted for publication November 10, 1998)
Fiz. Tekh. Poluprovodn. **33**, 719–722 (June 1999)

The parameters of charge localization centers in the skin layer of gallium arsenide treated in selenium-arsenic vapor are investigated by deep-layer transient spectroscopy. It is established that the addition of arsenic to the vapor phase slows down the reaction of heterovalent substitution of selenium for arsenic in GaAs and reduces the density of centers in the skin layer of GaAs. © *1999 American Institute of Physics.* [S1063-7826(99)02006-2]

To decrease the density of electron states on the surface of gallium arsenide, the substrate is treated in a chalcogen-containing medium,[1,2] selenium vapor, in particular.[3] In Ref. 4 the effect of selenium vapor on the density of surface electron states (SES) (Ref. 3 is attributed to (3×2) reconstruction of the GaAs(100) surface and the subsequent stabilization of this reconstruction by a tunnel-transparent pseudomorphic Ga_2Se_3(110) layer. Characteristically, the reduction of the SES [i.e., disappearance of the maximum corresponding to these states in the spectra obtained by deep-level transient spectroscopy (DLTS) (Ref. 4) and detachment of the Fermi level on the GaAs surface[1–3]] takes place independently of the particular chalcogen used for treatment (S, Se, or Te) and is also observed in combined treatment with selenium and arsenic vapors.[4]

We know from Ref. 5 that the presence of arsenic in a quasiclosed chamber during processes involving the treatment of a III–V semiconductor with a chalcogen can modify the nature of the heterovalent substitution reaction. In the same paper it has been established that not only the heterovalent substitution reaction rate, but also the mechanism of the reaction changes in the presence of arsenic, resulting in a decrease of the density of macroscopic structural defects in the boundary region of the heterojunction formed by this technique.

In this paper we analyze the influence of arsenic on the electrical characteristics of the surface of GaAs(100) treated in a quasiclosed chamber in selenium vapor with arsenic. The objects of investigation were Schottky barrier diodes formed by the spray deposition of Al contacts through a mask onto the untreated GaAs surface (which had been subjected only to chemodynamic polishing and removal of the natural oxide sublayer by the procedure described in Refs. 3 and 4) and onto the surface treated in selenium and selenium with arsenic. The vapor treatment was performed in the quasiclosed chamber under conditions similar to those used in Refs. 3 and 4.

Figure 1 shows DLTS spectra of Al–GaAs diodes (n-type GaAs, $n \simeq 10^{16}\,\mathrm{cm}^{-3}$) formed after treatment of the substrate both in selenium vapor (Fig. 1a) and in selenium vapor with arsenic (Fig. 1c) at fixed temperatures. The DLTS spectra have been analyzed in the temperature range 90–400 K to determine the activation energies of the centers. As in Ref. 4, the dependence of the amplitude of the spectral peaks on the amplitude of the injecting peaks was used to separate the contribution of surface states to the DLTS signal from the contribution of centers in the subsurface space-charge region.

As in Ref. 4, the maximum at $\ln\tau/\tau_0 \sim 9$, which corresponds to SES (the peak Π_3 in the notation convention of Ref. 4), vanished in the DLTS spectra, i.e., treatment in selenium vapor alone and in selenium with arsenic has essentially the same influence in reducing the density of SES, as mentioned previously.[3] The longer duration of the combined Se + As treatment is attributable to the decrease in the heterovalent substitution reaction rate of arsenic in GaAs on Se when arsenic vapor is present in the quasiclosed chamber. This time was decided from a comparison of the results of measuring the thickness of the treatment-formed chalcogenide layer by the method of current-voltage (I–V) curves of the height of the Schottky barrier (φ_b) and by ellipsometry. The resulting value $\varphi_b \simeq 0.46$ eV for samples with an Al contact after 5-min treatment in Se vapor was in line with the value $\varphi_b \simeq 0.44$ eV obtained for samples treated in Se vapor with arsenic for 45 min. The measured layer thickness in either case corresponded to 5 nm (within 5% error limits).

The states in the surface space-charge region of the gallium arsenide were found to be sensitive to the presence of arsenic in the quasiclosed chamber (Figs. 1c and 1d). The maximum of the DLTS signal for all types of centers in the space-charge region decreased after combined Se + As treatment in comparison with treatment in selenium alone. We note that the maximum at $\ln\tau/\tau_0 \sim 4$ (peak Π_2) even increased relative to a sample that had not been treated in selenium vapor (Fig. 1b).

The centers associated with the maxima in the DLTS spectra are also manifested in isothermal capacitance relax-

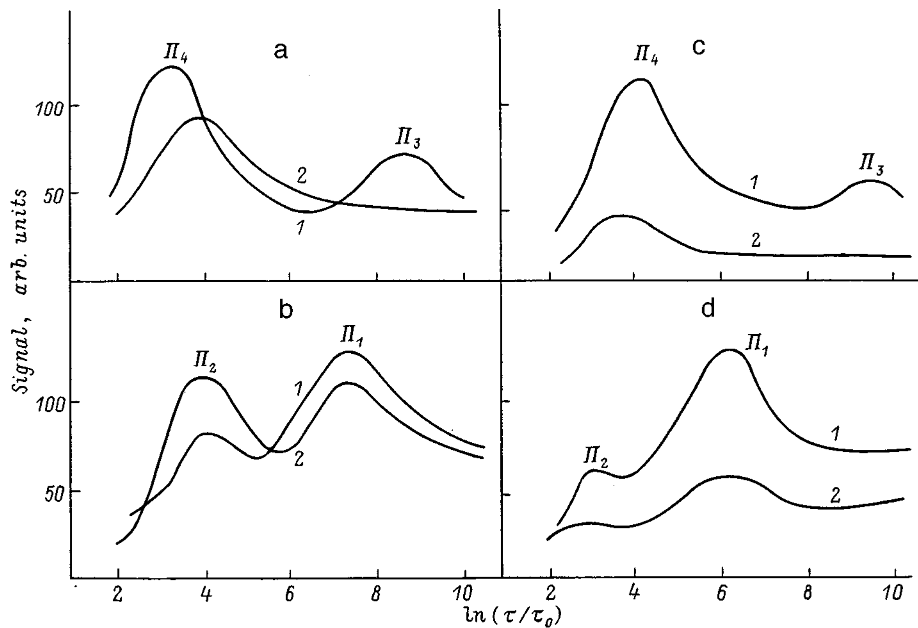

FIG. 1. Typical DLTS spectra at temperatures $T = 350$ K (a, c) and 170 K (b, d) for Al-GaAs structures prepared without pretreatment of the substrates (curves *1*), after treatment in Se vapor for 5 min (a, b, curves *2*), and after treatment of the substrates in Se + As vapor for 45 min (c, d, curves *2*). Here τ_0 is the maximum relaxation time specified in the experiments.

ation of the investigated heterostructures at room temperature (Fig. 2). Schottky diodes prepared immediately after chemodynamic polishing (without chalcogen treatment) are characterized by prolonging of the capacitance relaxation process (Fig. 2a, curve *1*). Treatment in selenium alone removes this long-time segment (Fig. 2a, curve *2*). After combined Se + As treatment the nature of the time dependence of the capacitance cannot be detected in the same time scale because of a substantial decrease in the time constant of the relaxation process. To ascertain the nature of this change in the relaxation characteristics of the investigated structures, we have investigated the temperature dependence of the time constant of the variation of the capacitance after the application of a depleting voltage pulse (Fig. 3). The values of the time constant for the final stages of relaxation in coordinates $\ln\tau$ versus $1/T$ provide a good fit to a straight line, whose slope corresponds to an activation energy of the order of 0.4 eV (Fig. 3, curve *1*). The latter corresponds to the SES

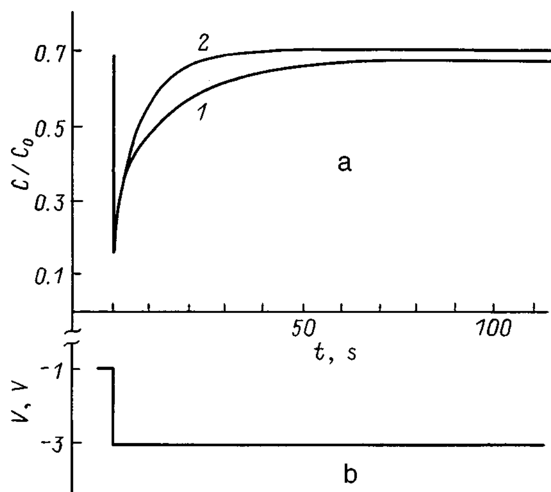

FIG. 2. Time variations of the capacitance of Al–GaAs heterostructures before (a) and after (b) the application of a depleting voltage pulse $V(t)$. Here C_0 is the capacitance of the structure before application of the voltage pulse. The curves in Fig. 1a are plotted without (*1*) and with (*2*) pretreatment of the substrate in Se.

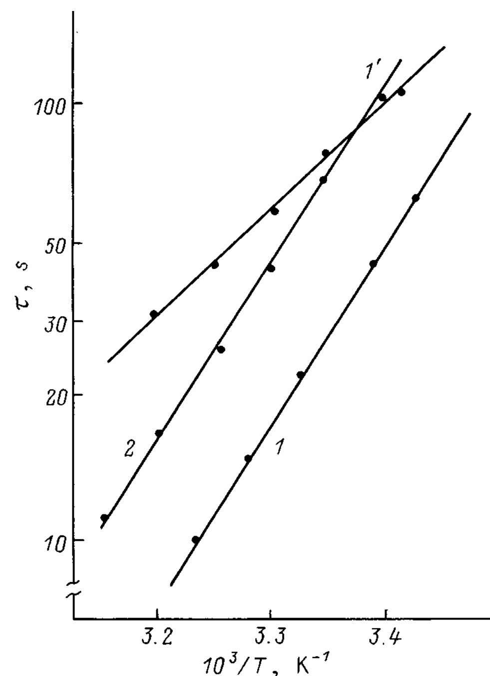

FIG. 3. Temperature dependence of the capacitance relaxation time for Al–GaAs heterostructures not treated in selenium (*1, 1′*) and treated in selenium vapor for 5 min (*2*); curves *1* and *1′* represent the values of the time constant in the initial and final segments of the capacitance relaxation curve, respectively.

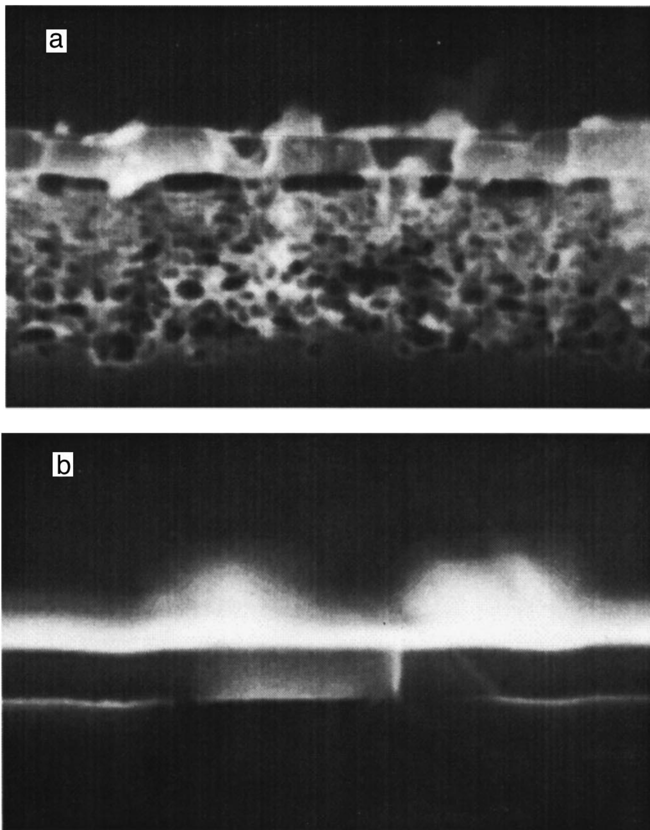

FIG. 4. Photomicrograph of transverse breaks in gallium arsenide samples treated in selenium vapor alone (a) and in selenium vapor with arsenic (b). The pictures were obtained in a scanning electron microscope with magnification ×150 000. To enable observation of the Ga_2Se_3 layer formed by the substitution reaction in the microscope, the vapor treatment was performed at higher temperatures than those indicated in Refs. 3 and 4.

activation energy determined by DLTS (peak Π_3 in Fig. 1a). As mentioned above, this maximum vanishes after treatment in selenium vapor (Fig. 1a, curve *2*). Again, the long-time segment is no longer observed in the capacitance relaxation curve after chalcogen treatment (Fig. 2). Consequently, the prolonging of relaxation of the capacitance of structures formed on GaAs substrates not treated in selenium is attributable to SES with an activation energy on the order of 0.4 eV. As the temperature varies, the plots of the time constants of the initial parts of the capacitance relaxation curve of structures, both treated (Fig. 3, curve *2*) and not treated (Fig. 3, curve *1'*) in selenium vapor, as a function of $1/T$, are also well described by a straight line in coordinates $\ln\tau$ versus $1/T$. Here the curves have an identical slope, which corresponds to an activation of the order of 0.7–0.8 eV. This energy corresponds to peak Π_4 in the DLTS spectra (Figs. 1a and 1c, curves *1* and *2*). The amplitude of this maximum is significantly lowered only by combined treatment of the substrates in selenium and arsenic vapor (Fig. 1c, curve *2*). This reduction of the density of centers in the surface space-charge region of GaAs is probably the main reason for the shortening of the capacitance relaxation time of structures whose substrates are pretreated in selenium vapor with arsenic in the quasiclosed chamber.

Combined Se + As treatment lowers the amplitudes of all the maxima (peaks Π_1, Π_2, and Π_4 in the DLTS spectra, Fig. 1) corresponding to centers in the space-charge region of gallium arsenide. The mechanism of this process cannot be determined from the sum-total of the experimental results analyzed in this paper. In our opinion, the most likely cause of such behavior of the centers in the space-charge region of GaAs is a decrease in the density of macroscopic defects in the surface region of the gallium arsenide (beneath the pseudomorphic Ga_2Se_3 layer formed by the substitution of selenium for arsenic[3,4]) as a result of the combined treatment in selenium with arsenic (Figs. 4a and 4b).

Thus, the presence of arsenic in the quasiclosed chamber predominantly influences the density of centers in the surface region of GaAs rather than the density of SES. This phenomenon is accompanied by a reduction in the number of macroscopic defects near the GaAs surface. Chalcogen treatment of the surface exerts a decisive influence on the density of SES in GaAs.

[1] P. Victorovich, Rev. Phys. Appl. **9**, 895 (1990).
[2] B. I. Bednyĭ and N. V. Baĭdus', Fiz. Tekh. Poluprovodn. **29**, 1488 (1995) [Semiconductors **29**, 776 (1995)].
[3] B. I. Sysoev, N. N. Bezryadin, G. I. Kotov, and V. D. Strygin, Fiz. Tekh. Poluprovodn. **27**, 131 (1993) [Semiconductors **27**, 69 (1993)].
[4] B. I. Sysoev, N. N. Bezryadin, G. I. Kotov, B. L. Agapov, and V. D. Strygin, Fiz. Tekh. Poluprovodn. **29**, 24 (1995) [Semiconductors **29**, 12 (1995)].
[5] B. I. Sysoev, B. L. Agapov, N. N. Bezryadin, T. V. Prokopova, and Yu. K. Shlyk, Neorg. Mater. **12**, 1449 (1976).

Translated by James S. Wood

Deep-level recombination spectroscopy in GaP light-emitting diodes

S. V. Bulyarskiĭ, M. O. Vorob'ev, N. S. Grushko, and A. V. Lakalin

Ul'yanovsk State University, 432700 Ulyanovsk, Russia

(Submitted September 22, 1998; accepted for publication September 23, 1998)
Fiz. Tekh. Poluprovodn. **33**, 723–726 (June 1999)

Deep-level parameters determined from an analysis of the differential coefficients of the forward-bias current-voltage curves are compared in the example of commercial GaP LEDs. It is shown that these parameters are suitable for deep-center diagnostics. The proposed measurements can be performed on semiconductor wafers in the industrial environment without sealing or dividing into individual crystals. © *1999 American Institute of Physics.*
[S1063-7826(99)02106-7]

Recombination in a space-charge region, theoretically grounded in the classical work of Shockley, Noyce, and Sah,[1] has received far less attention than it deserves. Charge injection into the space-charge region induces deep-level charge exchange accompanied by a change in the recombination rate.[2,3] This effect creates anomalous features in the forward-bias current-voltage (*I-V*) characteristics. These distinctive features are faint against the background of the exponential growth of the forward current and have therefore been ignored for a long time. A series of previous papers[4–6] has been devoted to the elucidation of these features and their utilization for determining the parameters of deep levels.

In this paper we compare various differential parameters of the forward-bias *I-V* characteristics and estimate their suitability for deep-center diagnostics in the example of commercial GaP light-emitting diodes (LEDs), in which nonradiative recombination channels lower the emission efficiency. To understand the recombination channels, it is necessary to determine the parameters of the defects which participate in nonradiative recombination and which lower its fraction in recombination processes. This problem is of utmost importance in LED technology.

The samples of GaP-based *p-n* junctions had standard parameters for commercial nitrogen-doped green-light LEDs. The epitaxially grown junction was sharp, asymmetric, and characterized by a density of electrons in the base $(3-9.5)\times 10^{15}\,\mathrm{cm}^{-3}$. The *I-V* curves were measured on an automated apparatus described in Ref. 5. The current was set by means of a V7-42É electrometer in the range from 10^{-12} A to 10^{-2} A, and the voltage was set by means of a V7-46 voltmeter with a step of 0.01 V. The data were entered into computer memory. A total of 15 diodes were investigated. Selected parameters of one of them are shown in Table I.

At a low injection level the recombination currents in the space-charge region of a wide-gap semiconductor *p-n* junction are generally higher than the diffusion currents. In this case the *I-V* curve is described by a characteristic equation of the form

$$J=A(U)\exp(qU/\beta kT), \tag{1}$$

where β assumes values from 1 to 2 ($\beta=1$ for the diffusion currents). The physics of the process is described in detail in Refs. 1–5. The proportionality factor $A(U)$ depends on the parameters of the deep centers, which can be determined under certain assumptions.

The recombination current in the space-charge region of a *p-n* junction with the participation of several, simple, doubly charged deep levels is described by the equation[5]

$$j_r=\sum_{m=1}^{s}\frac{qw(U)c_{nm}c_{pm}n_i^2(e^{qU/kT}-1)N_{tm}}{2n_i\sqrt{c_{nm}c_{pm}}e^{qU/kT}+c_{nm}n_{1m}+c_{pm}p_{1m}}\times\frac{2kT}{q(V_d-U)}, \tag{2}$$

where q is the electron charge, $w(U)$ is the width of the space-charge region, s is the number of deep levels

$$n_{1m}=N_c\exp\left(-\frac{E_{tm}}{kT}\right);\quad p_{1m}=N_v\exp\left(-\frac{E_{tm}}{kT}\right);$$

c_n and c_p are the electron and hole capture coefficients for the given center, averaged over all states, N_t is the density of deep levels, E_t is the position of a deep level in the band gap,

$$E_{tn}=E_c-E_t;\quad E_{tp}=E_1-E_v,$$

and V_d is the diffusion potential.

TABLE I. Deep-level activation energies determined by different methods for a GaP LED.

Method	E_7, eV	E_6, eV	E_5, eV	E_4, eV	E_3, eV	E_2, eV	E_1, eV	E_8, eV	E_9, eV	E_{10}, eV
TSCAP	⋯	0.35	⋯	⋯	⋯	0.53	0.63	0.66	0.81	1.0
R_{np}	0.29	0.33	⋯	⋯	0.48	0.56	0.61	⋯	⋯	⋯
$\frac{d\beta}{dU}$	0.27	0.32	0.38	0.42	0.48	0.52	0.61	⋯	⋯	⋯
γ	0.26	0.30	0.37	0.41	0.46	0.54	0.61	⋯	⋯	⋯

Note: E_i denotes the deep-level thermal activation energies calculated from Eq. (5) and determined by the TSCAP technique. Other methods used to determine E_i are described in the text.

 © 1999 American Institute of Physics

Equation (2) differs somewhat from the expressions in Ref. 1. This difference has already been analyzed in detail,[6] and we shall not discuss it further. The limits of applicability of Eq. (2) have been established previously.[2–5]

To analyze the *I-V* characteristics, it is convenient to introduce a different physical variable: the normalized recombination rate

$$R_{np}=\frac{i}{qwSn_i[\exp(qU/2kT)-1]}\frac{q(V_d-U)}{2kT}, \qquad (3)$$

where i is the current, and S is the area of the *p-n* junction. This quantity is related to the deep-center parameters by an equation taken from Refs. 2 and 3:

$$R_{np}=\frac{c_nc_pn_iN_t[\exp(qU/2kT)+1]}{2n_i\sqrt{c_nc_p}\exp(qU/2kT)+n_1c_n+p_1c_p}. \qquad (4)$$

The latter can be used to expand the total recombination process into individual components, using algorithms in Refs. 4–6. An example of such a partition for the investigated diodes is shown in Fig. 1. For each recombination process through a doubly charged deep center we can determine the voltage ($U_{0.5}$) at which the normalized recombination rate (4) decreases by one-half relative to saturation. Assuming that the deep center lies above the middle of the band gap (i.e., $c_pp_1 \ll c_nn_1$), we find

$$E_{tn}=\frac{E_g-qU_{0.5}}{2}+\delta, \qquad (5)$$

where

$$\delta=\frac{kT}{2}\ln\left(\frac{1}{4}\frac{c_nN_c}{c_pN_v}\right).$$

This quantity, like the capture coefficients, is unknown as a rule. However, the ratio of the capture coefficients can be determined by measuring the temperature dependence of the forward current.[2,3] The systematic error introduced when δ is disregarded does not exceed 0.06 eV for a ratio $c_n/c_p=100$. The activation energies calculated from Eq. (5) are given in Table I.

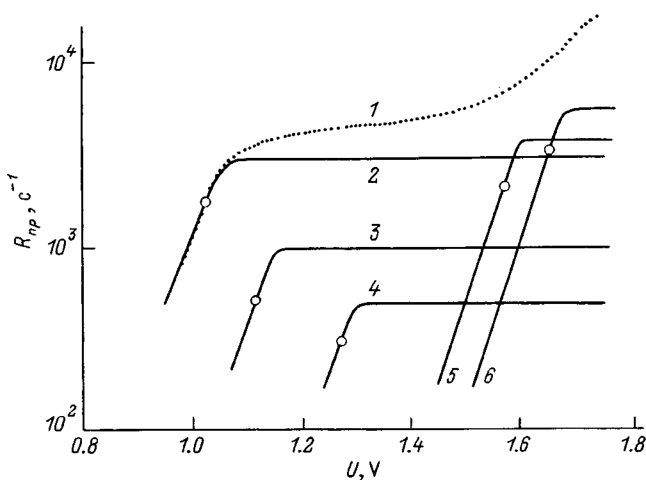

FIG. 1. Separation of recombination processes into components on the basis of the function $R_{np}=f(U)$. (*1*) Experimental; activation energies: (*2*) $E=0.61$ eV; (*3*) 0.56 eV; (*4*) 0.48 eV; (*5*) 0.33 eV; (*6*) 0.29 eV.

The deep-level activation energy can be determined from the extrema of the derivative of the differential slope of the *I-V* characteristic (β):

$$\beta=\frac{qJ_r}{kT}\left(\frac{\partial J_r}{\partial U}\right)^{-1}. \qquad (6)$$

Equation (5) can also be used to determine deep-level activation energies from the maxima of the function $d\beta/dU=f(U)$, but the expression for δ will not contain the factor 1/4 in this case.[4] If we assume that $c_n/c_p=10^2$, the systematic error at $T=300$ K is then $\delta\approx0.04$ eV for GaP.

The function $d\beta/dU=f(U)$ for one sample is plotted in Fig. 2. There is a noticeable correlation between the maxima of curve *2* and the features of the normalized recombination rate (see Fig. 1). Every time a new level enters into the recombination process, the derivative of the differential slope of the *I-V* characteristic acquires a maximum.

A drawback of the method is the need to calculate the second derivative of the experimental data, which requires special numerical methods. In this regard, it is more practical to use another differential coefficient, whose determination requires only the calculation of the first derivative:[4]

$$\gamma=\left(\frac{\partial R_{np}}{\partial U}\right)\frac{2kT}{q}\frac{1}{R_{np}}. \qquad (7)$$

The voltage at which the coefficient (7) is a minimum (Fig. 2) can be used to find the deep-center activation energy from Eq. (5). Certain conditions formulated in Ref. 4 must be satisfied. An approximate estimate shows that these conditions are usually met for deep levels formed in the fabrication of commercial semiconductor devices.

A function of the form (7) has minima at points U_{0m}; the amplitude of each minimum differs according to the contribution of the specific deep level to the total recombination current. The quantities U_{0m}, which depend on $c_{n(p)m}$ and N_{tm}, can be determined experimentally. Assuming that the deep level is situated above the middle of the band gap (i.e., $c_{pm}p_{1m} \ll c_{nm}n_{1m}$), we obtain an expression analogous to (5). The results obtained by this method for the investigated diode are also shown in Table I.

To refine the deep-center energies, we have determined them by the well-known thermally stimulated capacitance (TSCAP) technique, which is described, for example, in Refs. 7 and 8. In this technique the capacitance of the sample (C) is measured as the sample is heated at a constant rate. Deep levels in the space-charge region have been previously filled with electrons. The derivative of the capacitance with respect to the temperature is described by an expression whose one and only fitting parameter is the deep-level activation energy (E_t):

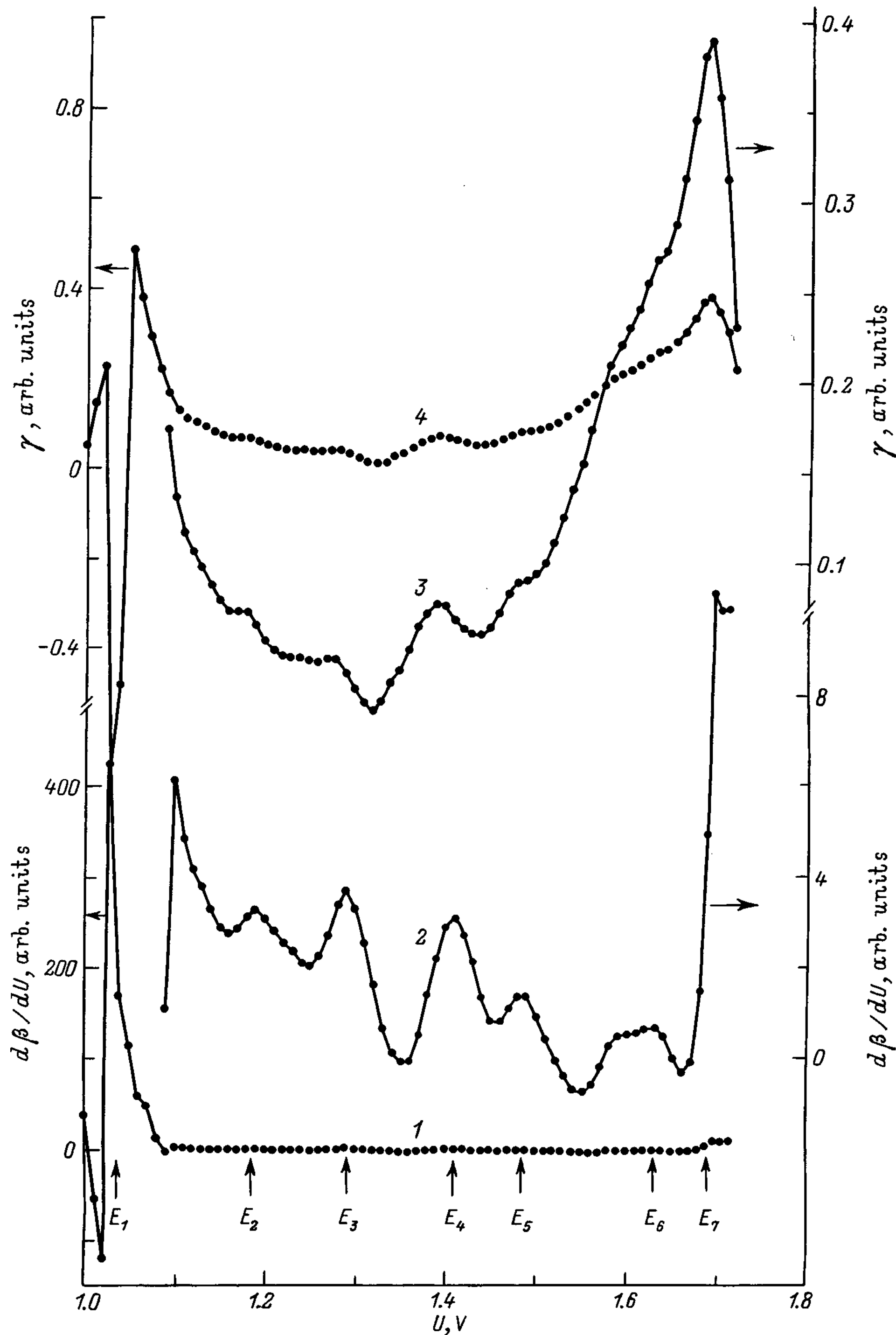

FIG. 2. Differential coefficients of the *I-V* characteristic. The extrema correspond to the levels in Table I.

$$\frac{dC}{dT}=A\left(\frac{T}{T_m}\right)^2\exp\left[\frac{E_t}{k}\left(\frac{1}{T_m}-\frac{1}{T}\right)\right]$$
$$\times\exp\left\{1-\left(\frac{T}{T_m}\right)^2\exp\left[\frac{E_t}{k}\left(\frac{1}{T_m}-\frac{1}{T}\right)\right]\right\}. \quad (8)$$

A certain difficulty is encountered in that the experimental curve comprises the superposition of ionization processes of the individual levels, each providing its own contribution to the capacitance. These processes can be separated by means of Eq. (8). It is more convenient to begin the breakdown in the high-temperature region, specifying the temperature of the maximum and the amplitude of the TSCAP peak. If the choice of E_t is smaller than the true value, the analytical curve is broader than the experimental curve. If the chosen energy E_t is greater than the true value, the curve calculated from Eq. (8) is narrower than the experimental curve. The energy can be selected very accurately with good agreement between the experimental and analytical curves. Figure 3 shows a graph plotted by the TSCAP technique, and Table I gives the activation energies determined from it.

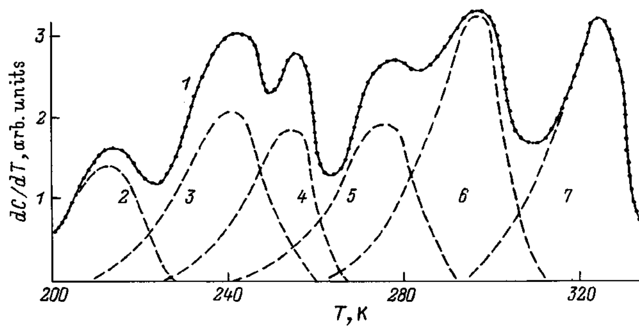

FIG. 3. Separation of deep levels on the basis of the function $dC/dU = f(T)$. (*1*) Experimental; activation energies: (*2*) $Et = 0.35$ eV; (*3*) 0.53 eV; (*4*) 0.63 eV; (*5*) 0.66 eV; (*6*) 0.81 eV; (*7*) 1.0 eV.

A comparison of the tabulated results shows that all the methods used here yield good agreement of the thermal activation energies. The differential parameters of the *I-V* characteristics are now measured at a fixed temperature — room temperature in our case, simplifying the experimental procedure. The measurements can be performed on semiconductor wafers in the industrial environment without having to seal them or divide them into individual crystals. The experiment itself can be easily automated in the part associated with measurement and processing.

[1] S. T. Sah, R. N. Noyce, and W. Shockley, Proceedings IRE **14**, 1228 (1957).
[2] S. V. Bulyarskiĭ and N. S. Grushko, *Physical Principles of the Functional Diagnostics of p-n Junctions Containing Defects* [in Russian] (Shtiintsa, Kishinev, 1992).
[3] S. V. Bulyarskiĭ and N. S. Grushko, *Generation-Recombination Processes in Active Elements* [in Russian] (MGU, Moscow, 1995).
[4] S. V. Bulyarskiĭ, N. S. Grushko, and A. V. Lakalin, Zavod. Lab., No. **7**, 25 (1997).
[5] S. V. Bulyarskiĭ, N. S. Grushko, and A. V. Lakalin, in *Proceedings of the International Conference on Deep-Level Centers in Semiconductors and Semiconductor Structures* [in Russian] (Ulyanovsk, 1997), p. 65.
[6] S. V. Bulyarskiĭ, N. S. Grushko, A. I. Somov, and A. V. Lakalin, Fiz. Tekh. Poluprovodn. **31**, 1148 (1997) [Semiconductors **31**, 983 (1997)].
[7] S. V. Bulyarskiĭ and S. I. Radautsan, Fiz. Tekh. Poluprovodn. **15**, 1443 (1981) [Sov. Phys. Semicond. **15**, 836 (1981)].
[8] S. V. Bulyarskiĭ, I. V. Stratan, and N. S. Grushko, Fiz. Tekh. Poluprovodn. **21**, 1730 (1987) [Sov. Phys. Semicond. **21**, 1047 (1987)].

Translated by James S. Wood

Influence of temperature on the spectral composition of the breakdown electroluminescence of silicon carbide *p-n* structures

M. V. Belous, A. M. Genkin, and V. K. Genkina

National Technical University of Ukraine, 252056 Kiev, Ukraine
(Submitted May 14, 1998; accepted for publication November 10, 1998)
Fiz. Tekh. Poluprovodn. **33**, 727–732 (June 1999)

The spectral dependence of the temperature coefficient of the quantum efficiency of breakdown electroluminescence of alloyed *p-n* structures based on silicon carbide is investigated. A similarity is observed between the profiles of the spectral distributions of the temperature coefficient and the relative slope of the spectrum. These curves were found to have characteristic features that depend on the crystal modification of the as-grown material and the working voltage of the structure. © *1999 American Institute of Physics.*
[S1063-7826(99)02206-1]

Silicon carbide-based radiators operating in the electrical breakdown regime hold considerable promise for the sensitivity calibration of spectral equipment and optoelectronic devices containing photomultipliers. They stand out from conventional standard radiators by virtue of their broad, flat spectrum, which resembles the spectrum of an absolute blackbody at a temperature of 6000–8000 K, and by the exceptionally high temperature stability of their total radiated power.[1]

It is all but unknown, however, how temperature influences the spectral composition of the radiation. This situation is probably attributable to difficulties of a methodological nature associated with the need for extremely accurate recording of weak optical radiation fluxes. Apart from its practical importance, the investigation of the influence of temperature on the emission spectrum can provide additional information about the mechanisms of the process — information that is impossible to obtain by analyzing the profile of broad, flat spectra.

Here we report the results of an experimental study of the effect of temperature on the spectral distribution of the quantum efficiency of the breakdown electroluminescence of alloyed silicon carbide *p-n* structures as a function of the crystal modification of the as-grown material and the working voltage of the structures.

The *p-n* structures were prepared by alloying Silumin disks with silicon carbide crystals, polytypes 6H and 15R grown by the Leighly method, and also with single crystals of cubic silicon carbide 3C-SiC prepared by the thermal decomposition of methyl trichlorsilane. The structures had diameters of $150-300\,\mu$m. The disks were fused into natural faces of the crystals perpendicular to the crystallographic **C** axis. For 3C-SiC fusion was performed into the most fully developed B-face. The density of uncompensated donors in the as-grown crystals was $10^{18}-10^{19}\,\text{cm}^3$.

As a rule, breakdown in the investigated structures was localized in microplasmas. Judiciously planned technological regimes involving the artificial injection of defects into the subsurface layer of the as-grown α-SiC layers yielded structures in which the microplasmas were tightly and uniformly packed into the entire area or were localized in a ring occupying a large part of the area of the *p-n* junction. For such samples luminescence from a large number of microplasmas was observed under the microscope, beginning with currents no greater than $J=0.1-1$ mA. In the absence of defects the microplasmas were localized around a circle in the peripheral region of the *p-n* junction.

In general, structures with microplasmas localized in a narrow ring in the peripheral region of the *p-n* junction were obtained on the basis of 3C-SiC. The breakdown voltages differed sharply in different growth sectors, ranging from one or two to hundreds of volts. Structures were obtained under certain conditions, in which breakdown electroluminescence observed visually under the microscope with ~100 magnification was viewed as essentially uniform in area, without microplasmas. The working voltage for these samples usually did not exceed $U=20$ V.

The structures to be measured were placed in heat-dissipating casings. Base contact was established by the vacuum spraying of Ti + Ni. The radiation from the samples was recorded through the thin *p* region.

In our selection of the structures and preparation of the samples we strove to minimize the influence of radiation scattered or reflected from the faces of the crystal.

The emission spectra were measured in the photon energy range $h\nu=1.8-3.8$ eV in steps $\Delta h\nu=0.05$ eV by means of a ZMR-3 monochromator. A photon counter utilizing an FÉU-79 photomultiplier, carefully selected to ensure the most stable possible detection of radiation, was used as the photodetector. The samples to be measured were placed in a special holder directly in front of the entrance slit to the monochromator. The holder afforded the possibility of regulating and stabilizing the sample temperature (T) in the range from room temperature to 400 K. The signal intensities $I(h\nu)$ from the measured sample were reproduced within at most 0.1% error limits over the entire spectral range during the time (~2 h) to measure two spectra (at two different temperatures).

 © 1999 American Institute of Physics

A TRSh-3000 ribbon-filament incandescent lamp was used for calibration. To obtain a smooth calibration curve free of anomalous features in differentiation, the experimental dependence was approximated by a fourth-degree polynomial. The absence of fine-structure anomalies in the photosensitivity spectrum of the FÉU-79 was additionally tested in the photon energy interval $h\nu = 3.3-3.8$ eV, where bands were observed in the breakdown electroluminescence spectra.

As a rule, the temperature curves of the spectral density of the quantum efficiency were linear in the temperature range 300–400 K, and they could therefore be used to characterize the relative temperature coefficient $\gamma_{h\nu}$ expressed in units of % / K.

To plot the spectral function $\gamma_{h\nu}(h\nu)$, the spectral distributions of the signal from the sample were measured in succession at room temperature T_1 and a temperature T_2 100 K above room temperature. The constancy of the photosensitivity of the recording system was monitored during this operation. The quantity γ_ν was determined for each photon energy in steps $\Delta h\nu = 0.05$ eV from the equation

$$\gamma_{h\nu} = \frac{I(T_2) - I(T_1)}{I(T_1)\cdot(T_2 T_1)} \times 100\% .$$

The spectral distributions of the quantum efficiency of the sample $N_{h\nu}(h\nu)$ and the relative slopes of the spectrum $\xi(h\nu) = (1/N_{h\nu})\Delta N_{h\nu}/\Delta h\nu$ were also recruited for a combined analysis.

An estimation of the internal quantum efficiency of breakdown electroluminescence within 100% error limits gives a value of the order of $10^{-7}-10^{-6}$ photons/electron·eV within the limits of the spectral interval $h\nu = 1.8-3.8$ eV for samples differing in their emission topography, working voltage, polytype structure, degree of doping, and purity of the as-grown crystals. The least scatter of the quantum efficiency was exhibited by samples prepared on the basis of industrial 6H-SiC crystals, with a working voltage higher than 16 V and a uniform field of microplasmas.

A low quantum efficiency from the entire set of samples was observed for structures with a low working voltage (14 V or lower for 6H-SiC), which probably corresponds to tunneling breakdown.[2]

The emission spectra of the α-SiC-based samples comprised a broad band with a not very pronounced structure (Figs. 1c and 2c). Differences between the polytypes 6H-SiC and 15R-SiC appeared only in the spectral structure manifested in the differential curves Figs. 1b, 2b, and 3b). For the majority of the samples the profile of the spectrum in all details was essentially independent of the working current J in the range from 10 mA to 100 mA (the corresponding differential curves in Figs. 1b and 3b merge together for all practical purposes).

The 3C-SiC samples contained, against the background of the wideband spectrum, a comparatively narrow band with a maximum near 3.1 eV (Fig. 4c), whose contribution relative to the background, as noted in an earlier paper,[3] diminished considerably as the excitation level was raised.

Exceptionally low values of $\gamma_{h\nu}$ were observed for the 6H-SiC and 15R-SiC samples over the entire investigated spectral range, generally not exceeding the interval $-0.05-0.05$ % / K.

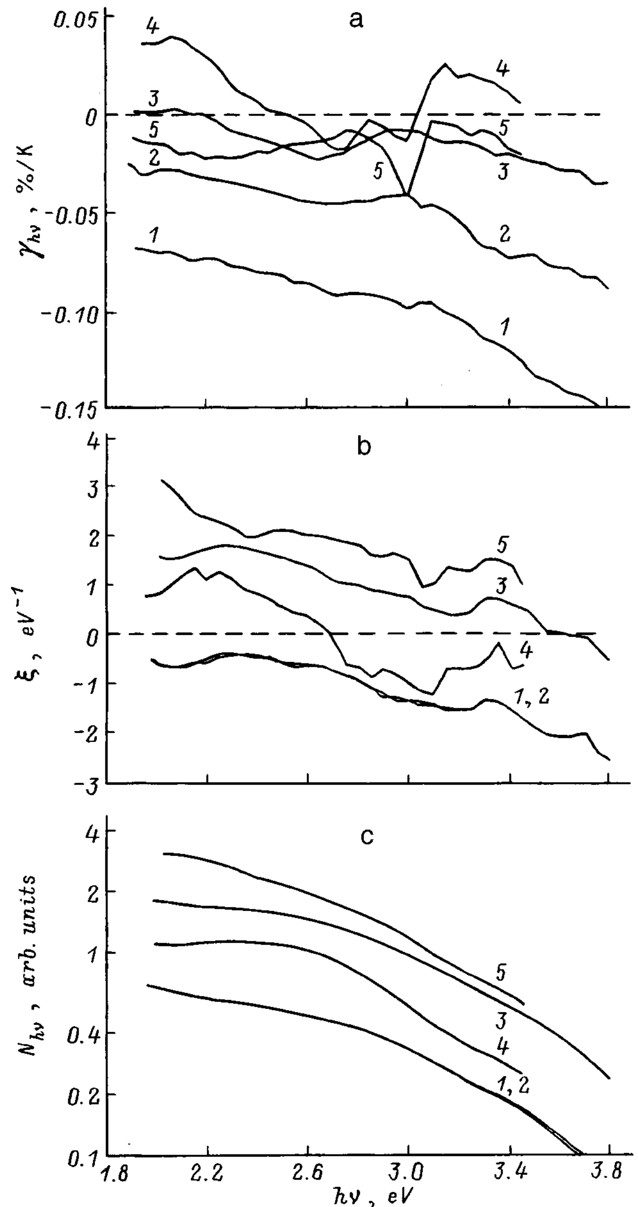

FIG. 1. Spectral distributions for 6H-SiC-based structures: (a) temperature coefficient of the quantum efficiency of breakdown electroluminescence; (b) relative slope of the spectral distribution of the quantum efficiency; (c) quantum efficiency. Sample number and measurement regime [J, mA/U, V]: (*1*) 164 [50/12.6]; (*2*) 164 [100/13.3]; (*3*) 86 [50/17.0]; (*4*) 11 [50/19.5]; (*5*) 28 [50/25.1]. (b) The curves are shifted upward by: (*1, 2*) 0; (*4*) 1 eV^{-1}; (*3*) 2 eV^{-1}; (*5*) 3 eV^{-1}.

Figure 5 shows the temperature coefficient of the quantum efficiency γ as a function of the voltage on the sample U (which is determined mainly by the density of uncompensated donors in the as-grown crystals) for a current $J = 50$ mA and a 6H-SiC p-n structure with a uniform microplasma field. The points indicate the total values of γ received by a nonselective photodetector; the vertical line segments indicate the maximum and minimum values of $\gamma_{h\nu}$ in the spectral interval $h\nu = 1.8-3.8$ eV. It is evident from the figure that a weak dependence of γ on U is observed. One exception is sample 164 ($U = 12.6$ V), in which tunneling

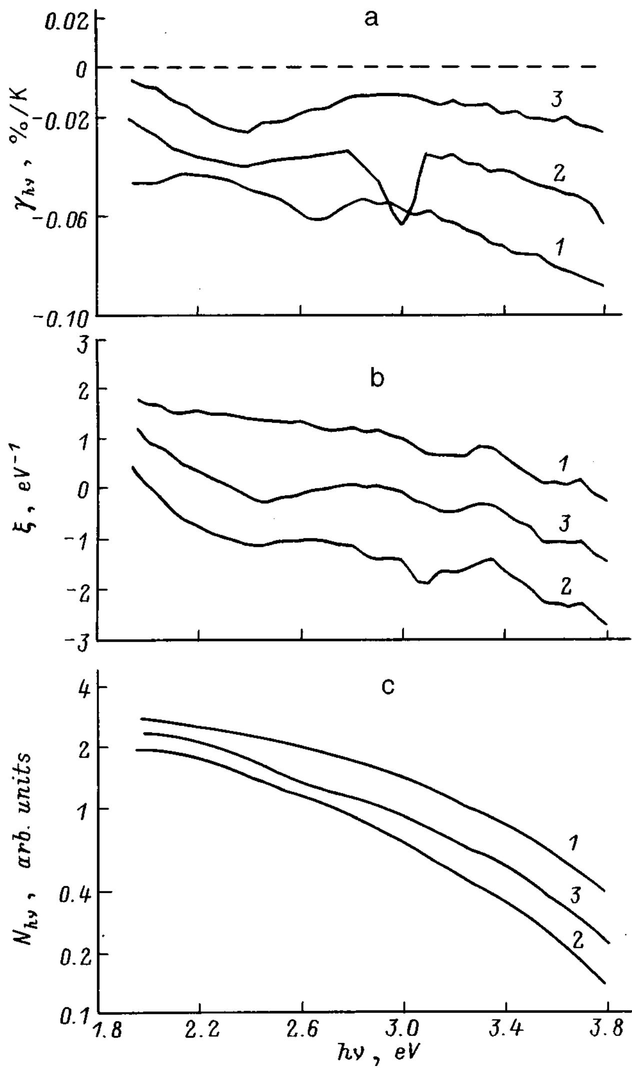

FIG. 2. Spectral distributions for 15H-SiC-based structures: (a) temperature coefficient of the quantum efficiency of breakdown electroluminescence; (b) relative slope of the spectral distribution of the quantum efficiency; (c) quantum efficiency. Sample number and measurement regime [J, mA/U, V]: (*1*) 41 [100/14.2]; (*2*) 28 [50/26.7]; (*3*) 92 [50/24.1]. (b) The curves are shifted upward by: (*2*) 0; (*3*) 1 eV^{-1}; (*1*) 2 eV^{-1}.

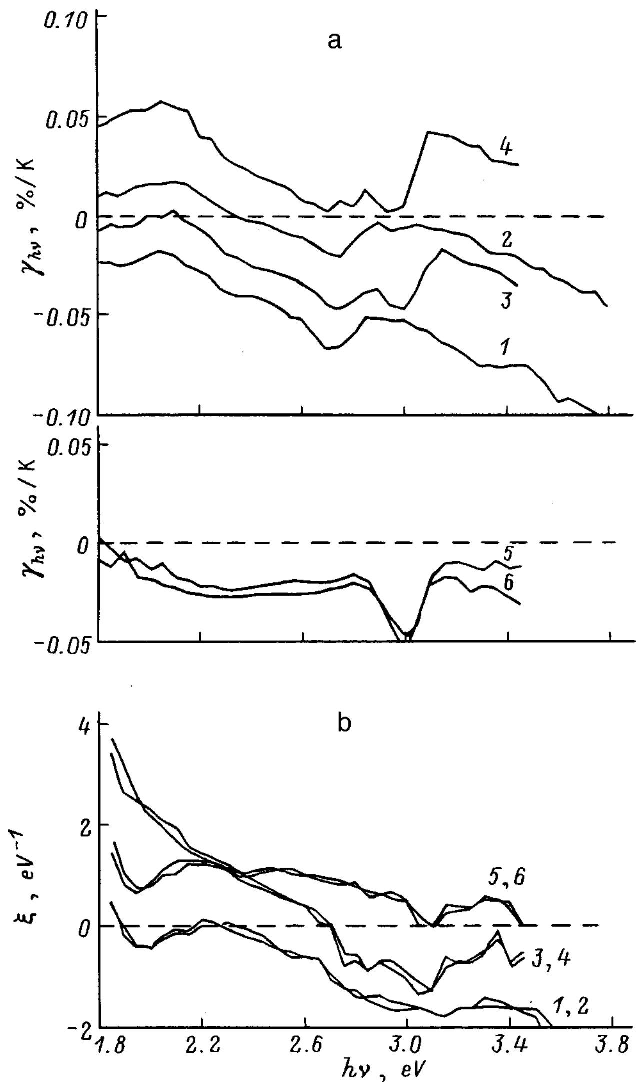

FIG. 3. Influence of excitation level on the spectral distributions for 6H-SiC structures: (a) temperature coefficient of the quantum efficiency of breakdown electroluminescence; (b) relative slope of the spectral distribution of the quantum efficiency; (c) quantum efficiency. Sample number and measurement regime [J, mA/U, V]: (*1*) 120 [10/16.6]; (*2*) 120 [100/176.6]; (*3*) 11 [10/18.5]; (*4*) 11 [100/20.0]; (*5*) 28 [10/23.1]; (*6*) 28 [100/25.1]. (b) The curves are shifted upward by: (*1, 2*) 0; (*3, 4*) 1 eV^{-1}; (*5, 6*) 2 eV^{-1}.

breakdown probably takes place; sample 11 ($U=19.4$ V) also stands out for its high positive values of γ.

The general behavior of the spectral curves $\gamma_{h\nu}(h\nu)$ and $\xi(h\nu)$ are well reproduced for all crystals of the given polytype, permitting typical individual cases to be treated separately. The curves contain highly pronounced features that are characteristic of each polytype.

Figure 1 shows the spectra of typical 6H-SiC samples with different working voltages.

It is evident from Figs. 1a and 1b that the nature of the spectral curves $\gamma_{h\nu}(h\nu)$ and $\xi(h\nu)$ is similar in many respects. It can be assumed in light of this similarity that one of the factors governing the temperature coefficient and its spectral dependence is the temperature shift of the main components of the radiation. Here the quantum efficiency increases on the leading slope of the spectral band and decreases on the trailing side, where the relative variation of the quantum efficiency (i.e., the value of $\gamma_{h\nu}$), exclusive of the influence of other factors, should be proportional to the relative slope of the spectrum in the given spectral region. In fact, for the quantity $\gamma_{h\nu}$ we can write

$$\gamma_{h\nu}=\frac{1}{N_{h\nu}}\frac{\partial N_{h\nu}}{\partial(h\nu)}\frac{d(h\nu)}{dT}+\frac{1}{N_{h\nu}}\frac{\partial N_{h\nu}}{\partial T}. \tag{1}$$

The quantities $(1/N_{h\nu})[\partial N_{h\nu}/\partial(h\nu)]$ and $d(h\nu)/dT$ in the first term are (respectively) the relative slope of the spectrum [whose approximate value $\xi(h\nu)$ we have determined experimentally] and the temperature coefficient of the band gap responsible for radiative transitions in the given region of the spectrum. The first term corresponds to the contribution of the temperature shift of the emission bands without any change in their profile and amplitude. The second term characterizes the influence of factors governing the variation of the profile and amplitude of the spectral bands. The principal factor here in the case of breakdown electroluminescence is

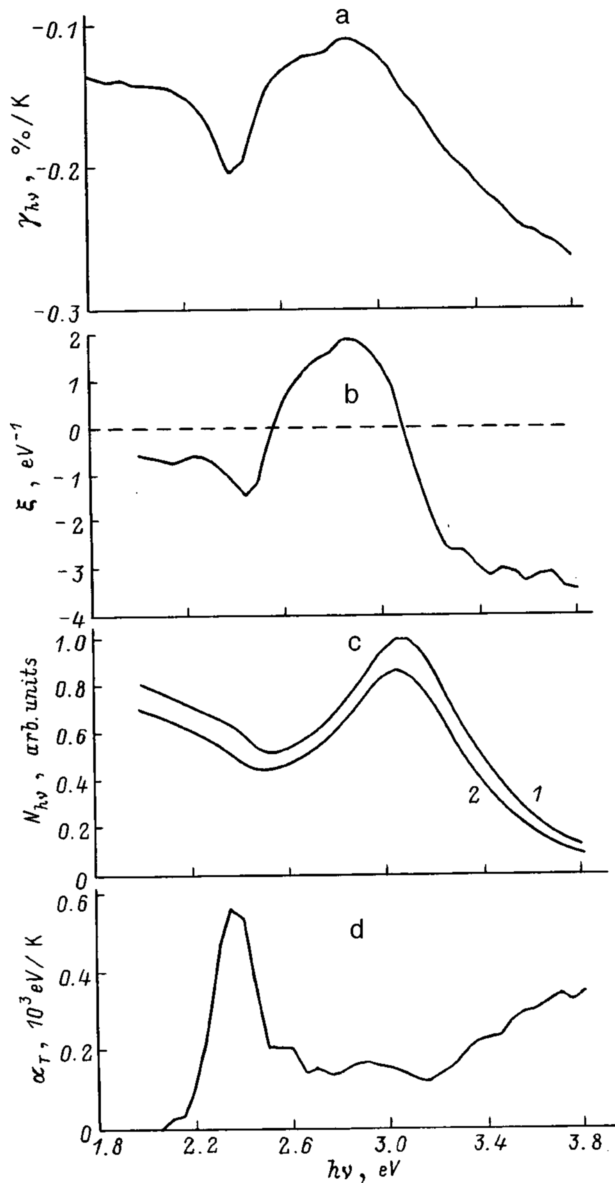

FIG. 4. Spectral distributions for 15H-SiC-based structures: (a) temperature coefficient of the quantum efficiency of breakdown electroluminescence; (b) relative slope of the spectral distribution of the quantum efficiency; (c) quantum efficiency. Sample 16, measurement regime: $J=50$ mA, $U=25.4$ V. Temperature: (*1*) 300 K; (*2*) 400 K.

probably the temperature dependence of the density of free carriers participating in radiative transitions. The similarity of the profiles of the spectral curves $\gamma_{h\nu}(h\nu)$ and $\xi(h\nu)$ implies that the quantities $d(h\nu)/dT$ and $(1/N_{h\nu})\times(\partial N_{h\nu}/\partial T)$ depend weakly on $h\nu$.

The part of the radiation reflected from the faces and scattered in the crystal is recorded together with the radiation transmitted through the thin p region and is subjected to self-absorption. It has been established that the influence of the temperature dependence of the optical absorption is manifested by a dip in the vicinity of 3 eV on the spectral curves $\gamma_{h\nu}(h\nu)$ (Fig. 1a, curves *4* and *5*). This feature is far less pronounced on the $\xi(h\nu)$ curves (Fig. 1b). A substantially stronger correlation is observed between other features of the $\gamma_{h\nu}(h\nu)$ and $\xi(h\nu)$ curves. This fact leads to the assumption that the temperature shift of the optical absorption bands is stronger than that of the emission bands, which are found to have significantly weaker ties with the band gap.

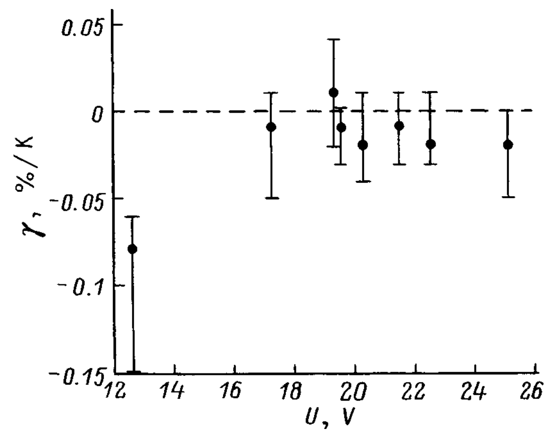

FIG. 5. Dependence of the temperature coefficient of the quantum efficiency of breakdown electroluminescence on the working voltage for 6H-SiC *p-n* structures.

It is evident from Fig. 1a that 6H-SiC has a characteristic feature in the form of a weak broad band on the $\gamma_{h\nu}(h\nu)$ curves with a maximum in the vicinity of 3 eV. The $\xi(h\nu)$ curves do not have this feature (Fig. 1b). The $\xi(h\nu)$ curves, in turn, have two extrema in the vicinity of 3.4 eV and 3.7 eV, indicating the presence of corresponding bands in the emission spectrum. However, these extrema do not appear on the $\gamma_{h\nu}(h\nu)$ curves.

It is also evident from Fig. 1a that the nature of the feature in the form of a broad maximum on the $\gamma_{h\nu}(h\nu)$ curves changes in a regular fashion with the working voltage. For sample 164 with $U<14$ V (curves *1* and *2*) this feature is not very pronounced on the $\gamma_{h\nu}(h\nu)$ curves (particularly at low current). The slope of the long-wavelength edge of the feature is greatest for samples having low breakdown voltages (curve *3*). For samples with comparatively high breakdown voltages (curve *5*) the given feature appears as a shallow maximum.

Considering that the bands located in the vicinity of 3.4 eV and 3.7 eV, which are very noticeable on the $\xi(h\nu)$ curves, scarcely alter the profile as the temperature varies, but do not show up on the $\gamma_{h\nu}(h\nu)$ curves, we can assume that their temperature shift is small in comparison with the corresponding shift of all other components of the radiation.

The behavior of the $\gamma_{h\nu}(h\nu)$ curves with variation of the current through the sample is dictated by U. Typical cases for samples with a uniform microplasma field, prepared on the basis of 6H-SiC, are shown in Fig. 3.

For a series of low-voltage samples a variation of the working current corresponds to a significant variation of the level of the $\gamma_{h\nu}(h\nu)$ curves with a slight variation of their profile (Fig. 3a, curves *1* and *2*). Mainly the second term in Eq. (1) varies in this case, indicating, on the one hand, that the type of radiative transitions is independent of the current and, on the other, that the current significantly influences free-carrier generation (most likely a variation of the temperature affects the density of carriers participating in radiative transitions in different degrees for different currents).

A weak current dependence of $\gamma_{h\nu}$ is observed for samples with $U>20$ V (Fig. 3a, curves *5* and *6*).

Sample 11 (Fig. 3a, curves *3* and *4*), which has positive values of the temperature coefficient of the breakdown electroluminescence quantum efficiency, resides at the threshold between the ranges of U corresponding to strong and weak current dependences of $\gamma_{h\nu}$ (to the best of our knowledge, examples of the observation of positive values have not been described in the literature). The density of carriers involved in radiative transitions probably increases as the temperature increases.

The positive sign of $\gamma_{h\nu}$ might be explained on the assumption that radiative transitions take place predominantly via high-energy holes resulting from impact ionization induced by electrons. In α-SiC a positive (''anomalous'') temperature dependence of the electronic impact ionization coefficient has been observed for an electric field directed parallel to the **C** axis and has been attributed to miniband splitting of the electron energy spectrum in the conduction band.[4] The state of sample 11 probably corresponds to a maximum fraction of high-energy holes with a density that depends ''anomalously'' on the temperature in the total free-carrier density specified by the electric current through the *p-n* junction. This state is the most probable for the threshold region between fully developed avalanche breakdown and the transition zone corresponding to impact ionization induced by tunneling electrons. It follows from previously published[2] curves of the differential resistance of *p-n* structures as a function of the working voltage, plotted for similar samples, that the voltage of sample 11 lies in this threshold region. However, a comparison of the characteristics of sample 11 and other samples with similar working voltages shows that the state of the ionization processes in the sample and the working voltage are probably not exactly related one-to-one for the investigated structures.

The occurrence of the above-indicated feature in the profile of the weak broad maximum on the $\gamma_{h\nu}(h\nu)$ curves is most likely a manifestation of a radiation component characterized by positive values of the temperature coefficient. A theoretical calculation[5] shows that a similar spectrum having a flat maximum in the energy range corresponding to $\sim 0.8E_g$ (E_g is the width of the band gap) is typical of direct radiative transitions between light-hole and heavy-hole subbands. If the possibility of an ''anomalous'' increase in the density of some of the free holes with increasing temperature (as mentioned above) is also taken into account, we can assume that the identified radiation component is associated with direct transitions of high-energy holes.

The spectra for several typical samples prepared on the basis of 15R-SiC are shown in Fig. 2. It is evident from Fig. 2a that the $\gamma_{h\nu}(h\nu)$ curves again have a weak broad band with a maximum near 2.8–2.9 eV, similar to the one observed for 6H-SiC. In contrast with 6H-SiC, however, a band of similar profile is also generally observed on the $\xi(h\nu)$ curves (Fig. 2b). On the whole, better correspondence is observed between the profiles of the $\gamma_{h\nu}(h\nu)$ and $\xi(h\nu)$ curves, except for the extrema in the vicinity of 3.4 eV and 3.7 eV, which are analogous to 6*H*-SiC. The reason for the difference in the properties of the samples prepared from 6H-SiC and 15R-SiC is still vague. The indicated disparity in the profiles of the curves for 6H-SiC is observed for all the investigated samples.

Spectra of a typical 3*C*-SiC sample are shown in Fig. 4. It is evident from Figs. 4a and 4b that conformity is observed in the nature of the $\gamma_{h\nu}(h\nu)$ and $\xi(h\nu)$ curves. The quantities $\gamma_{h\nu}$ assume negative values approximately an order of magnitude greater than for samples prepared on the basis of α-SiC. The $\xi(h\nu)$ curves do not exhibit any features in the vicinity of 3.4 eV and 3.7 eV.

The breakdown electroluminescence spectrum in the investigated range has at least two extrema: a maximum near 3.1 eV and a minimum near 2.5 eV (Fig. 4c). At these points the temperature shift is equal to zero, and $\gamma_{h\nu}$ is determined entirely by the second term in Eq. (1): $\gamma_{h\nu}=\gamma_e=(1/N_{h\nu})\times(\partial N_{h\nu}/\partial T)$. If this quantity is assumed to be independent of $h\nu$, the temperature shift of the emission bands can be estimated. An attempt to do so has been made for sample 16-1, for which the values of $\gamma_{h\nu}$ determined at the extremum points 3.1 eV and 2.5 eV essentially coincide (a slight difference in the values of $\gamma_{h\nu}$ at the extremum points is observed for the other samples). It follows from Eq. (1) that the coefficient of the temperature shift of the emission bands is

$$\alpha_T=\frac{d(h\nu)}{dT}=\frac{\gamma_{h\nu}-\gamma_e}{\xi}. \tag{2}$$

The spectral curves $\alpha_T(h\nu)$ determined from Eq. (2) are shown in Fig. 4d. The value of γ_e has been refined from the condition that α_T does not have any spikes in the vicinity of the extrema.

It is evident from Fig. 4d that a maximum is observed in the vicinity of the optical absorption edge (2.3 eV), with an amplitude $\sim 6\times10^{-4}$ eV/K, which agrees with published values of the temperature coefficient of the band gap.[6] In this region α_T is probably influenced by the temperature shift of the self-absorption edge. At all other points of the spectral curve α_T assumes values much smaller than the temperature coefficient of the band gap. The quantity α_T was found to increase smoothly as the photon energy increases.

Lacking any basis for assuming that the quantity $(1/N_{h\nu})(\partial N_{h\nu}/\partial T)$ is independent of $h\nu$, the resulting curve can only be interpreted as a crude estimate.

In summary, our investigation of the temperature dependence of the breakdown electroluminescence spectra of silicon carbide can be utilized to gain additional information about the mechanisms of the process. Moreover, such an investigation is a potential source of experimental data pertaining to the influence of temperature on the structure of the energy bands of the material.

[1] Yu. M. Altaĭskiĭ and A. M. Genkin, Zh. Tekh. Fiz. **52**, 543 (1982) [Sov. Phys. Tech. Phys. **27**, 350 (1982)].
[2] Yu. M. Altaĭskiĭ, A. M. Genkin, V. K. Genkina, and L. G. Ogneva, Élektron. Tekh., Ser. 2, No. 4 (190), 76 (1987).
[3] M. V. Belous, A. M. Genkin, V. K. Genkina, and O. A. Guseva, Fiz. Tekh. Poluprovodn. **31**, 213 (1997) [Semiconductors **31**, 169 (1997)].
[4] A. O. Konstantinov, Fiz. Tekh. Poluprovodn. **17**, 2124 (1983) [Semiconductors **17**, 1358 (1983)].
[5] W. Hacker, Phys. Status Solidi A **25**, 301 (1974).
[6] W. J. Choyke, *Silicon Carbide* (Mir, Moscow, 1972).

Translated by James S. Wood

LOW-DIMENSIONAL SYSTEMS

Self-organization of quantum dots in multilayer InAs/GaAs and InGaAs/GaAs structures in submonolayer epitaxy

G. É. Tsyrlin, V. N. Petrov, S. A. Masalov, and A. O. Golubok

Institute of Analytic Instrument Building, Russian Academy of Sciences, 198103 St. Petersburg, Russia
(Submitted October 27, 1998; accepted for publication November 18, 1998)
Fiz. Tekh. Poluprovodn. **33**, 733–737 (June 1999)

The experimental results of RHEED and scanning tunneling microscopy investigations of multilayer structures of InGaAs/GaAs quantum dots, obtained by submonolayer epitaxy on singular and vicinal GaAS (100) substrates, are reported. The results presented show that spatial ordering of nano-objects exists in multilayer structures for InAs and heteroepitaxial InGaAs layers. © *1999 American Institute of Physics.* [S1063-7826(99)02306-6]

1. INTRODUCTION

One of the main avenues in modern fundamental and applied surface physics is the study of the formation of nanostructures by self-organization of a surface during heteroepitaxial growth in lattice-mismatched systems.[1,2] This is because quantum dots and quantum wires formed as a result of the decomposition of a strained pseudomorphous layer at the interface of such semiconductors open up ways to produce new-generation optoelectronic devices[3,4] and make it possible to model and study the properties of ''artificial atoms.''[5] The progress made in the theory of nanostructure formation[6] and the discovery of ordering of quantum-size surface formations in the (InAs, InGaAs)/GaAs system directly during molecular-beam epitaxy (MBE)[7,8] give hope of obtaining quantum-size structures with prescribed geometric properties. In Ref. 9, a model of the process leading to self-organization of quantum dots, which consists in the production of multilayered structures, is proposed and supporting experimental data on ''effective'' self-organization of $Si_{0.25}Ge_{0.75}$ on an Si surface are presented. The results of Ref. 10 also confirm that this method is effective for producing quantum dots by classic molecular-beam epitaxy in the InAs/GaAs system. The use of so-called ''stacked'' quantum dots, i.e. multilayer systems with vertically electron-coupled quantum dots, as active regions in semiconductor lasers has made it possible already to improve substantially the device characteristics of the lasers (threshold current, radiation power, and characteristic temperature).[11,12]

Our objective in the present work is to use reflection HEED (RHEED) *in situ* and scanning tunneling microscopy (STM) *ex situ* to study the morphological characteristics of an ensemble of quantum dots which self-organize in multilayer InAs/GaAs and InGaAs/GaAs structures, obtained by submonolayer migration-stimulated epitaxy (SMSE) and submonolayer molecular-beam epitaxy (SMBE) on singular and vicinal GaAs (100) substrates.

2. EXPERIMENT

The growth experiments were preformed, using the ÉP1203 setup, on singular GaAs (100) substrates and on GaAs (100) substrates disoriented in the [011] direction. Samples (singular and vicinal), which had been chemically treated by the method described in Ref. 13, were glued, using indium, to the same molybdenum holder in a manner so as to reduce to a minimum the nonuniformity of the temperature field of the heater heating the sample and of the flux gradients at the surface. After the oxide layer was removed, a 300 nm thick GaAs buffer layer was grown in the growth chamber at substrate temperature $T_s = 610-630\,^\circ C$ in an As_4 flux, using the conventional MBE method, maintaining the 2×4 reconstruction of the surface and $T_s = 550\,^\circ C$. The buffer layer was doped with beryllium to a density of the order of $10^{16}\ cm^{-3}$ to ensure confinement of the tunneling current in the subsequent scanning tunneling microscopy investigation of the surface. After the buffer layer was grown, the sample temperature in the arsenic flux was lowered to $T_s = 470\,^\circ C$ (the moment at which the 2×4 surface reconstruction changed to 4×4). The As_4/Ga flux ratio was constant and equal to 3 in all experiments. The formation of each layer of InAs and InGaAs quantum dots was performed in the SMSE or SMBE growth regimes, described in detail in Ref. 14. In the SMSE regime the shutters for the group-V and -III elements are opened in succession, while in SMBE arsenic is deposited continuously, while the metal flux is directed onto the substrate cyclically.

In all cases three monolayers (MLs) of InGaAs or InAs were grown with successive cyclic deposition of 0.5 ML of the material (six cycles in all). Next, the three-dimensional nanoislands formed were buried with a GaAs:Be layer (the degree of doping $p = 10^{16}\ cm^{-3}$) by conventional MBE at the same temperature $T_s = 470\,^\circ C$ and the quantum-dot formation process was repeated. A special system for automatic control of the shutters of the molecular sources, following a predetermined program allowing for multiple repetition of the cycles inserted, was developed to grow multilayer struc-

 © 1999 American Institute of Physics

tures. After growth of the last layer of quantum dots was completed, the heater heating the sample was immediately switched off and removed from the sample-holder zone. The state of the surface was monitored *in situ* using an automatic system for detection and processing of RHEED patterns. The system consisted of a high-sensitivity video camera, a video recorder for recording the dynamics of the RHEED patterns during growth for further detailed processing, a computer for real-time processing of the video information, and an interface which coupled the video camera with the video recorder and the computer.[15] The GaAs and InAs growth rates were calibrated in advance using measurements of the oscillations of the intensity of the mirror reflection in the RHEED pattern from the calibration sample. The GaAs and InAs growth rates during the experiments were 0.3 and 0.8–0.1 ML/s, respectively.

The surface morphology of the samples was investigated *ex situ* by scanning tunneling microscopy (STM); the measurement method and regimes are described in Refs. 16 and 17. To perform prolonged STM measurements the samples were extracted from the growth chamber and placed in silicon-containing vacuum oil to protect their surface from oxidation. This made it possible to obtain reproducible STM images for one month after the samples were removed from the vacuum chamber. Reproducible and stable STM images were obtained on different sections of the experimental samples in the dc current regime with a positive bias on the sample.

3. RESULTS AND DISCUSSION

The *in situ* RHEED investigation of the heteroepitaxial growth of multilayer structures showed that the decomposition of the pseudomorphous layer in the top layers into an array of three-dimensional islands occurs at a smaller thickness of the deposited material than for the bottom layer. Thus, for InAs/GaAs SMSE when the first layer of the multilayer structure is formed three-dimensional islands form after the deposition of 1.7 ML, and the decomposition of the pseudomorphous layer on subsequent layers is observed after 1.0–1.1 ML. In our opinion this effect can be explained by the accumulation of strain due to the formation of three-dimensional islands in the bottom layers, which makes an additional contribution to the total elastic strain of the multilayer structure. It is expressed to a lesser degree during $In_{0.67}Ga_{0.33}As$/GaAs growth, where the decomposition of the pseudomorphous layer is observed at 3.0 ML on the first layer and at 2.7–2.8 ML on subsequent layers. This is probably due to weaker straining of the nanocrystallites or lower InGaAs islands in the gallium arsenide matrix than in the InAs case. A similar effect is observed for the SMSE regime.

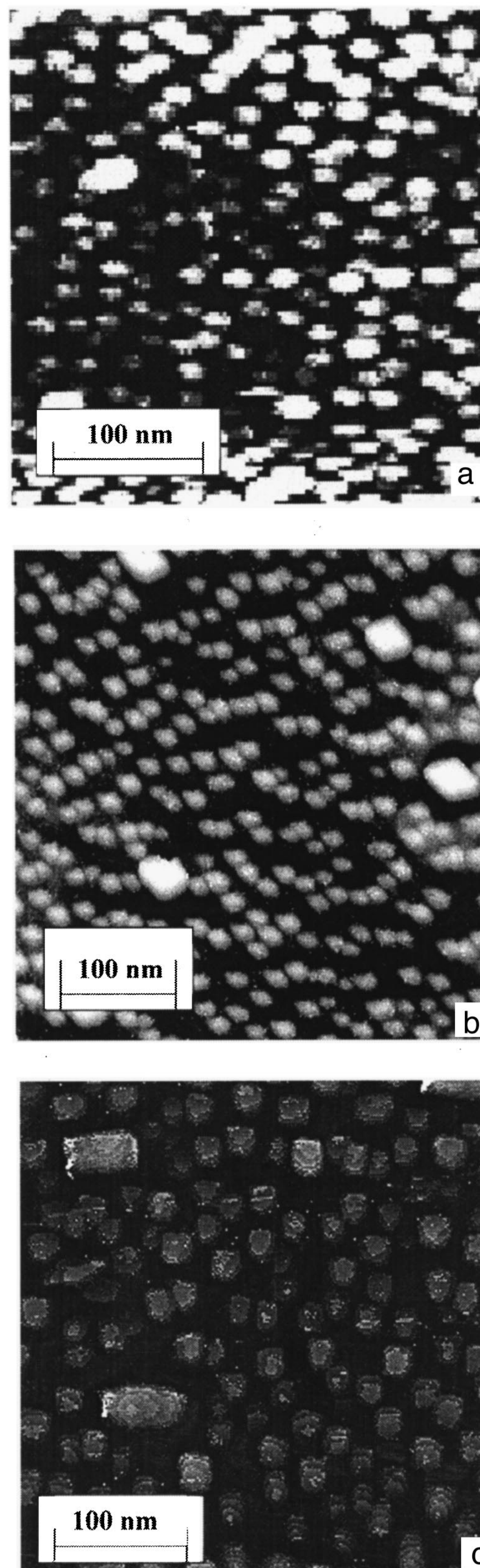

FIG. 1. STM images of sections of a surface after the deposition of one layer (a), five layers (b), and ten layers (c) of InAs on GaAs (100). The edges of the images are parallel to the [011] and [$0\bar{1}1$] directions.

Figures 1a–1c show STM images of the surface of samples after the deposition of one, five, and ten layers of InAs quantum dots in the SMSE regime on the singular GaAs (100) surface with an average thickness of the gallium arsenide layer between them of 5 nm. Statistical analysis of the images presented shows that as the number of layers in the multilayer structure increases, the lateral sizes of the quantum dots increase and the density of quantum dots decreases, which is especially noticeable with a large number

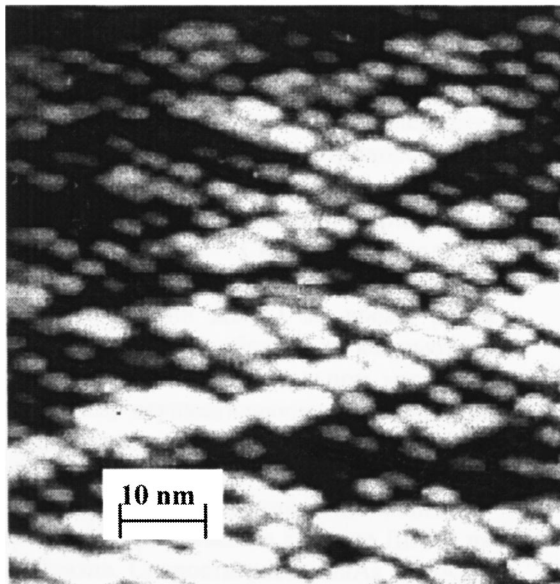

FIG. 2. STM image of the surface after the deposition of 10 layers of InAs quantum dots on a singular GaAs (100) surface with 6 nm thick GaAs layers between the quantum-dot layers. The edges of the image are parallel to the directions [011] and [0$\bar{1}$1].

of layers. Thus, the lateral sizes are $d=12$ and 18 nm and the surface density is $\rho=2.5\times10^{11}$ and 9×10^{10} cm^{-2} with one and ten layers of quantum dots, respectively. It should be noted that similar tendencies have also been observed in Refs. 11 and 12 by transmission electron microscopy on similar samples. As the number of layers increases, quantum-size crystallites with two distinct sizes appear at the same time as the deviation from the average sizes of islands decreases and the islands show local spatial ordering in rows in the [010] and [001] directions. The density of large islands is low and is approximately 1/100 of the total number of quantum dots.

Increasing the thickness of the GaAs layer between the quantum dots to 6 nm changes the surface morphology substantially. Figure 2 shows an STM image of the surface after the deposition of 10 layers of InAs quantum dots on the singular surface for this GaAs thickness. Three basic differences from Fig. 1c are observed: The degree of spatial ordering of the quantum dots in the [010] and [001] directions is higher, the density of quantum dots is higher, and there are no islands with different sizes. The average sizes and the surface density in this case are $d=18$ nm and $\rho=10^{11}$ cm^{-2}.

Changing the composition of the solid solution $In_xGa_{1-x}As$ ($x=0.67$) also produces large changes in the surface morphology. Figure 3 shows STM images of the surface after SMSE deposition of one layer (Fig. 3a) and ten layers (Fig. 3b) of quantum dots (the thickness between the layers is 50 nm). For one layer the quantum dots are arranged isotropically. The presence of anisotropy in the spatial arrangement of nano-objects along [010] and [001] directions and in the characteristic lateral dimensions in the [011] and [0$\bar{1}$1] directions are characteristic for a multilayer structure. The average size ratio in the latter case is 4. It should be noted that such an anisotropy has been observed in

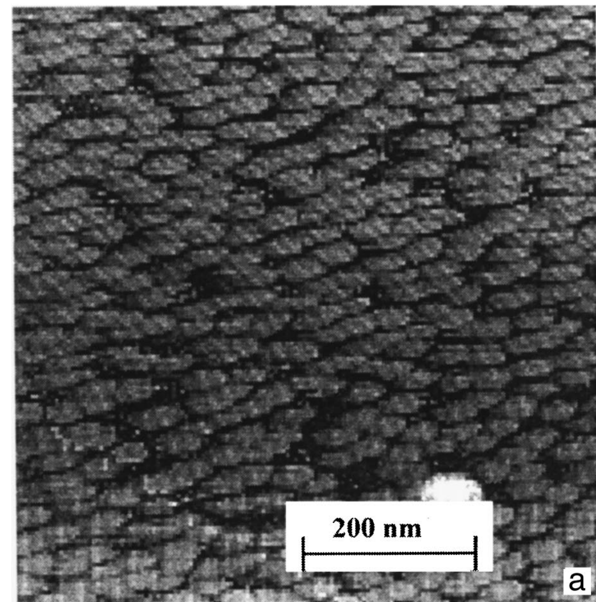

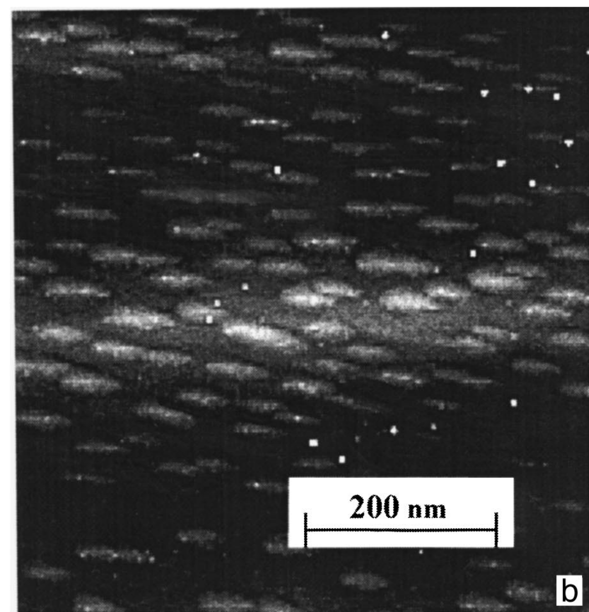

FIG. 3. STM images of the surface after SMSE deposition of one layer (a) and ten layers (b) of $In_xGa_{1-x}As$ ($x=0.67$) quantum dots with 50 nm thickness between the layers. The edges of the image are parallel to the directions [011] and [0$\bar{1}$1].

Ref. 18, which led to anisotropy of the working characteristics of heterolasers whose operating region consisted of an InGaAs/GaAs multilayer structure.

Further investigations showed that lateral ordering can be improved by using vicinal surfaces and (or) by increasing the number of layers of quantum dots. Figure 4 shows an STM image of a 2×2 μm^2 section of the surface in the case of GaAs (100) substrate, disoriented by 7° in the [011] direction with SMSE deposition of 20 layers of quantum dots. The surface sections are divided into smooth terraces located between steps with an average height of the order of 10–20 ML (3–6 nm). These steps probably form as a result of the well-known stacking of monatomic steps, initially formed on the vicinal surface during epitaxial growth.[19,20] Uniform

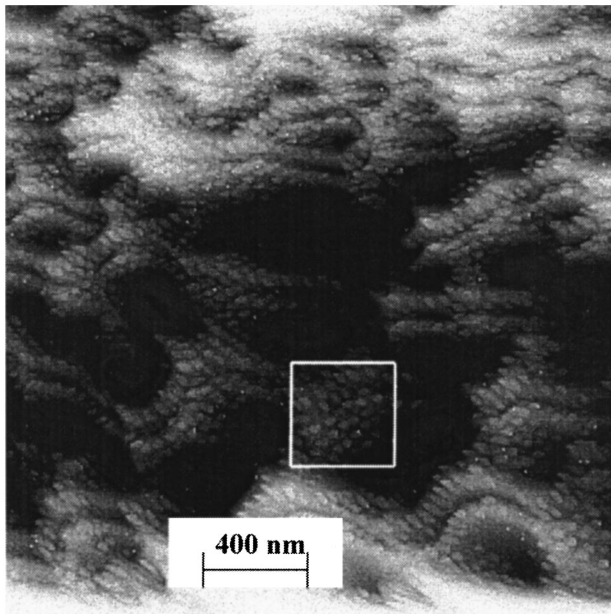

FIG. 4. STM image of a section of the surface using a GaAs (100) substrate disoriented by 7° in the [011] direction with the deposition of 20 quantum-dot layers by SMSE. The edges of the image are parallel to the directions [011] and $[0\bar{1}1]$.

quantum-dot arrays oriented in [010] and [001] directions form on the surface of a terrace (for example, inside the framed section in the image).

4. CONCLUSIONS

In summary, we have investigated by RHEED and STM the characteristic features of the formation of multilayer structures in a InGaAs/GaAs (100) system during submonolayer epitaxy from molecular beams. It was established that the critical thickness of quantum-dot formation decreases with increasing number of layers of nano-objects. This is especially noticeable during the deposition of the second layer. This effect can be explained by effective accumulation of elastic strain in the multilayer structure as the number of layers increases. It was shown that increasing the number of layers and (or) the vicinality of the surface gives a greater degree of ordering of the quantum dots in the top layers, increases their sizes, and decreases their density. This effect is characteristic for the InGaAs/GaAs and InAs/GaAs systems. Decreasing the thickness of the spacer between the quantum-dot layers changes the spatial distribution of the quantum dots in the upper layers.

We thank N. K. Polyakov, D. N. Demidov, N. P. Korneev, and Yu. B. Samsonenko for participating in the growth experiments and N. N. Ledentsov, D. Bimberg, and V. G. Dubrovskiĭ for helpful discussions.

This work was partially supported by the scientific program ''Physics of Solid-State Nanostructures'' (Grant No. 98-2029) and the Russian Fund for Fundamental Research (Grant No. 98-02-18317). G. É. Tsyrlin is grateful to INTAS for financial support (Grant No. YSF 98-54).

[1] L. Goldstein, F. Flas, J. Y. Marzin, M. N. Charasse, and G. Le Roux, Appl. Phys. Lett. **47**, 1099 (1985).
[2] Y.-W. Mo, B. S. Swartzentruber, R. Kariotis, M. B. Webb, and M. G. Lagal-Ly, Phys. Rev. Lett. **63**, 2393 (1989).
[3] N. Kirstaedter, N. N. Ledentsov, M. Grundmann, D. Bimberg, V. M. Ustinov, S. S. Ruvimov, M. V. Maximov, P. S. Kop'ev, Zh. I. Alferov, U. Richter, P. Werner, U. Gössele, and J. Heydenreich, Electron. Lett. **30**, 1416 (1994).
[4] N. N. Ledentsov, M. Grundmann, N. Kirstaedter, O. Schmidt, R. Heitz, J. Böhrer, D. Bimberg, V. M. Ustinov, V. A. Shchukin, A. Ya. Egorov, A. E. Zhukov, S. Zaitsev, P. S. Kop'ev, Zh. I. Alferov, S. S. Ruvimov, A. O. Kosogov, P. Werner, U. Gössele, and J. Heydenreich, Solid-State Electron. **40**, 785 (1996).
[5] N. N. Ledentsov, V. M. Ustinov, V. A. Shchukin, P. S. Kop'ev, Zh. I. Aferov, and D. Bimberg, Fiz. Tekh. Poluprovodn. **32**, 385 (1998) [Semiconductors **32**, 343 (1998)].
[6] V. A. Shchukin, N. N. Ledentsov, P. S. Kop'ev, and D. Bimberg, Phys. Rev. Lett. **75**, 2968 (1995).
[7] G. E. Cirlin, G. M. Guryanov, A. O. Golubok, S. Ya. Tipissev, N. N. Ledentsov, P. S. Kop'ev, M. Grundmann, and D. Bimberg, Appl. Phys. Lett. **67**, 97 (1995).
[8] M. Grundmann, J. Christen, N. N. Ledentsov, J. Böhrer, D. Bimberg, S. S. Ruvimov, P. Werner, U. Richter, U. Gössele, J. Heydenreich, V. M. Ustinov, A. Ya. Egorov, A. E. Zhukov, P. S. Kop'ev, and Zh. I. Alferov, Phys. Rev. Lett. **74**, 4043 (1995).
[9] J. Tersoff, C. Teichert, and M. G. Lagally, Phys. Rev. Lett. **76**, 1675 (1996).
[10] S. A. Komarov, G. S. Solomon, and J. S. Harris, Jr., in *Proceedings of the 5th International Symposium ''Nanostructures: Physics and Technology 97''* (St. Petersburg, Russia, 1997) p. 314.
[11] A. E. Zhukov, A. Yu. Egorov, A. R. Kovsh, V. M. Ustinov, N. N. Ledentsov, M. V. Maksimov, A. F. Tsatsul'nikov, S. V. Zaĭtsev, N. Yu. Gordeev, P. S. Kop'ev, D. Bimberg, and Zh. I. Alferov, Fiz. Tekh. Poluprovodn. **31**, 483 (1997) [Semiconductors **31**, 411 (1997)].
[12] Yu. M. Shernyakov, A. Yu. Egorov, B. V. Volovik, A. E. Zhukov, A. R. Kovsh, A. V. Lunev, N. N. Ledentsov, M. V. Maksimov, A. V. Sakharov, V. M. Ustinov, Zhao Zhen, P. S. Kop'ev, Zh. I. Alferov, and D. Bimberg, Pis'ma Zh. Tekh. Fiz. **24**(9), 50 (1998) [Tech. Phys. Lett. **29**, 351 (1998)].
[13] G. M. Gur'yanov, N. N. Ledentsov, V. N. Petrov, Yu. B. Samsonenko, G. É. Tsyrlin, and A. G. Filaretov, Pis'ma Zh. Tekh. Fiz. **19**(18), 64 (1993) [Tech. Phys. Lett. **19**, 591 (1993)].
[14] G. M. Guryanov, G. E. Cirlin, V. N. Petrov, N. K. Polyakov, A. O. Golubok, S. Ya. Tipissev, V. B. Gubanov, Yu. B. Samsonenko, N. N. Ledentsov, V. A. Shchukin, M. Grundmann, D. Bimberg, and Zh. I. Alferov, Surf. Sci. **352–354**, 651 (1996).
[15] G. M. Gur'yanov, V. N. Demidov, N. P. Korneeva, V. N. Petrov, Yu. B. Samsonenko, and G. É. Tsirlin, Zh. Tekh. Fiz. **67**(8), 111 (1997) [Tech. Phys. **42**, 956 (1997)].
[16] G. M. Guryanov, G. E. Cirlin, V. N. Petrov, N. K. Polyakov, A. O. Golubok, S. Ya. Tipissev, E. P. Musikhina, V. B. Gubanov, Yu. B. Samsonenko, and N. N. Ledentsov, Surf. Sci. **331–333**, 414 (1995).
[17] A. O. Golubok, S. A. Masalov, N. B. Ponomareva, V. N. Petrov, S. Ya. Tipisev, and G. É. Tsyrlin, Pverkhnost'. Rentgenovskie, sinkhrotronnye, i neĭtronnye issledovaniya, No. 2, 70 (1998).
[18] Yu. M. Shernyakov, A. Yu. Egorov, B. V. Volovik, A. E. Zhukov, A. R. Kovsh, A. V. Lunev, N. N. Ledentsov, M. V. Maksimov, A. V. Sakharov, V. M. Ustinov, Zhao Zhen, P. S. Kop'ev, Zh. I. Alferov, and D. Bimberg, Ps'ma Zh. Tekh. Fiz. **24**(9), 50 (1998) [Tech. Phys. Lett. **29**, 351 (1998)].
[19] T. Ide, A. Yamashita, and T. Mizutani, Phys. Rev. D **46**, 1905 (1992).
[20] P. Smilauer, Vacuum **50**, 115 (1998).

Translated by M. E. Alferieff

Dimensionality effects in the hot-electron photoluminescence of gallium arsenide: 2D–quasi-3D transition

V. F. Sapega, V. I. Perel', D. N. Mirlin, and I. A. Akimov

A. F. Ioffe Physicotechnical Institute, Russian Academy of Sciences, 194021 St. Petersburg, Russia

T. Ruf, M. Cardona, W. Winter, and K. Eberl

Max-Planck-Institut für Festkörperforschung, D-70569 Stuttgart, Germany

(Submitted January 25, 1999; accepted for publication January 27, 1999)
Fiz. Tekh. Poluprovodn. **33**, 738–741 (June 1999)

The influence of the miniband width in superlattices on the polarization characteristics of hot-electron photoluminescence (HEPL) is investigated. It is shown that the energy dependence and the magnetic field dependence of polarization change significantly as the width of the electron minibands increases. The limits of applicability are established for the tight-binding approximation in the calculation of optical transitions in superlattices. © *1999 American Institute of Physics.* [S1063-7826(99)02406-0]

We have recently shown[1] that the polarization of hot-electron photoluminescence (HEPL) depends on the dimensionality of the investigated GaAs samples.

In a bulk semiconductor the linear polarization (for a linearly polarized pump) ρ_l increases slightly as the recombining electron energy E increases (this dependence is dictated entirely by the influence of the spin-orbit split-off valence band). On the other hand, in a two-dimensional semiconductor (GaAs/AlAs quantum-well structure) the polarization $\rho_l=0$ at $E=0$ and increases to $\rho_l\sim0.5$ when $E>E_1$, where E_1 is the energy of the first quantum-well state.

In the intermediate case of superlattices the extrapolation of $\rho_l(E)$ brings it to a value of zero at an electron energy E close to the width of the first electron miniband Δ, rather than at $E=0$ as in a quantum-well structure. This behavior of $\rho_l(E)$ has been explained in the tight-binding approximation, which rests on the assumption of weak interaction of neighboring quantum wells. It has been shown[1] that this approximation is valid in superlattices in narrow electron minibands (in particular, in GaAs/AlAs superlattices with wide barriers $L_b\geqslant6$ Å and for quantum wells of fixed width $L_w=40$ Å). It was reasonable to expect the energy dependence $\rho_l(E)$ in superlattices with wide minibands to be similar to the dependence $\rho_l(E)$ in bulk GaAs.

Here we report an investigation of the transition from the two-dimensional (2D) to the bulk (quasi-3D) case by the polarized HEPL method. To do so, we have investigated the polarization characteristics in a series of superlattices [60 periods (40/6) Å of GaAs/$Al_xGa_{1-x}As$] over a wide range of barrier heights (i.e., Al contents in the barriers). These samples were grown by molecular-beam epitaxy on a semi-insulating, undoped, (001)-oriented substrate . The middle part of each GaAs quantum well (≈15 Å) was doped with Be ($N_a\sim10^{18}\,\mathrm{cm}^{-3}$).

RESULTS AND DISCUSSION

A. Linear Polarization of Hot-Electron Photoluminescence

Figure 1 shows the energy dependence of the linear polarization of HEPL ρ_l in superlattices with various Al contents ($x\sim0.3-1$), i.e., with various barrier heights U_b (0.29–1.06 eV). In this figure the calculated values of $\eta=\Delta_G/\Delta$ are shown for each case, where Δ_G is the band gap between the first and second electron minibands. Also shown in the figure, in the interest of clarity, are data obtained in quantum-well structures (dark squares in Fig. 1a) and in bulk GaAs (dark squares in Fig. 1f). In the case of bulk GaAs the experimental data are approximated by a dashed line, which is reproduced in all the graphs of Fig. 1.

The measured dependence $\rho_l(E)$ for superlattices with the highest barriers ($x=1$) (see the light circles in Fig. 1a and the solid line approximating them, which is reproduced in all other graphs of Fig. 1) is in good agreement with the analysis in the tight-binding approximation.

It follows from this discussion that the energy dependence of ρ_l in superlattices having the narrowest minibands is similar to that observed in the case of quantum-well structures. The similarity is distinctly evident from a comparison of the slopes of the $\rho_l(E)$ curves in these two cases in Fig. 1a. The same dependence $\rho_l(E)$ has been observed for a superlattice with $x=0.8$.

However, major changes in the dependence $\rho_l(E)$ occur in superlattices with $x\leqslant0.6$, where the lowering of the barrier height significantly modifies the energy dependence of ρ_l.

1. In the range of electron energies $0<E<\Delta$ the quantity $\rho_l(E)$ increases slowly, and the characteristic slope of the curve is smaller than for the superlattice in Fig. 1a [we note that $\rho_l(E)$ is close to zero in this energy range for superlattices with the highest barriers, i.e., with $x=1$).

2. The slope of the $\rho_l(E)$ curve for $E>\Delta$ gradually decreases as the barrier height decreases.

The most pronounced changes are observed for superlat-

 © 1999 American Institute of Physics

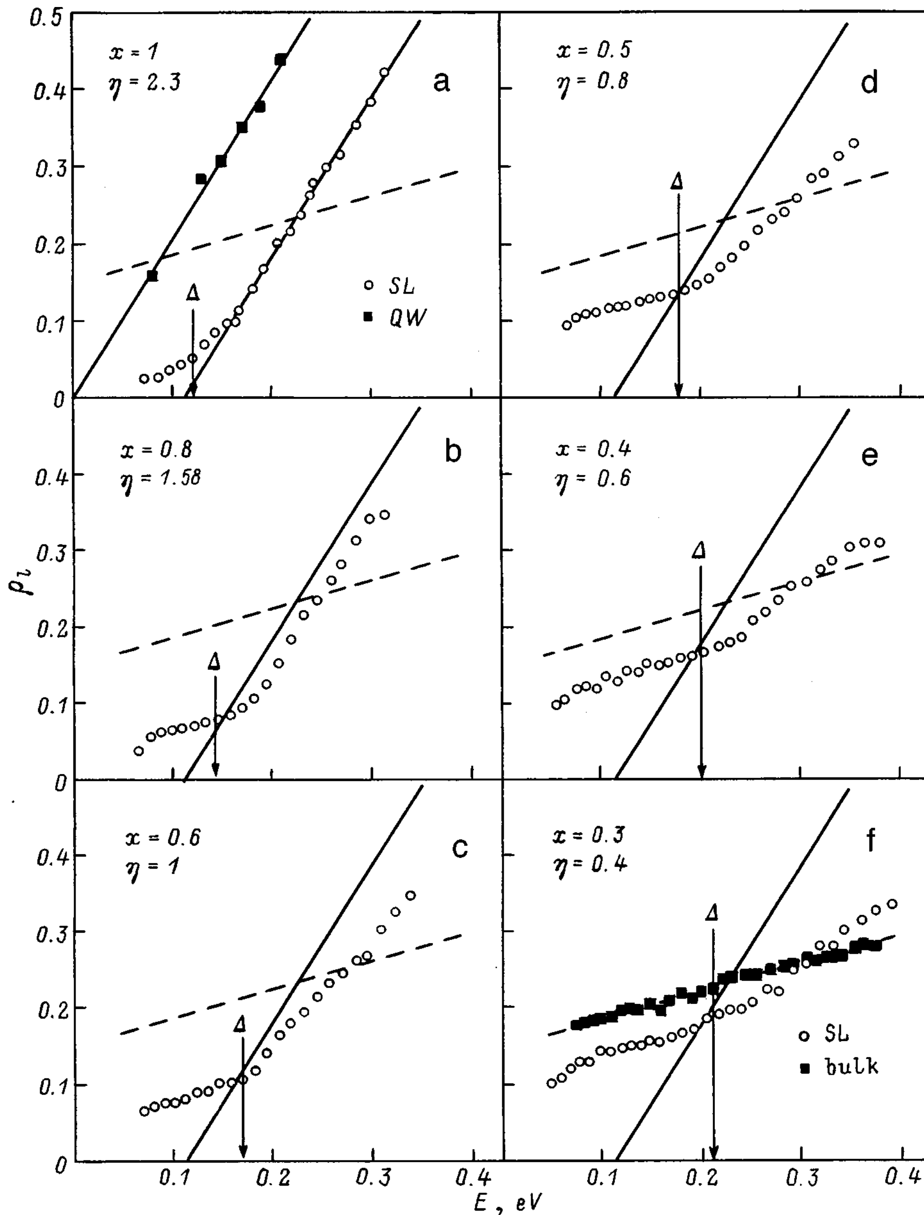

FIG. 1. Dependence of the linear polarization of hot-electron photoluminescence on the electron energy for quantum-well structures, superlattices, and bulk GaAs. The miniband width Δ varies from 0.12 eV to 0.22 eV as x is varied from 1 to 0.3. The evolution of $\rho_l(E)$ with variation of x, i.e., the barrier height, is clearly evident.

tices with $x=0.3$ (Fig. 1f), where the graph of $\rho_l(E)$ (light circles) is very similar to the bulk GaAs case (dark squares). However, certain details associated with the quasi-2D motion of electrons for $E>\Delta$ are preserved. This constancy is witnessed in the fact that the slope of the $\rho_l(E)$ curve for $E>\Delta$ differs from the slope for $0<E<\Delta$, since electrons having a kinetic energy higher than Δ move predominantly in the plane of the superlattice.

It can be shown that the energy at which the slope of $\rho_l(E)$ changes corresponds to the top of the electron miniband. These experimentally observable points are in good agreement with the values calculated in the Kronig–Penney model, which are indicated by vertical lines labeled Δ in Fig. 1.

B. Circular Polarization of Hot-Electron Photoluminescence

Another characteristic difference between HEPL in bulk GaAs and in quantum-well structures is associated with the circular polarization ρ_c of luminescence (in circularly polarized excitation). In the bulk case we encounter the so-called effect of spin-momentum correlation of photoexcited electrons, which is described by a term proportional to the expression $(\hat{\boldsymbol{\sigma}}\cdot\mathbf{k})(\mathbf{k}\cdot\mathbf{n})$ in their density matrix (here $\hat{\boldsymbol{\sigma}}$ denotes the Pauli matrices, and $\mathbf{n}$ is the unit vector along the angular momentum of the exciting photons).[2] This effect increases the circular polarization of luminescence.

Direct experimental confirmation of this effect has been obtained in Ref. 3, where ρ_c was observed to increase in a magnetic field B in Faraday geometry. The behavior of ρ_c as a function of the magnetic field showed that the influence of the magnetic field reduces to cyclotron rotation of the photoexcited electron momenta and, hence, to the breaking of spin-momentum correlation. The spin-momentum correlation effect does not occur in quantum wells; it is impossible to write an appropriate term for it, because the electron momentum does not have a component in the direction of the angu-

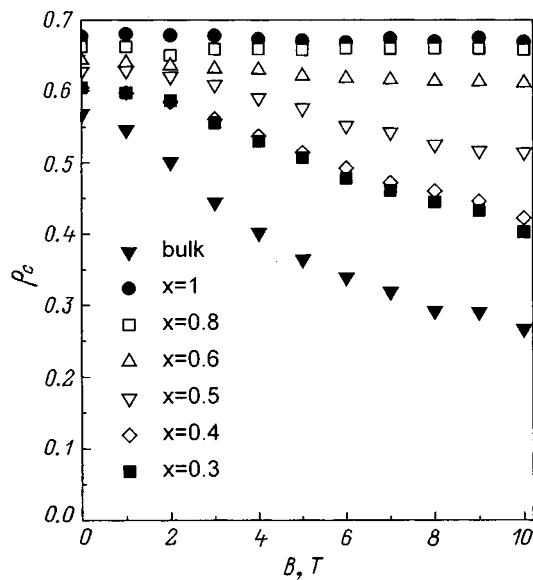

FIG. 2. Dependence of the circular polarization of hot-electron photoluminescence on the electron energy for superlattices and bulk GaAs. The results are given for the same samples as in Fig. 1. The spin-momentum correlation effect is restored in superlattices with wide minibands (see $x=0.4$ and $x=0.3$).

lar momentum **n** (**n** is assumed to be perpendicular to the plane of the quantum-well structure). Results given below attest to the onset of spin-momentum correlation in superlattices as the widths of their minibands increase.

Figure 2 shows the magnetic field dependence of ρ_c, measured in Faraday geometry, for electrons having a kinetic energy $E\sim 80-100$ meV. In bulk GaAs ρ_c decreases rapidly (dark inverted triangles) as the field B increases due to the breaking of spin-momentum correlation. Spin-momentum correlation does not occur in superlattices with narrow minibands, and ρ_c does not vary as B is increased [dark circles ($x=1$) and squares ($x=0.8$)]. In the case of wide-gap superlattices the circular polarization decreases as the magnetic field is increased. This effect becomes noticeable in superlattices with $x\leqslant 0.6$ and implies that the formation of a wide miniband restores the spin-momentum correlation effect. In superlattices with $x\sim 0.3$ (dark squares in Fig. 2) the breaking of spin-momentum correlation is already comparable with the same effect in the case of bulk GaAs.

In superlattices the spin-momentum correlation effect is described by the term $\beta(k,Q)(\hat{\boldsymbol{\sigma}}\cdot\mathbf{k})(\mathbf{Q}\cdot\mathbf{n})$ in the density matrix of the photoexcited electrons, where $\mathbf{k}$ is the quasi-wave-vector in the quantum well plane, and $\mathbf{Q}$ is the quasi-wave vector corresponding to the miniband. It can be shown that the coefficient β is proportional to the overlap integral of the electron and hole wave functions in neighboring wells and must therefore increase as the barrier height decreases. The enhancement of spin-momentum correlation as the barrier height decreases is manifested in the strong influence of the magnetic field on the circular polarization (see Fig. 2).

CONCLUSIONS

In the study we have discovered a strong dependence of the polarization of HEPL on the superlattice miniband width. This dependence undergoes significant changes upon transition from superlattices with narrow minibands to ''wide-gap superlattices,'' in which it becomes more like the analogous dependence in bulk GaAs. Other optical characteristics of superlattices can be expected to exhibit significant changes in the same interval of η corresponding to the 2D–quasi-3D transition.

In the dependence of the degree of linear polarization on the electron energy a characteristic bend is observed at energies corresponding to the miniband width.

We have established that the spin-momentum correlation effect, which is characteristic of the bulk material but does not occur in quantum wells, is restored in superlattices as the width of their minibands increases.

This work has received financial support through grants from the Russian Fund for Fundamental Research (RFFI, Nos. 96-02-16895, 96-15-96393, and 96-15-96392) and Volkswagen (No. 1/70958).

[1] V. F. Sapega, V. I. Perel', A. Yu. Dobin, D. N. Mirlin, I. A. Akimov, T. Ruf, M. Cardona, and K. Eberl, Phys. Rev. B **56**, 6871 (1997).
[2] V. D. Dymnikov, M. I. D'yakonov, and V. I. Perel', Zh. Éksp. Teor. Fiz. **71**, 2373 (1976) [Sov. Phys. JETP **44**, 1252 (1976)].
[3] I. Ya. Karlik, D. N. Mirlin, L. P. Nikitin, D. G. Polyakov, and V. F. Sapega, JETP Lett. **36**, 192 (1982).

Translated by James S. Wood

AMORPHOUS, GLASSY, AND POROUS SEMICONDUCTORS

Effect of substrate material on the rate of growth and the optical parameters of *a*-C:H layers

T. K. Zvonareva and L. V. Sharonova*)

A. F. Ioffe Physicotechnical Institute, Russian Academy of Sciences, 194021 St. Petersburg, Russia
(Submitted November 26, 1998; accepted for publication December 2, 1998)
Fiz. Tekh. Poluprovodn. **33**, 742–746 (June 1999)

a-C:H layers were grown by dc magnetron reactive sputtering of a graphite target in Ar + H_2 plasma. Ellipsometric measurements were carried out and analyzed at a wavelength of 6328 Å for three sets of *a*-C:H layers with different thicknesses (different sputtering times) on silicon, fused quartz, and glass-ceramic substrates. It was shown that the substrate material had a substantial effect upon *a*-C:H growth: *a*-C:H layers on Si substrates were uniform up to ~ 7000 Å thickness; for thin layers (<1000 Å) the growth rate was greater on quartz than on Si; the refractive index values of *a*-C:H were slightly different on quartz and Si substrates (1.60−1.65 and 1.65−1.72, respectively); *a*-C:H layers on glass-ceramic substrates were not uniform and had variable refractive index. © *1999 American Institute of Physics.*
[S1063-7826(99)02506-5]

Amorphous hydrogenated carbon has a number of unique properties, such as chemical stability and high hardness, and for this reason it is an attractive material for practical applications and physical studies. The properties of a material containing different phases (graphite-like phases, diamond-like phases, polymer clusters) depends strongly on the conditions of its fabrication. One of the fabrication parameters is the substrate material. The present study is a continuation of a number of studies investigating layers of amorphous hydrogenated carbon, fabricated by magnetron sputtering (see, e.g., Refs. 1–3), and has as its goal a comparative analysis of the growth rates and optical parameters of *a*-C:H layers on silicon, fused-quartz, and glass-ceramic substrates. The substrate materials in our experiments were chosen for the following reasons, namely, that layers are often grown on fused-quartz substrates for spectrum studies in the visible spectral range, on silicon substrates for infrared spectroscopy, and on glass-ceramic substrates for electrical measurements. Under such conditions, when results of different experiments are compared, there is no final certainty that one is considering one and the same material.

Layers of amorphous hydrogenated carbon (*a*-C:H) were deposited by reactive magnetron sputtering of a graphite target at constant current in an argon–hydrogen (80% Ar + 20% H_2) atmosphere. The layers were prepared on a 01NI-7-006 ''Oratoriya-5'' commercial setup with a flat annular cathode—the target, a grounded anode in the center of the ring, and a set of permanent magnets located under the cathode, creating a magnetic field. The setup was equipped with a planetary mechanism which provides a two-step revolution of the substrate holders with a rate of 30 revolutions per minute. This rate of revolution ensures uniform heating of the substrate and uniform layer growth in the substrate plane.

As the substrates, we used single-crystal silicon wafers (KDB-20) with [100] orientation, fused quartz, and glass-ceramic (ST32-1), all with mirror-smooth surfaces, and all of which were washed with organic solvents immediately before deposition of the *a*-C:H layer. The substrates were placed in the sputtering chamber after being heated to 200 °C. A voltage of 360 V was applied to the electrodes, with the discharge current being 1 A and the working gas pressure $\sim 10^{-2}$ Torr.

Obviously, the thickness of the grown *a*-C:H layer, without changing any other fabrication parameter, is controlled by the deposition time (target sputtering time). In our experiments we prepared samples under different deposition times (t) in the interval 0 to 30 min, and also under the deposition times $t = 1$ h, 2 h, and 5 h 15 min. During each growth shift, three substrates (silicon, fused quartz, and glass-ceramic) were loaded into the setup simultaneously. Thus, we prepared series of films of different thicknesses, obtained under identical conditions, but on different substrates.

We performed ellipsometric measurements on all of the samples using an LÉF-3M laser null-ellipsometer. As the radiation source we used a He–Ne laser, with radiation wavelength $\lambda = 6328$ Å. The measurements were made at different angles of incidence (reflection) of the light beam in the interval $\varphi = 50-70°$.

The essence of the ellipsometric method is that the accuracy of determination of the optical characteristics (complex refractive index) and thicknesses of the layers from the ellipsometric measurements depends strongly on the interplay of the conditions of measurement (wavelength, angle of

 © 1999 American Institute of Physics

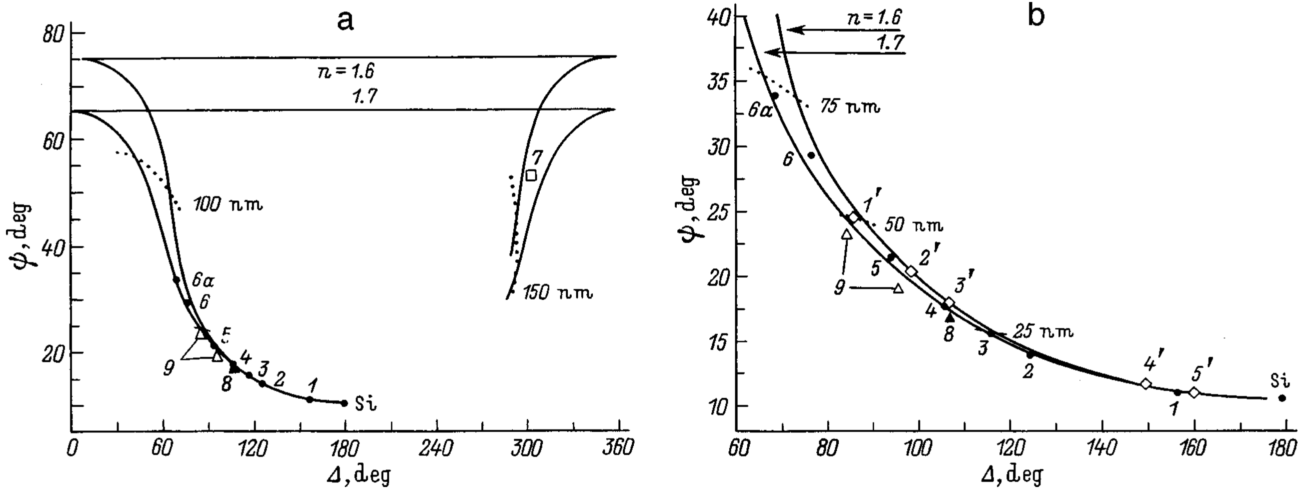

FIG. 1. General form (a) and segment (b) of the $\psi-\Delta$ nomogram for a-C : H layers on silicon with $\varphi=70°$. Points correspond to experiment; (*1–6*) correspond to layers grown at $t=2$, 7, 10, 13, 17, 30 min, *6a* — $t=30$ min, *7* — 1 h, *8* — 2 h, *9* — 5 h 15 min; *6, 6a* — two different samples, obtained for the same duration of deposition, but in different events; the two points labeled *9* correspond to two different points on the surface of the same sample; (*1′–5′*) — successive ion etching of a layer with growth time $t=30$ min (point *6*) for etch time equal to 2, +1, +1, +2, +5 min. Solid lines — calculation with the following parameter values: complex refractive index of silicon $N_{\mathrm{Si}}=3.882-i0.02$ (Ref. 6), refractive indices of the growing layer $n=1.6$ and 1.7 (indicated); markers indicating the thickness of the dielectric layer are provided in the first ellipsometric period.

incidence) and the parameters of the investigated structure (complex refractive index of the substrate, of the layer, and of the layer thickness) (see, e.g., Refs. 4 and 5). Therefore, in each series of samples, to facilitate analysis of the measurements, we chose data at specific angles of incidence for each substrate material: $\varphi=50$ and 70° for a-C:H on Si, $\varphi=50$ and 65° for a-C:H on quartz, and $\varphi=50$ and 55° for a-C:H on glass-ceramic. These were the data we used in our work.

We present the results of our measurements in the form of ellipsometric parameters—the amplitude parameter ψ and the phase parameter Δ entering into the basic equation of ellipsometery $\rho=\tan\psi\cdot\exp(i\Delta)=R_pR_s$, where R_p and R_s are the complex amplitude reflection coefficients for the electric vector of the light wave in the plane of incidence and perpendicular to it.[4,5] Solution of the inverse problem to determine the parameters of the a-C:H layers was not applied. To analyze the experimental data, we compared them with calculation (the direct problem) in the model of a uniform dielectric layer on substrate.

Since the function ρ (and consequently ψ and Δ) varies periodically with layer thickness and since the number of the period is not specified in the ellipsometric measurements, we estimated the thicknesses in order of magnitude using a Linnik interference microscope.

Figure 1a compares the results of measurements of ellipsometric parameters for a-C:H layers on silicon substrates with the calculated nomogram for two refraction indices of the growing layer, $n=1.6$ and 1.7, which subtends a large part of the ellipsometric period. Figure 1b plots a segment of this same plot, but with increased scale, where most of the points are concentrated. In the calculations we used the complex refractive index of silicon $N_{\mathrm{Si}}=3.882-i0.02$ (Ref. 6). It can be seen from the figure that the points *1–6* and *6a* corresponding to short deposition times, 30 min or less, and also points for samples with $t=1$ h (point *7*), 2 h (point *8*), 5 h 15 min (the two points labeled *9*) have some spread, but the refractive indices are packed into a narrow interval of values: $n=1.65-1.72$.

The calculated curves in Fig. 1a are labeled by markers indicating the thickness of the growing layer. To determine the thickness it is necessary to take into account the number of the period: point *8* belongs to the second period while points *9* belong to the fourth period. A period corresponds to a change in the layer thickness $d_0=\lambda/2(n^2-\sin^2\varphi)^{1/2}$, which for $n=1.72$ and $\varphi=70°$ amounts to ~2200 Å. Thus, for extended sputtering (5 h 15 min) layers of thickness $d\approx7000$ Å are obtained, and in this case the refractive index has the same value as is characteristic of thin layers. This means that a uniform dielectric layer is formed during the entire deposition process and the implemented calculational model, which assumes a constant refractive index over the thickness of the layer and zero (negligible) extinction, is valid.

Results of measurements for the series of samples which used wafers of fused quartz as the substrates are shown in Figs. 2a and 2b for two angles of incidence, $\varphi=50$ and 65° (on different sides of the Brewster angle for quartz). In this case, as in the preceding series of samples, points with small spread fall out of a calculation in the uniform layer model. However, in comparison with the samples on a silicon substrate, a tendency is observed toward lower refractive indices: $n=1.60-1.65$. For the calculations we used a value of the refractive index for quartz, $n_Q=1.456$, found experimentally. Note that point *8* in these figures, which corresponds to two-hour deposition, is found in the second ellipsometric period ($d_0=2360$ Å for $\varphi=65°$ and $d_0=2200$ Å for $\varphi=50°$).

It can be seen from Figs. 2a and 2b that as a result of measurements at different φ slightly different values of the refractive index correspond to the same sample (e.g., point *3* in one case lies on the curve corresponding to $n=1.62$, and in another case it lies on the curve corresponding to $n=1.64$). This fact can most likely be explained by nonuniformity of the sample in the layer plane and a different area

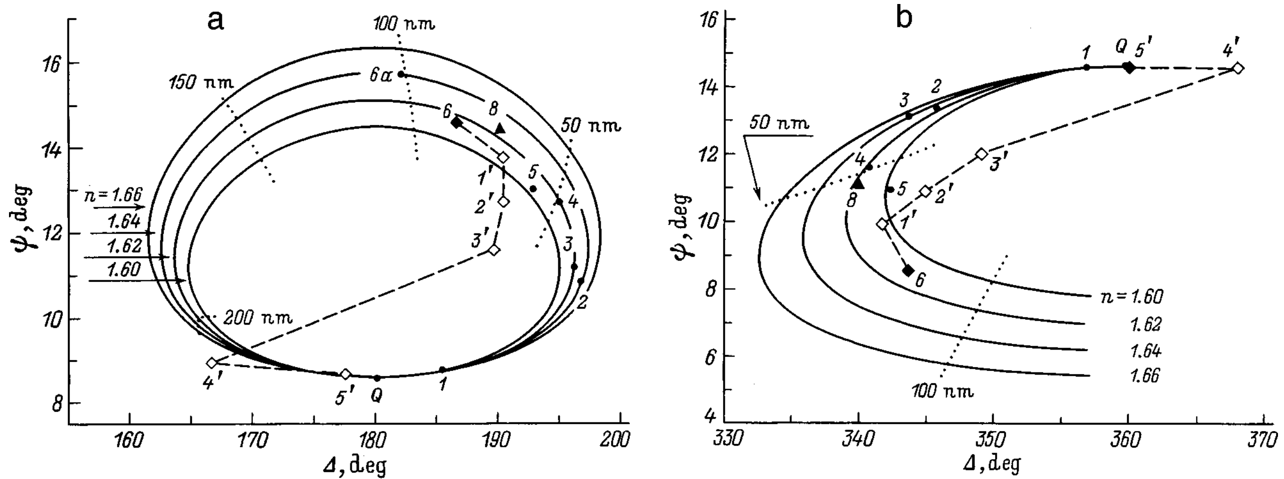

FIG. 2. $\psi-\Delta$ nomograms for *a*-C : H layers in quartz (*Q*) with φ=50° (a) and 65° (b). Points correspond to experiment; notation the same as in Fig. 1. Solid lines correspond to calculation with the following parameter values: complex refractive index of quartz $N_Q = 1.456 - i0.00$ (from experiment), refractive indices of the growing layer $n = 1.60$, 1.62, 1.64, 1.66 (indicated); markers indicating the thickness of the dielectric layer are provided in the first ellipsometric period.

of the light spot on the sample at different angles of incidence of the light beam.

Above, we only touched on estimates of the thicknesses of layers with long deposition times. At the same time, for each sample, from both series we determined an accurate value of the thickness from measurements at different angles of incidence, so that in the calculation (including the calculation of the period for thick samples) in each case we used the accurate experimental value of the refractive index and not the value averaged over the series of measurements. On the basis of these data we constructed dependences of the layer thickness (*d*) on substrates of silicon and quartz on the deposition time (*t*), which are shown in Fig. 3. The dependence $d(t)$ for *a*-C : H on Si is linear over the entire interval of thicknesses (points on the straight line *1*), i.e., deposition proceeds at a constant rate. The slope of the line allows us to determine the rate of growth, which is equal to 22.5 Å/min.

For samples of *a*-C : H on quartz we do not have data available corresponding to long deposition times. However, in Fig. 3, all the way up to $t = 2$ h the points for *a*-C : H on quartz lie above the line describing *a*-C : H on Si. The inset in Fig. 3 plots the initial segment of the scale, up to $t = 30$ min, on an expanded scale. It can be seen that at least for small *t* the growth rate of *a*-C : H on quartz is noticeably larger than on silicon: it is ~30 Å/min.

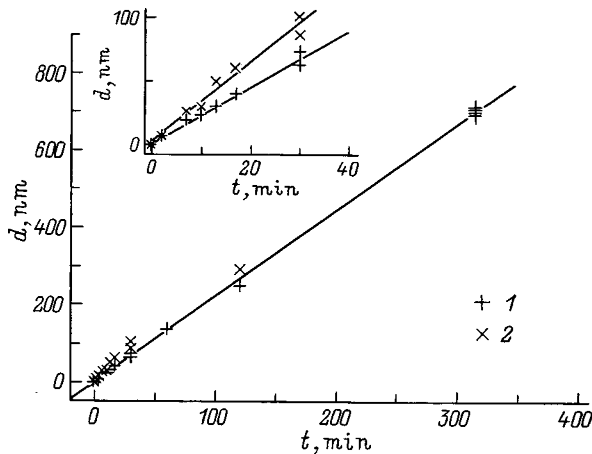

FIG. 3. Thickness of the *a*-C : H layer (*d*) on silicon (*1*) and quartz (*2*) substrates versus growth time (*t*). Inset shows a segment of the dependence for short growth times.

For the same two series of samples, *a*-C : H on silicon and on quartz, we attempted to remove the 30-min deposition layer (from point *6*) using ion etching in a high-frequency glow-discharge with a power of 0.15 kW at a residual air pressure of 10^{-1} Torr. The ellipsometric parameters for stepped ion action on the films is shown by points $1' - 5'$ in Figs. 1 and 2. The process of etching *a*-C : H on Si essentially follows the growth curve, and such a method can probably be used to decrease the thickness of the film. At the same time, for *a*-C : H films on quartz the process takes an unexpected course: after the first few minutes an abrupt deviation toward low refractive indices is observed. This apparently means that what takes place is not layer-by-layer etching, but an abrupt strong loosening of a significant part of the thickness of the layer.

Growth of *a*-C : H layers on glass-ceramic substrates proceeds quite differently than on substrates of silicon or quartz. We used ready-made commercial wafers of glass-ceramic with a mirror-smooth surface. Figure 4 plots the experimental points in the $\psi-\Delta$ plane for two angles of incidence φ=50 and 55°. For visual convenience these two sets of points are plotted separately. Both sets of points correspond to short deposition times, namely, 30 min or less. We emphasize that the considered samples (points *1–6* and *6a* in Fig. 4) were grown simultaneously, in the same growth shifts with the corresponding samples on quartz and silicon (points *1–6* and *6a* in Figs. 1 and 2). In Fig. 4 the points lie on curves with a salient point and a maximum. It is impossible to describe such curves in $\psi-\Delta$ coordinates in the model of a uniform dielectric layer or in the model of a uniform layer with nonzero extinction. The form of the curves indicates

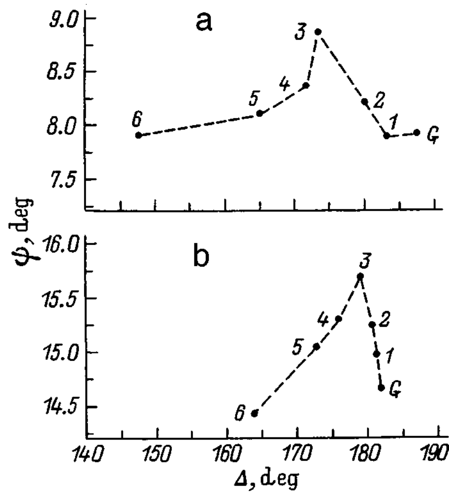

FIG. 4. Experimental values of the ellipsometric parameters for $\varphi=55°$ (a) and 50° (b) for a-C : H layers obtained for short deposition times, on glass-ceramic substrates. Notation of points the same as in Figs. 1 and 2. The point for glass-ceramic (G) was obtained experimentally.

that at this stage a layer whose optical parameters change during growth is formed. It is entirely probable that the deposited carbon interacts with components of the glass-ceramic substrate. After the salient point (point *5*, $t=17$ min), which is especially visible for $\varphi=55°$ (Fig. 4a), a tendency toward smooth variation of the curve is seen. Therefore it may be assumed that at $t=17$ min formation of the intermediate or transitional layer comes to an end and growth of the a-C : H layer itself commences. On this basis we attempted to compare the available experimental points at growth times $t>17$ min with the calculation for a uniform dielectric layer using as our calculational parameter for the starting point of layer growth the complex refractive index of some effective substrate $N_{\text{eff}}=1.746-i0.1$ corresponding to point *5* in the $\psi-\Delta$ plane (see Fig. 5). Replacing the optical parameters of the actual structure at which layer growth begins (which is in essence the glass-ceramic substrate with a

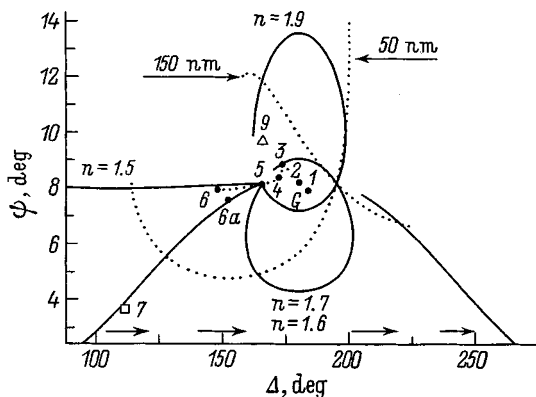

FIG. 5. Comparison of experimental points for a-C : H layers deposited on glass-ceramic (G) with calculated $\psi-\Delta$ nomogram for $\varphi=55°$. Notation of points the same as in Figs. 1 and 2. Calculation parameters: complex refractive index of the effective substrate, corresponding to point *5* ($t=17$ min) in the $\psi-\Delta$ plane, $N_{\text{eff}}=1.746-i0.1$; refractive indices of the growing dielectric layer $n=1.5$, 1.6, 1.7, 1.9 (indicated); lines of constant thickness are drawn for the thickness equal to 50 and 150 nm.

nonuniform transitional layer) by parameters of an effective homogeneous substrate corresponding to the same point in the $\psi-\Delta$ plane is an approximation. However, analogous curves, almost indistinguishable from those in Fig. 5, were obtained by calculating in another way, where the transitional layer was modeled by a set of layers with different complex refractive indices. Of course, when there is no information about the composition or structure of the transitional layer, any model is of necessity speculative in nature; therefore, we do not present modeling results here. At the same time, the coincidence of the ellipsometric nomograms for the two variants of the calculation suggest that the use of an effective substrate is permissible, and therefore we will consider to what extent the experimental points correspond to this calculation. As can be seen from Fig. 5, for $\varphi=55°$ the experimental points for the samples obtained under long deposition times do not lie on a calculated curve with a definite index of refraction, and the difference is large: $n=1.5-1.6$ for $t=30$ min, 1 h (points *6, 6a*, and *7*) and $n\approx1.9$ for $t=5$ h 15 min (point *9*). For $\varphi=50°$ point *9* corresponds in the analogous calculation to a curve with a still larger refractive index — $n\approx2.1$. Both of these interrelated facts—the displacement of the experimental points toward larger n with increase of the growth time of the a-C : H layer and the difference in the values of n obtained by comparing with calculation for different angles of incidence—imply that the model of a homogeneous dielectric layer is inapplicable for describing not only thin layers on a glass-ceramic substrate, but also the layer after 17 min of growth. Thus, the a-C : H layers that form on a glass-ceramic substrate are highly nonuniform, and questions about whether we are talking about a transitional layer, at what stage in the deposition process does growth of a uniform layer begin, and what are its optical characteristics remain unresolved.

To sum up, the study reported here allows us to draw the following conclusions.

1. Substrate materials strongly influence the growth rate and optical characteristics of a deposited a-C : H layer.
2. On a silicon substrate a uniform layer is formed up to thicknesses ~7000 Å.
3. The a-C : H layers on fused-quartz and silicon substrates have similar, only slightly different refractive indices for $\lambda=6328$ Å: 1.60−1.65 and 1.65−1.72, respectively.
4. For growth times up to 30 min (thicknesses <1000 Å) the growth rate on quartz is substantially greater (by a factor of ~1.3) than on silicon.
5. A nonuniform layer is formed on a glass-ceramic substrate.

We wish to thank Prof. V. I. Ivanov-Omskiĭ for helpful discussions and for support of this work.

*)E-mail: shar@nano.ioffe.rssi.ru

[1] V. L. Aver'yanov, T. K. Zvonareva, A. V. Chernyshev, and S. G. Yastrebov, Fiz. Tverd. Tela (Leningrad) **33**(11), 3410 (1991) [Sov. Phys. Solid State **33**, 2763 (1991)].

[2] G. A. Dyuzhev, V. I. Ivanov-Omskii, E. K. Kuznetsova, V. D. Rumyantsev, S. G. Yastrebov, T. K. Zvonariova, and M. I. Abaev, Mol. Mater. **8**, 103 (1996).

[3] V. I. Ivanov-Omskii, V. I. Siklitsky, A. A. Sitnikova, A. A. Suvorova, A. V. Tolmatchev, T. K. Zvonariova, and S. G. Yastrebov, Philos. Mag. B **76**(6), 973 (1997).
[4] R. M. Azzam and N. M. Bashara, *Ellipsometry and Polarized Light* (North-Holland, Amsterdam, 1977).
[5] V. K. Gromov, *Introduction to Ellipsometry* [in Russian], Leningrad State Univ. Press, Leningrad, 1986.
[6] D. E. Aspnes and A. A. Studna, Phys. Rev. B **27**(2), 985 (1983).

Translated by Paul F. Schippnick

THE PHYSICS OF SEMICONDUCTOR DEVICES

Photosensitivity of GaAlAs/GaAs heterophotoelements in linearly polarized light

V. Yu. Rud'

St. Petersburg State Technical University, 195251 St. Petersburg, Russia

Yu. V. Rud' and V. P. Khvostikov

A. F. Ioffe Physicotechnical Institute, Russian Academy of Sciences, 194021 St. Petersburg, Russia
(Submitted July 20, 1998; accepted for publication July 28, 1998)
Fiz. Tekh. Poluprovodn. **33**, 747–751 (June 1999)

The polarization photosensitivity of two types of GaAlAs/GaAs heterophotoelements has been investigated. It has been shown that in heterophotoelements without an antireflection coating the induced photopleochroism is governed by optical processes at the air–GaAlAs surface boundary, and the angular dependence of the short-circuit photocurrents is described by the Fresnel relations. It was found that the angular dependence of the photocurrents for *s* and *p* polarizations are similar in heterophotoelements with an antireflection coating and exhibits growth with increase of the angle of incidence. In the cleared region the induced photopleochroism is observed to fall to zero. It has been shown that heterophotoelements without an antireflection coating can be used as wideband photoanalyzers with a maximum azimuthal photosensitivity of up to 0.1 A/W·deg for an angle of incidence of 75°, while polarization photosensitivity spectroscopy makes it possible to carry out express diagnostics of the clearing effect in thin-film solar cells. © *1999 American Institute of Physics.*
[S1063-7826(99)02606-X]

Efforts to fabricate GaAlAs/GaAs heterophotoelements and investigate photoelectric phenomena in them have traditionally been oriented toward achieving a high quantum efficiency of photoconversion of solar radiation.[1–4] For this reason, the photoelectric properties of heterojunctions based on the isotropic semiconductors GaAs and GaAlAs are usually examined using unpolarized light. In the present paper we report the results of experimental studies of the photosensitivity of GaAlAs/GaAs heterophotoelements in linearly polarized light (LPL), which, as a result, has made it possible to uncover new potential applications of polarization photoelectric spectroscopy for diagnostics of the quality of prepared structures and point to a new area of application of these heterophotoelements.

The investigated heterophotoelements were grown at a temperature $\approx 550-750\,^\circ\mathrm{C}$ by liquid-phase epitaxy from solution–melts of the system Ga–Al–As. As the substrates we used (100) oriented wafers of GaAs:Sn with free electron density up to $10^{18}\,\mathrm{cm}^{-3}$ at $T=300\,\mathrm{K}$. The as-grown layers, according to microprobe studies, had composition $Ga_{0.15}Al_{0.85}As$ and thickness $d_1 \approx 0.15\,\mu\mathrm{m}$. The hole density in the wideband layers reached $10^{18}\,\mathrm{cm}^{-3}$ due to magnesium impurity doping. Efficiencies of 24.6% (AMO, 100 Suns) and 27.5% (AM 1.5, 100 Suns) were attained in solar cells based on such heterophotoelements.[4]

Photoelectric measurements were performed on two types of heterophotoelements. In one of them the incident radiation fell directly on the surface of the $Ga_{0.15}Al_{0.85}As$ epitaxial layer (*A* type). In the other type (*B* type), with the aim of reducing reflection losses, the surface of the wideband layer was subjected to anode oxidation in a neutral medium.[5] As a result, a single-layer antireflection coating was formed on the surface of the wideband layer. The area of the investigated heterophotoelements was $\approx 50-100\,\mathrm{mm}^2$.

1. In unpolarized light the spectral dependence of the current photosensitivity S_i of both types of heterophotoelements is rather similar for the most part, as can be seen from Fig. 1. Indeed, the long-wavelength photosensitivity edge is identical and is described by an exponential law, from which it follows that its slope $s=\delta(\ln S_i)/\delta(\hbar\omega)$ in such heterophotoelements corresponds to direct optical transitions in the substrate material. The energy position of the long-wavelength photosensitivity edge and salient point $\hbar\omega_1$ correspond to interband absorption in GaAs, but the spread in values of $\hbar\omega_1$ in the range 1.40–1.44 eV is probably due to some solubility of Al in the active region of the heterophotoelement. The observed differences in the full-width at half-maximum (FWHM) of the photosensitivity spectra $\delta_{1/2}$ and in the range of the maximum photosensitivity $\Delta\hbar\omega_m$ and its short-wavelength falloff for the investigated structures are governed by recombination in the region of the interface and by optical losses in the anode-oxide layers. This short-wavelength falloff is represented in Table I as the ratio of the short-circuit photocurrent at $\hbar\omega=2.5\,\mathrm{eV}$, $I_{2.5}$, to the maximum short-circuit photocurrent I_m. The highest maximum photosensitivity S_i^m is observed in heterophotoelements of *A* type (Fig. 1 and Table I), whereas there is a significant spread in the photoelectric parameters in the heterophotoele-

 © 1999 American Institute of Physics

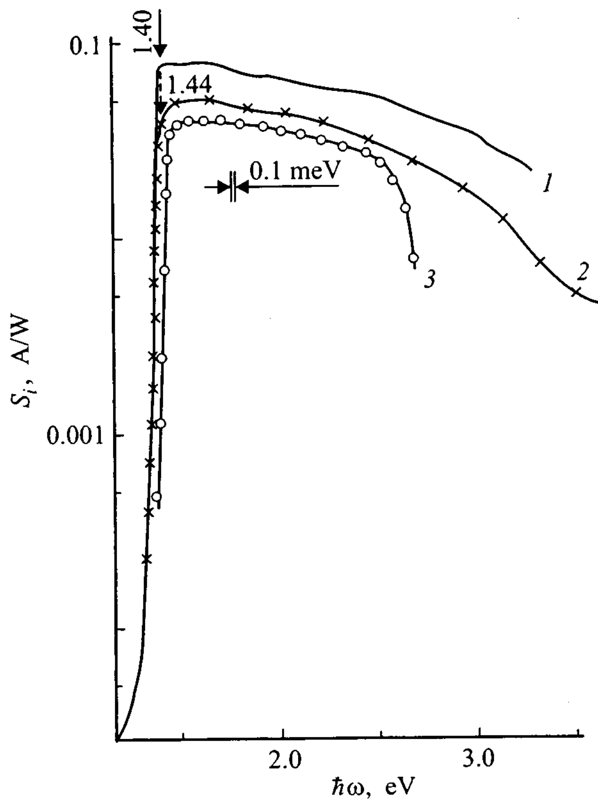

FIG. 1. Spectral dependence of the current photosensitivity of GaAlAs/GaAs (*1*) and Ox/GaAlAs/GaAs heterophotoelements (*2* — sample 3, *3* — sample 4) at $T = 300$ K in natural light.

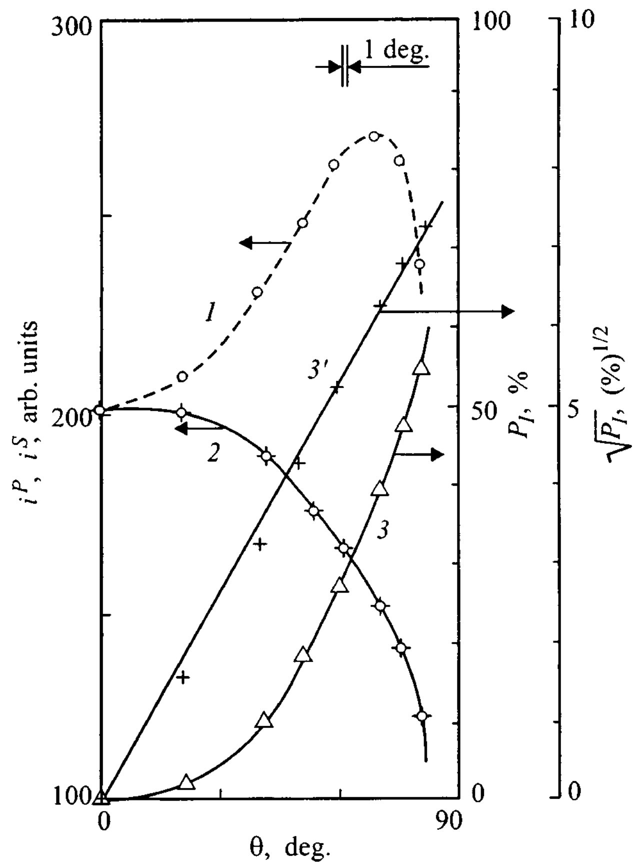

FIG. 2. Short-circuit photocurrents (i^P — *1*, i^S — *2*) and induced photopleochroism (*3, 3'*) of a GaAlAs/GaAs heterophotoelement versus angle of incidence of linearly polarized light on the surface of the GaAlAs layer ($\hbar\omega = 1.41$ eV, $T = 300$ K, sample *1*).

ments of *B* type due mainly to fluctuations in the properties of the oxide layer and active region of the heterophotoelement.

It can also be seen from Fig. 1 that the spectral dependence of the photosensitivity does not exhibit marked oscillations in either type of heterophotoelement.[6,7] Such marked oscillations usually accompany interference of the incident radiation in high-quality thin layers.

2. When a heterophotoelement was illuminated by linearly polarized light along the normal to the plane of the wideband layer, the photosensitivity of neither type of structures possessed an explicit dependence on the orientation of the light-wave electric field vector **E** relative to the principal crystallographic axes in the GaAs substrates, which correlates with the isotropic nature of the optical processes in cubic semiconductors and at once indicates the absence of substantial uniaxial deformations of the GaAlAs epitaxial layers.

TABLE I. Photoelectric properties of *p*-type $Ga_{0.15}Al_{0.85}As$ heterophotoelements at $T = 300$ K.

Type of HP	Sample No.	$\hbar\omega_1$, eV	s, eV^{-1}	$\delta_{1/2}$, eV	$\Delta\hbar\omega_m$, eV	$I_{2.5}/I_m$	S_i^m, mA/W
A	1	1.40	190	1.45	1.40–1.68	0.65	80
B	2	1.40	115	1.10	1.55–1.65	0.53	10
B	3	1.40	190	0.88	1.40–1.63	0.32	48
B	4	1.44	80	1.17	1.55–1.72	0.67	33
B	5	1.40	90	1.04	1.50–1.65	0.41	58

Polarization photosensitivity is observed only for inclined incidence of linearly polarized light on the (001) receiver plane of the heterophotoelement. During the course of these studies we found out that while the trends of the photoelectric processes are similar for both types of heterophotoelements in unpolarized light (Fig. 1), in linearly polarized light the photoelectric phenomena depend explicitly on the type of heterophotoelement.

Figure 2 shows typical curves for *A*-type heterophotoelements of the short-circuit photocurrent i^P, where the electric field vector **E** lies in the plane of incidence (PI) of the LPL (**E**$\|$PI) and the short-circuit photocurrent i^S, where the electric field vector **E** is perpendicular to the plane of incidence (**E**$\perp$ PI), as functions of the angle of incidence Θ for fixed photon energy in the photosensitivity region of the structures. It can be seen that for $\Theta > 0°$ the inequality $i^P > i^S$ takes hold, accompanied by substantial differences in the angular dependences of $i^P(\Theta)$ and $i^S(\Theta)$. Indeed, the photocurrent i^P at first grows, reaches a maximum near $\Theta \simeq 55°$, and then falls. At the same time, the photocurrent i^S exhibits a smooth falloff with growth of Θ in the range from 0 to 90°. Such behavior is as expected from an analysis of transmission of *s*- and *p*-polarized light across the air–receiver plane boundary of the structure on the basis of the Fresnel relations,[8,9] as was noted earlier in studies of the polarization photosensitivity of Schottky barriers.[10,11] According to these

studies, the increase in i^P is linked with the elimination of reflection losses of the p-polarized light, whereas for s-polarized light such an effect is absent. The induced photopleochroism coefficient

$$P_I=\{(i^P-i^S)/(i^P+i^S)\}\times 100\% \quad (1)$$

for an A-type heterophotoelement, as can be seen from Fig. 2 (curves *3* and *3'*), increases quadratically with growth of the angle of incidence of the LPL: $P_I\sim\Theta^2$, in complete agreement with Ref. 12. The above trends in the angular dependence of the photocurrents and the induced photopleochroism coefficient are characteristic of A-type heterophotoelements over the entire region of their photosensitivity.

According to a theoretical treatment, the induced photopleochroism is proportional to the refractive index n of the medium onto which the LPL is incident.[12] Therefore, we can estimate the refractive index for a wideband layer in an A-type heterophotoelement from the value $P_I\simeq 56-58\%$ at $\Theta=80°$ on the basis of Ref. 12. We find $n\simeq 3.2$ for $\hbar\omega=1.40$ eV, in good agreement with the ellipsometric data.[13]

In B-type structures equipped with a single anode-oxide layer antireflection coating in the wavelength range $0.5-0.75\ \mu$m, the angular dependences of the photocurrents and of P_I turn out to be completely different in relation to the case for A-type heterophotoelements. Typical examples of such dependences are shown in Fig. 3 for several wavelengths in the photosensitivity region of such heterophotoelements. The trends in these dependences are as follows.

The angular dependences of the photocurrents for both polarizations of the incident LPL are similar and indicate simultaneous elimination of reflection losses for both p and s polarizations, which is not in agreement with the results of analysis of the transmission of LPL across the boundary of two media based on the Fresnel relations.[8,9] From Fig. 3 it can also be seen that as the energy of the incident photons is varied, the angle Θ at which the maxima in the dependences $i^P(\Theta)$ and $i^S(\Theta)$ are reached also varies, as well as the spacing between these curves at identical values of Θ. Since the inequality $i^P>i^S$ is preserved over the entire photosensitivity range of the B-type heterophotoelement, the induced photopleochroism remains positive ($P_I>0$), but its magnitude, contrary to Ref. 12, begins to depend explicitly on the photon energy. Therefore, it can be asserted that the single-valued relation $P_I\sim n$ predicted by the theory is lost.[12] Such behavior of the photopleochroism is a consequence[6,7] of interference clearing, which was generally disregarded in the analysis in Ref. 12.

Figure 4 plots typical spectral curves of P_I for A-type (curve *1*) and B-type (curves *2* and *3*) heterophotoelements. Let us turn our attention to the fundamental difference in the nature of the spectral curves of the polarization photosensitivity in these two types of heterophotoelements.

In the case of heterophotoelements without an anode-oxide layer (A type) the induced photopleochroism at $\Theta=75°$ in the long-wavelength spectral region (1–2 eV) varies slightly within the limits 48–50%, then grows smoothly to 60%, remaining nearly constant at this level in the region 2.8–3.4 eV, and, finally, at $\hbar\omega>3.5$ eV begins to fall to

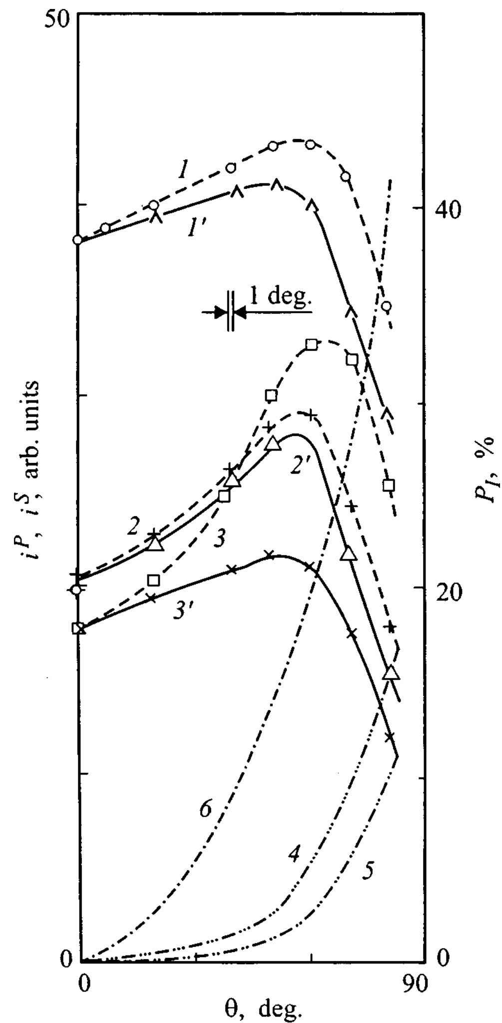

FIG. 3. Short-circuit photocurrents (i^P — *1–3*, i^S — *1'–3'*) and induced photopleochroism (*4–6*) of an Ox/GaAlAs/GaAs heterophotoelement versus angle of incidence of linearly polarized light on the surface of the anode oxide — Ox. (Sample 4; $T=300$ K; $\hbar\omega$, eV: *1, 1', 4* — 1.41, *2, 2', 5* — 2.07, *3, 3', 6* — 2.75).

$\simeq$50%. Note that the spectral dependence of P_I in an A-type heterophotoelement correlates with the nature of the analogous dependence of n for epitaxial layers of the solid solution AlGaAs with similar atomic composition,[13] and estimates of the refractive index from polarization photosensitivity measurements, based on the treatment in Ref. 12, agree with the experimental data.[13]

When we move over to B-type heterophotoelements, a characteristic "dip" arises on the spectral curves P_I, inside of which the photopleochroism remains close to zero. This disappearance of the induced photopleochroism is linked, according to Ref. 6, with the effect of clearing of the heterophotoelement surface by the anode-oxide single layer. It should be emphasized that the spectral range in which the criterion $P_I\rightarrow 0$ is satisfied coincides with that obtained from measurements of the reflection coefficient ($R\rightarrow 0$) of the same layers. Differences in the spectral range, where the minimum of P_I is reached, along with differences in the magnitude of P_I in the region of this minimum for two different B-type heterophotoelements (Fig. 4, curves *2* and *3*)

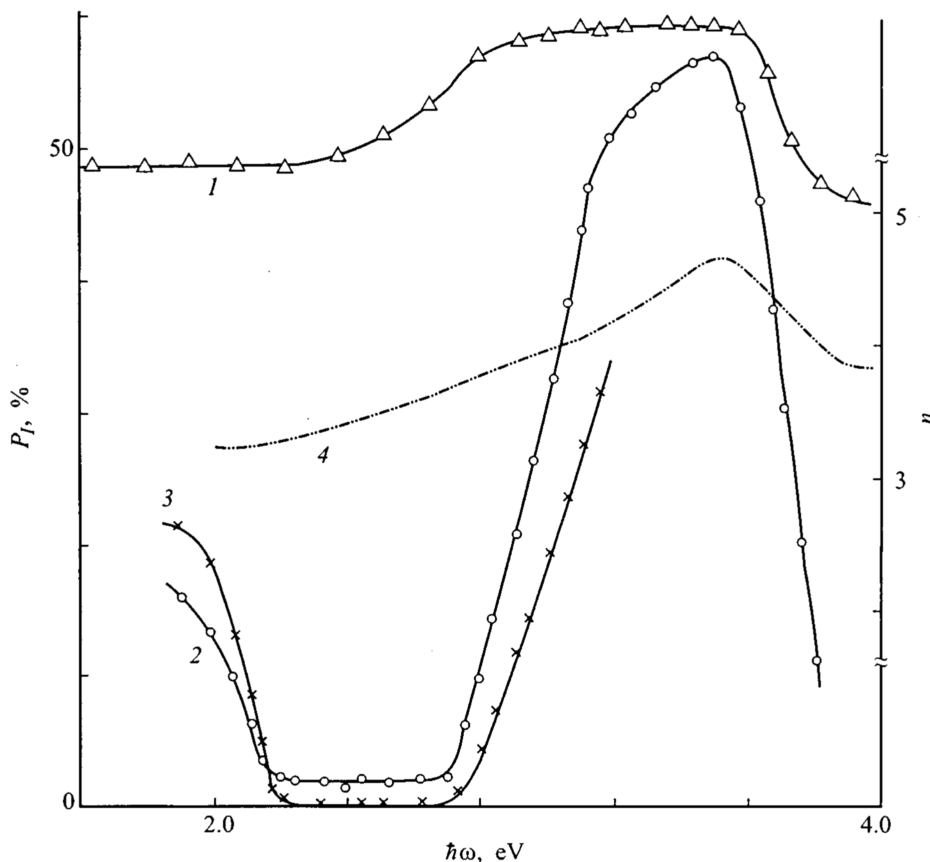

FIG. 4. Spectral dependence of the induced photopleochroism of heterophotoelements (*1–3*) and the refractive index of $Ga_{0.3}Al_{0.7}As$ (*4* — data from Ref. 13) at $T = 300$ K (type of heterophotoelement: *1* — GaAlAs/GaAs, sample 1; *2* — Ox/GaAlAs/GaAs, sample 4; *3* — Ox/GaAlAs/GaAs, sample 2).

demonstrate the possibilities of polarization spectroscopy for diagnostics of the spectral contour and magnitude of the clearing effect in prepared solar cells with a contact grid deposited on their receiver plane. It can also be seen from Fig. 4 that outside the clearing range the induced photopleochroism increases, tending to the values of P_I characteristic of heterophotoelements without an antireflection coating.

Thus, in the absence of an antireflection coating and without any changes in the fabrication of GaAlAs/GaAs heterophotoelements, which has already been brought to a high level of perfection,[4] these heterophotoelements are suitable for use as high-sensitivity photoanalyzers of linearly polarized light with maximum azimuthal photosensitivity $\Phi_I^m \simeq 0.1$ A/W·deg ($T = 300$ K, $\Theta = 75°$) over the wide spectral range extending from 1 to 3.5 eV. On the other hand, we also point out that polarization photosensitivity spectroscopy of solar cells equipped with an antireflection coating (e.g., Ox/GaAlAs/GaAs) allows express nondestructive diagnostics of the clearing effect in prepared solar cells, thereby affording an increase in the level of perfection of the fabrication process, and also the choice of material and parameters of the antireflection coatings, which is especially important for the case of multilayer coatings. The high locality of the proposed photoelectric technique (diameter of the light probe about 0.2 mm) makes it possible to monitor the uniformity of the clearing effect over the entire photodetector surface of the solar cell in the presence of a contact grid and regardless of the structure of the surface of the frontal layer of the photoconverter.

The authors are grateful to Prof. V. M. Andreev for support of this work and for helpful discussions of the results.

[1] Zh. I. Alfërov, Fiz. Tekh. Poluprovodn. **11**, 2072 (1977) [Sov. Phys. Semicond. **11**, 1216 (1977)].

[2] Zh. I. Alfërov, V. M. Andreev, E. L. Portnoĭ, and N. I. Protasov, Fiz. Tekh. Poluprovodn. **3**, 1324 (1969) [Sov. Phys. Semicond. **3**, 1103 (1969)].

[3] Zh. I. Alfërov, V. M. Andreev, N. S. Zimogorova, and D. N. Tret'yakov, Fiz. Tekh. Poluprovodn. **3**, 1633 (1969) [Sov. Phys. Semicond. **3**, 1373 (1969)].

[4] V. M. Andreev, A. B. Kazantsev, V. P. Khvostikov, E. V. Paleeva, V. D. Rumyantsev, and M. Z. Shvarts, in *Proceedings of the First WCEPSEC* (Hawaii, USA, Dec. 5–9, 1994), p. 2096.

[5] H. Hosegawa, K. E. Forward, and H. Hartnagel, J. Electron. Lett. **6**, 11 (1975).

[6] V. Yu. Rud' and Yu. V. Rud', Fiz. Tekh. Poluprovodn. **31**, 309 (1997) [Semiconductors Semiconductors **31**, 197 (1997)].

[7] V. M. Botnaryuk, A. V. Koval', A. V. Simashkevich, V. A. Shcherban', V. Yu. Rud', and Yu. V. Rud', Fiz. Tekh. Poluprovodn. **31**, 800 (1997) [Semiconductors **31**, 677 (1997)].

[8] G. S. Landsberg, *Optics* [in Russian], Nauka, Moscow, 1976.

[9] R. Azzam and M. Bashara, *Ellipsometry and Polarized Light* (North-Holland, Amsterdam, 1977).

[10] S. G. Konnikov, D. Melebaev, V. Yu. Rud', and M. Serginov, Pis'ma Zh. Tekh. Fiz. **18**, 39 (1992) [Tech. Phys. Lett. **18**, 42 (1992)].

[11] S. G. Konnikov, D. Melebaev, V. Yu. Rud', and L. M. Fedorov, Pis'ma Zh. Tekh. Fiz. **18**, 11 (1992) [Tech. Phys. Lett. **18**, 16 (1992)].

[12] G. A. Medvedkin and Yu. V. Rud', Phys. Status Solidi A **67**, 333 (1981).

[13] D. E. Aspnes, S. M. Kelso, R. A. Logan, and R. Bhat, J. Appl. Phys. **60** (2), 754 (1986).

Translated by Paul F. Schippnick

Increasing the power of broad-waveguide lasers by additional selection of transverse modes

I. A. Kostko, V. P. Evtikhiev, E. Yu. Kotel'nikov, and G. G. Zegrya*)

A. F. Ioffe Physicotechnical Institute, Russian Academy of Sciences, 194021 St. Petersburg, Russia

(Submitted October 27, 1998; accepted for publication November 2, 1998)
Fiz. Tekh. Poluprovodn. **33**, 752–758 (June 1999)

A new method is proposed for transverse mode selection in high-power, broad-waveguide, separate-confinement, heterostructure quantum-well lasers by orienting the front mirror at an angle other than normal to the direction of radiation propagation. The dependence of the mode reflection coefficients on the laser mirror parameters is investigated. Optimal values are found for the mirror inclination angles and the thicknesses and refractive indices of the dielectric coating at which the fundamental guide mode dominates. The possibility of a 1.2-fold increase in the output power of a broad-waveguide, separate-confinement, heterostructure quantum-well diode laser is demonstrated. © *1999 American Institute of Physics.* [S1063-7826(99)02706-4]

INTRODUCTION

Recent progress in the fabrication of high-power injection lasers has been tied to an increase in the width of the waveguide in quantum-well bilateral-heterostructure separate confinement (QW-BHS-SC) lasers and the fabrication of QW-BHS-SC lasers with a broad waveguide (BW-SCH-QW lasers).[1,2] Increasing the width of the waveguide leads to a reduction of internal losses in the laser, which makes it possible to fabricate long-cavity lasers, and to increase the power of catastrophic mirror damage as a result of a decrease in the power density at the mirror.[3,4] This has made it possible to obtain record radiative power levels in the quasicontinuous regime (14.3 W) in broad-waveguide lasers.[1] However, a further increase in the width of the waveguide with the aim of increasing the limiting power of single-mode emission is bounded by the width of the waveguide for which generation of the second transverse mode is observed. Obviously, this is accompanied by a decrease in the differential quantum efficiency and total efficiency of the laser.

The literature describes a means for suppressing higher-order modes by clearing the front mirror of the laser.[5] It has been experimentally shown that the mode makeup of the laser emission is affected by the thickness and refractive index of the antireflection coating. In this case, suppression of the second mode is that much stronger the better the front mirror is cleared. However, such a selection method due to the clearing has a natural limitation associated with growth of the threshold current density of the laser.

We propose a fundamentally new means of suppressing higher-order modes in an expanded waveguide. This method consists in orienting the output mirror at some angle θ instead of perpendicular to the direction of propagation (see Fig. 1). Such a configuration of the mirrors can be easily achieved by shearing a laser structure grown on a (001) vicinal substrate.

Our goal in this study was to theoretically investigate the possibility of fabricating a single-mode stripe laser with enhanced radiative power achieved by inclining the front mirror of the laser.

We have investigated the effect of the inclination angle θ on the magnitude of the losses due to radiation extraction for the zeroth and second modes. We base our treatment on the fact that modes of different order have different angles of incidence on the cavity mirror and consequently have different losses to radiation extraction. Therefore, varying the angle of incidence of the mode on the mirror can lead to a change in the ratio of losses to radiation extraction for different modes, and consequently to mode selection.

In this paper we theoretically investigate the dependence of the output losses for various laser modes on the mirror parameters.

We investigate in detail the reflection of modes (1) from the front mirror, obtained by shearing; (2) from a mirror with a dielectric coating; and (3) from the inclined front cavity mirror. We show that mode losses upon reflection depend on the thickness of the dielectric coating, the inclination angle of the front mirror, and the index of refraction of the dielectric coating.

We obtain optimal values of the inclination angle of the front mirror and the thickness and refractive index of the dielectric coating for which the fundamental mode dominates. We demonstrate the possibility of an increase in the width of the waveguide afforded by optimization of the cavity parameters, which in turn makes it possible to increase the power of single-mode emission.

1. REFLECTION FROM A COATED MIRROR

We consider an ordinary semiconductor laser with a three-layer symmetric planar dielectric waveguide. The mirror of such a laser is the face perpendicular to the z axis. We assume the dielectric constant of the regions to be constant for each layer, and we consider heterostructures in which the jump in the refractive index n is large enough that the imaginary part of the complex refractive index $\bar{N}=n-i\bar{k}$ may be

 © 1999 American Institute of Physics

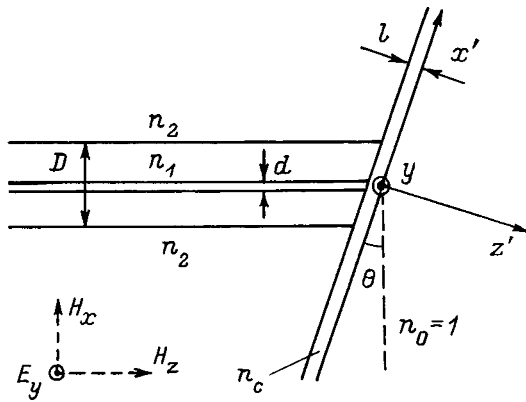

FIG. 1. Diagram of a BW-SCH-QW laser with inclined mirror.

ignored ($\bar{k}$ is the extinction coefficient). Note that within the framework of our model it is also possible to take into account the extinction coefficient.

To find the reflection coefficients, we employed a method expounded in Ref. 6. We assume that the mode of order m is incident upon the $z=0$ plane. The amplitude of its electric field is $E_y^{(m)}$, and of its magnetic field is $H_x^{(m)}$. The reflected wave is the sum of the total set of $N+1$ waveguide modes and emitted waves.[6,7] We obtain boundary conditions on the TE mode of order m incident upon the $z=0$ plane, from the condition of continuity of the tangential components of the electric and magnetic fields at the dielectric–vacuum interface ($z=0$):

$$E_y^{(m)}+\sum_{n=0}^{N} C_n E_y^{(n)}+\int_0^\infty C_\rho E_y^{(\rho)} d\rho=\int_{-\infty}^{\infty} C_v E_y^{(v)} dk_{vx}, \qquad (1)$$

$$H_x^{(m)}+\sum_{n=0}^{N} C_n H_x^{(n)}+\int_0^\infty C_\rho H_x^{(\rho)} d\rho=\int_{-\infty}^{\infty} C_v H_x^{(v)} dk_{vx}. \qquad (2)$$

Here $E_y^{(n)}$ is the amplitude of the electric field for the mode of order n (Ref. 7); $E_y^{(\rho)}$ is the amplitude of the electric field for the emitted waves; $E_y^{(v)}=\exp(-ik_{vx}x)$; C_n is the amplitude reflection coefficient for the mode of order n, $n=0,1\ldots N$; C_ρ is the coefficient for the emitted waves[7]; k_{vx} is the propagation constant of the wave in vacuum in the x direction, which is related to the propagation constant in the z direction by the relation $k_{vx}^2=k_0^2-k_{vz}^2$, $-\infty<k_{vz}<\infty$; and ρ is the propagation constant of the emitted waves in the x direction.

Eliminating C_v from system (1)–(2), we obtain a system of equations in the amplitude reflection coefficient C_m, the ith equation of which ($i=0,1\ldots N$) has the form

$$\begin{aligned} k_{zi}\delta_{mi}-C_i k_{zi}=&\frac{k_{zi}^*}{2\pi k_0}\int_{-\infty}^{\infty}\sqrt{k_0^2-k_{vx}^2}\,dk_{vx} \\ &\times\int_{-\infty}^{\infty} E_y^{(i)*}(x)\exp(-ik_{vx}x)dx \\ &\times\Bigg[\int_{-\infty}^{\infty} E_y^{(m)}(x)\exp(ik_{vx}x)dx \\ &+\sum_{n=0}^{N} C_n\int_{-\infty}^{\infty} E_y^{(m)}(x)\exp(ik_{vx}x)dx \\ &+\int_0^\infty\int_{-\infty}^{\infty} C_\rho E_y^{(\rho)}(x)\exp(ik_{vx}x)dx\,d\rho\Bigg], \end{aligned} \qquad (3)$$

where $k_0=\omega/c$, ω is the angular frequency of the radiation, c is the speed of light, and k_{zi} are the propagation constants of modes of orders i in the z direction, which are found numerically by solving the transcendental dispersion relations.[7]

Determining the amplitude reflection coefficient for the mode of order m, C_m, from system (3), we find the intensity reflection coefficient

$$R_m=|C_m|^2. \qquad (4)$$

Let us consider reflection of the mode of order m from a mirror with a coating whose refractive index is equal to n_c, where the thickness of the dielectric coating is equal to l. The field in the coating consists of the refracted wave, whose amplitude is C_{cov}^t, and the wave reflected from the air–vacuum boundary, with amplitude C_{cov}^r.

The propagation constants of the wave in the layer in the x and z directions are interrelated as follows: $k_{cx}^2=n_c^2k_0^2-k_{cz}^2$. The boundary conditions in the $z=0$ plane are written as follows:

$$\begin{aligned} &E_y^{(m)}+\sum_{n=0}^{N} C_n E_y^{(n)}+\int_0^\infty C_\rho E_y^{(\rho)} d\rho \\ &\quad=\int_{-\infty}^{\infty} C_{cov}^t E_y^{t,cov} dk_{cx}+\int_{-\infty}^{\infty} C_{cov}^r E_y^{r,cov} dk_{cx}, \end{aligned} \qquad (5)$$

$$\begin{aligned} &H_x^{(m)}+\sum_{n=0}^{N} C_n H_x^{(n)}+\int_0^\infty C_\rho H_y^{(\rho)} d\rho \\ &\quad=\int_{-\infty}^{\infty} C_{cov}^t H_x^{t,cov} dk_{cx}+\int_{-\infty}^{\infty} C_{cov}^r H_x^{r,cov} dk_{cx}. \end{aligned} \qquad (6)$$

We multiply Eq. (5) by $\exp(ik'_{cx}x)$ and Eq. (6) by $E_y^{(i)}(x)$, where i can take the values $i=0,1\ldots N$, and integrate in x within the limits $-\infty<x<\infty$. Simplifying the equations, we obtain a system of equations in which, in addition to C_i, the quantities C_{cov}^t and C_{cov}^r are also unknown

$$
\begin{aligned}
C^t_{cov}(k_{cx})+C^r_{cov}(k_{cx})
&=\frac{1}{2\pi}\left[\int_{-\infty}^{\infty}E_y^{(m)}(x)\exp(ik_{cx}x)dx\right.\\
&\quad+\sum_{n=0}^{N}C_c\int_{-\infty}^{\infty}E_y^{(n)}(x)\exp(ik_{cx}x)dx\\
&\quad\left.+\int_0^{\infty}\int_{-\infty}^{\infty}C_\rho E_y^{(\rho)}(x)\exp(ik_{cx}x)dxd\rho\right], \qquad (7)
\end{aligned}
$$

$$
\begin{aligned}
k_{zi}\delta_{mi}-C_ik_{zi}=\frac{k^*_{zi}}{k_0}\int_{-\infty}^{\infty}k_{cz}dk_{cx}\int_{-\infty}^{\infty}E_y^{(i)*}(x)\\
\times\exp(-ik_{cx}x)dx[C^t_{cov}(k_{cx})-C^r_{cov}(k_{cx})]. \qquad (8)
\end{aligned}
$$

On the other hand, the boundary conditions for the tangential components of the electric and magnetic fields for reflection of the wave from the coating–vacuum boundary have the form

$$
\begin{aligned}
&\int_{-\infty}^{\infty}C^t_{cov}(k_{cx})\exp(-ik_{cx}x-ik_{cz}l)dk_{cx}\\
&\quad+\int_{-\infty}^{\infty}C^r_{cov}(k_{cx})\exp(-ik_{cx}x+ik_{cz}l)dk_{cx}\\
&=\int_{-\infty}^{\infty}C_v(k_{vx})\exp(-ik_{vx}x-ik_{vz}l)dk_{vx}, \qquad (9)
\end{aligned}
$$

$$
\begin{aligned}
&\int_{-\infty}^{\infty}C^t_{cov}(k_{cx})\exp(ik_{cx}x-ik_{cz}l)\left(-\frac{k_{cz}}{k_0}\right)dk_{cx}\\
&\quad+\int_{-\infty}^{\infty}C^r_{cov}(k_{cx})\exp(-ik_{cx}x+ik_{cz}l)\left(\frac{k_{cz}}{k_0}\right)dk_{cx}\\
&=\int_{-\infty}^{\infty}C_v(k_{vx})\exp(-ik_{vx}x-ik_{vz}l)\left(-\frac{k_{vz}}{k_0}\right)dk_{vx}, \qquad (10)
\end{aligned}
$$

where C_0 is the amplitude of the transmitted wave in vacuum. Solving system (9)–(10), we obtain an equation that links C^i_{cov} and C^r_{cov}

$$
C^r_{cov}(k_{cx})=C^t_{cov}(k_{cx})\exp(-2ik_{cz}l)\frac{k_{cz}-k_{vz}}{k_{cz}+k_{vz}}. \qquad (11)
$$

Employing Eq. (11), we eliminate C^t_{cov} and C^r_{cov} from system (7)–(8). Finally, the system of equations for finding the reflection coefficient for the coated mirror takes the form

$$
\begin{aligned}
k_{zi}\delta_{mi}-C_ik_{zi}=\frac{k^*_{zi}}{2\pi k_0}\int_{-\infty}^{\infty}\sqrt{k_0^2-k_{cx}^2}dk_{cx}\int_{-\infty}^{\infty}E_y^{(i)*}(x)\\
\times\exp(-ik_{cx}x)dx\\
\times\left[\int_{-\infty}^{\infty}E_y^{(m)}(x)\exp(ik_{cx}x)dx\right.\\
+\sum_{n=0}^{N}C_n\int_{-\infty}^{\infty}E_y^{(m)}(x)\exp(ik_{cx}x)dx\\
\left.+\int_0^{\infty}\int_{-\infty}^{\infty}C_\rho E_y^{(\rho)}(x)\exp(ik_{cx}x)dxd\rho\right]\times K, \qquad (12)
\end{aligned}
$$

where

$$
K=\frac{1-\dfrac{\sqrt{k_0^2n_c^2-k_{cx}^2}-\sqrt{k_0^2-k_{cx}^2}}{\sqrt{k_0^2n_c^2-k_{cx}^2}+\sqrt{k_0^2-k_{cx}^2}}\exp\{-2i\sqrt{k_0^2n_c^2-k_{cx}^2}l\}}{1+\dfrac{\sqrt{k_0^2n_c^2-k_{cx}^2}-\sqrt{k_0^2-k_{cx}^2}}{\sqrt{k_0^2n_c^2-k_{cx}^2}+\sqrt{k_0^2-k_{cx}^2}}\exp\{-2i\sqrt{k_0^2n_c^2-k_{cx}^2}l\}}. \qquad (13)
$$

The factor K corresponds to reflection from the coating. Indeed, if the layer thickness is equal to zero, then system (12) reduces to the system derived above for the mirror without a coating (3) since K in this case is $K=k_{vz}/k_{cz}$. Similarly, if $n=1$, then $k_{cz}=k_{vz}$ and $K=1$, which also corresponds to system (3).

2. DEPENDENCE OF THE REFLECTION COEFFICIENT ON THE MIRROR INCLINATION ANGLE

Let us consider the laser shown in Fig. 1. The front mirror in it is not oriented perpendicular to the light propagation direction, but at an angle to it. We denote the angle between the normal to the active layer and the end-face by θ. The waveguide mode is incident on this mirror at an angle that differs from the angle of incidence of the mode in a laser with an ordinary mirror by the angle θ. To analyze the reflection coefficient for the mirror, we rotate the system of coordinates in the xz plane about the y axis by the angle θ, as shown in Fig. 1. Then, expressing the old coordinates x and z in terms of the new coordinates x' and z', we have

$$
\begin{cases}
z=z'\cos\theta+x'\sin\theta,\\
x=-z'\sin\theta+x'\cos\theta.
\end{cases} \qquad (14)
$$

The expressions for the electric field amplitudes for the TE modes at $z'=0$ are replaced in a laser with inclined mirror by the following expressions:

For the even TE modes

$$E_y(x')=A_e\cos(k_x\tilde{x}\cos\theta)\times\exp\{-ik_zx'\sin\theta\},\quad |x'|\cos\theta\leqslant\frac{d}{2};$$

$$E_y(x')=A_e\cos(k_xd/2)\times\exp\left\{-\gamma\left(\left|x'\right|\cos\theta-\frac{d}{2}\right)\right\}\times\exp\{-ik_zx'\sin\theta\},\quad |x'|\cos\theta\geqslant\frac{d}{2}. \tag{15}$$

For the odd TE modes:

$$E_y(x')=A_0\sin(k_xx'\cos\theta)\times\exp\{-ik_zx'\sin\theta\},\quad |x'|\cos\theta\leqslant\frac{d}{2};$$

$$E_y(x')=A_0\frac{|x'|}{x'}\sin(k_xd/2)\times\exp\left\{-\gamma\left(\left|x'\right|\cos\theta-\frac{d}{2}\right)\right\}\times\exp\{-ik_zx'\sin\theta\},\quad |x'|\cos\theta\geqslant\frac{d}{2}. \tag{16}$$

We replace the old coordinates x and z by the new coordinates x' and z' (14) in system of equations (12) and in the expressions for the electric field amplitudes E_y for the TE modes[7] ($x=x'\cos\theta-z'\sin\theta$, $z=x'\sin\theta-z'\cos\theta$). In what follows, it is convenient to introduce the notation $x'\cos\theta=x$, $z'=z$. Then the obtained system of equations for finding the reflection coefficients for the inclined mirror takes the form of system (12), and the expressions entering into it for the amplitudes E_y of the TE modes have the following dependence on the angle θ for the even TE modes:

$$E_y(x)=A_e\cos(k_xx)\exp\{-ik_zx\tan\theta\},\quad |x|\leqslant\frac{d}{2};$$

$$E_y(x)=A_e\cos(k_xd/2)\exp\left\{-\gamma\left(\left|x\right|-\frac{d}{2}\right)\right\}\times\exp\{-ik_zx\tan\theta\},\quad |x|\geqslant\frac{d}{2}. \tag{17}$$

For the odd TE modes:

$$E_y(x)=A_0\sin(k_xx)\exp\{-ik_zx\tan\theta\},\quad |x|\leqslant\frac{d}{2};$$

$$E_y(x)=A_0\frac{|x|}{x}\sin(k_xd/2)\exp\left\{-\gamma\left(\left|x\right|-\frac{d}{2}\right)\right\}\times\exp\{-ik_zx\tan\theta\},\quad |x|\geqslant\frac{d}{2}. \tag{18}$$

3. SELECTION CONDITION FOR THE FUNDAMENTAL MODE

The reduced losses of the waveguide mode for reflection from the end-face are defined by the expression

$$\alpha_{rm}=\frac{1}{2L}\ln\frac{1}{R_m}, \tag{19}$$

where L is the length of the waveguide.

For the generation to take place in the laser, it is necessary that the gain exceed the losses. The threshold condition for generation for the waveguide mode of order m has the form

$$\tilde{g}_m=\Gamma_mg=\alpha_i+\alpha^1_{rm}+\alpha^2_{rm}, \tag{20}$$

where Γ_m is the optical confinement coefficient Γ for the mode of order m; g is the gain coefficient in the active medium; $\tilde{g}_m$ is the modal gain coefficient; α^1_{rm} and α^2_{rm} are the losses of the waveguide mode upon reflection from the mirrors, defined by expression (19); and α_i are the internal losses in the waveguide.

For selection of the fundamental mode it is necessary that the threshold condition for the fundamental mode ($\tilde{g}_0=\Gamma_0g\geqslant\alpha_i+\alpha^1_{r0}+\alpha^2_{r0}$) be satisfied for some pump current and that it not be satisfied for the mode of order 2 ($\tilde{g}_2=\Gamma_2g<\alpha_i+\alpha^1_{r2}+\alpha^2_{r2}$). It follows from Eq. (20) that the selection condition for the fundamental mode has the form

$$(\alpha^1_{r0}\Gamma_2-\alpha^1_{r2}\Gamma_0)+(\alpha^2_{r0}\Gamma_2-\alpha^2_{r2}\Gamma_0)<0. \tag{21}$$

Assuming that the reflection coefficients for the back mirror are close to unity for all the modes, we considered only reflection from the front mirror. Then the selection condition for the fundamental mode takes the form

$$\Delta\alpha'\equiv\alpha^1_{r2}\Gamma_0-\alpha^1_{r0}\Gamma_2>0. \tag{22}$$

We introduce the dimensionless discrimination coefficient for the fundamental mode $\Delta\alpha\equiv\Delta\alpha'L=\ln 1/R_2\,\Gamma_0-\ln 1/R_0\,\Gamma_2$. The difference in the threshold current densities for the fundamental and second modes increases with increasing value of $\Delta\alpha$ for the front mirror of the waveguide.

4. RESULTS AND DISCUSSION

Calculations were performed for a $GaAs-Al_xGa_{1-x}As$ BW-SCH-QW laser with waveguide and emitter refractive indices $n_1=3.404$ and $n_2=3.080$, which corresponds to compositions $x=0.27$ and $x=0.8$, respectively, thickness of active medium $d=0.01\,\mu m$ and radiation wavelength $\lambda=0.86\,\mu m$; in this case the width of the waveguide was varied within the limits $D=0.6-0.8\,\mu m$. In a waveguide with these parameters there are only three waveguide modes: the fundamental mode, and the first- and second-order modes. To find the reflection coefficients for the modes from the front mirror, we solved system (12) numerically.

In an ordinary laser with a wide waveguide ($\theta=0°$) the emitted modes make only a small contribution to the reflected wave.[6] Obviously, in a cavity with an inclined mirror (Fig. 1) the contribution of the emitted modes depends on the angle θ. Following the method described in Ref. 7, we estimated the mode losses to emission as a function of the inclination angle of the front mirror θ. As the angle θ is increased, the mode losses to emission grow, but reach 10% only at $\theta=17°$. For small mirror inclination angles $\theta<8°$ the fraction of emitted modes in the reflected wave is small

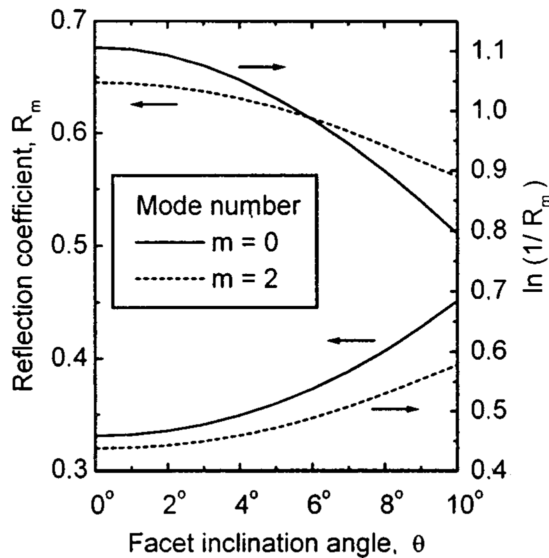

FIG. 2. Reflection coefficient R_m and the quantity ln $1/R_m$ [see Eq. (19)] for the fundamental mode ($m=0$) and the second-order mode ($m=2$) as functions of the facet inclination angle.

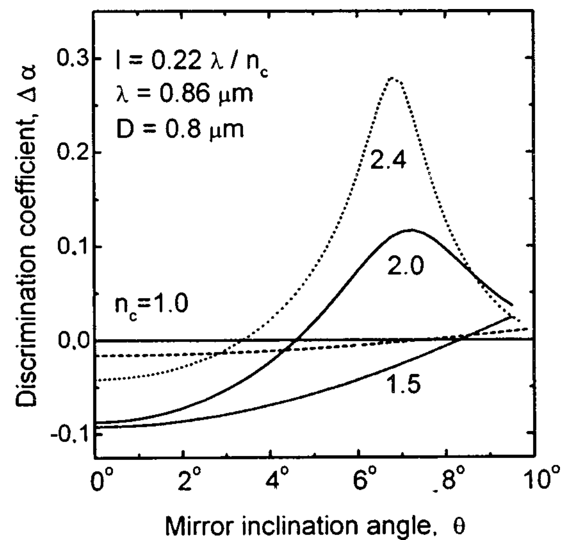

FIG. 3. Dimensionless discrimination coefficient of the fundamental mode $\Delta\alpha=\Delta\alpha' L$ [see Eq. (22)] plotted as a function of the mirror inclination angle for several values of the refractive index of the insulating coating n_c.

(<3%). Therefore, in our calculations [in the solution of system (12)] we have ignored the emitted modes.

Note that we did not make use of the behavior of the first-order mode as a function of the waveguide parameters and the parameters of the dielectric coating of the front mirror since the optical confinement coefficient Γ_m for the odd modes is substantially less than for the even modes. We also ignored the effect of mutual transformation of the fundamental and second mode during reflection on R_m.

Figure 2 plots the dependence of the power reflection coefficient on the mirror inclination angle for the zeroth-order R_0 and second-order R_2 mode. The reflection coefficient for the fundamental mode increases with θ while the reflection coefficient for the second-order mode decreases. The dependence of the reflection coefficients on the inclination angle of the front mirror θ can be explained as follows. It is well known that the reflection coefficient depends on the angle of incidence at the reflecting surface, and the higher-order modes in the zigzag wave model propagate in a waveguide at larger angles to the plane of the waveguide in comparison with the fundamental mode. It can thus be concluded that the reflection coefficients for the inclined mirror have a different dependence on θ for the fundamental mode and for the higher-order modes.

Figure 2 also plots the dependence of the quantity ln $1/R_m$ that enters into the mode selection condition (22) on the inclination angle θ for the fundamental mode and the second-order mode. Reflection losses for the fundamental mode are maximum for $\theta=0$ and decrease with growth of θ. It is obvious that by increasing θ it is possible to decrease losses of the fundamental mode and increase losses of the second mode and, consequently, facilitate generation of the fundamental mode.

Figure 3 plots the dependence of the dimensionless mode discrimination coefficient $\Delta\alpha$ on the angle θ for lasers with a coating ($l\approx\lambda/4n_c$ and without a coating ($l=0$). In the absence of a coating the discrimination coefficient $\Delta\alpha$ depends only weakly on the inclination angle θ and the selection condition for the fundamental mode (22) is satisfied for $\theta\simeq7.5°$. However, in the presence of a coating with thickness $l=0.22\lambda/n_c$ and refractive index $n_c=2.0$ the dependence of the coefficient $\Delta\alpha$ on the inclination angle is nonmonotonic, and $\Delta\alpha$ grows steeply in the angle interval $4°<\theta<7°$; condition (22) is satisfied for $\theta\simeq4.5°$. With increase of θ for coating thickness $l=0.22\lambda/n_c$ and refractive index $n_c=2.4$ $\Delta\alpha$ increases and becomes positive already at $\theta=3.5°$, which cannot be attained without the use of a coating.

The dependences obtained by us indicate that both the presence of a dielectric antireflection coating and increasing the inclination angle of the front mirror lead to an improvement in selection of the fundamental mode.

Clearly, the above-described means of fundamental mode selection in the range of mirror inclination angles $4°<0<8°$ should provide new possibilities for increasing the width of the waveguide.

Figure 4 plots the regions of maximum positive values of $\Delta\alpha$ as functions of two parameters: the coating refractive index n_c and the coating thickness l for a laser with $D=0.8\,\mu$m and $\theta=6°$. Such diagrams allow one to find optimal values for the thickness and refractive index of the dielectric coating. The optimal values for the given laser are $n_c>2.1$ and $l\simeq0.22\lambda/n_c$.

Figure 5 plots the dependence of $\Delta\alpha$ on the inclination angle θ for various widths of the waveguide D ($l=0.22\lambda/n_c$, $n_c=2.0$, $\lambda=0.86\,\mu$m). For example, for a waveguide of width $D=0.8\,\mu$m the quantity $\Delta\alpha$ attains larger values for the front-mirror inclination angle $\theta\simeq6°$ than in a waveguide of width $D=0.7\,\mu$m for $\theta=0°$. It is therefore legitimate to speak of fundamental mode selection in a laser with waveguide width $D=0.8\,\mu$m attained by inclining the front mirror. By the right choice of the thickness l and refractive index n_c of the coating, one can expand the wave-

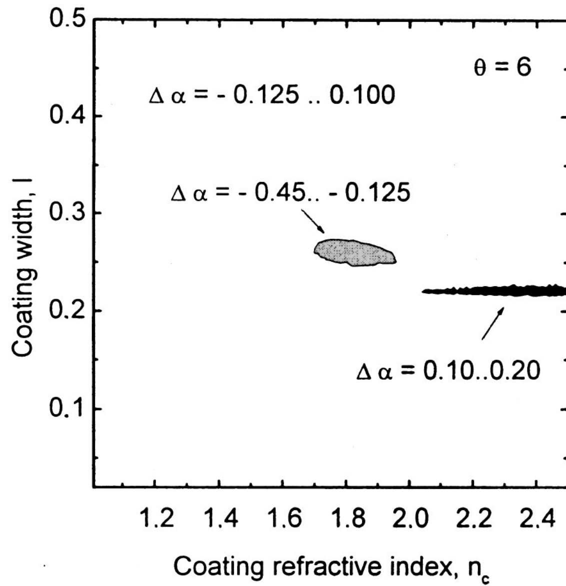

FIG. 4. Regions of values of the dimensionless mode discrimination coefficient $\Delta\alpha=\Delta\alpha' L$ [see Eq. (22)] versus the refractive index and width of the coating on the front mirror of the laser ($D=0.8\ \mu$m).

guide and yet obtain the same value of $\Delta\alpha$ as for a laser with a narrower waveguide but without an inclined mirror. Thus, inclining the front mirror facilitates selection of the fundamental mode by compensating for the increase in the width of the waveguide.

Figure 6 plots the dependence of $\Delta\alpha$ on the waveguide width D for $\theta=0°$ and $\theta=7°$. Because of the inclination of the front mirror ($n_c=2.0$, $l=0.22\lambda/n_c$,) the value of $\Delta\alpha$ for a laser with a wide waveguide ($D=0.65\ \mu$m) and $\theta=0°$ is equal to its value for the same laser but with an inclined mirror $D=0.8\ \mu$m and $\theta=7°$, which obviously makes it possible to lower the power density on the mirror by a factor of 1.2. We may add here that for the chosen coating the reflec-

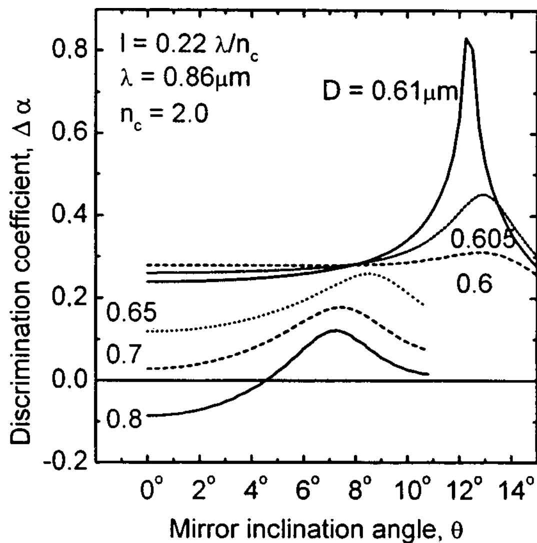

FIG. 5. Dimensionless discrimination coefficient of the fundamental mode $\Delta\alpha=\Delta\alpha' L$ [see Eq. (22)] plotted as a function of the mirror inclination angle for several values of the waveguide thickness D (μm).

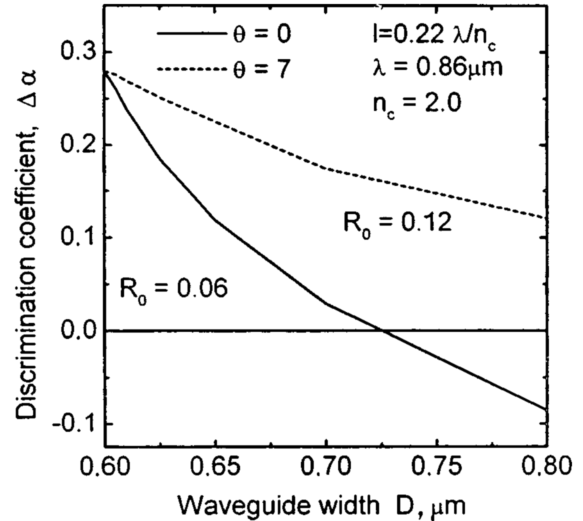

FIG. 6. Dimensionless discrimination coefficient of the fundamental mode $\Delta\alpha=\Delta\alpha' L$ [see Eq. (22)] plotted as a function of the waveguide width D (μm) for two values of the mirror inclination angle θ.

tion coefficient for the fundamental mode for $\theta=0°$ is $R_0=6\%$, and for $\theta=7°$ $R_0=12\%$, which makes it possible to significantly lower the threshold current density for the fundamental mode.

Our calculations show that thanks to inclining the mirror of a laser similar in design to the laser investigated in Ref. 5, it is possible to increase the reflection coefficient from $R_0=0.02$ to $R_0=0.07$ while preserving the discrimination coefficient $\Delta\alpha$ of the second mode, which makes it possible to decrease the length of the laser diode by roughly a factor of 1.5. Clearly, decreasing the length and consequently the area of the laser diode will lead to an increase in the yield of serviceable lasers and to an increase in the total number of lasers that can be obtained from an epitaxial wafer.

Another important result of the application of inclined mirrors is the possibility of a further increase in the width of the waveguide in high-power lasers while preserving the single-mode lasing regime. Obviously, increasing the area of the emitting region substantially (nearly linearly in our case) lowers the power density on the mirror. At the same time, increasing the linear dimensions of the emitting region narrows the far-field of the laser, which is governed by the diffraction limit.

Among the additional advantages of using a laser with inclined mirrors, we point out that the outgoing light propagates at an angle to the plane of the layers and leaves at a larger angle to the heat sink than in lasers with ordinary coatings, and this in turn facilitates the mounting of such lasers on the heat sink.

CONCLUSIONS

We have proposed a new means of additional selection of transverse modes in separate-confinement, bilateral heterostructure, quantum-well lasers which works by inclining the front mirror and allows a significant increase in the width of the waveguide while preserving generation of the fundamental transverse mode.

In this work we have considered a laser with thickness of the active medium such that selection of the fundamental waveguide mode is controlled only by its losses upon reflection from the end-face. We have delineated the dependence of the reflection losses on the facet (end-face) inclination angle. We have investigated reflection of *TE* modes from mirrors obtained by facet cleavage and from mirrors with an insulating coating. Numerical values of losses upon reflection from an inclined facet for a GaAs–AlGaAs BW SCH QW laser were obtained by the method of normal modes.

Optimal values of the facet inclination angles, thicknesses and refractive indices of the insulating coating of the mirror for BW SCH QW lasers with an inclined mirror, for which the fundamental mode of the emitted radiation dominates have been found for the first time. We have shown that depositing an insulating coating on the front mirror and increasing the facet inclination angle lead to an improvement in fundamental mode selection.

We have demonstrated the possibility of lowering the power density on the mirror by a factor of 1.2 while preserving generation of the fundamental mode and thereby increasing the power of the fundamental mode in BW SCH QW lasers by a factor of 1.2. We have proposed a suitable method for obtaining inclined mirrors in BW SCH QW lasers by cleaving structures grown on (001) vicinal surfaces.

This work was funded in part by the Russian Fund for Fundamental Research (Grants No. 98-07-90336, 97-02-18151, and 97-02-18153).

*)E-mail: zegrya@theory.ioffe.rssi.ru; Fax (812) 247-1017.

[1] A. Al-Muhanna, L. J. Mawst, D. Botez, D. Z. Garbuzov, R. U. Martinelli, and J. C. Connolly, Appl. Phys. Lett. **71**(9), 1142 (1997).
[2] D. Z. Garbuzov, M. R. Cokhale, J. C. Dries, P. Studenkov, R. U. Martinelly, J. C. Conolly, and S. R. Forrest, Electron. Lett. **33**(17), 1462 (1997).
[3] S. O'Bien, M. Zhao, A. Schoenfelder, and R. J. Lang, Electron. Lett. **33**(22), 1869 (1997).
[4] D. Botez, L. J. Mawst, A. Bhattacharya, J. Lopez, J. Li, T. F. Kuech, V. P. Iakovlev, G. I. Suruceanu, A. Caliman, and A. V. Syrbu, Electron. Lett. **33**(24), 2037 (1997).
[5] Zh. I. Alfërov, M. A. Ivanov, Yu. V. Il'in, A. V. Lyutetskiĭ, N. A. Pikhtin, and I. S. Tarasov, Pis'ma Zh. Tekh. Fiz. **21**(5), 64 (1995) [Tech. Phys. Lett. **21**, 195 (1995)].
[6] T. Ikegami, IEEE J. Quantum Electron. **QE-8**(6), 470 (1972).
[7] D. Marcuse, Bell Syst. Tech. J. **49**, 273 (1970).

Translated by Paul F. Schippnick

Gain and internal losses in InGaAsSb/InAsSbP double-heterostructure lasers

M. Aĭdaraliev, N. V. Zotova, S. A. Karandashev, B. A. Matveev, M. A. Remennyĭ, N. M. Stus', and G. N. Talalakin

A. F. Ioffe Physicotechnical Institute, Russian Academy of Sciences, 194021 St. Petersburg, Russia
(Submitted October 30, 1998; accepted for publication November 5, 1998)
Fiz. Tekh. Poluprovodn. **33**, 759–763 (June 1999)

We report on a study characterizing internal losses and the gain in InGaAsSb/InAsSbP diode-heterostructure lasers emitting in the mid-infrared ($3-4\ \mu$m). Numerical simulations of the current dependence of the intensity of spontaneous emission above the laser threshold and of the differential quantum efficiency allowed us to determine the intraband absorption $k_0 \approx 5.6\times 10^{-16}\,\mathrm{cm}^2$. The cavity-length dependence of the threshold current is used to estimate the internal losses at zero injection current $\alpha_0 \approx 5\ \mathrm{cm}^{-1}$. Calculations of the internal losses at laser threshold showed that they increase more than fourfold when the cavity length is decreased from 500 μm to 100 μm. The temperature dependence of the differential quantum efficiency is explained on the assumption that intraband absorption with hole transitions into a split-off band occurs. It is shown that the maximum operating temperature of ''short-cavity'' lasers is determined by the intraband absorption rather than by Auger recombination. The internal losses are shown to have a linear current dependence. The separation of the quasi-Fermi levels as a function of current demonstrates an absence of voltage saturation of the $p-n$ junction above threshold. © *1999 American Institute of Physics.*[S1063-7826(99)02806-9]

1. INTRODUCTION

At present, injection lasers are in wide use in spectroscopy,[1] in atmospheric pollution monitoring, and in fiber-optic transmission lines.[2] The wavelength range $3-4\ \mu$m subtends the absorption bands of many industrial and natural gases, the most interesting of which are methane CH_4 and formaldehyde H_2CO. In view of this circumstance, to advance the state of the art of spectroscopy in this spectral range, studies of loss mechanisms are needed to guide the development of low-threshold diode lasers, in particular, lasers based on InAs and solid solutions similar to it in composition.

One peculiarity of the band structure of InAs and solid solutions similar to it in composition is similarity of the values of the band gap E_g and spin-orbit splitting energy Δ. Therefore, the generated radiation undergoes strong absorption by holes which are excited into the spin-detached band. In Ref. 3 a microscopic analysis was carried out for the above-mentioned intraband absorption (IA), where it was shown that intraband absorption can be comparable with the gain for interband transitions from the conduction band to the valence band, and peculiarities in the temperature dependence of the differential quantum efficiencies were predicted. The internal losses in type-II lasers based on InAs/GaSb/InGaSb/GaSb superlattices ($\lambda = 3.02\ \mu$m) were measured in Ref. 4. It was shown there that the internal losses increase rapidly with increasing temperature and limit the operation of the laser at high temperatures more strongly than Auger recombination or device heating.

In this study we continue the investigation begun earlier[5,6] on mesa-stripe lasers based on InGaAsSb/InAsSbP double heterostructures (DHS) emitting in the spectral range $3.0-3.6\ \mu$m. We experimentally estimate the intraband absorption and internal losses at threshold and obtain the spectral dependence of the gain. We show that intraband absorption leads to a number of peculiarities of the laser characteristics.

2. OBJECTS OF STUDY AND EXPERIMENTAL PROCEDURE

Double heterostructures, consisting of an undoped n-InAs (111)A substrate ($n = 1-2\times 10^{16}\,\mathrm{cm}^{-3}$) and three epitaxial layers, were grown by liquid-phase epitaxy: a wideband cladding layer adjacent to the substrate, consisting of n-$InAs_{1-x-y}Sb_xP_y$ ($0.05 \leqslant x \leqslant 0.09$, $0.09 \leqslant y \leqslant 0.18$), the active layer of the laser, consisting of n-$In_{1-v}Ga_vAs_{1-w}Sb_w$ ($v \leqslant 0.07$, $w \leqslant 0.07$), and a wideband contact layer/emitter, consisting of p-(Zn)-$InAs_{1-x-y}Sb_xP_y$ ($0.05 \leqslant x \leqslant 0.09$, $0.09 \leqslant y \leqslant 0.18$). The thicknesses of the wideband layers ranged from 4 to 6 μm, and of the active layer d, from 1 to 4 μm. The lasers had a deep mesa-stripe design with stripe widths $w = 10$ and 20 μm.

Electroluminescence spectra and current–power characteristics were measured in the temperature range $77-160$ K using a technique described earlier in Ref. 5.

The gain spectra were obtained by processing the spontaneous emission spectra using values of the laser wavelength and internal losses at laser threshold.[7,8] ''Net'' gain spectra were obtained from the relation between the maxima and minima of the Fabry–Perot resonances in the spontaneous emission spectra.[9]

3. EXPERIMENTAL RESULTS AND DISCUSSION

A. Internal losses and differential quantum efficiency

The current–power characteristics of the lasers were sublinear (Fig. 1). We associated the decrease in the differential quantum efficiency η_d with the increase in the internal losses α_i:

 © 1999 American Institute of Physics

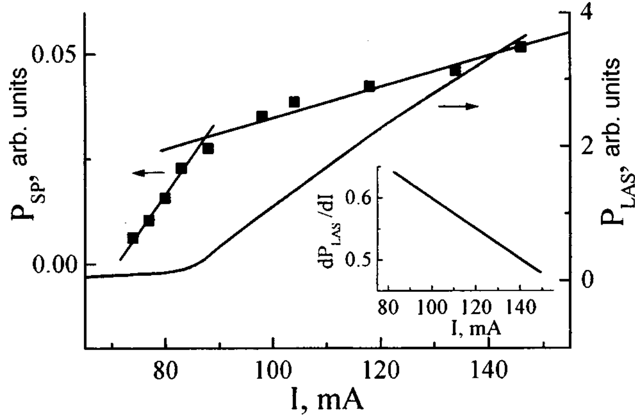

FIG. 1. Current dependence of the total intensity of spontaneous P_{SP} and laser P_{LAS} emission ($T=77$ K, $L=300$ μm); the inset plots the differential quantum efficiency as a function of the current.

$$\frac{d(1/\eta_d)}{dI}=\frac{L}{\eta \ln (1/R)}\frac{d\alpha_i}{dI},$$

where L is the cavity length, R is the reflection coefficient, and η is the internal quantum yield (η=0.75, Ref. 10),

$$\alpha_i=\Gamma(\alpha_0+\alpha_{FC}+k_0N)+(1-\Gamma)\alpha_c,$$

where α_0 are the ''intrinsic'' losses (losses in the active region in the absence of injection), α_{FC} is absorption on free carriers ($\alpha_{FC}\sim 1-2$ cm^{-1}, Ref. 11), k_0 is the intraband absorption coefficient, N is the injection carrier density, Γ is the optical confinement parameter (Γ=0.6), and α_c is the absorption in the cladding layers ($\alpha_c\sim\alpha_0$). As the current increases beyond the laser threshold, the intensity of spontaneous emission P_{SP} was found to increase with simultaneous decrease of η_d (Fig. 1). This increase is approximated by the dependence[12]

$$\frac{dP_{SP}}{dI}=2\frac{P_{SP}(I_{th})}{N_{th}}\frac{dN}{dI},$$

where $P_{SP}(I_{th})$ is the intensity of spontaneous emission at laser threshold, and N_{th} is the threshold concentration ($N_{th}=2\times10^{17}$ cm^{-3}). Using the relation

$$k_0=\frac{1}{\Gamma}\frac{d\alpha_i}{dN}=\frac{1}{\Gamma}\frac{d\alpha_i}{dI}\frac{dI}{dN},$$

we obtain a value for the intraband absorption coefficient: $k_0\approx5.6\times10^{-16}$ cm^2. The latter exceeds by more than an order of magnitude the value for lasers with an InGaAsP active region ($\lambda=1.55$ μm) (Ref. 12), in which resonance of E_g and Δ is absent.

The magnitude of the intrinsic losses α_0 was determined from the dependence of the threshold current density J_{th} on the inverse cavity length $1/L$ (Fig. 2a) (Ref. 13):

$$J_{th}=\frac{J_0 d}{\eta}+\frac{d}{\eta\Gamma\beta}\left(\alpha_i+\frac{1}{L}\ln\frac{1}{R}\right),$$

where J_0 is the nominal current density at the ''inversion threshold,'' d is the thickness of the active region, and β is the differential gain. We obtained the value $\alpha_0\approx5$ cm^{-1}.

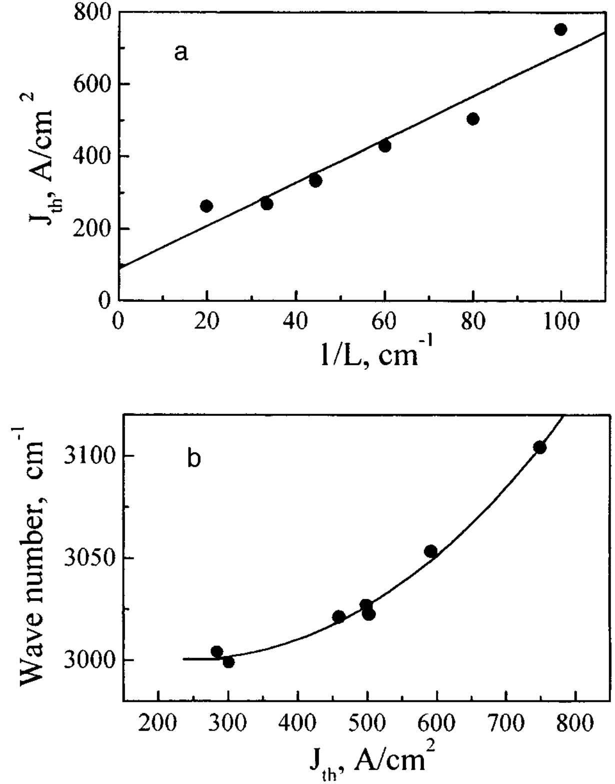

FIG. 2. Threshold current density versus inverse cavity length (a); spectral-threshold characteristic (b) ($T=77$ K).

The low value of α_0 reflects the structural perfection of the quaternary solid solution InGaAsSb, well matched with the substrate.[14]

With decreasing cavity length, the increase in the threshold carrier density as a result of the increase in the output losses leads to an increase in the intraband absorption and to a steeper dependence of $J_{th}(1/L)$ than in the absence of intraband absorption. For lasers with $L=100$, 200, 300, and 500 μm and $T=77$ K, Table I lists threshold current densities J_{th}; threshold currents I_{th}, threshold carrier densities calculated using the relation $N_{th}=J_{th}\tau/ed$ ($\tau=10^{-8}$ s); the internal losses at laser threshold $\Gamma k_0 N_{th}$ due to intraband absorption; the internal losses at laser threshold α_i^{th}; the differential quantum efficiencies, calculated in accordance with α_i^{th}, and the increase in the internal losses above the laser threshold for the current above the laser threshold by $\Delta I=10$ mA. As can be seen, the intraband absorption increases with increasing carrier density, and for $L=100$ μm is comparable with the gain attained in semiconductor lasers. This explains the similarity in the values of η_d in lasers with different L, where

TABLE I.

L, μm	J_{th}, A/cm^2	I_{th}, mA	N_{th}, cm^{-3}	$\Gamma k_0 N_{th}$, cm^{-1}	α_i^{th}, cm^{-1}	η_d	$\Delta\alpha_i^{10mA}$, cm^{-1}
100	750	15	5×10^{17}	169	174	0.3	45
200	360	14	2.4×10^{17}	81	86	0.31	23
300	235	14	1.6×10^{17}	54	59	0.3	15
500	172	17	1.1×10^{17}	37	42	0.27	9

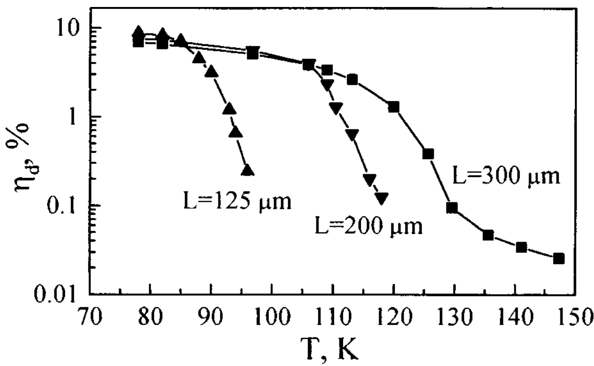

FIG. 3. Temperature dependence of the differential quantum efficiency of lasers with cavity lengths $L=125$, 200, and 300 μm.

an increase in the losses due to intraband absorption with decreasing cavity length L exceeds the increase in the output losses with decreasing L. The obtained values of α_i ($L=300\,\mu$m) turned out to be similar to values given for lasers based on the double heterostructure InAsSbP/InAsSb/InAsSbP, studied in the same spectral range ($\alpha_i=80-130\,\mathrm{cm}^{-1}$) (Ref. 15). The experimental values of the differential quantum efficiency ($\eta_d=7-15\%$) are $2-3$ times lower than those shown in the table. This is apparently due to the exaggerated value of the internal quantum yield ($\eta=0.75$) used in the calculation.

Figure 2b shows the spectral–threshold characteristic obtained from measurements of homotypic lasers with different cavity lengths. With growth of the threshold current density, the gain spectrum shifts toward shorter wavelengths, as is reflected in a shift of the laser line. The relatively large range over which the laser wave number varies ($\Delta\tilde{\nu}\approx 100\,\mathrm{cm}^{-1}$) is apparently due to the fact that lasing takes place between states in the tails of the bands, where their densities are relatively small.

Figure 3 shows the temperature dependence of the differential quantum efficiency of lasers with $L=125$, 200, and 300 μm. Raising the temperature causes the internal quantum yield to decrease due to an increase in the Auger recombination rate, which is reflected in the segments of approximately identical slope of $\eta_d(T)$ for lasers with different values of L. A further increase in the temperature gives rise to a situation in which, with decreasing cavity length, η_d falls off steeply, indicating that in this temperature region the slope of $\eta_d(T)$ is determined by the increase in internal losses. It is likely that at $T=120-130$ K the photon energy $h\nu$ is close to the spin–orbit splitting energy Δ, and that intraband absorption is maximum. As a consequence of temperature narrowing of the band gap at $T>130$ K, the photon energy $h\nu$ becomes less than Δ, intraband absorption saturates, and an inflection point appears. In this case, the slope of $\eta_d(T)$ is determined by Auger recombination and above-barrier leakage currents.

B. Gain

Figure 4 plots spontaneous emission spectra (a) and gain spectra (b) obtained from them[7,8] ($T=80$ K, $L=300\,\mu$m). The spontaneous emission spectrum, i.e., the spectrum of the spontaneous emission leaving the cavity through the mirror

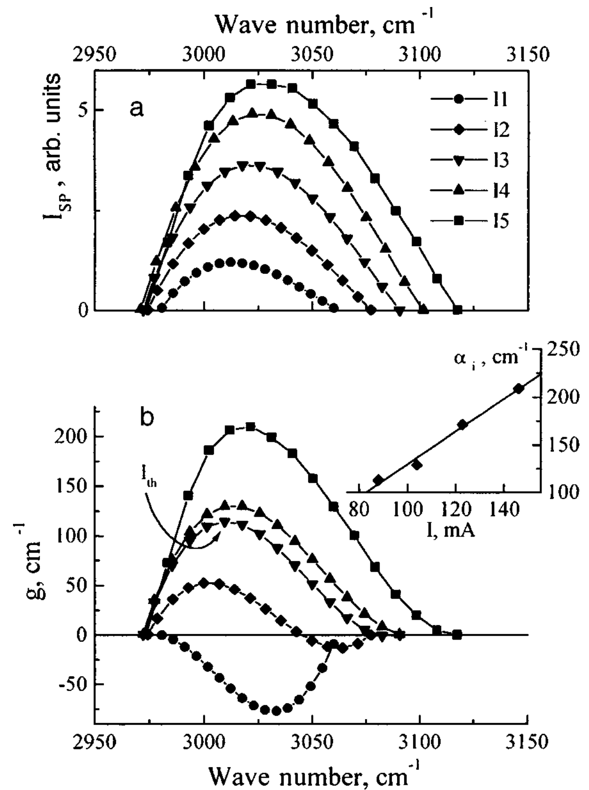

FIG. 4. Spontaneous emission spectra (a) and gain spectra (b) for currents, mA: *I1* — 74, *I2* — 80, *I3* — 88, *I4* — 104, *I5* — 146; the inset plots the current dependence of the total losses ($T=80$ K).

facets, can deform with increasing current because of the gain, with its shape approaching a Gaussian centered on the maximum of the gain line; therefore, in our analysis of the data we fitted the spectra on segments far removed from the laser line. In the laser regime the condition of equality of the gain and the total losses $g=\alpha_i+\alpha_r$ is satisfied. With growth of the current from 85 to 150 mA, the spectral maximum of the gain was found to increase from 110 to 210 cm^{-1}, which, taking $\alpha_r\sim 40\,\mathrm{cm}^{-1}$ into account, gives the result that α_i increases from 70 to 170 cm^{-1}. The growth of α_i with current and, correspondingly, with minority carrier density (see inset) is linear, consistent with the conclusion that intraband absorption is responsible for the increase in the internal losses.

In the calculation of the gain spectra we obtained a value for the separation of the Fermi quasilevels (ΔF) equal to $\Delta F=381$ meV at the laser threshold for the laser photon energy $h\nu=373$ meV and voltage drop across the structure $U=546$ mV. As the current is increased from 85 to 150 mA, the separation of the Fermi quasilevels increases to $\Delta F=386$ meV.

Figure 5 plots net gain spectra (a), the current dependence of the spectral gain maximum and of the gain itself at different wave numbers (b), obtained from the relation between the maxima and minima of the Fabry–Perot resonances. The net gain spectra were obtained for currents $I=140-220$ mA ($I_{\mathrm{th}}=192$ mA, $\Gamma=0.6$, $\alpha_r=44\,\mathrm{cm}^{-1}$). For $I\leqslant I_{\mathrm{th}}$ the current dependence of the gain at fixed wave number and of the wave number of the maximum gain is nearly

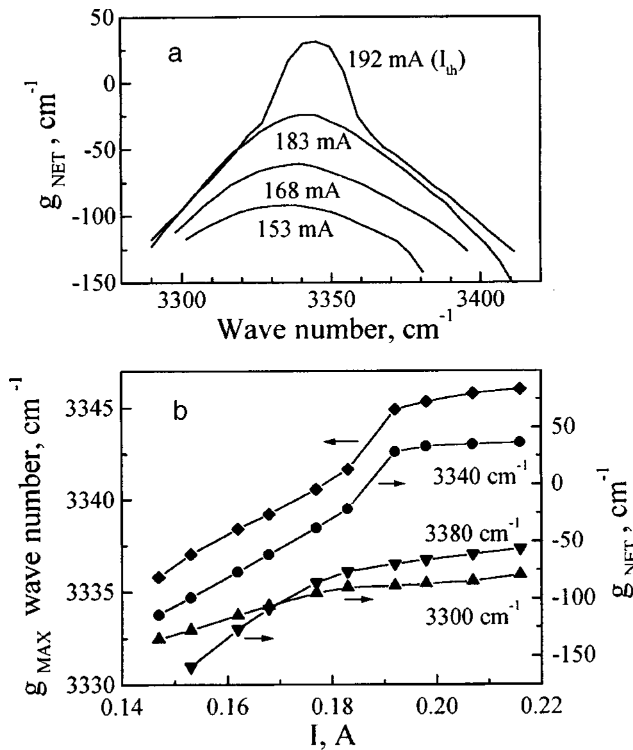

FIG. 5. ''Net'' gain spectrum (a), current dependence of the maximum spectral gain and the gain at different wave numbers (b) ($T = 80$ K).

linear, which suggests that doping of the active region is light.[16] The gain above laser threshold does not saturate completely, spreading toward large energies and increasing at the laser wave number, probably because of a degradation of the optical confinement caused by a decrease in the difference of refractive indices due to an increase in the minority carrier density above laser threshold. With increase of the wave number, the rate of growth of the gain with current grows, as could be expected, if the gain is associated with states whose density grows with energy.

C. Effect of intraband absorption on the laser parameters

The linear dependence of the internal losses on the minority carrier density and the saturation of the internal losses indicate that the main loss mechanism is intraband absorption. Its presence leads to a number of peculiarities characteristic of the given lasers: 1) an increase in the threshold current density with decreasing cavity length, which takes place more rapidly than if it were associated only with an increase in output losses; 2) a decrease in the differential quantum efficiency with decreasing cavity length; 3) limitation of the maximum working temperature of short-cavity lasers; 4) a sublinear current–power characteristic; 5) an increase in the separation of the Fermi quasilevels above threshold, manifested in an absence of saturation of voltage in the current–voltage characteristics; 6) a growth in the intensity of spontaneous emission above threshold and a degradation of optical confinement due to an increase in the minority carrier density.

It is clear that the increase in the minority carrier density above threshold, which is caused by an increase in the internal losses, decreases the refractive index of the active region and can thus lead to a large current retuning of the laser wavelength. This question goes beyond the scope of the present paper and will be discussed in a separate paper.

4. CONCLUSIONS

In summary, we have shown that the main loss mechanism in InGaAsSb/InAsSbP-based lasers that emit in the spectral range $3-4\ \mu$m is intraband absorption by holes with their transition to the spin-orbit-split band. The intraband absorption coefficient $k_0 \approx 5.6 \times 10^{-16}\ \mathrm{cm}^2$ turned out to be more than an order of magnitude larger than the published values for InGaAsP ($\lambda = 1.55\ \mu$m), which is due to the closeness of the band-gap energy and the spin–orbit splitting energy in solid solutions based on InAs. At the same time, the internal losses in the absence of injection amounted to $\alpha_0 \approx 5\ \mathrm{cm}^{-1}$, which is evidence of a high level of crystalline perfection of the fabricated structures. In short-cavity lasers the internal losses at threshold become comparable with the gain attained in semiconductor lasers; therefore, the maximum working temperature is governed by intraband absorption rather than by Auger recombination.

We wish to thank T. Beyer of the Fraunhofer Institute for Physical Measurement Techniques (IPM) for assistance in the measurement of the spectral characteristics of the lasers. We also thank Yu. P. Yakovlev for interest in this work.

This work was supported by the Ministry for Science and Technology Program of the Ministry of Science of the Russian Federation, ''Optics. Laser Physics,'' Project No. 4.14.

[1] R. U. Martinelli, Laser Focus World , 77 (1996).
[2] C. H. L. Goodman, Solid State Electron. Dev. **12**(5), 129 (1978).
[3] N. A. Gun'ko, G. G. Zegrya, N. V. Zotova, Z. N. Sokolova, N. M. Stus', and V. B. Khalfin, Fiz. Tekh. Poluprovodn. **31**, 1396 (1997) [Semiconductors **31**, 1407 (1997)].
[4] W. W. Bewley, C. L. Felix, I. Vurgaftman, J. R. Meyer, C.-H. Lin, S. J. Murry, D. Zhang, S. S. Pei, and L. R. Ram-Moham, J. Appl. Phys. **83**(5), 2384 (1998).
[5] M. Aĭdaraliev, N. V. Zotova, S. A. Karandashev, B. A. Matveev, M. A. Remennyĭ, N. M. Stus', and G. N. Talalakin, Pis'ma Zh. Tekh. Fiz. **24**(12), 40 (1998) [Tech. Phys. Lett. **24**, 35 (1998)].
[6] M. Aĭdaraliev, N. V. Zotova, S. A. Karandashev, B. A. Matveev, M. A. Remennyĭ, N. M. Stus', and G. N. Talalakin, Fiz. Tekh. Poluprovodn. **33**(2), 233 (1999) [Semiconductors **33**, 130 (1999)].
[7] C. H. Henry, R. A. Logan, and F. R. Merritt, J. Appl. Phys. **51**(6), 3042 (1980).
[8] V. P. Gribkovskiĭ, *Semiconductor Lasers* [in Russian], Minsk Univ. Press, Minsk, 1988.
[9] B. W. Hakki and T. L. Paoli, J. Appl. Phys. **44**(9), 4113 (1973).
[10] M. Aĭdaraliev, Author's Abstract, Candidate's Dissertation (A. F. Ioffe Physicotechnical Institute, Leningrad, 1991).
[11] J. Dixon and J. Ellis, Phys. Rev. **123**, 1560 (1961).
[12] I. Joindot and J. L. Beylat, Electron. Lett. **29**(7), 604 (1993).
[13] N. C. Gasey, Jr. and M. B. Panise, Heterostructure Lasers, Part A (Academic Press, New York, 1978).
[14] T. S. Argunova, R. N. Kyutt, B. A. Matveev, S. S. Ruvimov, N. M. Stus', and G. N. Talalakin, Fiz. Tverd. Tela **36**, 3071 (1994) [Phys. Solid State **36**, 1633 (1994)].
[15] A. A. Popov, V. A. Sherstnev, and Yu. P. Yakovlev, Fiz. Tekh. Poluprovodn. **32**, 1139 (1998) [Semiconductors **32**, 1240 (1998)].
[16] B. W. Hakki and T. L. Paoli, J. Appl. Phys. **46**, 1299 (1973).

Translated by Paul F. Schippnick

PERSONALIA

In Memory of Vadim Fedorovich Masterov

Fiz. Tekh. Poluprovodn. **33**, 764–765 (June 1999)
[S1063-7826(99)02906-3]

On January 28, 1999 Professor Vadim Fedorovich Masterov, distinguished scientist in the field of solid state physics, chairman of the experimental physics department of St. Petersburg State Technical University and doctor of physical and mathematical sciences, passed away unexpectedly at the age of 58.

Vadim Fedorovich was born December 17, 1941 in the city of Arkhangelsk. In 1959 after completing secondary school, he entered Leningrad Polytechnical Institute (LPI). From that time on without interruption, his entire life was connected with LPI, which was later renamed St. Petersburg State Technical University (SPbSTU). First, he was admitted into the department of mechanics and machine building and later, because of his great interest in physics, he transferred to the department of physics and mechanics. After graduating from the institute in 1964 with specialization in metal physics and metallurgy, he was admitted into the department of physics and mechanics of LPI to pursue work inexperimental physics. There he consecutively undertook the duties of a junior scientist (1965–1966), senior engineer (1966–1975), senior scientist and deputy chairman of the department in charge of scientific work (1975–1982), and then professor (1982–1991). Starting in 1991, Masterov assumed the position of chairman of the department. In 1971 he defended his dissertation in pursuit of the candidate's degree, and in 1979 he became doctor of physical and mathematical sciences.

The area of scientific interests of Masterov included solid state physics (the physics of semiconductors, high-temperature superconductivity, and the physics of fullerenes). In these fields he published more than 200 original scientific papers in domestic and foreign journals, two monographs, and five review articles in the journals ***Physics and Technology of Semiconductors*** and ***Solid State Physics***.

His experimental and theoretical studies of the electronic structure of deep multielectron centers in semiconductors won him international acclaim, and the results of these studies were incorporated into monographs and review articles by Soviet and foreign authors. In 1980, Masterov and coworkers were the first to record photoluminescence, and in 1982 electroluminescence on intracenter transitions in III–V semiconductors doped with rare-earth elements. In those years they used the method of electron spin resonance to investigate the structure of a series of impurity centers created by rare-earth elements in indium phosphide. His studies of the electronic structure of iron group and rare-earth impurities in semiconductors have become classics. In those studies, in particular, he demonstrated the potential of using rare-earth-doped semiconductors to create coherent and incoherent infrared sources. At present, work in this direction has advanced in the scientific centers of many countries, and two volumes of conference papers on "Rare-Earth-Doped Semiconductors," which include papers presented by Masterov, have been published (in the Proceedings of the Materials Research Society, USA, 1993 and 1996). In 1993 he proposed and laid the groundwork for the use of low-dimensional semiconductor structures for enhancing the efficiency of $f-f$ emission. In 1996 he (together with G. G. Zegrya) theoretically demonstrated the possibility of creating a laser emitting at 1.54 μm based on the erbium-doped heterostructure InP/InGaAsP/InP with two types of quantum wells.

From 1987 onward, Masterov took an active part in the study of high-temperature superconductivity of complex copper metal-oxides, and in 1992 the superconductivity of metal fullerenes. He was one of the first to suggest that high-

1063-7826/99/33(6)/2/$15.00 © 1999 American Institute of Physics

temperature superconductors be treated as a multiple Josephson medium. The phenomenon of microwave absorption in superconductors containing internal Josephson junctions was discovered in his laboratory, simultaneously with its discovery by other research groups in Russia and abroad and independently of them. Together with A. G. Aronov, he proposed and developed an original method for investigating violations of time reversal symmetry in high-temperature superconductors. Masterov and coworkers developed a new method for investigating the charge-density spatial distribution in complex copper metal-oxides based on emission Mössbauer spectroscopy. The most interesting result in the field of fullerene physics may be considered to be the discovery of a high-temperature superconducting phase in copper-based metal fullerene with a record superconducting transition temperature of 120 K for fullerenes.

On Masterov's initiative, a laboratory for electron spectroscopy was created in the department of experimental physics (under the direction of Prof. Yu. A. Mamaev), in which unique high-vacuum experimental setups were developed and built for studying solids by slow-electron polarization spectroscopy. Under Masterov's direction, a theoretical group was organized in his laboratory in which such well-known physicists—including professors and department chairmen—as V. K. Ivanov, V. G. Karpov, D. A. Parshin, A. V. Subashiev, and V. A. Kharchenko continue to work.

Masterov's scientific activity was inseparably associated with the leading scientific centers of Russia and several foreign countries. He carried out scientific research together with scientists at the A. F. Ioffe Physicotechnical Institute (RAS), the S. I. Vavilov State Optical Institute, the St. Petersburg Institute of Nuclear Physics (RAS), the Institute of Silicate Chemistry (RAS), the Scientific-Research Institute ''Domain,'' and also with scientists in the USA, Germany, Holland, and Italy. Starting in 1994, Masterov was a consultant for the University of Arizona (Tucson, USA), in 1995–1996 he held a contract with the European Office of Aerospace Research and Development (London, UK), and he took part in projects funded by a grant from INTAS–RFBR together with scientists of the Physicotechnical Institute (RAS), the Physical Institute (RAS), SPbSTU, the University of Milan (Italy), and the University of Amsterdam (Holland).

Masterov was a member of the organizing committees and program committees of many international and national conferences and seminars. He was a member of the editorial board of the journal ***Physics and Technology of Semiconductors***, and was a member of the Scientific Committee on Fullerenes and Atomic Clusters, the State Program ''Current Problems in Condensed-Matter Physics,'' and the scientific committee and the scientific-technical committee of SPbSTU. He was a member of the Materials Research Society (USA) and the International Society of Researchers on Electron Spin Resonance in Semiconductors (Holland).

Masterov took an active part in the scientific-methodological work of SPbSTU. He was the author of 32 studies on scientific methodology and methods of instruction, including six textbooks. On his initiative, with the support of the dean of the graduate school, and under his leadership and with direct active participation, the instructional physics laboratory of the university was modernized at the end of the 1970s. The practical work in physics at LPI became one of the best in the country, for which it received the Diploma of First Rank in VDNKh of the USSR in 1979. Together with I. P. Ipatova, Masterov revised the general physics curriculum and prepared a textbook for it for publication. In 1992–1997 he was a member of the scientific-methodological committee on physics for the Ministry of Higher Education and joined the scientific-methodological committe of SPbSTU. In 1994, on his initiative a new program granting bachelor's and master's degrees with specialization in physics (in the field of condensed-matter physics) was opened in the department of experimental physics, a plan was developed and a series of special courses was prepared for students with this specialization.

Masterov did a great service in the preparation of highly qualified scientific professionals. Sixteen Candidate's Dissertations were successfully defended under his direct scientific guidance, and four Doctor's Dissertations were successfully defended with his support.

The shining memory of Vadim Fedorovich Masterov, who dedicated himself fully to science and education, will forever be preserved in the hearts of his many students, friends, and colleagues.

Zh. I. Alferov, Yu. S. Vasil'ev, A. G. Zabrodskiĭ, B. P. Zakharchenya, I. P. Ipatova, F. P. Kesamanly, V. V. Kozlovskiĭ, V. N. Kolgatin, V. I. Perel', V. V. Emtsev, C. A. J. Ammerlaan, and S. Pizzini.

Editorial Board of the Journal Physics and Technology of Semiconductors.

Translated by Paul F. Schippnick